Dissertation

submitted to the
Combined Faculties of Natural Sciences and for Mathematics
of the Ruperto-Carola University of Heidelberg, Germany
for the degree of
Doctor of Natural Sciences

Put forward by
MSc. Mischa Herbert Joseph Ismael Breuhaus
born in Stühlingen, Germany
Oral examination: July 28$^{\text{th}}$, 2022

Towards an Understanding of Galactic Ultra-high Energy γ-ray Emission

Abstract

Just recently, we are starting to explore the γ-ray sky at energies above 100 TeV. A detailed understanding of the emission at these extreme energies is therefore of paramount importance. γ rays at these energies are produced by highly energetic particles, the so-called cosmic rays. This thesis investigates three different aspects related to the ultra-high energy emission.

The first aspect concerns the leptonic or hadronic origin of sources at these energies. While the suppression of inverse Compton emission at these energies disfavours a leptonic origin, it is shown that in environments with sufficiently high radiation energy densities or low magnetic fields, leptonic ultra-high energy emitters are possible. Furthermore, the viability of such leptonic emitters is confirmed by modelling newly detected sources in this energy regime.

The second aspect concerns hadronic emission, specifically the effects of different compositions of the hadronic particles producing γ rays at these energies. These effects are thoroughly investigated in this thesis. It is shown that the presence of heavier cosmic ray species decreases the resulting emission and shifts spectral features to lower energies. The influence of different compositions on the diffuse Galactic emission at ultra-high energies is investigated. For this use case, the composition can have an important influence on the resulting γ-ray and neutrino production. The models are compared to current data. Although current measurements do not allow to constrain the composition of the Galactic cosmic rays, future observations will be able to do so.

For the third aspect, the particle acceleration and γ-ray emission by colliding stellar winds is investigated. This is done in the case of the colliding wind binary η Carinae. The developed time-dependent model is able to explain the resulting flux and variability properties of the emission detected from η Carinae. The γ-ray emission is likely produced by the collisions of accelerated hadronic particles and not by electrons. The variability in the X-ray emission is explained by the inhibition of electron injection and heating during the closest approach of the two stars.

Einleitung

Erst seit Kurzem beginnen wir den Himmel im γ-Strahlenbereich bei Energien über 100 TeV zu erkunden. Ein detailliertes Verstehen der Emissionsprozesse bei diesen Energien ist deshalb von höchster Bedeutung. γ-Strahlung mit solch hohen Energien wird durch hochenergetische Teilchen erzeugt, den sogenannten kosmischen Strahlen. Diese Dissertation untersucht drei verschiedene Aspekte, die mit der Ultrahochenergiestrahlung zusammenhängen.

Der erste Aspekt betrifft den leptonischen oder hadronischen Ursprung von Gammastrahlenquellen bei diesen Energien. Während die Unterdrückung der inversen Comptonstrahlung bei hohen Energien leptonische Quellen benachteiligt, wird hier gezeigt, dass in Umgebungen mit genügend hoher Strahlungsenergiedichte oder geringen Magnetfeldern leptonische Ultrahochenergiestrahlung möglich ist. Des Weiteren wird die Realisierbarkeit solcher leptonischer Quellen durch die Modellierung von kürzlich entdeckten γ-Strahlenquellen bestätigt.

Der zweite Aspekt betrifft die hadronische Emission, insbesondere die Effekte verschiedener Teilchenarten an der produzierten Strahlung. In dieser Arbeit werden diese Effekte gründlich untersucht. Es wird gezeigt, dass die Gegenwart von schwereren Atomkernen die resultierende Emission vermindert und spektrale Merkmale zu niedrigeren Energien verschoben werden. Der Einfluss der elementaren Zusammensetzung für die galaktische diffuse Emission wird ebenfalls untersucht. In diesem Fall kann die Zusammensetzung der kosmischen Strahlen einen bedeutenden Einfluss auf die Produktion der γ-Strahlen haben. Die Modelle werden mit Daten verglichen. Obwohl gegenwärtige Beobachtungen es noch nicht möglich machen die Zusammensetzung der galaktischen kosmischen Strahlung einzuschränken, werden zukünftige Beobachtungen dazu in der Lage sein.

Für den letzten Aspekt wurde die Teilchenbeschleunigung und die γ-Strahlenemission in sogenannten Colliding Wind Binaries untersucht. Dies wird am Beispiel des Colliding Wind Binary Systems η Carinae gemacht. Das entwickelte zeitabhängige Modell ist in der Lage den resultierenden Strahlungsfluss und die Variabilität der Beobachtungen des η Carinae Systems zu erklären. Die γ-Strahlung wird wahrscheinlich durch Kollisionen von beschleunigten hadronischen Teilchen produziert und nicht von Elektronen. Die Variabilität der Röntgenstrahlung kann durch eine Behinderung der Elektroneninjektion in den Beschleunigungsprozess und des Aufheizens während des engsten Kontaktes der beiden Sterne erklärt werden.

Acknowledgements

Contents

1 Introduction

Since the early times of human history, people have looked up into the sky, wondering about the phenomena they saw. With the invention of optical telescopes, they were able to take a closer look at individual objects and find out more about their origin and the physical processes taking place. However, the human eye is only sensitive to a small part of the electromagnetic spectrum, and most of the radiation emitted by astrophysical objects is invisible to us. At the highest energies, above more than a hundred thousand times the energies of the optical band we see with our naked eyes, lies the γ-ray regime.

Because γ rays are blocked by the atmosphere, they have to be observed either from space, or indirectly by observations of air showers. These air showers are created when a γ-ray photon enters the atmosphere. First detections of γ rays were made with the Explorer XI satellite (Kraushaar & Clark, 1962). Then, the first γ-ray bursts were detected by the Vela spacecraft (Klebesadel et al., 1973), and the first observations of the Galactic plane were achieved with the OSO-3 satellite (Kraushaar et al., 1972). These observations were constantly improved by following missions, such as the second Small Astronomy Satellite (SAS-2, Fichtel et al., 1975), the COS-B mission (Bignami et al., 1975), the Energetic Gamma Ray Experiment Telescope (EGRET, Hartman et al., 1999), or the International Gamma-Ray Astrophysics Laboratory (INTEGRAL, Winkler, 1995). Today, the Large Area Telescope onboard the Fermi satellite is one of the most important γ-ray observatories (Fermi-LAT, Atwood et al., 2009), observing at energies from 20 MeV up to more than 300 GeV.

Observations at higher energies are performed not with space-based observatories, but with ground-based observatories to detect γ-ray induced air showers. Current facilities are, for example, the High Energy Stereoscopic System (H.E.S.S., Hinton & HESS Collaboration, 2004), the Major Atmospheric Gamma Imaging Cherenkov telescope

(MAGIC, Bigongiari, 2005), the Very Energetic Radiation Imaging Telescope Array System (VERITAS, Krennrich et al., 2004), the High-Altitude Water Cherenkov observatory (HAWC, DeYoung & HAWC Collaboration, 2012), the Tibet ASγ experiment (Huo et al., 1990), and the recently completed Large High Altitude Air Shower Observatory (LHAASO, di Sciascio & Lhaaso Collaboration, 2016; Bai et al., 2019). More data from LHAASO and the future Southern Wide-field Gamma-ray Observatory (Albert et al., 2019; Huentemeyer et al., 2019) and the Cherenkov Telescope Array (CTA, CTA Consortium et al., 2019) will improve current measurements significantly.

γ rays are produced by accelerated particles, the so-called cosmic rays (CRs). CR particles are also directly observed on Earth (e.g. The Pierre Auger Collaboration et al., 2015). However, they are deflected and scattered in turbulent magnetic fields of the interstellar medium (ISM), and as a result, the directional information about their birthplace is largely lost. Nevertheless, the CRs diffusing in the Milky Way interact with the material of the ISM and produce the diffuse Galactic emission. Direct CR measurements provide an invaluable tool to help to predict this diffuse emission. On the other hand, γ-ray observations can help to constrain the CR spectrum and density throughout the Milky Way. Hence, CR physics and γ-ray astronomy are two entangled and complementing research fields. γ-ray observations do reveal not only diffuse emission, but also emission from distinct Galactic and extragalactic sources. In fact, since the spectrum of the diffuse CRs is steeper than the spectra produced at individual sources, the Galactic diffuse emission becomes less prominent at higher energies (e.g. Funk, 2015). γ-ray observations of individual sources can give insights into the most extreme places and events in the universe. Since γ rays probe environments impossible to produce in experiments, their observations are also important for fundamental questions of other research areas, such as constraining theories about Lorentz invariance violation (e.g. Satunin, 2021) and searches for dark matter (e.g. Esmaili & Serpico, 2021). To increase our understanding of γ-ray sources and the related processes, it is crucial to combine γ-ray measurements with astronomical observations in other wavelength regimes.

To push γ-ray observations to higher and higher energies is a challenging task. Recently, we started to explore the γ-ray sky above 100 TeV, which is crucial to reveal the origin of the most energetic Galactic particle accelerators. The first detection of sources above these energies was achieved by the HAWC collaboration, which published the first catalogue of such sources in 2020 (Abeysekara et al., 2020). Figure 1.1 shows the Galactic
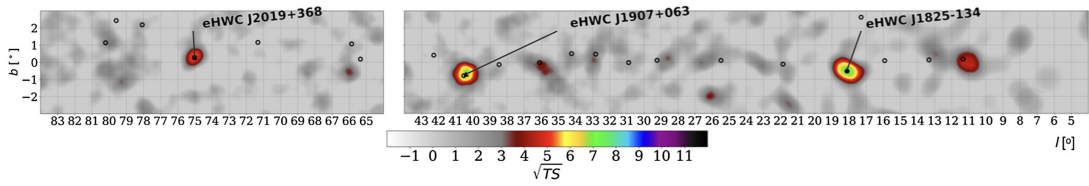
FIGURE 1.1: γ-ray emission above 100 TeV in the Galactic plane observed by the HAWC collaboration. Credits: Abeysekara et al. (2020).

γ-ray sky above 100 TeV from Abeysekara et al. (2020) with only three significantly detected sources. These observations were followed by the LHAASO observatory, which announced the detection of 12 souces above 100 TeV (Cao et al., 2021). New detections of sources in this energy regime are constantly achieved. For example, the Tibet ASγ collaboration detected the Cygnus cocoon above energies of 100 TeV (Amenomori et al., 2021a), and announced the detection of diffuse emission (Amenomori et al., 2021b). The famous Crab Nebula was detected until energies of up to 1.1 PeV by the LHAASO collaboration (Lhaaso Collaboration et al., 2021). With more observation time from HAWC, LHAASO, and the future Southern Wide-field Gamma-ray Observatory (SWGO) and CTA, the highest energy γ-ray sky will be explored in even better detail, and more ultra-high energy (UHE, >100 TeV) Galactic γ-ray sources will be discovered. Possible source candidates are pulsar wind nebulae (PWN), supernova remnants (SNRs), and also star-forming regions (SFRs). All of them are associated with astrophysical shocks: the pulsar wind interacting with the remainings of the previous supernova explosion or the interstellar medium, shock waves from the remnants of supernova explosions, or shocks created by combined stellar winds from massive stars. This makes shock acceleration seem to be the most likely acceleration process for particles generating UHE γ rays (the acceleration processes will be discussed in Section 2.4). However, the origin of the γ-ray sources at these energies is not clear yet and poses many questions. In this thesis, I investigated and studied three different aspects of these questions.

The first question deals with a potential leptonic origin of UHE γ-ray sources. γ-ray emission is produced by leptonic as well as hadronic accelerated particles. Accelerated leptonic particles can produce γ rays in very extreme cases via synchrotron emission, but usually via Bremsstrahlung and inverse Compton scattering of low energy photons. Accelerated protons or heavier nuclei in our Galaxy produce γ rays mainly via collisions

with other particles in the interstellar medium (for details about the emission mechanisms, see Section 2.1). Synchrotron emission is usually not important at very-high energies, because the energies required by the particles producing the radiation have to be many orders of magnitude larger. For Bremsstrahlung being dominant over IC emission, one would need very large densities in the ambient medium. Therefore, IC emission is generally expected to be the dominant UHE emission mechanism for leptons. If the energy of the photon to be scattered, transformed into the electron rest frame, is comparable to the electron rest mass, recoil effects become important. These recoil effects suppress the cross-section of the scattering process compared to lower energies. This makes hard spectra from IC emission only possible, if the accelerated electrons or positrons follow a sufficiently hard power-law distribution. Emission from protons or heavier nuclei does not have this suppression and therefore is often associated with emission above 100 TeV. One part of this thesis is devoted to answer the question whether sites facilitating UHE γ-ray emission produced by leptonic IC emission exist in our Galaxy (Chapter 3).

The second aspect which needs a special investigation concerns the effects caused by different compositions of accelerated particles. If γ rays are produced by collisions of CR nuclei with ambient matter, the composition of the CRs and the ambient medium will affect the produced spectrum, which is often ignored in high energy γ-ray astrophysics. These effects are of exceptional interest in the case of the diffuse Galactic emission at energies above $\sim$100 TeV. At these high energies, the composition of the CR spectrum at Earth is unknown due to the difficulty of inferring it from air showers. Measuring γ rays or neutrinos could provide an independent probe of the composition and probably also allow to detect changes in the composition across the Galaxy, which is impossible with direct CR measurements on Earth. Thus, the second subject of this thesis deals with the question of how γ-ray and neutrino spectra are influenced by the composition, and if future observatories might be able to detect such changes (Chapter 4).

The last question being addressed in this thesis is related to UHE γ-ray production in SFRs. Observations of the CR spectrum at Earth reveal a softening of the spectral index above energies of $\sim$1 PeV, the so-called 'knee'. This feature could be induced by the rigidity dependent cutoff of accelerated particles from one class of Galactic sources

accounting for the bulk of CRs below the knee. Although SNRs were suggested to be this source type (e.g. Ginzburg & Syrovatskii, 1964), there is so far no observational evidence showing that they indeed are the dominant sources for the acceleration of particles up to PeV energies (see e.g. Aharonian et al., 2019). Furthermore, current theories of shock acceleration struggle to explain acceleration up to such energies during the later phases of the SNR evolution (e.g. Bell et al., 2013). On the contrary, recent observations indicate that SFRs or young massive star clusters emit γ rays above 100s of TeV (e.g. Aharonian et al., 2019; Abeysekara et al., 2021; Amenomori et al., 2021a). SFRs have a high supernova explosion rate. Additionally, the combined winds of massive stars can create multiple shocks, where particles are accelerated (see e.g. Bykov et al., 2020, and references therein). To interpret the γ-ray emission and particle acceleration induced by massive stars is of paramount importance. To understand the particle acceleration from collisions of combined stellar winds better, it will be tremendously beneficial to understand the emission from binary systems, whose winds are colliding and accelerating particles. Additionally, these binary systems might be good candidates to test current particle acceleration theories, investigate the effects of CR composition, and study their escape into the ISM. The latter point is especially important for the possible significant contribution of massive star clusters to the Galactic CR spectrum. η Carinae is the only conclusively detected colliding wind binary system in γ rays, although there is strong evidence for γ-ray emission from γ^2 Velorum (Pshirkov, 2016; Martí-Devesa et al., 2020). The third part of this thesis is, therefore, dedicated to explore the non-thermal emission from the η Carinae system and its possible implications for particle acceleration theories (Chapter 5).

The thesis is organized as follows: In Chapter 2 I give a concise overview of the relevant background. The following three chapters deal with the three research projects. First, the investigation of possible sites for leptonic γ-ray emission in the Milky Way is outlined in Chapter 3. This chapter is followed by the exploration of the effects of different hadronic species on the production of γ rays and neutrinos given in Chapter 4. Lastly, the non-thermal emission mechanisms in the colliding wind binary system η Carinae are explored in Chapter 5. Finally, the results are discussed in Chapter 6.

All figures in Chapter 2 were produced by myself, except Figure 2.9, which was taken from Cerutti & Beloborodov (2017).

In Chapter 3, I acknowledge the preparatory work by Joachim Hahn and Jim Hinton. Brian Reville initially did the calculations presented in Section 3.2.1, and the derivation of the upper limits from IRAS data in Section 3.4 was done by Richard Tuffs. I also made use of the implementation of the $\gamma\gamma$ absorption coefficient in the GAMERA Code by Carlo Romoli.

In Chapter 4, I acknowledge the contribution of Jim Hinton for the parametrisation of the γ-ray spectra in Section 4.3 and for Figure 4.5.

The analysis of the Fermi-LAT data in Chapter 5 was done by Richard White. He also wrote the code for Figure 5.3 and Figure 5.5, which was modified by me to make the two figures in this thesis, and I acknowledge preparatory work from him for Figure 5.4. Modifications to the Code from Ohm et al. (2015) were done by Stefan Ohm and Ruslan Konno, and Brian Reville contributed significantly to the physical considerations described in Section 5.2. I also acknowledge the calculation of secondary electrons from $\gamma\gamma$ pair production by Francesco Conte used in Section 5.2.6 and the preparatory work from Joachim Hahn for the implementation of anisotropic IC scattering into the GAMERA code.

2 Background

2.1 Non-thermal radiation emission mechanisms and other interaction processes

2.1.1 Synchrotron radiation

Electrons gyrating around magnetic field lines produce electromagnetic waves, the so-called synchrotron radiation. This process was extensively studied in many articles (e.g. Schwinger, 1949; Westfold, 1959; Ginzburg & Syrovatskii, 1965; Blumenthal & Gould, 1970).

An electron with energy E_e and a pitch angle θ, which is the angle between the velocity vector and the magnetic field direction, will lose energy at a rate of (e.g. Blumenthal & Gould, 1970)

$$-\frac{\mathrm{d}E_e}{\mathrm{d}t} = 2\sigma_T c U_B \left(\frac{E_e}{m_e c^2}\right)^2 \sin^2(\theta). \tag{2.1}$$

Here, c is the speed of light, $U_B = B^2/8\pi$ is the magnetic energy density for a magnetic field with strength B, and m_e is the electron mass. σ_T is the Thomson cross-section for the electron,

$$\sigma_T = \frac{8\pi}{3}\left(\frac{e^2}{m_e c^2}\right)^2 = \frac{8\pi}{3}r_0^2 = 6.6524 \times 10^{-25}\,\mathrm{cm}^2, \tag{2.2}$$

where e is the elementary charge and r_0 the classical electron radius. In astrophysical environments, the pitch angle θ is expected to be randomised due to, for example, irregularities in the magnetic field. Therefore, averaging Equation 2.1 over different

pitch angles gives the total electron energy loss rate

$$-\frac{\mathrm{d}E_\mathrm{e}}{\mathrm{d}t} = \frac{4}{3}\sigma_\mathrm{T} c U_\mathrm{B} \left(\frac{v}{c}\right)^2 \left(\frac{E_\mathrm{e}}{m_\mathrm{e} c^2}\right)^2. \tag{2.3}$$

The energy lost by the electron is transferred to electromagnetic radiation. Thus, the total amount of emitted radiation is proportional to B^2. In the relativistic case, the total synchrotron power emitted by a single electron has the following spectrum (e.g. Blumenthal & Gould, 1970, in units of $\mathrm{erg\,s^{-1}\,Hz^{-1}}$):

$$P_\nu(\gamma) = \frac{\sqrt{3}e^3 B \sin(\theta)}{m_\mathrm{e} c^2} F\left(\frac{\nu}{\nu_\mathrm{c}}\right). \tag{2.4}$$

The function F is defined as $F(x) = x \int_x^\infty K_{5/3}(x')\mathrm{d}x'$, where $K_{5/3}$ is the modified Bessel function of order $5/3$. ν is the frequency of the emitted radiation, and ν_c the so-called critical frequency,

$$\nu_\mathrm{c} = \frac{3}{4\pi}\gamma^2 \frac{eB}{m_\mathrm{e} c} \sin(\theta). \tag{2.5}$$

The function F peaks close to $\nu = \nu_\mathrm{c}$ and a large part of the total power is emitted at the frequency ν_c. To obtain the total synchrotron spectrum, one has to integrate $P_\nu(\gamma)$ over the whole electron distribution.

For power-law distributed electrons $\propto E^{-\alpha}$, the resulting synchrotron power also follows a power-law (e.g. Blumenthal & Gould, 1970):

$$\frac{\mathrm{d}E}{\mathrm{d}\nu \mathrm{d}t} \propto B^{(\alpha+1)/2} \nu^{-(\alpha-1)/2}. \tag{2.6}$$

Hence, the spectral number density follows a power-law of $\mathrm{d}N_\gamma/(\mathrm{d}E \mathrm{d}t) \propto E^{-(\alpha+1)/2}$.

Figure 2.1 shows the spectral energy distribution from electrons distributed as $\mathrm{d}N_\mathrm{e}/\mathrm{d}E_\mathrm{e} \propto E_\mathrm{e}^{-\alpha}\exp(-E_\mathrm{e}/E_\mathrm{cut})$. Above $1\,\mathrm{GeV}$, the total electron energy was $10^{40}\,\mathrm{erg}$, and the electrons were assumed to be located at a distance of $1\,\mathrm{kpc}$. The magnetic field was taken to be $5\,\mu\mathrm{G}$. The synchrotron spectrum follows a power-law with a cutoff above few $10^{-9}\,\mathrm{TeV}$. Only in very extreme cases, synchrotron emission can reach the γ-ray regime. The process is mainly important as an energy loss mechanism rather than a source of γ-ray production.
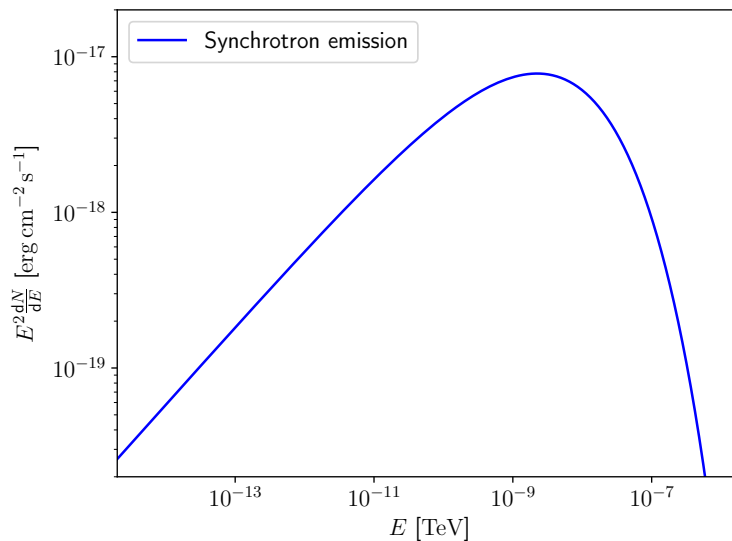
FIGURE 2.1: Synchrotron emission from exponential cutoff power-law distributed electrons. The power-law index is $\alpha = 2$ and the cutoff energy $100\,\mathrm{TeV}$. The total energy in electrons above $1\,\mathrm{GeV}$ is $10^{40}\,\mathrm{erg}$, and the tentative source is located at a distance of $1\,\mathrm{kpc}$. The magnetic field was set to $5\,\mathrm{\mu G}$.

Synchrotron radiation also occurs for other charged particles and behaves identically for electrons and positrons. Since the cross-section scales with $1/m^2$ (m is the mass of the particle), the synchrotron losses or emissions are usually negligible for protons.

2.1.2 Inverse Compton scattering

Inverse Compton (IC) scattering occurs during the interaction of accelerated electrons with photons. In the scattering process, the electron transfers energy to the photon and the photon can transform into a γ-ray. The case of isotropically distributed electrons and photons was investigated in detail by Jones (1968); Blumenthal & Gould (1970); Coppi & Blandford (1990). In the electron rest frame, the energy of the incident photon is (e.g. Blumenthal & Gould, 1970)

$$E'_{\mathrm{rad}} = \gamma E_{\mathrm{rad}}(1 - \beta \cos\theta) \tag{2.7}$$

with the Lorentz factor $\gamma = E_{\mathrm{e}}/(m_{\mathrm{e}}c^2)$, $\beta = v/c$, and the angle θ between the electron and the photon. E_{rad} is the energy of the photon in the laboratory frame, and E'_{rad} the energy in the electron rest frame. If the rest mass energy of the electron is large compared to the energy of the photon in the electron rest frame, $E'_{\mathrm{rad}} \ll m_{\mathrm{e}}c^2$, the

electron will not suffer significant recoil effects. This approximation is the so-called Thomson limit. The energy of the photon after scattering in the electron rest frame will be approximately the same, $E'_\gamma \approx E'_{\mathrm{rad}}$, where E'_γ is the energy of the photon after scattering in the electron rest frame. To get the resulting γ-ray photon energy in the lab frame, another Lorentz transformation has to be done.

On average, the transformation into the electron rest frame increases the photon energy by a factor of γ. The same applies to the backwards transformation. Therefore, the resulting photon energy in the lab frame after the scattering process in the Thomson regime is approximately $E_\gamma \sim \gamma^2 E_{\mathrm{rad}}$. Although this is a huge increase in energy, it is still small compared to the electron energy. The total energy loss rate in the Thomson regime for a monochromatic isotropic photon field can be approximated with (Blumenthal & Gould, 1970)

$$-\frac{\mathrm{d}E_{\mathrm{e}}}{\mathrm{d}t} = \frac{4}{3}\sigma_{\mathrm{T}}cU_{\mathrm{rad}}\left(\frac{E_{\mathrm{e}}}{m_{\mathrm{e}}c^2}\right)^2.\tag{2.8}$$

$U_{\mathrm{rad}} = E_{\mathrm{rad}}n_{\mathrm{rad}}$ is the energy density of the photon field, with the photon number density n_{rad}, and $\sigma_{\mathrm{T}} = \frac{8\pi}{3}r_0^2$ the Thomson cross-section with the classical electron radius r_0. The energy loss rate in the Thomson regime directly allows to compute a more accurate estimate of the mean photon energy, resulting in $\langle E_\gamma \rangle = \frac{4}{3}\gamma^2 \langle E_{\mathrm{rad}} \rangle$.

The photon production rate for isotropically distributed photons in the Thomson regime is (Jones, 1968)

$$\frac{\mathrm{d}N_{\gamma,E_{\mathrm{rad}}}}{\mathrm{d}t\mathrm{d}E_\gamma} = \frac{\pi r_0^2 c}{2\gamma^4}\frac{n_{\mathrm{rad}}(E_{\mathrm{rad}})\mathrm{d}E_{\mathrm{rad}}}{E_{\mathrm{rad}}^2}\left(2E_\gamma \ln\left(\frac{E_\gamma}{4\gamma^2 E_{\mathrm{rad}}}\right) + E_\gamma + 4\gamma^2 E_{\mathrm{rad}} - \frac{E_\gamma^2}{2\gamma^2 E_{\mathrm{rad}}}\right).\tag{2.9}$$

In the general case, where the Thomson approximation can not be applied, modifications to the calculations taking into account the recoil of the electron and quantum mechanical effects are required. This gives (Jones, 1968):

$$\frac{\mathrm{d}N_{\gamma,E_{\mathrm{rad}}}}{\mathrm{d}t\mathrm{d}E_1} = \frac{2\pi r_0^2 m_{\mathrm{e}}c^3}{\gamma}\frac{n_{\mathrm{rad}}(E_{\mathrm{rad}})\mathrm{d}E_{\mathrm{rad}}}{E_{\mathrm{rad}}}\cdot\left[2q\ln(q) + (1+2q)(1-q) + \frac{1}{2}\cdot\frac{(\Gamma q)^2}{1+\Gamma q}(1-q)\right]$$
$$\text{with}\qquad \Gamma = 4E_{\mathrm{rad}}\gamma/mc^2,\qquad q = E_1/\Gamma(1-E_1),\qquad E_1 = \frac{E_\gamma}{\gamma m_{\mathrm{e}}c^2}.\tag{2.10}$$

To obtain the total γ-ray flux, one has to integrate over the electron and photon energy distributions:

$$\frac{\mathrm{d}N_{\mathrm{tot}}}{\mathrm{d}t\mathrm{d}E_\gamma} = \int \int N_{\mathrm{e}}(\gamma)\mathrm{d}\gamma \left(\frac{\mathrm{d}N_{\gamma,E_{\mathrm{rad}}}}{\mathrm{d}t\mathrm{d}E_\gamma} \right). \tag{2.11}$$

Note that the term $\frac{\mathrm{d}N_{\gamma,E_{\mathrm{rad}}}}{\mathrm{d}t\mathrm{d}E_\gamma}$ defined in Equation 2.10 already contains the term $\mathrm{d}E_{\mathrm{rad}}$ used for the second integral.

The parameter Γ in Equation 2.10 determines the regime of the scattering process. In the Thomson limit, $\Gamma \ll 1$ and Equation 2.10 reduces to Equation 2.9. The other extreme case is $\Gamma \gg 1$, the so-called Klein-Nishina limit. In this regime, the energy loss rate for monochromatic photons can be approximated with (Blumenthal & Gould, 1970)

$$-\frac{\mathrm{d}E_{\mathrm{e}}}{\mathrm{d}t} = \frac{3}{8} \frac{\sigma_{\mathrm{T}} m_{\mathrm{e}}^2 c^5 n_{\mathrm{rad}}}{E_{\mathrm{rad}}} \left(\ln \left(\frac{4E_{\mathrm{rad}}\gamma}{m_{\mathrm{e}}c^2} \right) - \frac{11}{6} \right). \tag{2.12}$$

Comparing the above equation with the energy loss rate in the Thomson regime (Equation 2.8), the losses in the Klein-Nishina regime increase only logarithmically with the electron energy. In each collision, the electron transfers a very large fraction of its energy to the γ-ray. This is again different from the Thomson regime, where the electron only loses a small fraction of its energy.

For electrons $\propto E_{\mathrm{e}}^{-\alpha}$, the resulting shape of the γ rays follows a power-law distribution, too. In the Thomson regime, the γ rays are $\propto E_\gamma^{-(\alpha+1)/2}$, and in the Klein-Nishina regime $\propto E_\gamma^{-(\alpha+1)}$. Thus, the transition from the Thomson to the Klein-Nishina regime introduces a break in the resulting γ-ray spectrum, and the emission will soften at higher energies.

Figure 2.2 shows the IC spectrum from exponential cutoff power-law distributed electrons $\propto E_{\mathrm{e}}^{-\alpha} \exp(-E_{\mathrm{e}}/E_{\mathrm{cut}})$. The power-law index was set to $\alpha = 2$ and the cutoff energy to $100\,\mathrm{TeV}$. The normalisation of the spectrum corresponds to a total energy in electrons above $1\,\mathrm{GeV}$ of 10^{40} erg, located at a distance of $1\,\mathrm{kpc}$. The photon field was assumed to have a temperature of $5 \times 10^3\,\mathrm{K}$ and an energy density of $3\,\mathrm{eV\,cm^{-3}}$. The spectral break around few hundred GeV corresponds to the transition from the Thomson to the Klein-Nishina regime. Below the break, the γ rays have a power-law index of $-\frac{3}{2}$, which occurs as an index of $-\frac{3}{2} + 2 = \frac{1}{2}$ in the $E^2\mathrm{d}N/\mathrm{d}E$ plot. The spectrum softens
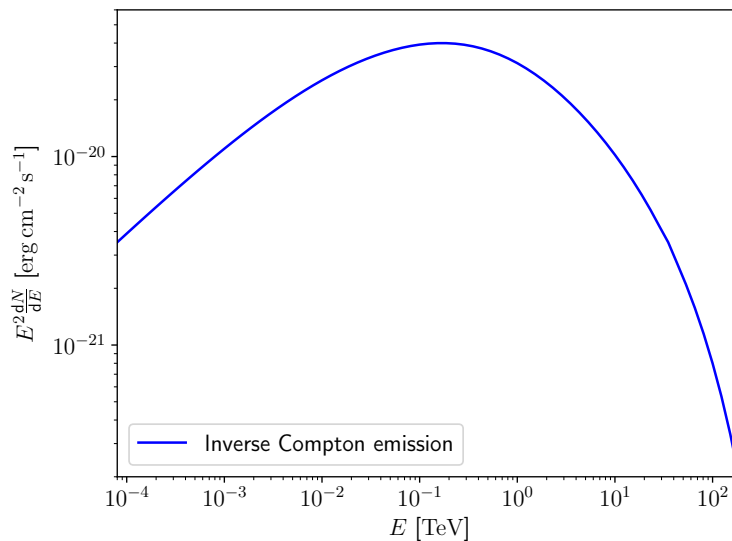
FIGURE 2.2: Inverse Compton emission from exponential cutoff power-law distributed electrons. The power-law index is $\alpha = 2$ and the cutoff energy $100\,\mathrm{TeV}$. The total energy in electrons above $1\,\mathrm{GeV}$ is $10^{40}\,\mathrm{erg}$, and the tentative source is located at a distance of $1\,\mathrm{kpc}$. The photon field was assumed to have a temperature of $5 \times 10^3\,\mathrm{K}$ and an energy density of $3\,\mathrm{eV\,cm^{-3}}$.

to a power-law with an index of -3 in the Klein-Nishina regime. This softening nearly masks the cutoff close to $100\,\mathrm{TeV}$.

2.1.3 Bremsstrahlung

Relativistic electrons traversing matter are deflected by the electric fields of atoms, ions and molecules. In this process, the electron with initial energy E_0 emits a photon with an energy $\hbar\omega$ ($\hbar$ is the reduced Planck constant and $\omega = 2\pi\nu$ the angular frequency). The final electron energy is $E_1 = E_0 - \hbar\omega$. The cross-sections for these interactions were calculated by Bethe & Heitler (1934). In general, the differential cross-section $\mathrm{d}\sigma$ depends on the type of particle participating in the reaction. For an unshielded static charge Ze and for large energies compared to $m_\mathrm{e}c^2$, the differential cross-section is

$$\mathrm{d}\sigma = 4Z^2\alpha_\mathrm{F}r_0^2\frac{\mathrm{d}\omega}{\omega}\frac{1}{E_0^2}(E_0^2 + E_1^2 - \frac{2}{3}E_0E_1)\left(\ln\frac{2E_0E_1}{m_\mathrm{e}c^2\hbar\omega} - \frac{1}{2}\right), \qquad (2.13)$$

where Z is the charge number of the interacting atom, α_F the fine-structure constant and r_0 the classical electron radius. For the general case, the cross-section is where Z is the charge number of the interacting atom, α_F the fine-structure constant and r_0 the

classical electron radius. For the general case, the cross-section is

$$d\sigma = \Phi(E_\gamma)dE_\gamma = \alpha_F r_0^2 \frac{dE_\gamma}{E_\gamma} \frac{1}{E_0^2} \cdot \left(\left(E_0^2 + E_1^2 \right) \phi_1 - \frac{2}{3} E_0 E_1 \phi_2 \right). \tag{2.14}$$

Here, $E_\gamma = E_0 - E_1$ and ϕ_1 and ϕ_2 are functions of E_0, E_1 and E_γ. The exact shape of ϕ_1 and ϕ_2 depends on the type of environment.

The total Bremsstrahlung γ-ray emission is calculated as

$$\frac{dN}{dtdE_\gamma} = c \sum_i n_i \frac{d\sigma_i}{dE_\gamma}. \tag{2.15}$$

The index i stands for the respective particles, and $\frac{d\sigma_i}{dE_\gamma} = \Phi_i(E_\gamma)$ is given by Equation 2.14 with the respective funtions $\phi_{j(i)}$, with $j \in \{1, 2\}$. n_i is the corresponding number density of the environment. The energy loss rate

$$-\frac{dE_e}{dt} = \int dE_\gamma E_\gamma \frac{dN}{dtdE_\gamma}$$

can not always be calculated analytically. However, the approximate energy transfer to a γ-ray photon is $E_\gamma = \frac{1}{2}E_0$. With this simplification and with $\phi_1 \approx \phi_2$, the energy loss rate is (e.g. Blumenthal & Gould, 1970)

$$-\frac{dE_e}{dt} \approx \alpha_F r_0^2 c \left[\sum_i n_i \phi_{(i)}(E_\gamma) \right] E_0. \tag{2.16}$$

Hence, the energy losses are approximately proportional to the electron energy.

For power-law distributed electrons ($dN/dE_e \propto E_e^{-\alpha}$), the resulting γ-ray spectrum also follows a power-law with essentially the same spectral index as the electrons, $dN/dE_\gamma \propto E_\gamma^{-\alpha}$. Figure 2.3 shows the γ-ray spectrum of electrons distributed according to an exponential cutoff power-law with $\alpha = 2$ and $E_{cut} = 100\,\text{TeV}$. The normalisation corresponds to a total energy of electrons above $1\,\text{GeV}$ of $10^{40}\,\text{erg}$, a source distance of $1\,\text{kpc}$, and a hydrogen ISM with a number density of $1\,\text{cm}^{-3}$. The emission follows a power-law with an index approximately the same as the electron spectrum, and a cutoff at $\approx E_{cut}/2$.
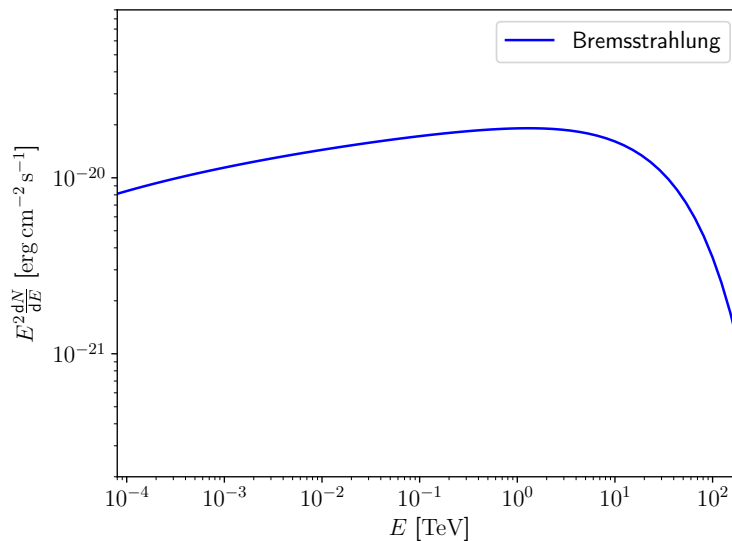
FIGURE 2.3: Bremsstrahlung spectrum from electrons distributed according to an exponential cutoff power-law. The power-law index is $\alpha = 2$ and the cutoff energy 100 TeV. The total energy in electrons above 1 GeV is 10^{40} erg, and the tentative source is located at a distance of 1 kpc. The number density of the ISM was taken to be $1\,\mathrm{cm}^{-3}$.

2.1.4   Ionisation and excitation losses

Additionally to the emission of Bremsstrahlung, electrons also lose energy due to excitation and ionisation of the ambient matter (Gould, 1975). For γ-ray astrophysics, the process only serves as an energy loss mechanism. Sometimes, these processes are also referred to as Coulomb interactions. Protons are subject to ionisation losses too, but in typical Galactic environments above few hundreds of MeV, losses by hadronic interactions dominate (see e.g. Schlickeiser, 2002). Hence, ionisation losses do not affect the proton spectrum relevant for the production of γ rays, and we will only talk about the energy losses for electrons. Ionisation and excitation losses for electrons are extensively discussed in Gould (1975).

In a plasma, the electron energy loss rate is (e.g. Schlickeiser, 2002)

$$-\frac{\mathrm{d}E_\mathrm{e}}{\mathrm{d}t} = \frac{3}{4}\sigma_\mathrm{T} n_\mathrm{e} m_\mathrm{e} c^3 \left[74.3 + \ln\left(\frac{E_\mathrm{e}/(m_\mathrm{e}c^2)}{n_\mathrm{e}/1\,\mathrm{cm}^{-3}}\right)\right], \qquad (2.17)$$

where n_e is the density of the plasma electrons. Since the logarithmic term in the bracket is small compared to 74.3, $\mathrm{d}E_\mathrm{e}/\mathrm{d}t$ is essentially energy independent.

In neutral matter, the energy loss rate is given by

$$-\frac{\mathrm{d}E_\mathrm{e}}{\mathrm{d}t} = \frac{9}{4}\sigma_\mathrm{T} m_\mathrm{e} c^3 \sum_i n_i Z_i \left[\ln\left(\frac{E_\mathrm{e}}{m_\mathrm{e}c^2}\right) + \frac{2}{3}\ln\left(\frac{m_\mathrm{e}c^2}{\langle\Delta E\rangle_i}\right) \right]. \qquad (2.18)$$

The index i denotes different atomic species, n_i is the corresponding number density, Z_i the number of atomic electrons, and $\langle\Delta E\rangle_i$ the mean excitation energy. For hydrogen, it is $\langle\Delta E\rangle_i = 15.0\,\mathrm{eV}$, and for helium $\langle\Delta E\rangle_i = 41.5\,\mathrm{eV}$. The logarithmic dependence of the energy loss rate is again negligible. The energy lost by the cosmic rays is transformed into an increased degree of ionisation and thermal energy of the plasma.

2.1.5 Hadronic mechanisms

The emission mechanisms discussed in the previous sections are primarily relevant for electrons and positrons. For accelerated protons or other nuclei, mechanisms like synchrotron emission still occur. However, because the proton is three orders of magnitude heavier, synchrotron emission or synchrotron losses are negligible compared to the electron. Instead, other hadronic processes and interactions are important; the two most important ones are pp and $p\gamma$ interactions. The 'p' stands for protons, but the same processes also occur for heavier nuclei. Since the protons are by far the most abundant species, in this section, we only talk about the case of interacting protons or hydrogen nuclei. The effects of heavier nuclei on the resulting γ-ray emission from pp interactions are the subject of Chapter 5 and will be discussed in detail there.

$p\gamma$ interactions are interactions of a CR proton or a nucleus with a photon. The result of such an interaction is the photo-pion or photo-meson production ($\phi\pi$), the photo-pair production (ϕe), and the photo-disintegration for heavier nuclei. In the photopion production, a pion is produced, which subsequently decays into γ rays or e^+/e^- and neutrinos. In the photo-pair production, the interaction with the photon produces an e^+-e^- pair. The last process, the photo-disintegration, can occur only for heavier nuclei. Due to the reaction with the photon, a proton, neutron, or a light nuclei escapes from the original nucleus.

The most relevant processes for the production of γ rays for this thesis stem from the pp interaction. In this process, a CR collides inelastically with a nucleus of the ambient matter. As a result, secondary particles such as pions (π^0, π^+, π^-), kaons, η-mesons

or hyperons (a baryon containing at least one strange quark, but no charm, bottom or top quark) are produced. All unstable particles decay over many different channels, and γ rays, e^+/e^- and neutrinos are produced. The most important contributors are the neutral and charged pions. Heavy particles will decay quickly into lighter ones and produce many pions. The π^0 (or other less abundant light mesons such as the η-meson) decays directly into two γ rays:

$$\pi^0 \diagup\!\!\!\diagdown \begin{matrix} \gamma \\ \gamma \end{matrix}$$
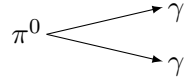
The charged pions decay into muons and neutrinos. The muons decay further into e^+/e^- and the corresponding neutrinos:

$$\pi^+ \longrightarrow \begin{matrix} \mu^+ \longrightarrow \begin{matrix} e^+ \\ \nu_e \\ \bar{\nu}_\mu \end{matrix} \\ \nu_\mu \end{matrix}$$
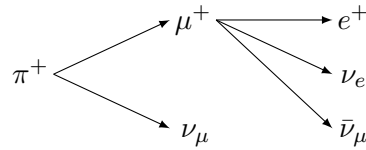
The negatively charged pions decay as follows:

$$\pi^- \longrightarrow \begin{matrix} \mu^- \longrightarrow \begin{matrix} e^- \\ \bar{\nu}_e \\ \nu_\mu \end{matrix} \\ \bar{\nu}_\mu \end{matrix}$$
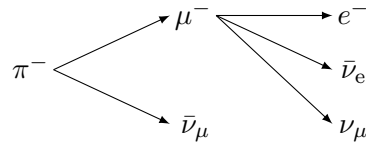
To be able to produce π^0 particles, a minimum kinetic threshold energy of

$$E_{\text{th}} = 2m_{\pi^0}c^2 \left(1 + \frac{m_{\pi^0}}{4m_{\text{p}}}\right) \approx 279.7\,\text{MeV} \tag{2.19}$$

is needed. Here, $m_{\pi^0} = 134.97\,\text{MeV}$ is the mass of the pion, and $m_{\text{p}} = 938.27\,\text{MeV}$ the proton mass. Whereas the lifetime of the π^0 is $\approx 8.4 \times 10^{-17}\,\text{s}$, the charged pions decay after $\approx 2.6 \times 10^{-8}\,\text{s}$. The amount of π^0, π^+ and π^- particles produced in the inelastic pp collisions is similar. Due to the longer decay time of the charged pions, in very high density environments, the interaction time of the π^+/π^- with the ambient matter or with photons can be shorter than the decay time. Therefore, the pions will lose energy before the decay, which can result in lower fluxes of neutrinos and e^+/e^- compared to γ rays at very-high energies.

The total inelastic cross-section σ_{inel} of the pp interaction is typically deduced from collider experiments. Different authors have suggested different parametrisations (e.g.

Kelner et al., 2006; Kamae et al., 2006; Kafexhiu et al., 2014). The newest and most accurate one stems from Kafexhiu et al. (2014), who used the so far largest dataset. They found the following parametrisation:

$$\sigma_{\text{inel}} = \left[30.7 - 0.96 \log\left(\frac{E_{\text{p}}}{E_{\text{th}}}\right) + 0.18 \log^2\left(\frac{E_{\text{p}}}{E_{\text{th}}}\right)\right] \times \left[1 - \left(\frac{E_{\text{th}}}{E_{\text{p}}}\right)^{1.9}\right]^3 \text{mb.} \quad (2.20)$$

E_{p} is the kinetic proton energy, and E_{th} the threshold energy for the π^0 production as in Equation 2.19. The left panel of Figure 2.4 shows the inelastic *pp* cross-section from Equation 2.20 compared to the cross-section from Kelner et al. (2006). Despite of small differences at energies between 1 GeV and 10 GeV and the behaviour at energies above several 100 TeV, both cross-sections show the same behaviour. After a fast increase for energies above E_{th}, σ_{inel} rises logarithmically above ~ 2 GeV.

Part of the energy lost in the inelastic collisions leads to the production of π^0. The total number of produced π^0 particles per collisions is $N_{\pi^0} = \sigma_{\text{inel}}(E_{\text{p}}) \times \langle n_{\pi^0}\rangle(E_{\text{p}})$. $\langle n_{\pi^0}\rangle(E_{\text{p}})$ is the average pion multiplicity. At low energies, $\langle n_{\pi^0}\rangle(E_{\text{p}})$ can be determined from experiments, but higher energies usually require the use of sophisticated Monte Carlo codes such as SIBYLL (Fletcher et al., 1994; Ahn et al., 2009a), QGSJET (Ostapchenko, 2006), PYTHIA (Sjöstrand et al., 2006) or GEANT (Agostinelli et al., 2003). The calculation of the resulting γ rays requires an integration over different π^0 energies taking the kinematics and the spectra of the decay products into account. For applications in astrophysics, analytical parametrisations of the whole process were derived by, for example, Kelner et al. (2006); Kamae et al. (2006); Kafexhiu et al. (2014). The total γ-ray production rate can then be calculated as an integration over the proton spectrum for energies larger than the γ-ray energy:

$$\frac{dN(E)}{dE} = cn \int_E^\infty \sigma_{\text{inel}}(E_{\text{p}}) J_{\text{p}}(E_{\text{p}}) F(E, E_{\text{p}}) \mathrm{d}E_{\text{p}}. \quad (2.21)$$

Here, n is the number density of the ambient medium, $J_{\text{p}}(E_{\text{p}})$ the proton spectrum, and $F(E, E_{\text{p}})$ the analytical parametrisation function of the production of γ rays. While the functions derived by Kafexhiu et al. (2014) can be directly plugged in into Equation 2.21, Kelner et al. (2006) define their functions in a slightly different way, such that $\mathrm{d}E_{\text{p}}$ has to be substituted with $\mathrm{d}E_{\text{p}}/E_{\text{p}}$ in Equation 2.21.

The right panel of Figure 2.4 shows the spectral energy distribution of the γ-ray emission
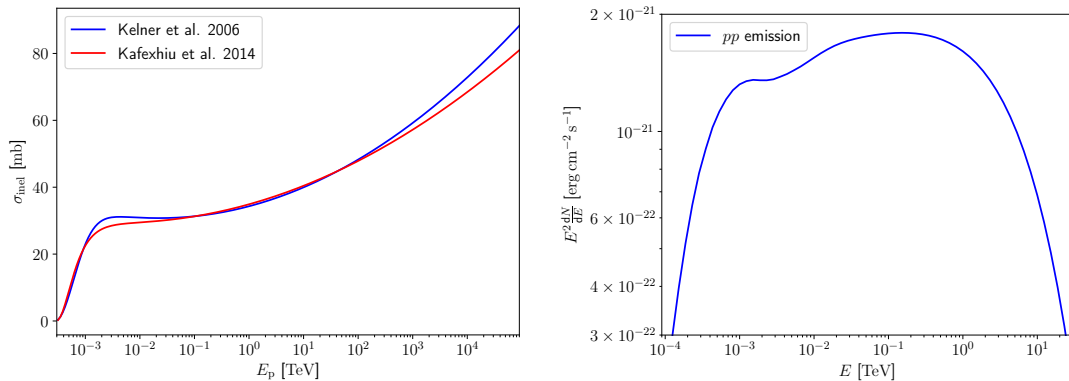
FIGURE 2.4: Left: Inelastic pp cross-sections from Kelner et al. (2006) and Kafexhiu et al. (2014). E_p is the kinetic energy of the proton. Right: γ-ray spectrum from pp collisions. The particle spectrum was an exponential cutoff power-law with $\alpha = 2$ and $E_\mathrm{cut} = 100\,\mathrm{TeV}$. The total CR particle energy was $1.0 \times 10^{40}\,\mathrm{erg}$ and the tentative source was assumed to be located at a distance of $1\,\mathrm{kpc}$ in an environment with a number density of $1\,\mathrm{cm}^{-3}$.

from pp interactions. The spectrum was calculated for exponential cutoff power-law distributed protons with a cutoff energy of $100\,\mathrm{TeV}$ and a power-law index of $\alpha = 2$. The CR particles carried a total energy of $10^{40}\,\mathrm{erg}$ and were located at a distance of $1\,\mathrm{kpc}$ in an environment with a number density of hydrogen atoms of $1\,\mathrm{cm}^{-3}$. The emission rises sharply between $\sim 100\,\mathrm{MeV}$ and $\sim 1\,\mathrm{GeV}$. This sharp rise occurs, because in the decay of the π^0, the photons always carry a minimum energy corresponding to the rest-mass energy. Slightly below $10\,\mathrm{TeV}$, there is a cutoff in the emission caused by the cutoff in the proton spectrum producing the emission. Between the sharp rise and the cutoff, the γ-ray spectrum is relatively constant with a moderate increase because of the increasing cross-section σ_inel. If instead of $E^2\mathrm{d}N/\mathrm{d}E$, the differential number density $\mathrm{d}N/\mathrm{d}E$ is plotted, the emission between the sharp rise and the cutoff declines, producing a bump-like γ-ray spectrum. Therefore, the low energy part with the sharp rise of the spectrum is called the pion bump. It is a characteristic signature of the hadronic emission process and can help to distinguish leptonic from hadronic emission observationally.

Between GeV and TeV energies, a mean fraction of $\kappa_\pi \approx 0.17$ of the proton kinetic energy is transferred to the pion (e.g. Gaisser, 1990). This explains the position of the cutoff in the γ rays at $\sim 10\,\mathrm{GeV}$ for a cutoff energy of $100\,\mathrm{TeV}$ in the proton spectrum.

The production of electrons, positrons and neutrinos from the decay of charged pions can be calculated in the same way as the production of γ rays. The only difference is, that
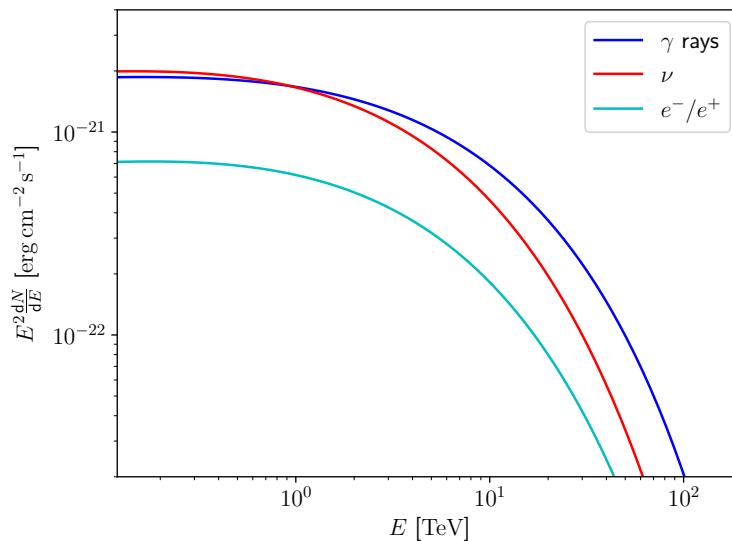
FIGURE 2.5: Comparison of spectral energy distributions of γ rays, neutrinos, and electrons/positrons. The setup was the same as in the right panel of Figure 2.4.

the function $F(E, E_\mathrm{p})$ in Equation 2.21 has to be exchanged with the respective neutrino or e^+/e^- production function. Figure 2.5 compares the production of γ rays from the right panel of Figure 2.4 with the total neutrino and e^+/e^- spectra. The calculations were done with the parametrisation from Kelner et al. (2006), which is only valid above energies of $100\,\mathrm{GeV}$. The parametrisation does not distinguish between particles and their corresponding antiparticles. Since the number of produced π^+ mesons is only slightly larger than the number of produced π^- mesons and the differences are smaller than the accuracy of the analytical approximations of the parametrisation, neglecting these effects is a valid assumption. The total neutrino production curve shown in Figure 2.5 contains all neutrino flavours.

The spectral shape of γ rays, neutrinos and electrons is very similar. However, the cutoff energies of the electrons and neutrinos are below the cutoff in the γ rays. The overall normalisation is also different. While the total neutrino emission slightly exceeds the γ-ray emission below $1\,\mathrm{TeV}$, the production of electrons is lower.

The energy losses in hadronic collisions are nearly energy independent. For an accurate calculation, an integration over all pion energies is required. However, an approximate estimate of the energy loss rate can be obtained using the mean fraction of kinetic energy

κ_π transferred to neutral pions. Neglecting any energy dependence, the loss rate is

$$-\frac{\mathrm{d}E}{\mathrm{d}t} = cn\sigma_{\mathrm{inel}}f, \tag{2.22}$$

where f is the average energy lost per interaction. Approximately the same amount of energy is lost to π^0, π^+ and π^- mesons, and thus $f \approx 3\kappa_\pi = 0.51$. If pp interactions are the dominant loss mechanism, the proton spectrum will keep its spectral shape because of the approximate energy independence of the losses.

2.1.6 $\gamma\gamma$ pair production and absorption

γ rays with sufficient energies can interact with ambient photon fields and produce an electron-positron pair. As a result, the γ-ray is lost, and this process serves as an absorption mechanism and is called $\gamma\gamma$ pair production or $\gamma\gamma$ absorption. Since a minimum energy is required for the production of the e^+/e^- pair, a strict energy threshold has to be fulfilled for the reaction to take place:

$$E_\gamma E_{\mathrm{rad}}(1 - \cos(\theta)) \geq 2m_{\mathrm{e}}c^2. \tag{2.23}$$

Here, E_γ is the energy of the γ-ray, E_{rad} the energy of the photon, and θ the angle of the collision.

Expressions of the total cross-section $\sigma_{\gamma\gamma}$ can be found for example in Gould & Schréder (1967); Agaronyan et al. (1983); Coppi & Blandford (1990); Vernetto & Lipari (2016). For the case of isotropic and monoenergetic photon fields, an approximate form with an accuracy better than 3% was derived in Agaronyan et al. (1983):

$$\sigma_{\gamma\gamma} = \frac{3\sigma_{\mathrm{T}}}{2s_0} \left[\left(s_0 + \frac{1}{2}\ln(s_0) - \frac{1}{6} + \frac{1}{2s_0} \right) \ln(\sqrt{s_0} + \sqrt{s_0 - 1}) - \left(s_0 + \frac{4}{9} - \frac{1}{9s_0} \right) \sqrt{1 - \frac{1}{s_0}} \right], \tag{2.24}$$

where $s_0 = E_\gamma E_{\mathrm{rad}}/(m_{\mathrm{e}}^2 c^4)$. Thus, the cross-section only depends on the product of the γ-ray and photon energies. Approaching the threshold energy, which corresponds to $s_0 \to 1$, $\sigma_{\gamma\gamma}$ goes to zero. For very large values of s_0, $\sigma_{\gamma\gamma} \approx 2/3\sigma_{\mathrm{T}}\ln(s_0)/s_0$ decreases. The maximum of the cross-section occurs for s_0 between 3.5 and 4 and reaches a value of $\approx 0.2\,\sigma_{\mathrm{T}}$. For each photon, there exists a range of γ-ray energies, where the absorption

is most significant. This range is at lower γ-ray energies for large values of E_{rad} and vice versa.

The optical depth is calculated by integrating over the path towards the observer and the energy spectrum of photons:

$$\tau_{\gamma\gamma}(E_\gamma) = \int_0^R \int_{E_{\mathrm{rad,min}}}^{E_{\mathrm{rad,max}}} \sigma_{\gamma\gamma}(E_\gamma, E_{\mathrm{rad}}) n_{\mathrm{rad}}(E_{\mathrm{rad}}, r) \mathrm{d}E_{\mathrm{rad}} \mathrm{d}r. \tag{2.25}$$

Here, $n_{\mathrm{rad}}(E_{\mathrm{rad}}, r)$ is the photon number density for energy E_{rad} at distance r between the minimum and maximum energies $E_{\mathrm{rad,min}}$ and $E_{\mathrm{rad,max}}$. The absorbed spectrum is multiplied with $\exp(-\tau_{\gamma\gamma})$.

The e^+/e^- pairs created in the absorption process can produce γ rays themselves and provide an additional contribution to the detected emission. The energy from the absorption is therefore not lost, but transferred to lower energies. If the pair-produced electrons emit γ rays at sufficiently high energies, these γ rays themselves can be absorbed, initiating a cascading process. An approximation for the produced spectrum of the e^+/e^- pairs for $E_{\mathrm{rad}} \ll m_{\mathrm{e}}c^2$ and $E_\gamma \gg m_{\mathrm{e}}c^2$ can be found for example in Agaronyan et al. (1983):

$$\begin{aligned}
\frac{\mathrm{d}N(E_{\mathrm{e}})}{\mathrm{d}E_{\mathrm{e}}} = \frac{3\sigma_{\mathrm{T}} m_{\mathrm{e}}^4 c^8}{32 E_{\mathrm{rad}}^2 E_\gamma^3} &\left[\frac{4E_\gamma^2}{(E_\gamma - E_{\mathrm{e}})E_{\mathrm{e}}} \ln \frac{4E_{\mathrm{rad}}(E_\gamma - E_{\mathrm{e}})E_{\mathrm{e}}}{E_\gamma m_{\mathrm{e}}^2 c^4} - \frac{8E_{\mathrm{rad}}E_\gamma}{m_{\mathrm{e}}^2 c^4} + \right. \\
&\left. \frac{2(2E_{\mathrm{rad}}E_\gamma - m_{\mathrm{e}}^2 c^4)E_\gamma^2}{(E_\gamma - E_{\mathrm{e}})E_{\mathrm{e}} m_{\mathrm{e}} c^4} - \left(1 - \frac{m_{\mathrm{e}}^2 c^4}{E_{\mathrm{rad}}E_\gamma}\right) \frac{E_\gamma^4}{(E_\gamma - E_{\mathrm{e}})^2 E_{\mathrm{e}}^2} \right].
\end{aligned} \tag{2.26}$$

The electron energy lies between the range

$$\frac{E_\gamma}{2}\left(1 - \sqrt{1 - \frac{1}{E_{\mathrm{rad}}E_\gamma}}\right) \leq E_{\mathrm{e}} \leq \frac{E_\gamma}{2}\left(1 + \sqrt{1 - \frac{1}{E_{\mathrm{rad}}E_\gamma}}\right). \tag{2.27}$$

On average, the secondary electron carries an energy of $E_\gamma/2$, but for very large values of s_0, this is not the case anymore. To obtain the total electron spectrum, Equation 2.26 has to be integrated over all γ-ray and photon energies.

2.1.7   Triplet pair production

The so-called triplet pair production (TPP) is a third-order QED process[1], in which an electron or positron interacts with a photon creating an additional electron-positron pair:

$$e + \gamma \rightarrow e + e^+ + e^-$$

Cross-sections for this reaction were calculated by several authors, for example Votruba (1948); Mork (1967); Haug (1975). A simple analytical expression for the total cross-section with a relative error less than $0.3\,\%$ was developed by Haug (1981):

$$\sigma_{\mathrm{TPP}} = \alpha_{\mathrm{F}} r_0^2 f(k), \tag{2.28}$$

where $\alpha_{\mathrm{F}} \approx 1/137$ is the fine structure constant, r_0^2 the classical electron radius and k the energy of the incident photon in the electron rest frame, expressed in units of the electron rest energy $m_{\mathrm{e}} c^2$. The form of the function $f(k)$ depends on the value of k (for the full expressions see Haug, 1981). Because it is a third order QED process, TPP is mostly subdominant compared to IC scattering and the process is normally ignored in γ-ray astronomy. However, in the Klein-Nishina regime, the IC cross-section decreases, but σ_{TPP} continuous to be logarithmically constant (see e.g. Schlickeiser, 2002). Therefore, σ_{TPP} will eventually be larger than the Klein-Nishina cross-section σ_{KN}. At collision energies satisfying $E \cdot E_{\mathrm{rad}}/(m_{\mathrm{e}}^2 c^4) \approx 250$, both cross-sections are equal (Mastichiadis, 1991). Here, E_{rad} is the energy of the photon.

Semianalytical expressions for the energy loss rate can be found, for example, in Mastichiadis et al. (1986). According to Dermer & Schlickeiser (1991), the energy loss rate can be approximated with

$$-\frac{\mathrm{d}E}{\mathrm{d}t} \cong \frac{4}{3} \alpha_{\mathrm{f}} m_{\mathrm{e}} c^3 \sigma_{\mathrm{T}} n_{\mathrm{rad}} \sqrt{\frac{E}{E_{\mathrm{rad}}}}, \tag{2.29}$$

where n_{rad} is the number density of the photons. For $E \cdot E_{\mathrm{rad}}/(m_{\mathrm{e}}^2 c^4) \geq 10^4$, the energy losses start to become comparable to IC losses, at lower energies, they can be ignored (Mastichiadis, 1991).

---

[1]QED = quantum electrodynamics

The distribution of produced particles peaks strongly at low energies $\cong E/k$. While no direct γ rays are produced in the TPP interactions, the new created electrons and positrons will radiate via IC, Bremsstrahlung and synchrotron emission. For power-law distributed electrons, the steady-state particle distribution and the produced photon spectra will become softer at high energies when the effects of triplet pair production are included. However, this will only be noticeable for particle spectra with spectral indices > -2 (Mastichiadis, 1991).

2.2   Motion in electromagnetic fields and diffusion

2.2.1   Uniform static magnetic field

A charged particle in a uniform static magnetic field with zero electric fields will follow a simple gyro-motion with a constant velocity parallel to the B-field direction and a circular motion around the field line. If m_0 is the rest mass and Ze the charge of the particle, where e is the elementary charge, the gyration radius is (see e.g. Longair, 2011)

$$r_{\mathrm{g}} = \frac{\gamma m_0 v \sin(\theta) c}{ZeB} = \left(\frac{pc}{Ze}\right) \frac{\sin(\theta)}{B} = R\frac{\sin(\theta)}{B}. \tag{2.30}$$

p is the relativistic momentum of the particle, and $R = pc/(Ze)$ is the so-called rigidity. The rigidity value determines the motion of the particle, and particles with the same value of R behave in the same way.

If additionally to the magnetic field, an electric field is present, the motion of particles will change. For an electric field $\vec{E}$ parallel to $\vec{B}$, the particle is accelerated along the field line. In the other case, if $\vec{E}$ is perpendicular to $\vec{B}$, the combined forces on the particle result in a circular motion combined with a velocity perpendicular to the magnetic and the electric field, the so-called drift velocity $\vec{v}_{\mathrm{D}}$ (e.g. Kippenhahn & Moellenhoff, 1975):

$$\vec{v}_{\mathrm{D}} = c \cdot \frac{\vec{E} \times \vec{B}}{B^2}. \tag{2.31}$$

This drift is only relevant in special environments where an unscreened electric field can exist.

In many astrophysical environments, the magnetic field will not be uniform and static. In such environments, the cosmic rays are scattered by plasma waves and in turbulent magnetic fields, which allows them to diffuse. Now, let us assume that a magnetic field line has an irregularity of size λ. If the gyroradius of a charged particle is much smaller than λ, the particle will simply gyrate around the field line and follow the B-field direction. In the case of $r_{\mathrm{g}} \gg \lambda$, the particles do not feel the disturbance and move according to the large-scale mean magnetic field. However, if r_{g} is comparable to λ, the disturbance will affect the motion of the particle.

An accurate calculation of the diffusion coefficients of relativistic particles scattered by a given spectrum of magnetic irregularities was perfomed, for example, by Jokipii (1973). Here, let us assume that the irregularities in the magnetic field are random, and their phases are randomly distributed. In this case, the particle will experience the influence of one particular component for approximately one wavelength before the next one with another random phase. Since the magnetic field in the next encounter has a different direction caused by the new irregularity, the pitch angle of the particle will change. To change the pitch angle with 1 radian, for $\delta B \ll 1$ an approximate distance of $\lambda_{\mathrm{sc}} \approx r_{\mathrm{g}} B_0^2/(\delta B)^2$ has to be traversed (see e.g. Longair, 2011). δB is the amplitude of the random component, and it is $\vec{B} = \vec{B}_0 + \delta\vec{B}$. This gives a diffusion coefficient of

$$D = \frac{v r_g}{3} \frac{B_0^2}{(\delta B)^2}. \tag{2.32}$$

The total power in magnetic field fluctuations is

$$\langle (\delta\vec{B})^2 \rangle = \int \frac{\mathrm{d}^3 k}{(2\pi)^3} A(k), \tag{2.33}$$

where $A(k)$ is the power spectrum of the turbulence and $|\vec{k}| = k = 2\pi/\lambda$ the wavenumber of the perturbations. If $A(k)$ follows a power-law $\propto k^{-q}$, the diffusion coefficient of the CRs otained from quasilinear theory follows a power-law in energy (see e.g. Schlickeiser, 2002),

$$D \propto E^{2-q}. \tag{2.34}$$

Therefore, the diffusion coefficient depends on the turbulence spectrum. In Kolmogorov turbulence it is $q = 5/3$, and in Kraichnan turbulence $q = 3/2$.

The disturbances scattering off the particles can be turbulent magnetic field lines but also plasma waves, such as Alfvén and whistler waves. The accelerated particles will interact with the waves and transfer energy to them. The waves can be excited and amplified by the CRs (see e.g. Wentzel, 1974; Bell, 1978; Cesarsky, 1980).

A lower limit on the diffusion coefficient for magnetised transport is the Bohm diffusion coefficient. In Bohm diffusion, it is assumed that the mean free path is exactly one gyro radius, leading to $D_{\mathrm{Bohm}} = r_{\mathrm{g}} c/3$ for particles moving at a velocity close to c. Often, it is convenient to parametrise D in terms of D_{Bohm} as (see e.g. Aharonian, 2004)

$$D(E) = \eta \frac{r_{\mathrm{g}} c}{3}, \qquad \text{with} \qquad \eta \geq 1, \tag{2.35}$$

where η is the ratio between $D(E)$ and D_{Bohm}.

2.2.2 Diffusion-loss equation

The general behaviour of the cosmic rays is obtained with the diffusion-loss equation. The particles will lose energy by, for example, the mechanisms discussed in Section 2.1 or can gain energy by acceleration. At the same time, they move through space by diffusion or advection processes. The total number of CRs $N(E)$ changes with time:

$$\frac{\mathrm{d}N(E)}{\mathrm{d}t} = \frac{\mathrm{d}}{\mathrm{d}E}\left[b(E)N(E)\right] + \nabla \cdot D \nabla N(E) - \nabla \cdot (\vec{v} \cdot N(E)) + Q(E,t). \tag{2.36}$$

$b(E)$ is the total energy loss rate, and $Q(E,t)$ is the injection or removal rate of accelerated particles. The first term on the right-hand side accounts for the change of the number of particles at a specific energy due to losses or energy gains, the second term for changes due to particle diffusion with the diffusion coefficient D, and the third term is the advection term.

Equation 2.36 can be solved numerically or in specific cases analytically. For example, in the absence of losses, particles injected continuously from a source diffusing radially will establish a radial profile $\propto 1/r$, where r is the radius. To propagate beyond a certain radius R, the particle will need a time (see e.g. Aharonian, 2004)

$$t_{\mathrm{diff}} = \frac{R^2}{2D(E)}. \tag{2.37}$$

upstream   downstream

$$\rho_1, v_1, p_1 \qquad\qquad \rho_2, v_2, p_2$$
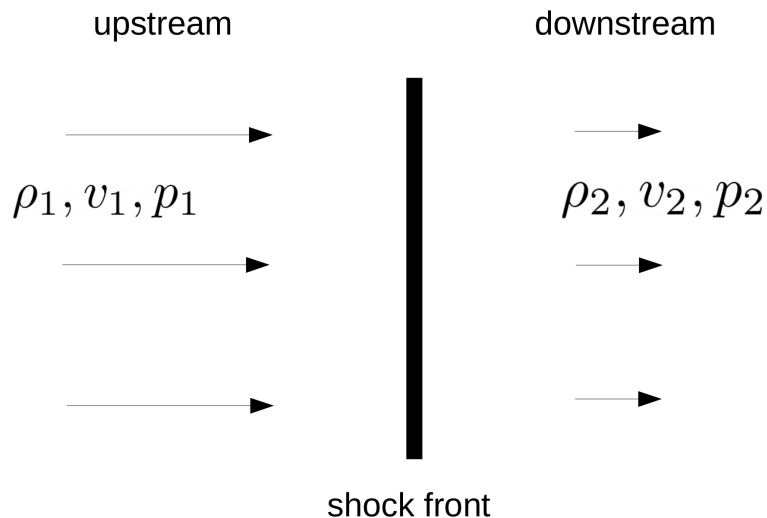
shock front

FIGURE 2.6: Sketch of a shock in the shock rest frame. The thick vertical line is the shock front, and the arrows represent the velocity vectors.

2.3   Astrophysical shocks

Astrophysical shocks play an essential role in high energy astrophysics. The most important particle acceleration process for the topics considered in this thesis is the diffusive shock acceleration. Understanding this process requires to first understand the nature of shocks. In general, a shock is a thin transition region which separates regions with different properties such as velocities, densities, pressure, temperature and magnetic field. A shock usually travels through space, such as the blast wave of a supernova explosion, but its physics can be best understood in the shock reference frame. In this frame, the shock front is at rest.

A sketch of a shock in its rest frame is shown in Figure 2.6. The thick black line represents the shock front. The flow enters from the upstream side with a density ρ_1, velocity v_1 and pressure p_1 and flows into the downstream region with a different velocity v_2, pressure p_2 and density ρ_2. For plasma shocks, there is additionally a magnetic field with field strength B_1 in the upstream region and B_2 downstream. Typically, large density or pressure gradients would dissipate, but if the flow speed into the shock is larger than small disturbances can travel, the shock will not disappear. Details about the physics of shocks relevant to astrophysics can be found, for example, in the books by Kirk et al. (1994); Schlickeiser (2002); Longair (2011); Balogh & Treumann (2013).

2.3.1 Hydrodynamical shocks

The effect of a shock on a hydrodynamic flow is to compress and heat the gas. Across the shock, the energy, momentum, and mass have to be conserved. With these requirements, one obtains the so-called Rankine-Hugoniot jump relations:

$$\frac{\rho_2}{\rho_1} = \frac{(\gamma_{\rm ad}+1)M_1^2}{2+(\gamma_{\rm ad}-1)M_1^2}, \qquad \frac{v_2}{v_1} = \frac{2+(\gamma_{\rm ad}-1)M_1^2}{(\gamma_{\rm ad}+1)M_1^2}, \qquad \frac{p_2}{p_1} = \frac{2\gamma_{\rm ad}M_1^2-(\gamma_{\rm ad}-1)}{\gamma_{\rm ad}+1}.$$

$$(2.38)$$

Here, $\gamma_{\rm ad}$ is the adiabatic index and $M_1 = v_1/c_{\rm s,1}$ is the Mach number with the speed of sound $c_{\rm s,1} = \sqrt{\gamma_{\rm ad}p_1/\rho_1}$. Due to mass conservation, $\rho_2/\rho_1 = v_1/v_2$. Different consequences follow from these equations:

- The Mach number has to be $M_1 \geq 1$,

- $v_2 \leq c_{\rm s,2}$, such that the flow is subsonic in the downstream region,

- $p_2 \geq p_1$ and $\rho_2 \geq \rho_1$, the flow is compressive,

- $v_2 \leq v_1$ and $T_2 \geq T_1$, where T_1 and T_2 are the temperatures upstream and downstream of the shock.

Therefore, the shock compresses, slows down, and heats the gas. The flow in the shock frame changes from being supersonic upstream of the shock to being subsonic in the downstream region.

For very large Mach numbers, $M_1 \gg 1$, the pressure ratio $p_2/p_1 \propto M_1^2$ theoretically could grow without limitations. In contrast, the density ratio ρ_2/ρ_1 will approach the asymptotic value $(\gamma_{\rm ad}+1)/(\gamma_{\rm ad}-1)$. For a monoatomic gas, $\gamma_{\rm ad} = 5/3$, which implies $\rho_2/\rho_1 = 4$ (or $v_1/v_2 = 4$, since $\rho_2/\rho_1 = v_1/v_2$). Such shocks are called strong shocks.

2.3.2 Magnetohydrodynamical shocks

Astrophysical shocks are magnetohydrodynamical shocks, and the magnetic field plays an important role. Typically, most shocks are collisionless, and interactions occur nearly exclusively via electromagnetic interactions. The magnetic field direction is defined with respect to the shock normal. This means, that the magnetic field of a perpendicular

shock is directed parallel to the shock front of the upstream flow. The left panel of Figure 2.7 shows a sketch of such a perpendicular shock. In a parallel shock, the B-field direction is parallel to the shock normal, as illustrated in the right panel of Figure 2.7.

We first consider the case of a perpendicular shock. Additionally to mass, momentum and energy, the magnetic flux has to be conserved across the shock front. In this case, one can obtain the following relations

$$\frac{v_1}{v_2} = \frac{\rho_2}{\rho_1} = \frac{B_{2,\perp}}{B_{1,\perp}}. \tag{2.39}$$

The shock is compressive, meaning that $\rho_2 > \rho_1$. The magnetic field direction does not change but its field strength is increased in the same way as the density. It is $1 < B_2/B_1 < (\gamma_{\mathrm{ad}}+1)/(\gamma_{\mathrm{ad}}-1)$. For $\gamma_{\mathrm{ad}} = 5/3$, the magnetic field is increased maximally by a factor of four. The flow velocity v_1 has to be larger than the magnetosonic speed of $\sqrt{c_{\mathrm{s},1}^2 + v_{\mathrm{A},1}^2}$, where $v_{\mathrm{A},1} = B_1/\sqrt{4\pi\rho_1}$ is the Alfvén speed.

Another case is the parallel shock, where the magnetic field is parallel to the shock normal. In this case, the magnetic field strength is constant along the flow, and

$$\frac{\rho_2}{\rho_1} = \frac{(\gamma_{\mathrm{ad}} + 1)M_1^2}{(\gamma_{\mathrm{ad}} - 1)M_1^2 + 2} = \frac{(\gamma_{\mathrm{ad}} + 1)M_{\mathrm{A},1}^2}{(\gamma_{\mathrm{ad}} - 1)M_{\mathrm{A},1}^2 + 2\beta_1}, \tag{2.40}$$

where β is the plasma beta number

$$\beta_1 = \frac{4\pi\gamma_{\mathrm{ad}}p_1}{B_1^2} = \frac{c_{\mathrm{s},1}^2}{v_{\mathrm{A},1}^2} = \frac{M_{\mathrm{A},1}^2}{M_1^2}. \tag{2.41}$$

Therefore, for strong shocks with $M_{\mathrm{A},1} \gg 1$, the compression ratio ρ_2/ρ_1 is approximately $(\gamma_{\mathrm{ad}} + 1)/(\gamma_{\mathrm{ad}} - 1)$. For a monoatomic gas with $\gamma_{\mathrm{ad}} = 5/3$, the material is compressed by a factor of four.

In the general case of oblique shocks, the situation is more complex, and the magnetic field direction can change. There are different types of oblique shocks, the slow shock, the fast shock, and the Alfvén type shock. These types correspond to the slow, the fast, and the normal Alfvén plasma waves. The speed v_1 has to be larger than the corresponding wave speed. Additionally, two other shock types exist, the so-called switch-on and the switch-off shock (see e.g. Kirk et al., 1994; Schlickeiser, 2002).
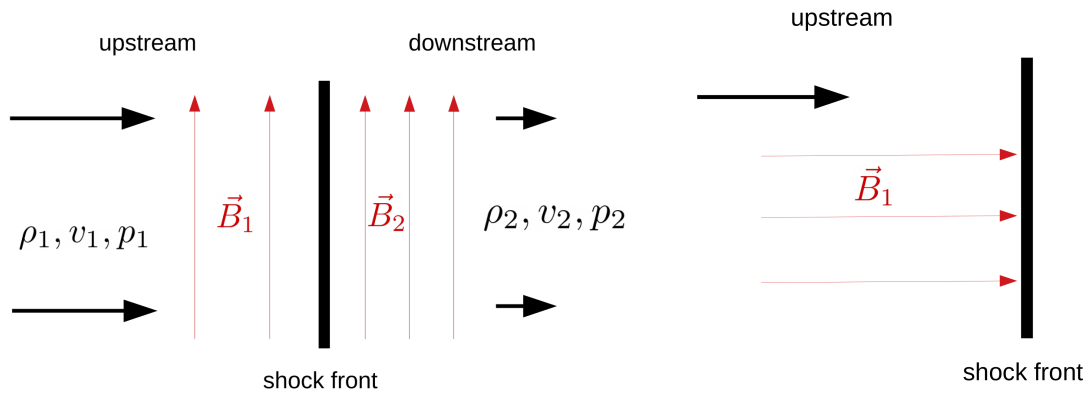
FIGURE 2.7: Sketch of a perpendicular (left) and the upstream side of a parallel shock (right). The black arrows indicate the flow velocity, and the magnetic field is shown with red arrows. The thick black vertical line marks the shock front.

2.4   Particle acceleration processes

Particles can be accelerated by several processes. Here, we will only focus on Fermi acceleration and the diffusive shock acceleration, which is the relevant process for this thesis. An early review about this mechanism was done by Blandford & Eichler (1987).

2.4.1   Fermi acceleration

A first attempt to explain the spectral power-law shape of the cosmic rays (CRs) was made by Fermi (1949). He noted that for a steady injection of CRs into an acceleration region with an energy independent escape probability, the resulting particle spectrum is a power-law. If the particles gain energy with a rate of $\mathrm{d}E/\mathrm{d}t = E/\tau_{\mathrm{acc}}$, where τ_{acc} is the acceleration time scale, and the escape probability is $1/\tau_{\mathrm{esc}}$, the steady-state particle distribution is

$$\frac{\mathrm{d}N}{\mathrm{d}E} \propto E^{-(1+\tau_{\mathrm{acc}}/\tau_{\mathrm{esc}})}. \tag{2.42}$$

As an acceleration process, Fermi (1949) assumed, that the CRs were scattered by clouds moving with a velocity of v. A head-on collision increases the energy of the particle by a factor of $\sim v/c$. However, if the CR collides with the cloud in an over-taking motion, it will lose an energy $\sim v/c$. Because collisions increasing the energy are favoured, the particles will gain an average energy of $\Delta E/E \propto (v/c)^2$ per collision. The acceleration time is proportional to $\tau_{\mathrm{acc}} \sim (c/v)^2$. Although in practice the Fermi acceleration process has

difficulties, the basic ideas are applicable to acceleration processes such as diffusive shock acceleration or shear acceleration. Acceleration processes where the average energy gain is $\Delta E/E \propto (v/c)^2$ are called second-order Fermi acceleration processes, and processes with $\Delta E/E \propto (v/c)$ first-order processes.

An accurate calculation that accounts for the stochastical nature of the process and the spreading of the energy spectrum by scattering was given by Blandford & Eichler (1987), who obtained the accurate expression for the energy dependence of the resulting particle spectrum $\propto E^{-x}$ with

$$x = \frac{3}{2}\left(1 + \frac{4cL}{3v^2\tau_{\mathrm{esc}}}\right)^{1/2} - \frac{1}{2},\tag{2.43}$$

where L is the mean free path between clouds.

2.4.2   Diffusive shock acceleration

In diffusive shock acceleration, particles at a shock gain energy by crossing from one side of the shock to the other side. In the framework of Fermi acceleration, the particle 'collides' with the opposite shock front. For a particle in the fluid on one side of the shock, the other side always has a relative velocity towards the particle, and the collision is head-on. Hence, the average energy gain is proportional to v/c, and the diffusive shock acceleration is a first-order process.

Diffusive shock acceleration follows the basic idea, that accelerated particles at each side of the shock have randomised directions due to scattering by magnetohydrodynamical waves. In the downstream side of the shock, the waves can be generated by, for instance, shock-induced turbulence, a clumpy structure of the interstellar medium (ISM) and instabilities. Upstream, the energetic particles themselves can excite the wave modes. A particle crossing the shock front will have an additional velocity component compared to the isotropised particles on the other side. If the direction of the new particle gets randomised, it will keep the additional velocity contribution. Consequently, the particle has a larger kinetic energy than before. Considering that the bulk flow at the downstream side is moving away from the shock, there is the probability that the accelerated particles are advected away from the shock, leaving the acceleration region.

2.4.3   Non-relativistic shocks

To derive the power-law distribution of particles accelerated at strong non-relativistic shocks, one can do some simple arguments. For an accurate treatment, one has to use a Fokker-Planck type equation as it was done by Axford et al. (1977); Krymskii (1977); Blandford & Ostriker (1978). In the non-relativistic case, the energy change on crossing the shock front is

$$\frac{\Delta E}{E} = \frac{v_1 - v_2}{c} \cos(\theta), \tag{2.44}$$

where θ is the crossing angle, v_1 and v_2 the velocities at the upstream and downstream side of the shock, and we assume $v \approx c$, where v is the velocity of the particle. The probability for a particle which crosses the shock front to arrive with the angle θ is proportional to $\sin(\theta)\mathrm{d}\theta$. The rate at which this occurs is proportional to the velocity component normal to the shock, $c\cos(\theta)$. Therefore, the probability for a particle to cross the shock is proportional to $c\cos(\theta)\sin(\theta)\mathrm{d}\theta$. Normalising this distribution over all particles crossing the shock ($0 < \theta < \pi/2$) gives the probability $2\sin(\theta)\cos(\theta)\mathrm{d}\theta$. Then, the average energy gain per crossing is

$$\left\langle \frac{\Delta E}{E} \right\rangle = \frac{v_1 - v_2}{c} \int_0^{\pi/2} 2\sin(\theta)\cos^2(\theta)\mathrm{d}\theta = \frac{2}{3}\frac{v_1 - v_2}{c}.$$

For a complete cycle consisting of crossing and re-crossing, the energy gain is

$$\left\langle \frac{\Delta E}{E} \right\rangle = \frac{4}{3}\frac{v_1 - v_2}{c}. \tag{2.45}$$

We now consider the resulting spectrum of the particles. If P is the probability for a particle to remain within the acceleration region after completing one cycle, after k cycles, there will be $N = N_0 P^k$ particles with an energy $E = E_0 \kappa^k$, where $\kappa = 1 + \frac{4}{3}\frac{v_1 - v_2}{c}$. One can obtain the following relation:

$$\frac{\ln(N/N_0)}{\ln(E/E_0)} = \frac{\ln P}{\ln \kappa} \qquad \Rightarrow \qquad \frac{N}{N_0} = \left(\frac{E}{E_0}\right)^{\ln P/\ln \kappa}. \tag{2.46}$$

The number N is the number of particles reaching at least energy E, and thus

$$N(E)\mathrm{d}E \propto E^{-1+\ln P/\ln \kappa}\mathrm{d}E. \tag{2.47}$$

To calculate the probability $P = 1 - P_{\text{esc}}$, where P_{esc} is the escape probability, one can follow for example Bell (1978) to obtain $P_{\text{esc}} = 4v_2/c$. For a non-relativistic shock, P_{esc} is small. With these relations and $r = v_1/v_2$ one obtains

$$\ln(P) = \ln\left(1 - \frac{4v_2}{c}\right) \approx -\frac{4v_2}{c} \qquad \text{and} \qquad \ln(\kappa) = \ln\left(1 + \frac{4}{3}\frac{v_1 - v_2}{c}\right) \approx \frac{4}{3}\frac{v_1 - v_2}{c}.$$

This gives $\ln P/\ln \kappa = -3/(r-1)$ and Equation 2.47 becomes

$$N(E)\mathrm{d}E \propto E^{-\frac{r+2}{r-1}}\mathrm{d}E. \tag{2.48}$$

For a strong shock, the compression ratio is $r = 4$, which gives E^{-2} in the above equation. Modifications to the standard model of diffusive shock acceleration can occur, for example, if effects of the magnetic field direction are considered. The shock can be parallel, perpendicular or oblique, and the compression ratio $r = v_1/v_2$ could be different to four. In such cases, the particle energy distribution can differ from $\propto E^{-2}$.

The acceleration time t_{acc}, which is the time it takes a particle to be accelerated to a certain energy, depends on the frequency of scattering. A very rough estimate (see e.g. Malkov & Drury, 2001; Aharonian, 2004) is

$$t_{\text{acc}} \approx 10\frac{D}{v_1^2} \approx \eta\frac{r_{\text{g}}c}{v_1^2} \tag{2.49}$$

where D is the diffusion coefficient in the upstream region and η the scaling of D with respect to the Bohm diffusion coefficient.

2.4.4   Relativistic shocks

In contrast to a non-relativistic gas, the adiabatic index of relativistic gases is $\gamma_{\text{ad}} = 4/3$. Therefore, relativistic shocks with $v_1 \gtrsim 0.1\,c$ are more compressible and in principle could reach values of $\rho_2/\rho_1 = 7$. However, termination shocks of pulsars are cold and only reach compression ratios of ~ 3 in the shock rest frame. This compression ratio implies an outflow in the downstream region with a velocity of $\approx c/3$. A review about particle acceleration at relativistic shocks can be found, for example, in Sironi et al. (2015). Relativistic shocks impose difficulties for particle acceleration. For instance, a perpendicular magnetic field advected downstream with a velocity of $c/3$ makes it

challenging for particles to cross the shock. The treatment of particle acceleration at relativistic shocks is more complex compared to the non-relativistic case. However, theory and simulations show, that acceleration is possible (Kirk et al., 2000; Achterberg et al., 2001). As at non-relativistic shocks, particle acceleration at relativistic shocks is expected to produce power-law distributed particles. The spectral index in the ultra-relativistic limit is (see e.g. Achterberg et al., 2001; Sironi et al., 2015)

$$\frac{\mathrm{d}N}{\mathrm{d}E} \propto E^{-2.2}. \tag{2.50}$$

The diffusion of the particles is thought to originate from turbulence driven by plasma instabilities such as the Weibel instability or self-generated turbulence. The downstream turbulence level can influence the resulting power-law spectrum (e.g. Giacinti & Kirk, 2018).

2.4.5   Particle injection

To allow the diffusive shock acceleration process, the charged particles have to be able to be scattered in the ambient plasma from the lowest to the highest energies. If no resonant scattering is possible at low energies, the particles can not be injected into the acceleration process. Protons and other nuclei can resonate with Alfvén waves from thermal energies upwards. For electrons, the situation is different. Above energies of $20\,\mathrm{MeV}$, electrons can resonate with Alfvén waves and between $0.5\,\mathrm{MeV}$ and $20\,\mathrm{MeV}$ can be scattered by whistler waves. Levinson (1992) found, that self-generated whistler waves could control the electron injection, if $M_\mathrm{A} > 43/\sqrt{\beta_\mathrm{e}}$, where β_e is the ratio between the thermal electron pressure and the magnetic pressure inside the shock. Therefore, low Mach numbers could prevent the injection of electrons into the acceleration process, unless the electrons are pre-accelerated by another mechanism.

2.4.6   Maximum particle energies

The maximum energies of the particles can be constrained by different means. A basic theoretical limit for the maximum particle energies is the so-called Hillas limit (Hillas, 1984). It originates from the requirement that the accelerated particles have to be confined in the acceleration region such that they can still participate in the acceleration

process. The confinement requires the Larmor radius of the particle to be smaller than $L/2$, where L is the size of the acceleration region. This results in the following condition

$$\frac{B}{1\,\mu\text{G}}\frac{L}{1\,\text{pc}} > \frac{2E}{1\,\text{PeV}Z\beta}, \tag{2.51}$$

where Z is the number of elementary charges of the particle and β the scattering velocity in units of c.

Energy losses can also limit the acceleration. For example, synchrotron losses are an important loss mechanism at high energies for electrons. The energy loss rate increases $\propto E^2$, and thus will eventually become larger than the acceleration rate. An upper limit for the maximum energy, in this case, can be obtained by equating the cooling time with the acceleration time.

Lastly, the age of the source or the time the particles are in the acceleration region can constrain the maximum achievable energies. This can apply, for example, to very young sources or transient events. Another example is the colliding wind binary system η Carinae (see Chapter 5).

2.4.7   Magnetic field amplification

In strong shock waves in a fully ionised plasma, the density and the magnetic field are increased by a factor of four. This relatively low amplification of the magnetic field imposes a problem if one requires supernova remnants to be able to accelerate particles to energies above 10^{14} eV (Lagage & Cesarsky, 1983). As discussed by Völk et al. (2005), X-ray observations of supernova remnants, such as Cassiopeia A or Tycho, suggest an amplification of the magnetic field by a significant amount. This was also shown by numerical simulations and theoretical analysis (e.g. Lucek & Bell, 2000; Bell & Lucek, 2001; Bell, 2004).

The magnetic field can be amplified as a result of instabilities, such as the streaming instability proposed by Bell (1978) in the upstream region of the shock or non-resonant instabilities driven by the cosmic ray current (Bell, 2004). If δB is the fluctuating magnetic field, some fraction χ of the CR pressure P_{CR} is transferred to these fluctuations, and $\delta B^2/4\pi = \chi P_{\text{CR}}$. This relation can be rewritten by using the Alfvén Mach number

$M_A = v_1/v_A$:

$$\frac{\delta B^2}{B_0^2} = \chi \left(\frac{P_{CR}}{\rho v_1^2} \right) M_A^2 \,, \tag{2.52}$$

where B_0 is the background magnetic field. Bell (2004) found, that the energy density in the magnetic field will saturate for values of $\chi \approx v_1/c$. This implies, that for large Alfvén Mach numbers, the magnetic field can be amplified by several orders of magnitude.

2.5   Cosmic Rays

Cosmic rays (CRs) are non-thermal particles accelerated by different astrophysical sources. If they escape the acceleration site, they can eventually reach Earth. Victor HESS achieved the first discovery of these highly energetic particles in 1912 during several balloon flights (Hess, 1912). Today, their spectrum and composition is measured by space-based (e.g. Aguilar et al., 2021; Grebenyuk et al., 2019) and ground-based experiments (e.g. The Pierre Auger Collaboration et al., 2015; Ivanov, 2015). Due to the deflection in magnetic fields, the directional information about the CR acceleration sites is normally lost.

Figure 2.8 shows a compilation of the CR all-particle spectral energy distribution (gray) measured by IceCube/IceTop (Rawlins & IceCube Collaboration, 2015), KASCADE-Grande (Schoo et al., 2015), NUCLEON (Grebenyuk et al., 2019), the Pierre Auger Observatory (The Pierre Auger Collaboration et al., 2015), the Telescope Array (Ivanov, 2015), and the Tunka-133 Array (Prosin et al., 2014) together with the hydron CR spectrum (red) measured by AMS-02 (Aguilar et al., 2015) and NUCLEON (Grebenyuk et al., 2019). At energies below $\sim 10\,\text{GeV}$, there is a cutoff in the hydrogen CR spectrum. This feature is also observed in the spectra of other CR species at the same energy per nucleon and is caused by the scattering of low energy CRs in the outflowing solar wind. At higher energies, the CR spectrum follows a power-law $\mathrm{d}N/\mathrm{d}E \propto E^{-\alpha}$ with a spectral index of $\alpha \sim 2.7$ over many orders of magnitudes. However, there are several spectral features in the all-particle spectrum. At $\sim 3\,\text{PeV}$, the all-particle CR is softening slightly. This region is called the CR knee. Another softening of the spectrum occurs at $\sim 4 \times 10^{17}\,\text{eV}$, the so-called second knee. At energies above $\sim 3 \times 10^{18}\,\text{eV}$, the spectrum hardens, and at an order of magnitude higher energies, signatures of a cutoff
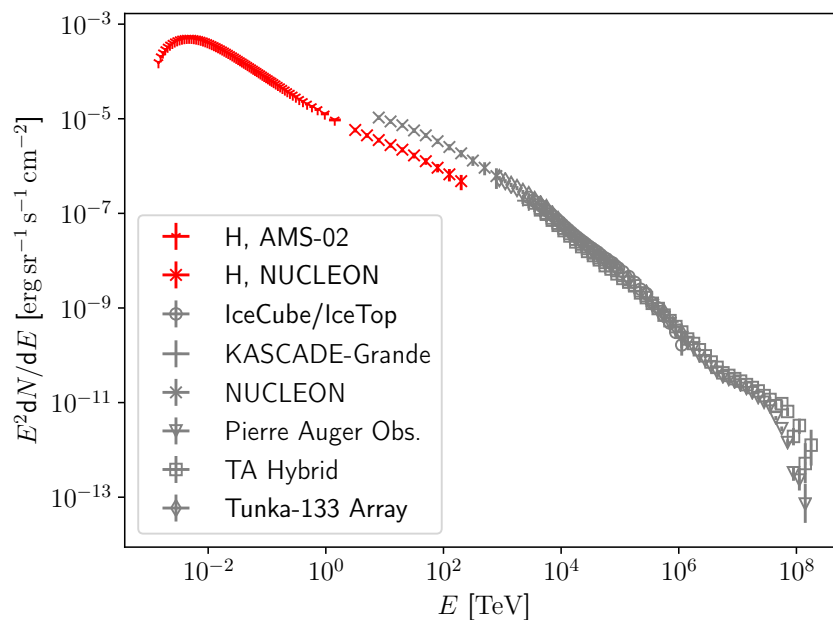
FIGURE 2.8: Hydrogen and all-particle CR spectrum measured on Earth. The data was retrieved from the Cosmic-Ray DataBase (Maurin et al., 2014, 2020). The hydrogen CR data is from AMS-02 (Aguilar et al., 2015) and NUCLEON (Grebenyuk et al., 2019), and the all-particle data from IceCube/IceTop (Rawlins & IceCube Collaboration, 2015), KASCADE-Grande (Schoo et al., 2015), NUCLEON (Grebenyuk et al., 2019), the Pierre Auger Observatory (The Pierre Auger Collaboration et al., 2015), the Telescope Array (Ivanov, 2015) and the Tunka-133 Array (Prosin et al., 2014).

are observed. This cutoff is assumed to be caused by the interaction of CRs with the cosmic microwave background (CMB) during their propagation to Earth, the so-called GZK cutoff (Greisen, 1966; Zatsepin & Kuz'min, 1966).

At the energies around the ankle and above, the Galactic magnetic field is not able to confine the CRs to the Galaxy (Hillas, 1984). Therefore, it is believed that the hardening at the ankle is caused by extragalactic CRs accelerated in sources outside of the Milky Way. It is not yet clear at which energies the transition between Galactic and extragalactic CRs occurs. One possibility is that the knee marks this transition. Since the particle acceleration of different particle species is expected to be rigidity dependent, the second knee would mark the highest energies for iron in this case. To fill in the gap between the second knee and the ankle, an additional extragalactic source population would be required. In principle, there might also be a different Galactic source population accounting for fluxes above the second knee, and extragalactic sources are only responsible for the CR spectrum above the ankle. Although the exact transition between Galactic and extragalactic CRs is unknown, it should occur between the knee

at few $\sim\!10^{15}\,$eV and the ankle at few $\sim\!10^{18}\,$eV.

The abundances of CR species are similar to the solar system abundances, but there are also differences (Lund, 1984). For example, the light CR elements beryllium and boron are overabundant compared to the solar system values. These overabundances of light elements can be explained if these elements are produced in spallation processes by heavier CR species colliding with other atoms. Hence, the ratio between, for example, carbon and boron CRs, can provide important insights into the transport processes of the CRs in the Galaxy (e.g. Amato & Blasi, 2018). The same applies to differences in the spectral shape of the individual species.

Measurements of the composition at energies greater than $100\,$TeV are more challenging. The data is consistent with the knee being a rigidity dependent feature (see e.g. Di Sciascio, 2022, and references therein). Towards the ankle, the composition seems to get lighter, whereas after the ankle, it becomes heavier (see e.g. Aloisio, 2012, and references therein). More data and better models at these energies are needed to constrain the composition further.

The CR electron spectrum is roughly a factor of 100 lower than the CR proton spectrum at GeV energies (e.g. Aguilar et al., 2019a). The spectral index of the electrons is softer than for CR protons. Between $\sim\!20\,$GeV to $1.4\,$TeV, the index changes between $\alpha = 3.3$ and $\alpha = 3.2$. Knowing that electrons suffer significant synchrotron losses, a softer spectral index with respect to the hadronic species is expected. Some fraction of the electron CRs is the result of secondary electrons produced in collisions of hadronic CRs with other material in the Galaxy. CR positrons are also detected (Adriani et al., 2013; Aguilar et al., 2013, 2019b). A distinct feature of the positron spectrum is a significant excess starting at $\sim\!25\,$GeV. Above $\sim\!300\,$GeV, the spectrum drops off. The low energy positrons can be explained by secondary positrons produced by collisions of hadronic CRs, but to account for the positron excess above $\sim\!25\,$GeV, an additional contribution is needed. The origin of this positron excess is still under debate. While it could be explained by a contribution from positrons accelerated by pulsars (López-Coto et al., 2018; Evoli et al., 2021), it might also be the result of dark matter decay (Bergström et al., 2008; Cholis & Hooper, 2013).

It was long thought that supernova remnants (SNRs) are the main contributors to the production of Galactic CRs until the knee. If $\sim\!10\,\%$ of their bulk explosion energy is

transformed into CRs, SNRs can provide sufficient power. In principle, SNRs are able to accelerate particles up to $1\,\mathrm{PeV}$, but only during the early years after their explosion (Bell et al., 2013). Therefore, other scenarios, such as the acceleration in massive stellar clusters, have been proposed (Aharonian et al., 2019). Until today, the origin of the Galactic CRs remains an open question.

CRs diffusing through the Milky Way and interacting with the interstellar matter produce the diffuse Galactic emission (e.g. Ackermann et al., 2012). Hence, they are an essential contributor to the γ-ray sky. Given that the CR spectrum extends to energies above $1\,\mathrm{PeV}$, CRs provide an important contribution to the Galactic γ-ray emission until the highest energies detected so far. However, since their spectrum is soft, the contribution of the diffuse emission relative to single sources decreases with energy.

2.6   Astrophysical γ-ray sources

This section contains a short overview of some of the Galactic γ-ray sources that are relevant for this thesis. It mainly serves to give some background for the research outlined in Chapters 3 to 5. The sources to be briefly described include supernova remnants, pulsars, pulsar wind nebulae and colliding wind binaries.

2.6.1   Supernova remnants

Massive stars will eventually explode in spectacular supernova events. During such an explosion, a total energy of $\sim 10^{51}\,\mathrm{erg}$ is released (see e.g. the book by Vink, 2020). Between two to three supernova explosions occur on average during one century in the Milky Way (Tammann et al., 1994). If several per cent of this energy would be converted into the acceleration of CRs, supernova explosions could account for the total CR spectrum until the knee (Ginzburg & Syrovatskii, 1964).

The supernova ejecta expand and interact with the surrounding material. This leads to the formation of a supernova remnant (SNR). A SNR goes through different phases until he ultimately disappears (e.g. Woltjer, 1972). A summary and more details about the different phases can be found, for example, in the book by Vink (2020). The collision of the outermost and fastest ejecta of the explosion with the ambient medium creates

a shock. This shock is also called the forward shock. The forward shock heats the material, and a shock-heated shell is formed. Because the shell will decelerate, ejecta moving outwards inside the shell collide with it. A second shock can form if the collision is supersonic. This second shock is called the reverse shock, and it can heat the ejecta again.

Several SNRs have been detected in γ rays so far (see e.g. H. E. S. S. Collaboration, 2018). In 2013, Ackermann et al. (2013) detected signatures of the pion-bump feature in the SNRs IC 443 and W44. These findings directly showed that protons are accelerated at SNR shocks, and that they produce the majority of the emission above GeV energies in these two sources. However, the situation is less clear in other SNRs, and a distinction between leptonic, hadronic, or mixed models is not obvious. Hadronic models for SNRs, such as the ones from Helder et al. (2010) and Zirakashvili & Aharonian (2010), generally require around $10\,\%$ of the available shock power to be converted to protons, and a fraction of $\sim10^{-4}$ to 10^{-2} of the energy in accelerated protons to be transferred to accelerated electrons.

Most likely, the conditions for acceleration of particles up to PeV energies are only given in young SNRs (e.g. Bell et al., 2013). So far, no SNR was firmly identified to accelerate particles up to these energies, even not the $\sim100\,$yrs old youngest known Galactic SNR G1.9+0.3 (see e.g. Aharonian et al., 2019, and references therein). A thorough discussion about many aspects of SNRs can be found, for example, in the book by Vink (2020).

2.6.2   Pulsars and pulsar wind nebulae

Radio pulsars were first detected in 1967 (Hewish et al., 1968). They are fast rotating magnetized neutron stars with radii of $\sim10\,$km and masses similar to our Sun. Their surface magnetic fields are very strong, with values between $10^8\,$G for millisecond pulsars up to at $10^{15}\,$G in the case of magnetars (see e.g. Gaensler & Slane, 2006). Pulsars are detected in γ rays (Abdo et al., 2009a), and recently γ rays at $1\,$PeV have been detected from the Crab Nebula (Lhaaso Collaboration et al., 2021). Some pulsars are surrounded by nebulae, the so-called pulsar wind nebulae (PWN).

If the pulsed radio signal from pulsars can be measured accurately, one can determine their period P, as well as the period derivative, $\dot{P} = \mathrm{d}P/\mathrm{d}t$. The rotational energy loss

is the so-called spin down luminosity $L_{\mathrm{SD}} = -\mathrm{d}E_{\mathrm{rot}}/\mathrm{d}t$, where E_{rot} is the rotational energy. L_{SD} can be calculated in the following way (e.g. Gaensler & Slane, 2006):

$$L_{\mathrm{SD}} = 4\pi I \frac{\dot{P}}{P^3}. \tag{2.53}$$

Here, I is the moment of inertia. For a mass of $1.4\,\mathrm{M}_\odot$ and a radius of $10\,\mathrm{km}$ one obtains $I = 10^{45}\,\mathrm{g\,cm^{-2}}$. Pulsars can have a vast range of spin-down luminosities from $3 \times 10^{28}\,\mathrm{erg\,s^{-1}}$ (PSR J2144-3933) up to $\approx 5 \times 10^{38}\,\mathrm{erg\,s^{-1}}$ for the Crab pulsar or PSR J0537-6910 (Manchester et al., 2005). If one assumes the relation $\dot{\Omega} = -k\Omega^n$, where $\Omega = 2\pi/P$, one can calculate the age of the pulsar to be (Manchester & Taylor, 1977)

$$\tau = \frac{P}{(n-1)\dot{P}} \left[1 - \left(\frac{P_0}{P} \right)^{n-1} \right], \tag{2.54}$$

with the initial period P_0 and the so-called braking index n, where $n \neq 1$ is assumed to be constant. If a pulsar loses its energy via magnetic dipole radiation, the braking index is $n = 3$. Only for few pulsars, n has been determined so far. In all cases, n was between values of two and three. For $P_0 \ll P$ and $n = 3$, Equation 2.54 reduces to

$$\tau_{\mathrm{c}} = \frac{P}{2\dot{P}}, \tag{2.55}$$

where τ_{c} is the so-called characteristic age of the pulsar. If the requirement $P_0 \ll P$ is not valid, the term in brackets in Equation 2.54 is smaller than one and $\tau_c > \tau$. Assuming energy losses by magnetic dipole radiation, one can also infer the equatorial surface magnetic field strength (e.g. Gaensler & Slane, 2006)

$$B = 3.2 \times 10^{19} \sqrt{P\dot{P}}\ \mathrm{G}, \tag{2.56}$$

where the period is measured in seconds. Typical magnetic field strengths for pulsars with strong PWN have magnetic fields between $10^{12}\,\mathrm{G}$ and $5 \times 10^{13}\,\mathrm{G}$.

For an initial spin-down luminosity of $L_{\mathrm{SD},0}$ and assuming n to be constant, the energy loss rate evolves as (e.g. Pacini & Salvati, 1973)

$$L_{\mathrm{SD}} = L_{\mathrm{SD},0} \left(1 + \frac{t}{\tau_0} \right)^{-\frac{(n+1)}{(n-1)}}, \tag{2.57}$$

with the initial spin-down timescale $\tau_0 = P_0/((n-1)p_0)$. Then, the spin-down power is relatively constant until $t = \tau_0$. The period will evolve as

$$P = P_0 \left(1 + \frac{t}{\tau_0}\right)^{\frac{1}{n-1}}. \tag{2.58}$$

The total theoretically available rotational energy from a maximally spinning neutron star, implying a period $P \approx 1.5\,\mathrm{ms}$, is $\sim 10^{52}\,\mathrm{erg}$ (e.g. Vink, 2020). With such a luminosity, a pulsar can provide as much energy as a supernova explosion.

The physics of pulsar magnetospheres is not yet fully understood, but it is very likely that our current general understanding is close to reality. A review of the current understanding of pulsar magnetospheres can be found, for example, in Cerutti & Beloborodov (2017); Beskin (2018). One of the earliest magnetosphere models was the so-called vacuum solution, which describes the pulsar as a rotating dipole in vacuum (Pacini, 1967, 1968; Ostriker & Gunn, 1969). In this model, the energy loss rate of a pulsar is

$$L_{\mathrm{SD}} = \frac{2}{3}\frac{\mu^2 \Omega^4}{c^3}\sin^2\chi, \tag{2.59}$$

where μ is the magnetic moment, Ω the angular velocity, and χ the angle of the magnetic moment with the rotation axis. If the magnetic moment is aligned with the rotation axis, there is no energy loss.

However, the vacuum solution leads to a strong unscreened electric field outside the pulsar. It was soon noticed by Goldreich & Julian (1969) that the electric force in this model is larger than the gravitational force. This leads to the lifting of negative charges in the polar region and positive charges in the equatorial region, forming a torus in the equatorial and a dome in the polar region. The left panel of Figure 2.9 shows the results from a particle in cell (PIC) simulation of this so-called electrosphere solution from Cerutti & Beloborodov (2017). The magnetic field was assumed to be aligned with the rotation axis. The red region shows the charges in the torus, and the blue region the ones in the dome. Both regions are corotating. Between the dome and the torus, there is a vacuum gap, where no charges are located. In equilibrium, the electrosphere produces no pointing flux and, therefore, no spin-down power. The charge density in the
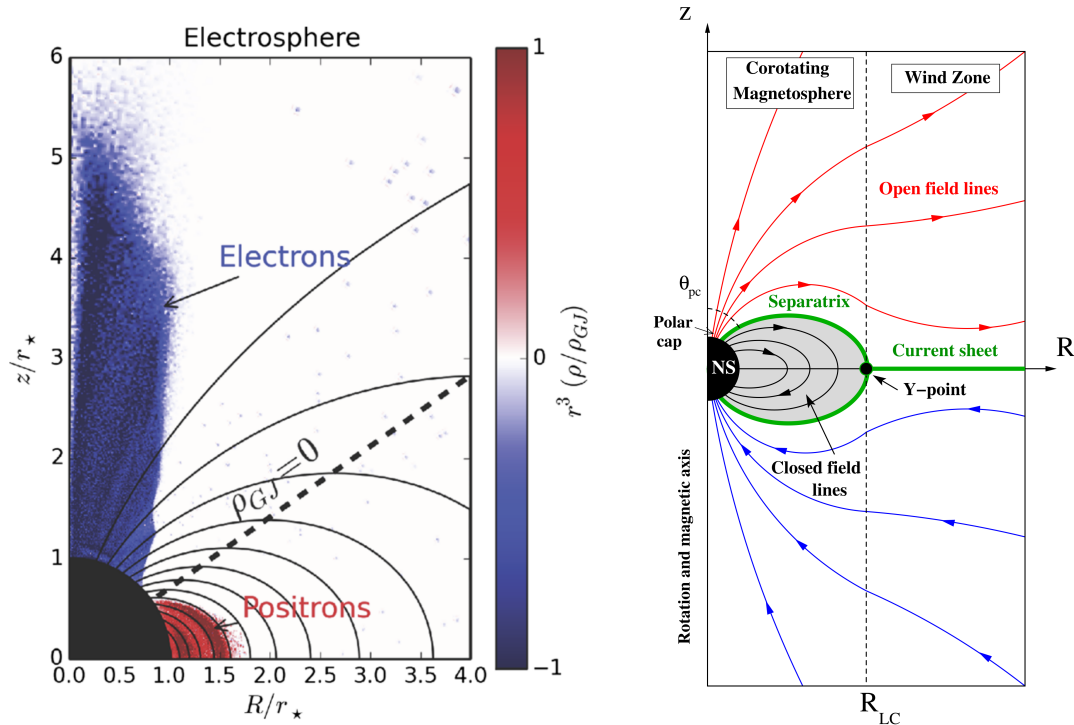
FIGURE 2.9: Axisymmetric particle in cell (PIC) simulation of the electrosphere solution (left) and a sketch of the ideal force-free magnetosphere (right). The plots are taken from Cerutti & Beloborodov (2017).

magnetosphere is called the Goldreich-Julian charge density (Goldreich & Julian, 1969):

$$\rho_{\mathrm{GJ}} = -\frac{\vec{\Omega} \cdot \vec{B}}{2\pi c}. \tag{2.60}$$

Thus, the model is unstable against perturbations, and there might be an additional outflow. This outflow is likely too weak to account for the measured spin-down powers of pulsars and might only be applicable to inactive old neutron stars.

A more realistic model for active pulsars is the force-free solution. Suppose there is a strong unscreened electric field parallel to $\vec{B}$ in the pulsar magnetosphere, and a single electron is placed in this region. In that case, the electron will be accelerated along the field line. The movement of the electron produces curvature radiation, which creates new e^+/e^- pairs. These e^+/e^- are again accelerated and a cascade of particle production develops until the parallel electric field is screened. Such a cascade could also be triggered by a γ-ray photon interacting with the strong magnetic field (Erber, 1966).

The right panel of Figure 2.9 shows a sketch of a force-free magnetosphere for a pulsar with a B-field aligned with the rotation axis taken from Cerutti & Beloborodov (2017).

The dashed vertical line shows the so-called light cylinder $R_{\mathrm{LC}} = c/\Omega$. Dipolar field lines inside R_{LC} can close back to the pulsar, but field lines in the polar region are open. In the closed field-line region, the magnetosphere is filled with a plasma corotating with the star, which has the Goldreich-Julian charge density ρ_{GJ}. In the polar region, the field lines are open and the angle of the so-called polar cap region is given by $\sin^2 \theta_{\mathrm{pc}} = R_\star / R_{\mathrm{LC}}$ (see e.g. Cerutti & Beloborodov, 2017). This opening region is the active region, where rotational energy of the neutron star is lost. The green lines in the right panel of Figure 2.9 is a current sheet separating different regions. For the non-aligned rotator, the energy loss rate can be approximated with (Spitkovsky, 2006)

$$L \approx \frac{\mu^2 \Omega^4}{c^3}(1 + \sin^2 \chi). \tag{2.61}$$

The force-free approximation breaks down in the current sheet. There might also still be a residual parallel electric field able to accelerate particles. Particles could also be accelerated in the equatorial current sheet outside the light cylinder. Nevertheless, the qualitative behaviour of a realistic active magnetosphere is likely similar to the force-free case.

Regardless of the details, an active pulsar will launch a relativistic wind with a total energy rate equal to the spin-down luminosity. The wind will be comprised of both magnetic flux and relativistic electrons and positrons that were created in the magneto-sphere. Then, the energy loss rate of a pulsar can be formulated as

$$L_{\mathrm{SD}} = 4\pi r^2 \Gamma n_{\mathrm{e}} m_{\mathrm{e}} c^3 (1 + \sigma), \qquad \text{with} \qquad \sigma = \frac{B^2}{4\pi \Gamma n_{\mathrm{e}} m_{\mathrm{e}} c^2}. \tag{2.62}$$

n_{e} is the combined electron and positron number density and Γ the bulk Lorentz factor of the electron-positron flow. The pulsar wind will end in a relativistic termination shock, where efficient particle acceleration can take place. Since the pulsar wind is loaded with electrons and positrons, the accelerated particles are expected to be mainly of leptonic origin. At larger distances than the termination shock, the wind will form a pulsar wind nebula. A spherical symmetric magnetohydrodynamical model of pulsar winds was obtained by Kennel & Coroniti (1984). The properties of the flow depend on the magnetisation parameter σ defined in Equation 2.62. When σ is large, the magnetic field in the postshock flow at large distances decreases as $1/r$.

The particle acceleration at the termination shock of pulsars can be very efficient and PeV energies can be reached (e.g. de Oña Wilhelmi et al., 2022). An example is the Crab Nebula, where photons up to 1.1 PeV were recently detected (Lhaaso Collaboration et al., 2021).

2.6.3   Colliding wind binaries

Massive stars can emit non-thermal radio emission, which might originate from particle acceleration at shocks in the stellar wind (White, 1985). These stars also show significant X-ray emission. However, binaries of massive stars are usually much brighter in X-rays than single stars. Their strong thermal X-ray emission has long been believed to originate from the wind collision region (Prilutskij & Usov, 1975; Pittard & Stevens, 1997). Considering the correlation between the thermal X-ray and the non-thermal radio emission, it is likely that the non-thermal radio emission also originates from the wind collision region. Non-thermal X-ray (Hamaguchi et al., 2018) and γ-ray (e.g. Reitberger et al., 2012; Balbo & Walter, 2017) emissions have been detected from the colliding wind binary (CWB) η Carinae, which established CWBs as a separate γ-ray source class.

The collision of the stellar winds can lead to the formation of shocks and the acceleration of particles (e.g. Eichler & Usov, 1993; Reimer et al., 2006). A sketch of the wind collision region is shown in Figure 2.10. The green and blue circles represent the stars, and the arrows around them indicate the stellar winds. Where the ram pressures of both winds are equal, the so-called contact discontinuity (CD) forms. The CD is shown with the thick black curve in Figure 2.10. On each side of the CD, there is a shock associated with each stellar wind. Behind each shock, the material flows outwards along the CD and gets accelerated (e.g. Usov, 1992; Parkin & Pittard, 2008).

The position of the CD is determined as the region, where the ram pressures of both winds equal each other. The total mass-loss rate $\dot{M}$ of each star is $\dot{M} = 4\pi r^2 v \rho$, where r is the distance and v the velocity. Assuming that both winds already reached their terminal wind velocities v_∞, the ram pressure condition gives

$$\frac{\dot{M_1}}{r_1^2} v_{\infty,1} = \frac{\dot{M_2}}{r_2^2} v_{\infty,2}, \tag{2.63}$$
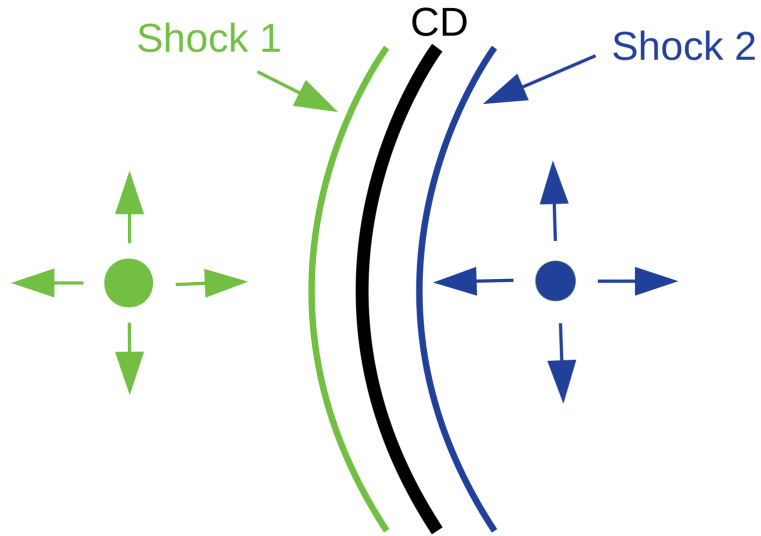
FIGURE 2.10: Sketch of the wind collision region of a CWB. The two stars are marked with a green and a blue circle. The thick black line in the middle is the contact discontinuity (CD), and the green and the blue line on each side of the CD the two shocks associated with each star. The arrows around the stars indicate the stellar winds.

where the indices 1 and 2 refer to each star. For the virtual line connecting the stars with each other, which are separated by a distance D, using the above condition and $D = r_1 + r_2$, one obtains the following expressions (see also Eichler & Usov, 1993):

$$r_1 = \frac{\sqrt{\eta}}{1 + \sqrt{\eta}}D, \qquad r_2 = \frac{1}{1 + \sqrt{\eta}}D, \qquad \text{with} \qquad \eta = \frac{\dot{M}_1 v_{\infty,1}}{\dot{M}_2 v_{\infty,2}}. \tag{2.64}$$

If $\dot{M}_1 v_{\infty,1} > \dot{M}_2 v_{\infty,2}$, it follows that $r_1 > r_2$, and the contact discontinuity is located closer to the second star. Because it is unlikely that the pressure from both winds is the same, the CD is expected to be bent towards the star with the weaker wind, as indicated in Figure 2.10. The opening angle of the contact discontinuity θ, defined as the angle between the connecting line of the stars and the CD tangential line, can be approximated with (Eichler & Usov, 1993)

$$\theta \approx 2.1 \left(1 - \frac{\eta^{2/5}}{4}\right) \eta^{1/3}, \qquad \text{with} \qquad \eta = \frac{\dot{M}_2 v_{\infty,2}}{\dot{M}_1 v_{\infty,1}} \tag{2.65}$$

At large distances from the apex of the shock cap, angles between the stellar wind velocities will be more parallel. Hence, the shocks will disappear, and the outflowing material from both shocks will mix (e.g. Parkin & Pittard, 2008). The outflow of the material is expected to be approximately ballistically, and this region was therefore

designated as the ballistic region by Parkin & Pittard (2008). The inner region, including the CD and the two shocks, is referred to as the shock cap. The shock cap can be twisted with respect to the direct connection line between the stars due to the orbital motion.

If the magnetic field of each star is a dipole, the rotation and the outflow from the stars will change with increasing radius from a dipolar field to a radial directed field to a toroidal field (Weber & Davis, 1967; Usov & Melrose, 1992). The B-field strength and its geometry can be written as (Usov & Melrose, 1992)

$$
B \approx B_{\mathrm{s}} \times
\begin{cases}
\left(\frac{R_\star}{r}\right)^3 & \text{for } R_\star \leq r < r_{\mathrm{A}} \text{ (dipole)}, \\[2mm]
\frac{R_\star^3}{r_{\mathrm{A}} r^2} & \text{for } r_{\mathrm{A}} \leq r < R_\star \frac{v_\infty}{v_{\mathrm{rot}}} \text{ (radial)}, \\[2mm]
\frac{v_{\mathrm{rot}}}{v_\infty} \frac{R_\star^2}{r_{\mathrm{A}} r} & \text{for } R_\star \frac{v_\infty}{v_{\mathrm{rot}}} \leq r \text{ (toroidal)},
\end{cases}
\tag{2.66}
$$

where B_{s} is the magnetic field at the surface of the star, v_{rot} the rotation velocity at the stellar surface, $R_\star$ the stellar radius, and r_{A} the Alfvén radius (see e.g. Eichler & Usov, 1993, for a definition). Typical values for the rotation velocity of early-type stars are $v_{\mathrm{rot}} \sim 0.1\, v_\infty$ to $0.2\, v_\infty$ (Conti & Ebbets, 1977; Hutchings, 1981; Uesugi & Fukuda, 1982). The Alfvén radius ranges typically from $\sim R_\star$ up to $2\, R_\star$ to $3\, R_\star$ (Usov & Melrose, 1992). Hence, the magnetic field direction at the two shocks depends on the stellar parameters and the orbital separation. For example, if the primary star is a Wolf-Rayet (WR) star and the secondary star an OB star, the shock at the side of the WR star is likely quasi-perpendicular because it is located in the toroidal B-field region (Eichler & Usov, 1993). This is not necessarily the case for the OB star. For highly eccentric orbits, it might be possible that the magnetic field direction at one of the shocks changes from quasi-perpendicular to quasi-parallel.

To have particle acceleration at one of the two shocks, several requirements have to be fulfilled (see e.g. Eichler & Usov, 1993). Firstly, the shock has to be collisionless. Furthermore, the Alfvén waves should be able to grow faster than the damping rate. To additionally allow electrons to be injected into the acceleration process, the phase velocity of whistler waves travelling along the shock normal must be well below the shock velocity.

3 Ultra-high Energy Inverse Compton Emission from Galactic Electron Accelerators

Pulsars are well-established electron accelerators, and the surrounding pulsar wind nebulae (PWN) are powered by synchrotron and IC emissions from accelerated electrons and positrons. Although CR protons and ions might also be present, the leptons are expected to be the dominant particle species. But because of the suppression of IC emission in the Klein-Nishina regime, hard leptonic emission is difficult to maintain until energies of $100\,\mathrm{TeV}$. Thus, hadronic processes are favoured at these energies. However, in special environments where IC cooling dominates over synchrotron cooling until sufficiently high energies, the reduced energy losses in the Klein-Nishina regime produce a hardening in the electron spectrum. This hardening compensates for the suppression of the γ-ray emission (Blumenthal & Gould, 1970; Agaronyan & Ambartsumyan, 1985; Zdziarski & Krolik, 1993; Moderski et al., 2005; Hinton & Aharonian, 2007). While it was shown that this effect allows the explanation of the γ-ray emission until tens of TeV from the Galactic centre (Hinton & Aharonian, 2007) or observations of the BL Lac object Markarian 421 (Zdziarski & Krolik, 1993) with IC emission, a detailed investigation for potential Galactic UHE emitters is lacking. Strong magnetic fields around pulsars could prevent the dominance of IC energy losses until sufficiently high energies in realistic Galactic conditions. Nonetheless, particles might be able to move quickly enough into adjacent regions with more favourable environments.

The questions about a possible leptonic origin of ultra-high energy (UHE) γ rays became increasingly important with the first detections of sources emitting above $100\,\mathrm{TeV}$ by HAWC (Abeysekara et al., 2020) and LHAASO (Cao et al., 2021). For all three HAWC sources and 10 out of the 12 LHAASO sources, known pulsars close to the sources exist. This is a strong indicator that pulsars are frequently accelerating particles up to energies of $100\,\mathrm{TeV}$ and beyond and strengthens the case of leptonic UHE γ-ray emitters (see also Albert et al., 2021a).

The understanding of UHE γ-ray sources is not only of great importance for γ-ray astronomy but also for other research areas. For example, the CR positron excess observed on Earth (Adriani et al., 2013; Aguilar et al., 2013) might be produced by one or several nearby pulsars (e.g. López-Coto et al., 2018). However, dark matter annihilation is an alternative explanation (Bergström et al., 2008; Cholis & Hooper, 2013) and a detailed understanding of particle acceleration in pulsars, their γ-ray emission and spatial distribution is necessary to shed light on this question. UHE γ-ray sources also provide unique laboratories to test new physics, e.g. the violation of Lorentz Invariance (Martínez-Huerta & Pérez-Lorenzana, 2017). Recently, measurements of the Crab nebula by LHAASO allowed to compute the tightest constraints on Lorentz-invariance violation theories (Li & Ma, 2022).

This chapter investigates under which conditions leptonic sources may produce hard UHE γ-ray emission. In Section 3.1, the concept for producing hard UHE IC spectra in an equilibrium between electron injection and losses is explored in detail. Additionally, the requirements for magnetic and radiation fields are investigated. In Section 3.2, requirements for potential accelerators and further constraints on the emission region are explored. After these requirements are known, it is investigated if they can be fulfilled in the Milky Way (Section 3.3). Furthermore, it is investigated, if the three HAWC sources detected above 100 TeV and the three LHAASO sources for which detailed spectra are provided by Cao et al. (2021) can be explained by IC emission (Sections 3.4 and 3.5). The results are discussed in Section 3.6. The content is based on the publications Breuhaus et al. (2021); Breuhaus et al. (2021); Breuhaus et al. (2022b).

3.1 Equilibrium spectra in radiation-dominated environments

3.1.1 Equilibrium spectra for single temperature radiation fields

Accelerated electrons or positrons that are constantly injected into an environment establish an equilibrium between injection and losses if the cooling times of the particles are smaller than the timeframe under consideration, and the injection spectrum does not change significantly in shorter times. The total cooling time, considering only IC

emission in the Thomson regime and synchrotron radiation, can be approximated with (Breuhaus et al., 2021)

$$t_{\text{cool}} \approx 300 \left(\frac{E_{\text{e}}}{1\,\text{PeV}} \right)^{-1} \left(\frac{U_{\text{B}} + U_{\text{rad}}}{1\,\text{eV}\,\text{cm}^{-3}} \right)^{-1} \text{yrs.} \qquad (3.1)$$

Here, U_{B} is the magnetic and U_{rad} the radiation field energy density. In the case of synchrotron cooling (and in the Thomson regime of IC cooling) the energy loss rate is proportional to E^2 (see Equations 2.8 and 2.3 in Section 2.1). If $\Xi_{\text{IC}} \equiv U_{\text{rad}}/U_{\text{B}} \ll 1$ synchrotron cooling dominates over IC cooling at all energies. In this case and for an equilibrium between injection and energy losses, the diffusion-loss Equation 2.36 simplifies to

$$0 = \frac{\text{d}N(E)}{\text{d}t} = \frac{\text{d}}{\text{d}E} \left[b(E)N(E) \right] + Q(E,t) \qquad \text{with} \qquad b(E) \propto E^2. \qquad (3.2)$$

For a power-law injection spectrum ($Q(E,t) \propto E^{-\alpha}$), this equation can be easily solved, resulting in $\text{d}N/\text{d}E \propto E^{-(\alpha+1)}$. In the Thomson regime, the resulting IC γ-ray emission follows a power-law $\text{d}N_{\gamma}/\text{d}t\text{d}E \propto E^{-(\alpha+2)/2}$. The power-law index softens to $-(\alpha+2)$ in the Klein-Nishina regime.

If instead $\Xi_{\text{IC}} \gg 1$, IC losses dominate. In the Thomson regime, the resulting equilibrium power-law index is the same as in the case of the domination of synchrotron losses. However, in the Klein-Nishina regime, the electron spectrum gets harder because the energy losses only increase proportionally to $\ln(4E_{\text{ph}}E_{\text{e}})$. The hardening in the electron spectrum can easily compensate for the suppression of the γ-ray emission in the Klein-Nishina regime. Since the synchrotron losses increase with E^2, they will inevitably dominate over the reduced losses in the Klein-Nishina regime above a certain energy E_{X}, where $t_{\text{cool,IC}}(E_{\text{X}}) = t_{\text{cool,sync}}(E_{\text{X}})$, $t_{\text{cool,IC}}$ and $t_{\text{cool,sync}}$ are the IC and synchrotron cooling times. However, this transition can happen at energies well above the Klein-Nishina transition in radiation-dominated environments, allowing the possibility of hard γ-ray spectra.

To investigate the relation between the transition energy E_{X} and the resulting γ rays, the left and middle panel of Figure 3.1 shows the cooling times and γ-ray spectra resulting in an equilibrium situation for different values of Ξ_{IC}. The magnetic field was fixed to $5\,\mu\text{G}$, and the radiation field consisted of a single temperature field with a temperature
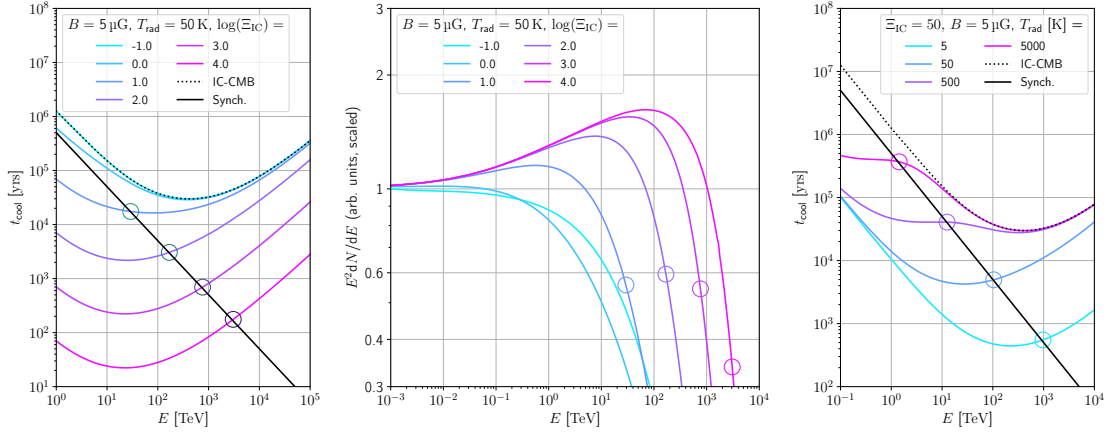
FIGURE 3.1: Cooling times (left and right panel) and steady-state γ-ray spectra (middle panel) for different environmental parameters. The left panel shows cooling times for different values of Ξ_{IC} for a fixed magnetic field of $B = 5\,\mu\text{G}$ and a 50 K radiation field plus the CMB. Coloured lines show the IC cooling times, the solid black line the synchrotron cooling time and the dotted black line the cooling time of the CMB. The middle panel shows the corresponding equilibrium γ-ray spectra normalised to their respective value at 1 GeV. The right panel shows the cooling times for a fixed value of $\Xi_{IC} = 50$, $B = 5\,\mu\text{G}$ and different temperatures of the radiation field. As in the left panel, coloured curves represent the IC cooling times, the solid black line the synchrotron cooling time and the dotted black line the IC cooling time of the CMB. The circles mark the respective value of E_X in all three panels. The electron injection spectrum followed a power-law with $\alpha = 2$ and $E_{cut} = 10\,\text{PeV}$. Adapted version of Figure 1 in Breuhaus et al. (2021).

of 50 K and different energy densities plus the CMB. The injection spectrum was, in each case, an exponential cutoff power-law

$$\frac{\mathrm{d}N}{\mathrm{d}t\mathrm{d}E} = N_0 \cdot E^{-\alpha} \exp\left(\frac{E}{E_{cut}}\right) \tag{3.3}$$

with $\alpha = 2$ and $E_{cut} = 10\,\text{PeV}$. The very large cutoff value was chosen to avoid signatures in the γ-ray spectra from the cutoff. The coloured lines in the left panel of Figure 3.1 show the IC cooling times, the solid black line the synchrotron cooling time, and the dotted black line the IC cooling due to the cosmic microwave background (CMB). The IC cooling times show a minimum corresponding to the transition between the Thomson and the Klein-Nishina regimes. Because of the increase after the minimum, the constantly falling synchrotron cooling time dominates over the IC cooling time at E_X, if it was subdominant in the Thomson regime. E_X is marked with a small circle for each curve, and it always occurs in the Klein-Nishina regime (if it exists, which means that IC cooling has to dominate over synchrotron cooling in the Thomson regime).

The middle panel shows the corresponding γ-ray spectra normalised to the respective

value at $1\,\mathrm{GeV}$ to facilitate a comparison of the shapes. E_X is marked with circles as in the left panel. Because in the Klein-Nishina regime a huge fraction of the electron energy is transferred to the photon, E_X manifests itself in the γ-ray spectra at essentially the same energy. All γ-ray curves show a cutoff at slightly lower energies than E_X. Before the cutoff, hard γ-ray spectra are obtained for sufficiently large values of Ξ_IC. The hardening of the emission in the Klein-Nishina regime below E_X is caused by the increased cooling times.

3.1.2   Influence of the radiation field temperature

The transition energy E_X and therefore the cutoff energy in the IC spectra depends strongly on the temperature of the underlying photon field. For the left and middle panels of Figure 3.1, where a $50\,\mathrm{K}$ radiation field was used, values of Ξ_IC several times larger than ten are required to push E_X close to $100\,\mathrm{TeV}$ and to obtain detectable emission at $100\,\mathrm{TeV}$. The right panel of Figure 3.1 shows the cooling time for a fixed value of $\Xi_\mathrm{IC} = 50$ and $B = 5\,\mathrm{\mu G}$, but for different temperatures of the radiation field. For smaller temperatures, the transition to the Klein-Nishina regime is shifted to lower energies, which allows dominance of IC losses until higher energies. Therefore, lower temperatures are advantageous because lower values for Ξ_IC are sufficient for the production of hard IC spectra until a certain energy.

The effect of the radiation field temperature is illustrated in Figure 3.2. The coloured shaded regions show the excluded parameter space of Ξ_IC for different temperatures of the radiation field and different values of E_X. The B-field was fixed to $5\,\mathrm{\mu G}$, and the CMB was added. The gray band shows the range of typical Galactic dust temperatures of $10 - 50\,\mathrm{K}$ (Bernard et al., 2010; Zhu & Huang, 2014) and the black dashed lines mark the temperature of the CMB and the minimum Ξ_IC value for $E_\mathrm{X} \geq 100\,\mathrm{TeV}$. For a temperature of $100\,\mathrm{K}$, Ξ_IC has to be above 100 for transition energies of $E_\mathrm{X} = 100\,\mathrm{TeV}$ or higher. The case is very different for the CMB, where only values of $\Xi_\mathrm{IC} \sim 3$ are needed. This corresponds to a magnetic field of $1.8\,\mathrm{\mu G}$ and therefore, in regions with magnetic fields close to $1\,\mathrm{\mu G}$, hard IC spectra until $100\,\mathrm{TeV}$ are possible. Also, low B-field values still above $1.8\,\mathrm{\mu G}$ reduce the required value of Ξ_IC because the effects of the omnipresent CMB become noticeable. Temperatures above several hundred K require $\Xi_\mathrm{IC} > 1000$. Such strong radiation fields are unrealistic in reasonable Galactic
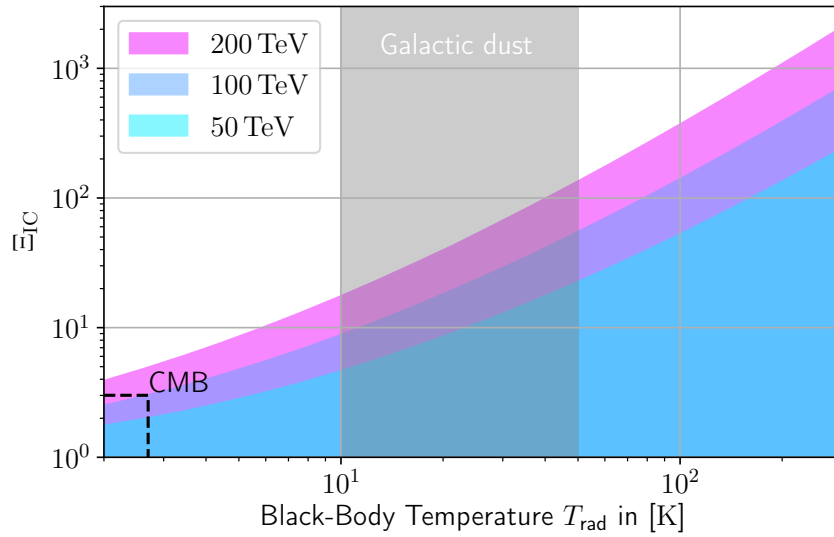
FIGURE 3.2: The shaded regions in different colours show the excluded parameter space in the $T_{\text{rad}} - \Xi_{\text{IC}}$ plane for different values of E_{X}. The grey band shows the region of typical Galactic dust temperatures, and the dashed black line marks the case of the CMB for $E_{\text{X}} = 100\,\text{TeV}$. B was fixed to $5\,\mu\text{G}$, and the CMB was added to the total radiation field. Adapted version of Figure 2 in Breuhaus et al. (2021).

environments, which is the reason why they are not shown in the figure. Strong IR radiation provides the important ingredient in creating hard UHE IC spectra.

3.1.3   Effects of different injection spectra

Evidently, the parameters of the injection spectrum have an effect on the resulting γ-ray spectra as well. To produce the γ-ray spectra in the middle panel of Figure 3.1, the equilibrium electron spectrum was calculated with an exponential cutoff power-law injection spectrum $\propto E^{-\alpha} \cdot \exp\left(-E/E_{\text{cut}}\right)$ for $\alpha = 2$ and $E_{\text{cut}} = 10\,\text{PeV}$. A lower cutoff energy has a similar effect as a reduced value of Ξ_{IC}: the cutoff of the γ-ray spectrum occurs at lower energies. The left plot in Figure 3.3 shows this effect, by assuming the injection of an E^{-2} electron spectrum with exponential cutoff energies $E_{\text{cut}} = 0.1\,\text{PeV}$, $1\,\text{PeV}$ and $10\,\text{PeV}$ for $\Xi_{\text{IC}} = 10$ (solid lines) and $\Xi_{\text{IC}} = 1000$ (dashed lines). The B-field was fixed to $5\,\mu\text{G}$, the temperature of the radiation field to $50\,\text{K}$ and for simplicity, the CMB was neglected. The two curves with matching product of $\Xi_{\text{IC}} \times E_{\text{cut}}$ are indistinguishable, illustrating that a lower cutoff in the injection spectrum has the same effect as a lower E_{X}.
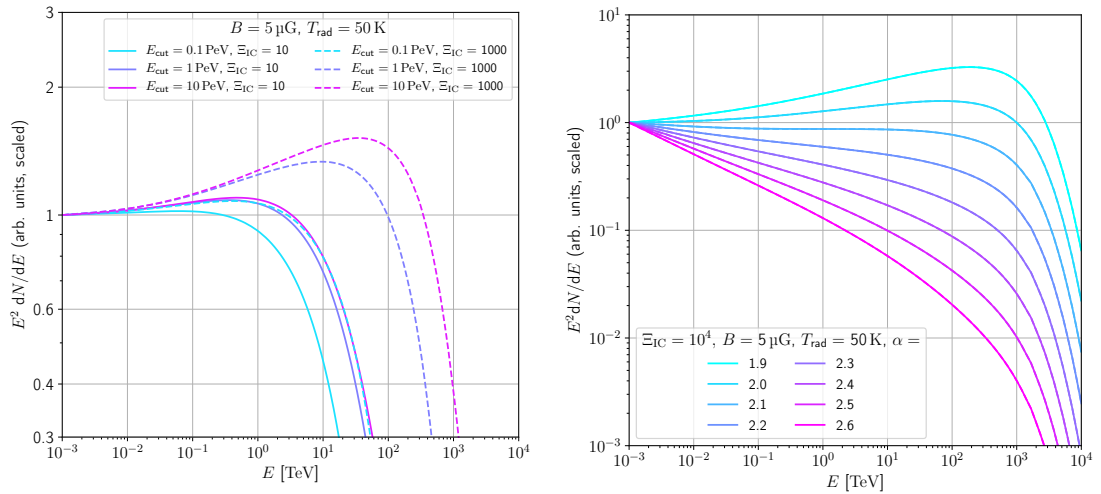
FIGURE 3.3: Left: Steady-state γ-ray spectra assuming different energy densities for a 50 K radiation field and a fixed magnetic field of 5 µG. The γ-ray spectra are those arising in equilibrium from constant injection of an E^{-2} electron spectrum with exponential cutoff energies at 0.1 PeV, 1 PeV and 10 PeV for $\Xi IC = 10$ and $\Xi IC = 1000$. Right: Steady-state γ-ray spectra assuming a fixed magnetic field of 5 µG and a fixed 50 K radiation field for $\Xi_{IC} = 10^4$. The γ-ray spectra are those arising in equilibrium from constant injection of an $E^{-\alpha}$ electron spectrum with an exponential cutoff energy of 10 PeV and $\alpha \in [1.9, 2.6]$.

The power-law index α also influences the slope of the γ-ray spectrum. The right hand plot in Figure 3.3 shows the resulting spectral energy distributions for $B = 5$ µG, $T = 50$ K, $\Xi_{IC} = 10^4$, $E_{cut} = 10$ PeV and $\alpha \in [1.9, 2.6]$, where the large value for Ξ_{IC} was taken to offset the effects of a low value of E_X. Higher temperatures produce harder spectra, because the transition energy to the KN-regime is shifted to lower energies. If $\alpha \gtrsim 2.3$, it is difficult to produce IC spectra close to $\propto E^{-2}$ or harder at 100 TeV.

3.1.4   More complex radiation fields

Realistic Galactic photon fields are different from the single temperature fields used in the previous figures. In the Milky Way, there are contributions from direct starlight, dust, and the CMB (e.g. Popescu et al., 2017). For energies where the IR fields are suppressed by Klein-Nishina effects, the CMB is the dominant photon field for the γ-ray production. This explains the differences in shape between the $\Xi_{IC} = 0.1$ curve and the $\Xi_{IC} = 1$ case in the middle panel of Figure 3.1: Because the relative contribution of the CMB in the $\Xi_{IC} = 0.1$ curve is larger than for $\Xi_{IC} = 1$, the former one is harder, although Ξ_{IC} is lower. In both cases, synchrotron cooling dominates over IC losses. For more complex and realistic target photon fields, lower temperature photons gradually

become more important at higher energies. This can change the shape of the resulting equilibrium γ-ray spectra. To investigate these effects, the Galactic radiation model from Popescu et al. (2017) was employed. As an exemplary location relevant for the modelling of the HAWC and LHAASO sources, the field at the anticipated location of the source eHWC J1907+063 (Abeysekara et al., 2020) was used. The distance to Earth was assumed to be the same as the associated pulsar PSR J1907+0602. To make reasonable comparisons with single temperature radiation fields with a higher value of Ξ_{IC}, the total dust emission was rescaled accordingly.

Figure 3.4 compares the shapes of equilibrium γ-ray spectra of the more complex radiation field to single black-body radiation field scenarios. The left panel shows with the dashed lines the equilibrium spectra for three different single temperature radiation fields normalised to their respective value at $1\,\mathrm{GeV}$. It was $\Xi_{\mathrm{IC}} = 50$, $B = 5\,\mu\mathrm{G}$, and the injection spectrum had a power-law index of $\alpha = 2$. The red and black solid lines show spectra for the more complex radiation field for injection power-law indices of $\alpha = 2$ (red) and $\alpha = 1.95$ (black). The normalisation was different from the other dashed curves and chosen such that the cutoff energies can be compared best. The cutoffs match the case of $T_{\mathrm{rad}} = 40\,\mathrm{K}$ very well. Looking at the case with $\alpha = 2$, the same injection index as for the single temperature scenarios, the slope of the γ-ray emission is less hard before the cutoff. At an energy of $\sim 10\,\mathrm{GeV}$, there is a bump in the spectrum. The softening of the emission directly after the bump is caused by the highest energy photons reaching the Klein-Nishina regime. Because more and more photons gradually reach this regime, the observed power-law index gets softer. This softening can be easily compensated by a harder injection spectrum of $\alpha = 1.95$, shown in black. Above $1\,\mathrm{TeV}$, the $\alpha = 1.95$ scenario is indistinguishable from the single-temperature case with $T_{\mathrm{rad}} = 40\,\mathrm{K}$, which was calculated for $\alpha = 2$. The right panel of Figure 3.4 shows equilibrium spectra from the realistic photon field for different values of Ξ_{IC} compared to single temperature scenarios for $T_{\mathrm{rad}} = 50\,\mathrm{K}$ with the same Ξ_{IC}. The power-law injection index was $\alpha = 2$ in all cases. For lower Ξ_{IC} values, the realistic photon fields lead to a less sharp cutoff of the emission due to the increasing importance of the CMB.
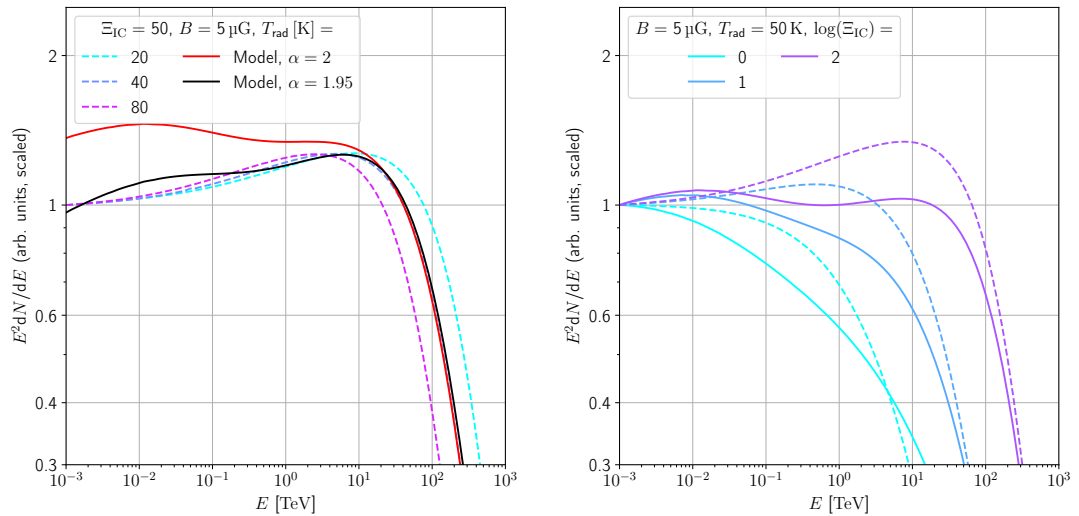
FIGURE 3.4: Equilibrium γ-ray spectra from single temperature radiation fields compared to scenarios with a more realistic Galactic photon field. The realistic photon field was from the model of Popescu et al. (2017) at the anticipated location of the source eHWC J1907+063 plus the CMB. The normalisations of the dust contribution of the realistic radiation field were adapted such that the dust emission accounts for the same Ξ_{IC} values as in the single temperature cases. In the left panel, Ξ_{IC} was fixed to 50. The dashed curves show the single temperature model for three different temperatures for a fixed power-law injection index of $\alpha = 2$. The equilibrium spectra for the realistic photon fields are shown with the solid lines, for $\alpha = 2$ (red) and $\alpha = 1.95$ (black). In the right panel, $T_{rad} = 50\,\mathrm{K}$ is fixed, but Ξ_{IC} is varying instead. Dashed lines show the single temperature, and solid lines the corresponding realistic photon field scenarios. All curves are normalised to their respective value at $1\,\mathrm{GeV}$, except the solid lines in the left panel, which are normalised to compare the cutoff energies. $B = 5\,\mu\mathrm{G}$ in all cases. Adapted version of Figure 5 in Breuhaus et al. (2021).

3.2   Possible electron accelerators and constraints on the emission region

In the previous calculations, it was assumed that particles can be accelerated up to sufficiently high energies and that they can be confined in the emission region. However, this might not necessarily be the case. The confinement of electrons with energies of 100 TeV into a small region requires high magnetic fields, which implies unrealistically high radiation energy densities to meet the requirements discussed in the previous Section 3.1. On the other hand, high energy radiation fields, which are needed for hard UHE IC emission, will absorb γ rays. If the emitting region is large, it could become optically thick to the UHE γ rays. Additionally, triplet pair production could potentially become important in the Klein-Nishina regime. These issues are investigated in the following.

3.2.1   Acceleration requirements

Pulsars are well-established electron accelerators. If their spin-down luminosity exceeds $10^{36}\,\mathrm{erg\,s^{-1}}$, they potentially can accelerate electrons to PeV energies. If the acceleration at the shock is limited by synchrotron losses, an upper limit on the maximum energy can be determined by requiring that the cooling time scale is equal to the gyration time (Giacinti & Kirk, 2018). This leads to

$$E_{\mathrm{max,sh}} = \sqrt{\frac{6\pi e}{\sigma_{\mathrm{T}} B}}\, m_{\mathrm{e}} c^2.$$

σ_{T} is the Thomson cross-section, e the electron charge and m_{e} the electron mass. Expressing the magnetic flux through the shock at r_0 in terms of the spin-down luminosity, $4\pi r_0^2 U_B c = \eta_{\mathrm{eq}} L_{\mathrm{SD}}$, where $U_B = 1/(8\pi) B^2$ is the magnetic energy density, L_{SD} the spin-down power and $\eta_{eq} < 1$ an equipartition factor describing the fraction of the spin-down power transformed into magnetic flux, B can be substituted in the above equation, giving

$$E_{\mathrm{max,sh}} \approx 10 \left(\frac{r_0}{0.1\ \mathrm{pc}}\right)^{1/2} \left(\frac{\eta_{\mathrm{eq}} L_{\mathrm{SD}}}{10^{36} \mathrm{erg\ s^{-1}}}\right)^{-1/4}\ \mathrm{PeV}. \tag{3.4}$$

Another estimate for the maximum energy is the Hillas limit. Rewriting the B-field in terms of η_{eq} and L_{SD} as for $E_{\mathrm{max,sh}}$, and for a scattering velocity of $\beta \approx 1$, one obtains

$$E_{\mathrm{Hillas}} = e\beta B r_0 \approx 2.5 \left(\frac{\eta_{\mathrm{eq}} L_{\mathrm{SD}}}{10^{36} \mathrm{erg\ s^{-1}}}\right)^{1/2}\ \mathrm{PeV}. \tag{3.5}$$

For $L_{\mathrm{SD}} \gtrsim 10^{36}\,\mathrm{erg\,s^{-1}}$, and sufficiently large values of η_{eq} and r_0 in the case of $E_{\mathrm{max,sh}}$, both limits for the maximum energy allow acceleration of PeV electrons.

There are strong hints, observationally and theoretically, that the Crab nebula pulsar is a PeV accelerator (Bühler & Blandford, 2014). Last year, this was confirmed observationally when the LHAASO observatory detected photons of up to $1.1\,\mathrm{PeV}$ from the Crab nebula (Lhaaso Collaboration et al., 2021). Although the spectrum of the Crab is not very hard, this is direct observational evidence that powerful pulsars can accelerate particles to PeV energies.

However, the strong magnetic fields close to a pulsar imply that in order to fulfil the condition of $\Xi_{\mathrm{IC}} \gg 1$ for UHE IC emission (see Section 3.1), the particles have to be accelerated at sufficiently large distances from the pulsar with lower B-field. If

equipartition between the spin-down luminosity L_{SD} and the magnetic energy flux holds, the magnetic field is approximately

$$B_{\mathrm{eq}} \approx 3 \cdot \sqrt{\frac{L_{\mathrm{SD}}}{10^{36}\,\mathrm{erg\,s^{-1}}}} \cdot \frac{1\,\mathrm{pc}}{r} \mathrm{\mu G}, \qquad (3.6)$$

where r is the radial distance.

Another option is that the particles are accelerated in a region with a high B-field and consequently $\Xi_{\mathrm{IC}} \ll 1$, but diffuse outwards into a region with $\Xi_{\mathrm{IC}} \gg 1$ without suffering substantial synchrotron losses. To investigate this scenario, we adopted the model of Kennel & Coroniti (1984). In their post-shock solution for highly magnetised flows, the B-field decreases as $1/r$. Therefore, synchrotron cooling becomes less critical for large radii, and IC cooling can dominate eventually. For simplicity, only the case of diffusion of the particles is considered. If the relativistic particles would instead be transported with the outgoing flow, they would suffer strong adiabatic losses. This means that for detectable emission at $100\,\mathrm{TeV}$, the non-thermal particles have to be adiabatically decoupled from the background plasma. For a locally isotropic diffusion coefficient and spherical symmetry, one obtains the diffusion loss equation

$$\frac{\partial N}{\partial t} + \frac{1}{4\pi r^2}\frac{\partial j}{\partial r} + \frac{\partial}{\partial E}\left[b(E,r)\cdot N\right] = 0 \qquad \text{with} \qquad j(E,r) = -4\pi r^2 D\frac{\partial N}{\partial r}. \qquad (3.7)$$

$j(E,r)$ is the radial flux due to diffusion, $b(E,r)$ the cooling rate, D the diffusion coefficient and $N \equiv N(E,r)$ the differential number density. $b(E,r)$ is assumed to contain only synchrotron cooling as the dominant cooling mechanism, with a magnetic field proportional to $1/r$. Hence, according to Equation 2.3, $b(E,r)$ is proportional to E^2/r^2.

Additionally, it is assumed that electrons and positrons are injected with a constant rate at radius $r = r_0$ and the equation is solved for the steady-state solution. The injection of particles can be modelled as a boundary condition for the diffusive flux $j(E,r)$ at r_0. j is assumed to follow an exponential cutoff power-law as expected from diffusive shock acceleration at the termination shock:

$$j(r_0, E) = Q_0 E^{-\alpha} e^{-E/E_{\mathrm{cut}}}\,. \qquad (3.8)$$

Given the condition at $r = r_0$, another boundary condition for $r = \infty$ is needed. The

physically motivated requirement is to demand $N(r = \infty) = 0$. The solution to the equation for the simplifying asssumption of an energy and radius independent scalar diffusion coefficient D was done previously by Webster & Longair (1971). Here, D is assumed to be energy dependent, $D = D_0 E^\delta$. This generalizes the solution from Webster & Longair (1971). For $0 \leq \delta < 1$, and following the same method as in Webster & Longair (1971), the solution is

$$j(r, E) = \frac{Q_0}{\sqrt{\pi}} E^{-\alpha} \frac{r}{r_0} \int_{z_0}^{\infty} \left(1 - \frac{z_0^2}{z^2}\right)^{\frac{\delta+\alpha-2}{1-\delta}} \exp\left[-\frac{E}{E_{\text{cut}}}\left(1 - \frac{z_0^2}{z^2}\right)^{\frac{1}{\delta-1}}\right] \exp\left[-\left(\frac{\ln(r/r_0) + z^2}{2z}\right)^2\right] dz$$
(3.9)

with

$$z_0 = \sqrt{\frac{(1-\delta)r_0^2}{D\, t_{\text{cool},0}} \ln\left(\frac{r}{r_0}\right)} \qquad \text{and} \qquad t_{\text{cool},0} = \left.\frac{E}{\dot{E}_{\text{cool}}}\right|_{r=r_0} .$$

For $\delta = 0$ and $1/E_{\text{cut}} \to 0$, the same result as in Webster & Longair (1971) is obtained. With these simplifying assumptions and setting $\alpha = 2$, the integral in Equation 3.2.1 can be solved, resulting in

$$j(r, E) = \frac{Q_0}{2} E^{-2} \left[\text{erfc}(Z_-) + \frac{r}{r_0}\text{erfc}(Z_+)\right]$$

with the complementary error function $\text{erfc}(x)$ and

$$Z_\pm = \frac{\sqrt{D\, t_{\text{cool},0}}}{2r_0}\left[\frac{r_0^2 \ln(r/r_0)}{D\, t_{\text{cool},0}} \pm 1\right]$$

The term containing Z_- is dominating for the scenarios being discussed here. Therefore, the break in the spectrum occurs for $Z_- \approx 1$. Solving for the energy, one obtains

$$E_{\text{br}} \approx \frac{3m_e^2 c^3 D}{4r_0^2 \sigma_{\text{T}} U_B(r_0)}\left[\frac{1 + \sqrt{1 + \ln(r/r_0)}}{\ln(r/r_0)}\right]^2$$
(3.10)
$$\approx 0.5 \left(\frac{D}{10^{26}\ \text{cm}^2\ \text{s}^{-1}}\right)\left(\frac{\eta_{eq} L_{\text{SD}}}{10^{36}\text{erg s}^{-1}}\right)^{-1} \text{PeV}$$

Therefore, for pulsars with sufficiently high spin-down powers $L_{\text{SD}} \gtrsim 10^{36}$ erg s^{-1} and $D \gtrsim 10^{26}\,\text{cm}^2\,\text{s}^{-1}$, electrons are able to diffuse sufficiently fast into regions favourable for UHE IC emission while maintaining hard spectra until energies far above $100\,\text{TeV}$. With the extensions of the three HAWC sources given by Abeysekara et al. (2020) and demanding consistency with special relativity, meaning that the particles do not diffuse faster than the speed of light, one gets the restriction $D \ll 10^{28}(R/\text{pc})\ \text{cm}^2\ s^{-1}$,

where R is the source size. This is not in contradiction with $D \gtrsim 10^{26} \, \mathrm{cm}^2 \, \mathrm{s}^{-1}$, and therefore the required diffusion coefficients are not excluded. To conclude, high spin-down power pulsars can accelerate particles to sufficiently high energies, and electrons are able to diffuse into regions with $\Xi_{\mathrm{IC}} > 1$ without suffering significant energy losses if the acceleration site is magnetically dominated.

3.2.2   Opacity requirements

Strong far-infrared (FIR) fields are necessary for hard IC spectra up to $100 \, \mathrm{TeV}$. Unfortunately, the produced γ rays will be absorbed by these fields. The position of the maximum absorption is $E_\gamma \approx 3.5 E_{\mathrm{KN}}$, caused by photons with the wavelength $\lambda_{\mathrm{peak}} \approx 136 (E_\gamma / 100 \, \mathrm{TeV}) \mu\mathrm{m}$. For E_γ around $100 \, \mathrm{TeV}$, FIR radiation fields, which are at the same time important for the production of hard IC spectra, provide the critical absorbing photons. The total absorption depends on the details of the whole photon spectrum, and it gets stronger when the spatial extent of the absorbing photon fields gets larger. This sets a maximum limit on the size of the emission region: for a given B-field value, there is a minimum radiation energy density to fulfil $E_{\mathrm{X}} \geq 100 \, \mathrm{TeV}$, and for this minimum radiation energy density, there is a maximum size of the emission region to avoid significant absorption. At the same time, it has to be ensured that the electrons can be accelerated and are confined in the emission region without escaping before radiating most of their energy.

In Figure 3.5, the corresponding limits are displayed. The magenta and cyan lines show the upper limits on the size due to absorption of $100 \, \mathrm{TeV}$ photons for different magnetic field values. The limits were calculated for a maximum attenuation of $1/e$ in two different FIR temperature fields: $T_{\mathrm{rad}} = 50 \, \mathrm{K}$ (cyan) and $T_{\mathrm{rad}} = 10 \, \mathrm{K}$ (magenta), requiring values of $\Xi_{\mathrm{IC}} = 55$ and 8.8, respectively. For low magnetic field values, the presence of the CMB will allow lower Ξ_{IC} values, and therefore the limits can be relaxed in such environments. The chosen temperatures represent the range of typical Galactic dust temperatures shown in Figure 3.2.

For higher γ-ray energies, the absorption effects can be larger, and for energies above $\sim 300 \, \mathrm{TeV}$, the dominant absorbing photon field is the CMB (e.g. Vernetto & Lipari, 2016; Popescu et al., 2017). However, for the extent of the HAWC sources, the CMB
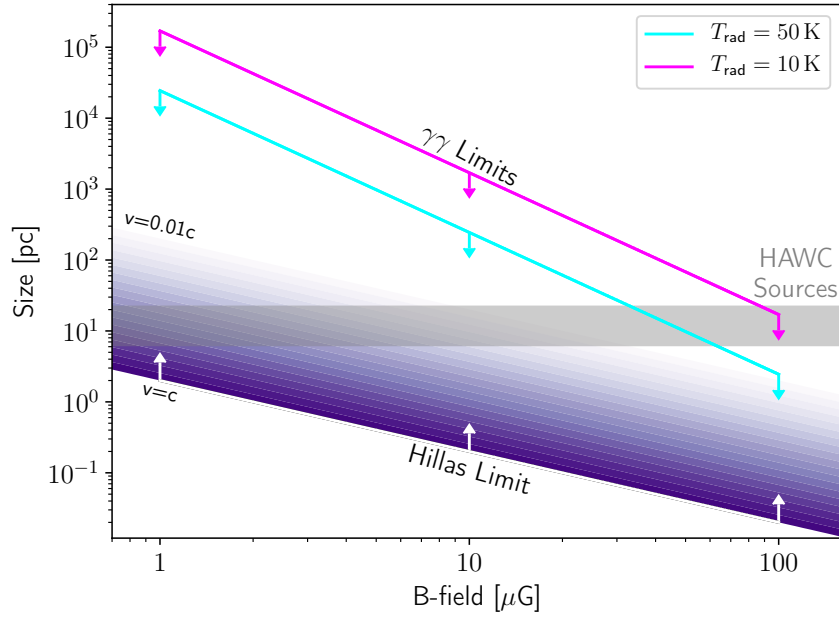
FIGURE 3.5: Constraints on the size of potential UHE emission regions for different magnetic fields due to $\gamma\gamma$ absorption and acceleration/confinement. The purple shaded regions show the Hillas constraints for different scattering velocities for electrons with an energy of 1 PeV. The cyan and magenta line are the limits due to $\gamma\gamma$ absorption for a 50 K and a 10 K radiation field with $\Xi_{\rm IC} = 55$ and 8.8 to ensure $E_{\rm X} = 100$ TeV. The maximum allowed attenuation of 100 TeV γ rays was $1/e$. The gray band area shows the anticipated sizes of the HAWC sources (Abeysekara et al., 2020). Adapted version of Figure 3 in Breuhaus et al. (2021).

does not play an important role for internal absorption. Additionally to the local, source-specific radiation fields, the γ rays will also be absorbed by the large-scale Galactic radiation during the travel from the source to the Earth. To test the significance of these effects, the large-scale radiation model from Popescu et al. (2017) was used. The transmission at 100 TeV is always $e^{-\tau_{\gamma\gamma}} > 0.5$ ($\tau_{\gamma\gamma}$ is the optical depth), even in the worst-case scenario for a source located at the opposite edge of the Galaxy behind the Galactic centre.

The white arrows and the purple shaded regions in Figure 3.5 show the Hillas limits for different scattering velocities. There is a large available parameter space between the Hillas and the absorption limits for different magnetic fields and source sizes. The grey band shows the anticipated sizes of the three HAWC sources above 100 TeV detected by Abeysekara et al. (2020). For B-field values below few tens of µG down to ~1 µG, their sizes fall in the permitted parameter space.

3.2.3   Influence of triplet pair production

At energies deep in the Klein-Nishina regime, the triplet pair production (TPP) process could potentially have influences on the resulting electron and γ-ray spectra, because for $E \cdot E_{\mathrm{rad}}/(m_{\mathrm{e}}^2 c^4) \approx 250$ both cross-sections are equal, and at higher energies σ_{TPP} dominates (see Section 2.1.7). As can be noticed from Equation 2.29, the energy loss rate of the TPP process behaves more gradual than the IC loss rate in the Klein-Nishina regime since only a small fraction of the energy of the electron is transferred to the $e^+ - e^-$ pair. As explored by Mastichiadis (1991), energy losses from TPP interactions can become noticeable for $E \cdot E_{\mathrm{rad}}/(m_{\mathrm{e}}^2 c^4) \geq 10^4$. Considering electrons with an energy of $100\,\mathrm{TeV}$, the photons need energies above $E_{\mathrm{rad}} > 25\,\mathrm{eV}$. Strong UV radiation fields carrying a large fraction of the total radiation field energy density may produce the spectral hardening due to reduced Klein-Nishina energy losses less pronounced. For higher electron energies, less energetic photons are needed. To avoid the dominance of synchrotron losses, extreme radiation energy densities of $\Xi_{\mathrm{IC}} \sim 10^9$ are required (Dermer & Schlickeiser, 1991), and therefore TPP effects will not have an influence on the shape of the electron spectrum in typical Galactic environments.

However, the TPP-produced electrons and positrons will provide additional contributions to the total γ-ray emission, which can soften the resulting spectrum. But, as mentioned in Section 2.1.7, this will only play a role for hard electron injection spectra with $\alpha < 2$ (Mastichiadis, 1991). In many cases, TPP effects can be neglected, as it was done in the modelling of the HAWC and LHAASO sources in Sections 3.4 and 3.5. In unique environments, the γ-ray spectra could be altered, but TPP effects will not negatively affect the possibility of hard leptonic UHE IC spectra.

3.3   Galactic emission regions

3.3.1   Conditions on large scales

While hard IC spectra at energies of $100\,\mathrm{TeV}$ are possible, it has to be assessed if the required environmental conditions exist in the Milky Way. First, the conditions on large scales are investigated. To do so, a large-scale radiation and B-field model are needed to compare IC and synchrotron cooling times.

For the radiation field, the model from Popescu et al. (2017) is used. Their model uses an axisymmetric radiative transfer model adapted to all-sky emission in the near-, mid-, far-infrared and submillimeter domains. Optical and UV observations were not considered because the Milky Way is opaque at these wavelengths. The total radiation field does not only contain the photon spectrum in the IR and submillimeter domains but also describes the UV and the optical bands. The emission is calculated self-consistently with radiation transfer techniques, considering the UV and optical starlight emission absorbed and re-radiated by dust. The same techniques have been applied previously to model external galaxies, which confirmed that the method can reliably connect observations in different wavelengths to the total spectra (e.g. Popescu et al., 2000; Misiriotis et al., 2001; Bianchi, 2007; MacLachlan et al., 2011; De Looze et al., 2014). Davies et al. (2016) showed that comparing the radiation transfer method with other methods resulted in the most consistent estimates of star-formation rate - stellar-mass relations. Hence, the radiation field model from Popescu et al. (2017) is a reliable estimate of the true radiation fields created by dust and starlight emission. The Sun was assumed to be at a radial distance of 8 kpc in this model. Because of the axisymmetry, variations due to the spiral arm structure could introduce enhancements within a factor of a few locally. The radiation model is defined for Galactic radii below 24 kpc and distances below 10 kpc above and below the disk. It does not include the CMB, but in the following investigations, it was added.

Estimates for the magnetic field are more uncertain. Here, the model from Jansson & Farrar (2012a,b) is used, where the B-field is inferred from Faraday rotation measures and polarised synchrotron radiation. The total magnetic field in this model consists of different components: The large-scale regular field, containing the disk field, the toroidal halo field, and the X-shaped field. Additionally, there are two random components: The random striated field, which is a component aligned with the large-scale regular field but with random strength and sign, and the completely random component. For the two random field components, their root mean square strength is given. The random fields are of comparable strength compared to the regular field, and therefore, the magnetic field can vary locally significantly. However, an electron moving on large scales will suffer total synchrotron losses from the regular and random fields combined. The B-field model includes modifications due to the spiral arm structure, and the Sun is located at $x = -8.5$ kpc. For Galactic radii above 20 kpc, the field was set to zero by Jansson

& Farrar (2012a). Nonetheless, in the calculations following, the field was assumed to continue smoothly for $r > 20\,\mathrm{kpc}$ to explore the full radial range of the radiation model. Intergalactic magnetic fields might be important at these radii as well. The magnetic field is also not defined for distances closer than $1\,\mathrm{kpc}$ to the Galactic centre because local effects in this region most likely dominate the field.

Figure 3.6 shows the transition energy E_X, where IC and synchrotron cooling time equal each other for a scan in the $x - y$-plane (top) and the $x - z$-plane (bottom). The white regions on the edges of the upper panel show regions with Galactic radii, where the radiation model is not defined, and the inner white circle in the upper and lower panel shows the inner region, where the B-field is not defined. The black regions show the places where synchrotron losses dominate over IC losses at all energies. Regions with E_X above or below $100\,\mathrm{TeV}$ are divided by the white line. The position of the Sun is marked with a green circle. As can be seen, the regions with $E_\mathrm{X} > 100\,\mathrm{TeV}$ lie either at very large Galactic radii or high above and below the disk. This is the case because the magnetic field gets sufficiently low such that the CMB, which has the same energy density everywhere, permits the formation of hard IC spectra. However, potential sources will mostly be located in the inner disk, where the large-scale conditions prevent the formation of hard IC spectra. Therefore one can conclude that the large-scale environments do most likely not provide the necessary conditions.

3.3.2   Local regions

While on large scales, the magnetic and the radiation fields most likely do not allow hard UHE IC spectra to occur, locally, the conditions can be different. Specifically, regions with high radiation energy densities or low magnetic fields could be potential candidates. Examples are regions of increased star formation, which creates strong optical and UV radiation. The optical and UV radiation heats the surrounding environment, which increases the FIR radiation energy densities. Potential γ-ray sources, such as SNR or pulsars, are linked to star formation because both are produced in the death of massive stars. Young, powerful pulsars, who did not travel far from their birthplace, might be still close to active star-forming regions with enhanced radiation fields. Whereas individual pulsars can have very high kick velocities, Hansen & Phinney (1997) determined a mean velocity between $\sim 250\,\mathrm{km\,s^{-1}}$ to $300\,\mathrm{km\,s^{-1}}$. Other works suggest even lower speeds
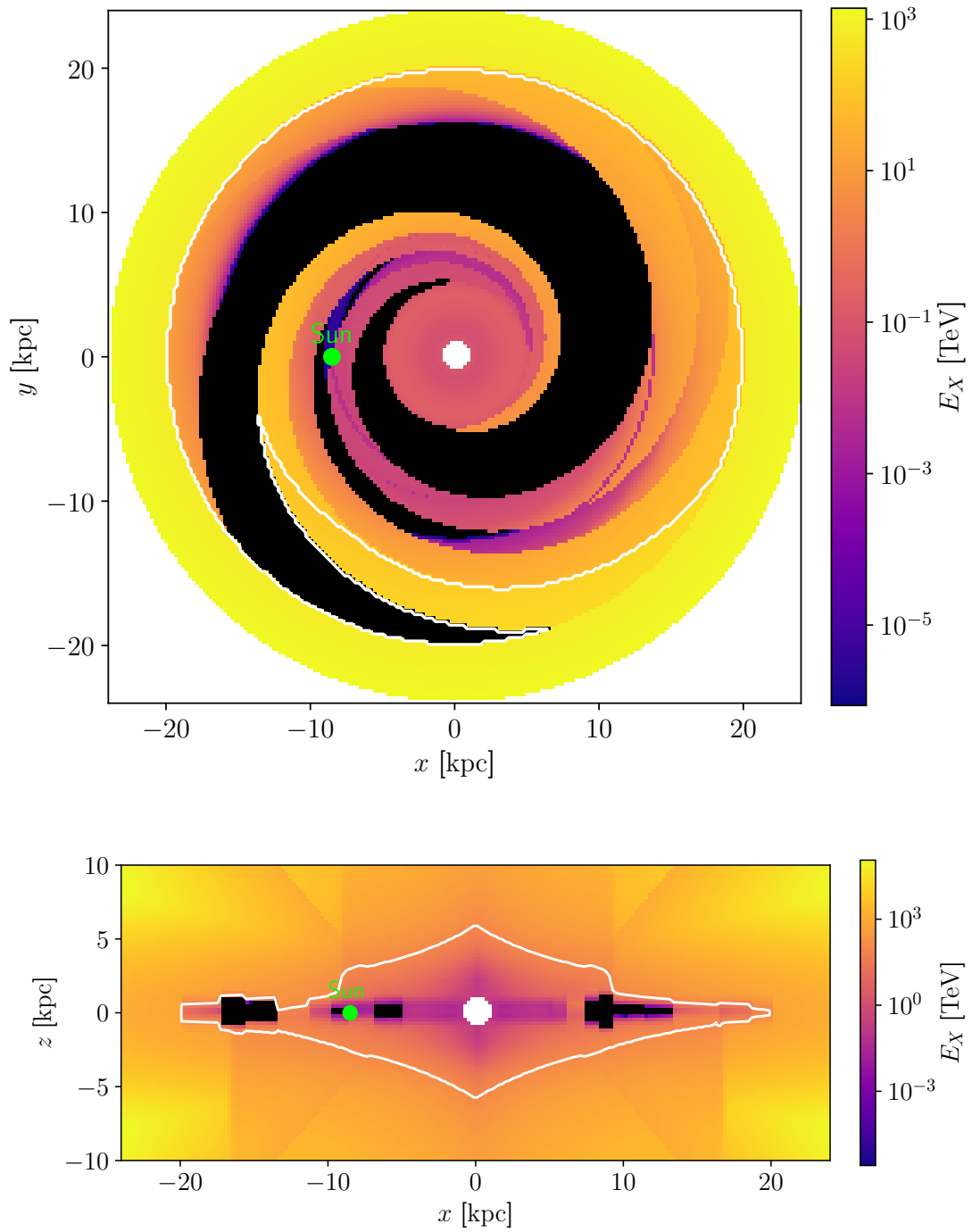
FIGURE 3.6: Scan through the Galactic disk for $z = 0$ (top) and $y = 0$ (bottom) for E_{X}. For the calcuations, the Galactic radiation field model from Popescu et al. (2017) and the magnetic field model from Jansson & Farrar (2012a,b) were used. Regions with $E_{\mathrm{X}} > 100\,\mathrm{TeV}$ and $E_{\mathrm{X}} > 100\,\mathrm{TeV}$ are separated with a white line and the green circle shows the position of the Sun. White areas are regions, where either the radiation field model or the magnetic field model are not defined and in the black regions, $t_{\mathrm{cool,IC}} > t_{\mathrm{cool,sync}}$ for all energies such that E_{X} can not be calculated. Adapted version of Figure 4 in Breuhaus et al. (2021).

(Yang et al., 2021). For example, a young pulsar with an age of $20\,000$ yrs and a kick velocity of $300\,\mathrm{km\,s^{-1}}$ will have travelled a distance of $\sim 6\,\mathrm{pc}$. This distance is well below typical sizes of star-forming regions, which often have extensions of hundreds of parsec in spiral galaxies (Gusev, 2002). Observed TeV γ-ray sources are also spatially linked to star-forming activity (Aharonian et al., 2006; H. E. S. S. Collaboration, 2018).

In compact massive star clusters, the radiation fields can differ significantly from the normal Galactic average fields. Evolutionary models of massive star-forming regions surrounded by dusty photodissociation regions yield non-ionising UV radiation with energy densities of several hundreds of $\mathrm{eV\,cm^{-3}}$. The reprocessing of the incident emission by the surrounding dust regions can lead to FIR radiation fields with energy densities of $\sim 100\,\mathrm{eV\,cm^{-3}}$ in large parts of the star-forming region (Popescu et al., 2011; Dopita et al., 2005; Groves et al., 2008). The radiation energy densities depend on the mass of the star cluster, the age of the system and the spatial distribution of the surrounding dust clouds. For a typical Galactic magnetic field strength of $5\,\mathrm{\mu G}$, a FIR radiation energy density of $\sim 100\,\mathrm{eV\,cm^{-3}}$ ensures $\Xi_{\mathrm{IC}} > 150$. This is more than sufficient for hard UHE IC spectra, and consequently, star-forming regions provide optimal conditions.

Enhanced radiation energy densities compared to the axisymmetric model from Popescu et al. (2017) do also occur in spiral arms. These enhancements are approximately proportional to the inverse of the volume filling factor of the arms in the disk. Within the spiral arms themselves, there are local variations in the radiation energy density because of variations in the star formation activity away from stellar clusters and changes in the distribution of dust.

Unfortunately, the magnetic field is also increased in the spiral arms compared to the regions in between, which can counterbalance the increased radiation energy densities. However, the strongest contribution to the B-field strength does not come from the regular field but from local random components causing significant variations on scales of $100\,\mathrm{pc}$ and below (Gaensler & Johnston, 1995; Haverkorn et al., 2008; Jansson & Farrar, 2012b). The direction of the random component can be opposite to the regular field, and low values of $B < 3\,\mathrm{\mu G}$ can occur frequently. For example, the magnetic field in superbubbles is expected to be very low (Korpi et al., 1999). Very close to a PWN, the electrons might also flow into a low-density and low-B-field region (Giacinti et al., 2020).

Superbubbles and enhanced FIR energy densities are both associated with past or current star-forming activity, and the same applies to the creation of pulsars. Therefore, it is expected that low B-field regions, strong FIR radiation regions, and young pulsars are spatially coincident or located within proximity to each other. Consequently, powerful pulsars might frequently exist in regions providing the necessary conditions for UHE IC emission, and leptonic UHE sources can potentially occur along any line of sight through the Galactic disk.

3.4   Application to the ultra-high energy HAWC sources

As a proof of principles, simple leptonic equilibrium models will be applied to the three HAWC sources detected above 100 TeV. A more detailed time-dependent modelling of sources detected by LHAASO is done later in Section 3.5. The positions of the HAWC sources are not associated with any known region with high star formation rates (Murray & Rahman, 2010), but the surrounding environment is complex. To investigate possible enhancements of the radiation fields, maps from the Infrared Astronomical Satellite (IRAS Neugebauer et al., 1984) for wavelengths of 12 μm, 25 μm, 60 μm and 100 μm were used, covering the range of potential dust emission. Several objects in the vicinity of the HAWC sources can be identified, which can potentially contribute to the radiation fields. Assuming that these sources are located at the same distance as the corresponding HAWC sources, one can derive strict upper limits on additional contributions to the radiation fields. These upper limits are shown in Table 3.1.

Name	u_{discrete} [eV cm^{-3}]			
	12μm	25μm	60μm	100μm
J1825−134	< 2.6	< 4.6	< 13.6	< 12.7
J1907+063	< 0.9	< 0.5	0.0	0.0
J2019+368	< 0.19	< 0.33	< 0.96	< 0.99

TABLE 3.1: Upper limits on contributions to the large-scale radiation energy densities from local sources at the locations of the HAWC sources obtained from IRAS data. The limits do not depend on the distance of the sources. Table 2 in Breuhaus et al. (2021).

All sources can be potentially associated with pulsars with spin-down luminosities above $10^{36}\,\mathrm{erg\,s^{-1}}$, and an angular distance from the source centres less than 0.5° (Abeysekara et al., 2020). For the source eHWC J1825-134, there are even two possible associations

Name	u_{ISRF} [eV cm^{-3}]			
	12μm	25μm	60μm	100μm
J1825−134, 3.61 kpc	0.17	0.15	0.37	0.67
J1825−134, 1.55 kpc	0.09	0.06	0.13	0.31
J1907+063	0.09	0.06	0.14	0.32
J2019+368	0.06	0.04	0.07	0.18

TABLE 3.2: Energy densities at the IRAS wavelengths from the large-scale radiation model of Popescu et al. (2017) at the locations of the HAWC sources. The sources are assumed to be located at the same distance as the associated pulsars. The first and second rows show the energy densities for J1825−134, assuming an association to PSR1826−1334 (3.61 kpc from Earth), and PSR1826−1256 (1.55 kpc from Earth). Table 1 in Breuhaus et al. (2021).

with high spin-down power pulsars. As shown in Section 3.2, such powerful pulsars can accelerate electrons to sufficiently high energies, which is also confirmed by observations of the Crab nebula (Abeysekara et al., 2019; Lhaaso Collaboration et al., 2021). For the pulsar parameters, the same values provided in Abeysekara et al. (2020) are used, which were originally obtained from the ATNF Pulsar Catalogue (https://www.atnf.csiro.au/research/pulsar/psrcat/ ; Manchester et al., 2005). The characteristic ages $P/2\dot{P}$ are between 17 and 21 kyrs. Assuming that the sources are at the same distances as the pulsars, the acceleration and absorption constraints for $T = 50$ K and $B < 10$ µG are fulfilled, as shown in Figure 3.5. Combined with no clear correlation with target material, these facts make an IC origin of the sources likely.

To model the sources, electrons following an exponential cutoff power-law with a fixed power-law index of $\alpha = 2$ were injected into a region with a constant magnetic field of $B = 3$ µG and the equilibrium electron and γ-ray spectra were calculated. The minimum electron injection energy was 1 GeV, and the radiation field was the one inferred from the model of Popescu et al. (2017) at the pulsar locations together with the CMB. Additionally, a local enhancement of the radiation fields by a factor η was permitted. Table 3.2 shows the energy densities at the locations of the HAWC sources without enhancement for the same wavelengths as the IRAS limits from Table 3.1.

The radiation fields used for the modelling, together with the upper limits, are displayed in Figure 3.7. The dashed lines show the emission from the radiation model without enhancement, and the solid lines in the same colours the ones used for the modelling. The upper limits on the total energy density are shown in the respective colours too, calculated as the sum of the values deduced from IRAS data in Table 3.1 and the local radiation field energy densities in Table 3.2. For the source eHWC J1907+063,
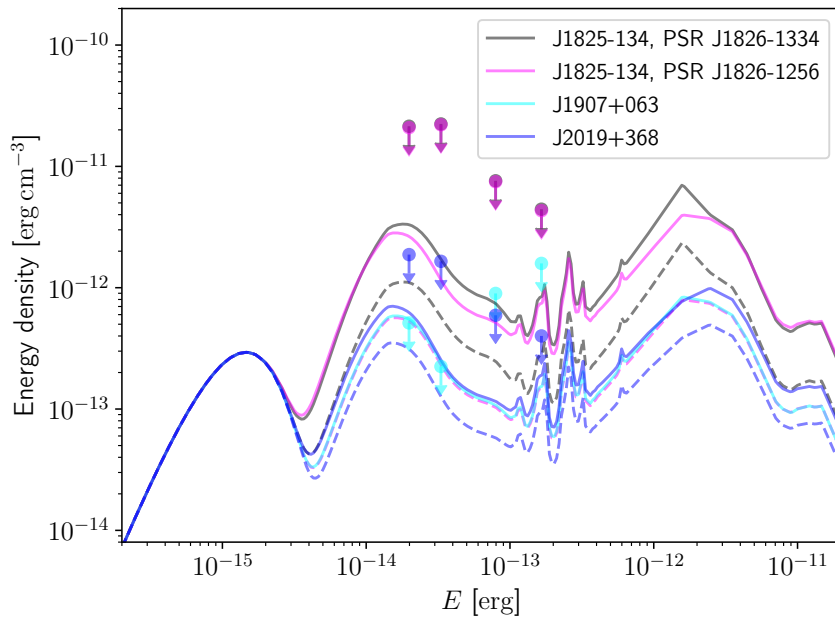
FIGURE 3.7: Photon spectra used for the equilibrium models and the upper limits derived from IRAS maps. Each colour represents one specific source location. Dashed lines show the radiation fields without enhancement, and solid lines the fields used for the modelling. For J1907+063, no enhancement was used, and the solid and dashed lines overlap. Both possible pulsar associations for the source J1825−134 are shown, and the respective total upper limits do overlap. This is the case, because differences in the energy densities from the large-scale field are small compared to the possible additional contribution.

no enhancement was used in the modelling, and therefore the solid and dashed lines overlap. For eHWC J1825−134, the upper limits for both pulsar associations overlap as well because the additional contribution is huge compared to the large-scale radiation field and the same for both associations. The bump at the lowest energies is the CMB. All photon fields are consistent with the corresponding upper limits. The internal absorption due to the enhanced photon fields is below 0.25 % and is therefore negligible. As stated in Section 3.2, the absorption due to the large-scale radiation fields at 100 TeV allows even in the worst-case transmissivities larger than 0.5. Because the most distant associated pulsar is only 3.61 kpc away from Earth, the large-scale absorption will be ignored too.

Figure 3.8 shows the systematic errors and the statistical error band from the best fit of the three sources from Abeysekara et al. (2020) together with the equilibrium models of the emission. For the source eHWC J1825−134, there are two pulsar associations given by Abeysekara et al. (2020). Only the curve for an association to PSR J1826−1334 is shown in Figure 3.8; the one for PSR J1826−1256 is nearly identical. The other model parameters are listed in Table 3.3. The value for Ξ_{IC} was calculated by using

the complete target photon spectrum. It is already fixed by η but listed in the table for completion. All enhancement factors are compatible with the limits derived from IRAS data, but values of for example $\eta = 3$ could also be explained by an increased energy density due to the spiral arm structure.

Name	η	E_{cut}	$\dot{E}_{\mathrm{inj}>1\,\mathrm{GeV}}/L_{\mathrm{SD}}$	Ξ_{IC}
J1825−134 / PSR J1826−1334	3	350 TeV	54 %	42
J1825−134 / PSR J1826−1256	5	350 TeV	45 %	34
J1907+063	1	480 TeV	20 %	8
J2019+368	2	400 TeV	5 %	9

TABLE 3.3: Parameters of the equilibrium models. It was $\alpha = 2$ and $B = 3\,\mu\mathrm{G}$ in all cases. η is the enhancement factor of the large-scale Galactic radiation field at the source location and $\dot{E}_{\mathrm{inj}>1\,\mathrm{GeV}}/L_{\mathrm{SD}}$ the fraction of the spin down luminosity of the pulsar injected into electrons above $1\,\mathrm{GeV}$.

The data can be matched well for the sources eHWC J1825-134 and eHWC J1907+063. The spectrum for eHWC J2019+368 is not matched for energies lower than $\sim$10 TeV, where a break in the electron spectrum would be needed. Such a break can be achieved when the finite source age is taken into account, and below 10 TeV the electrons are still uncooled and not yet in equilibrium (see e.g. Joshi, 2019; Albert et al., 2021c). This shows the limitations of equilibrium models, which are only applicable at sufficiently high energies. The cutoff energies are all above 300 TeV and $\Xi_{\mathrm{IC}} > 1$ in all cases. Table 3.3 also shows the faction of spin-down energy of the associated pulsars injected into electrons above 1 GeV, which are between 5 % (J2019+368) and 54 % (J1825−134 associated to PSR J1826−1334). However, these numbers should be interpreted carefully because the electrons would not be in equilibrium at low energies for the finite pulsar ages. For energies below 10 TeV, the characteristic ages are well below the cooling times for the model parameters chosen, and no equilibrium between injection and energy losses is established. For energies above 10 TeV, between 1 % and 13 % of the spin-down power of the pulsars is required to account for the observed flux levels.

The model parameters are not unique because different setups can lead to very similar γ-ray spectra. The shape at the highest energies is influenced by Ξ_{IC}. An increase in the enhancement parameter η and a lower magnetic field both shift the cutoff feature to higher energies. If the cutoff energy of the injection spectrum is reduced at the same time, the γ-ray cutoff can be shifted to the lower energies where it was before. For a reduced radiation energy density or an increased B-field the contrary happens, except that the CMB will have a more important influence changing the slope slightly for low
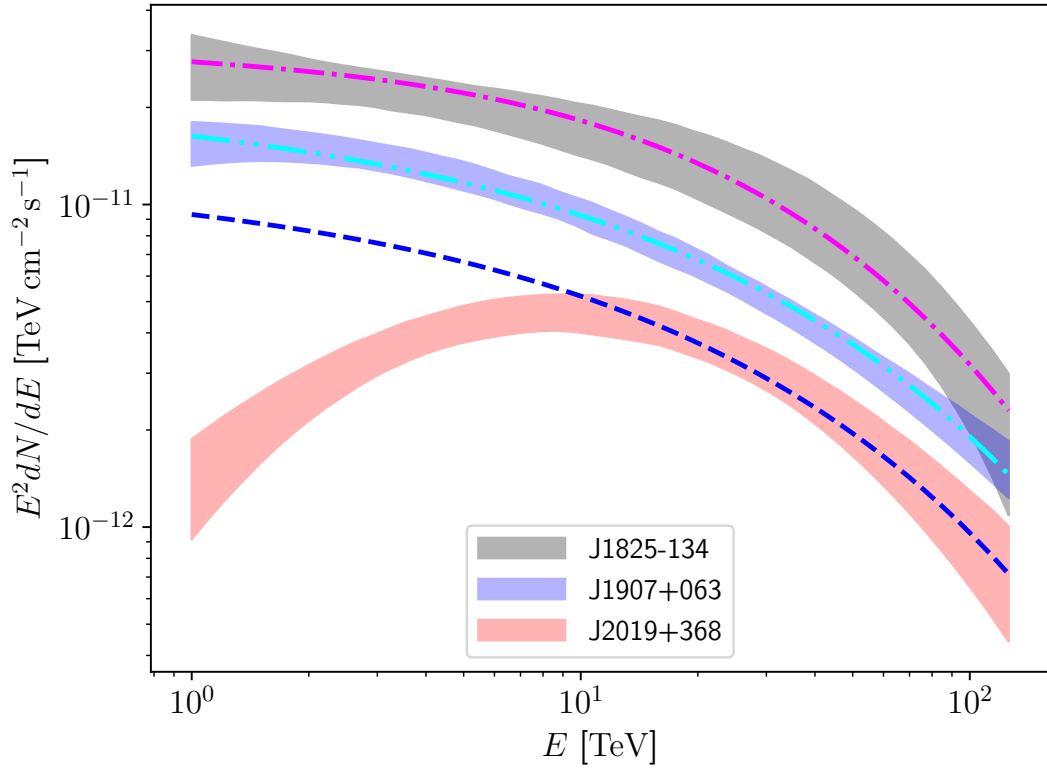
FIGURE 3.8: Data and equilibrium models for the three eHWC sources. The power-law index of the injection spetra was $\alpha = 2$, and the B-field was fixed to $3\,\mu G$ in all cases. The photon field was the one from Popescu et al. (2017) at the location of the sources with an additional multiplication factor η together with the CMB. The other parameters are: $\eta = 3$ ($\Xi_{IC} = 42$), $E_{cut} = 350\,TeV$ (J1825−134 / PSR J1826−1334), $\eta = 1.0$ ($\Xi_{IC} = 8$), $E_{cut} = 480\,TeV$ (J1907+063) and $\eta = 2$ ($\Xi_{IC} = 9$), $E_{cut} = 400\,TeV$ (J2019+368). The curve for J1825−134 associated to PSR J1826−1256 is nearly identical to the one shown here for PSR J1826−1334. The error bands include the systematic and the statistical errors of the best fit given by Abeysekara et al. (2020), the systematic error was extracted manually from Figue 3 in Abeysekara et al. (2020). Adapted version of Figure 4 in Breuhaus et al. (2021).

B-fields, which can be compensated with a different value for α. For instance, the source J1907+063 can be equally well matched with $\eta = 0.5$ or $\eta = 1.5$, and the source J2019+368 for $\eta = 1$.

To discriminate between different models, more information about the source and its environment is needed. For the simple equilibrium models, multiwavelength data at lower energies do not necessarily help in this regard because the electrons are not in equilibrium at these energies. However, the only exception is synchrotron emission in the X-ray regime, which is produced by the same electrons creating the IC emission above energies of $10\,TeV$. The ratios between the IC and the synchrotron emission will scale approximately with Ξ_{IC}. For the source eHWC J2019+368, this is approximately

consistent with X-ray measurements from Suzaku (Mizuno et al., 2017). Data from different wavelengths must always be compared carefully because it can originate from regions with different sizes and could even be produced by different emission mechanisms or particle populations. Because already simple equilibrium models with reasonable scenarios match the HAWC measurements, one can conclude that leptonic sources might very well be the origin of the UHE emission.

3.5   Time-dependent models for LHAASO sources

For modelling energies below the equilibrium state, time-dependent models are needed. This became obvious for the case of eHWC J2019+368 below 10 TeV. Time-dependent models for this source were already developed by Joshi (2019); Albert et al. (2021c), which showed that leptonic models can account for the observations at the HAWC energies and below. For the other sources, a cooling turnover could avoid the necessity of enhancements in the radiation field. Furthermore, it is important to assess if leptonic models are able to explain emission from energies even higher than detected by the HAWC observatory. Last year, the LHAASO collaboration announced the detection of 12 sources above 100 TeV with a detection of more than $7\,\sigma$ (Cao et al., 2021). For three of these sources, Cao et al. (2021) provided spectral energy distributions: LHAASO J2226+6057, LHAASO J1908+0621 and LHAASO J1825−1326. The latter two sources are counterparts to the HAWC sources modelled in the previous section, eHWC J1907+063 and eHWC 1825−134. Here, we will therefore do a time-dependent modelling of these three sources, including data from the HAWC observatory and investigate consistency with radio observations.

3.5.1   Method

As in the previous section, it is assumed that the electrons are injected into a region with constant isotropic and homogeneous magnetic and radiation fields. The injection spectrum of the electrons is again assumed to follow an exponential cutoff power-law with the following definition of the parameter $\dot{N}_0$:

$$Q(E) = \dot{N}_0 \cdot \left(\frac{E}{1\,\mathrm{erg}} \right)^{-\alpha} \cdot \exp\left(-\frac{E}{E_{\mathrm{cut}}} \right). \tag{3.11}$$

The electrons are injected over a finite time interval of the same length as the pulsar's age with the same injection rate. This ignores the pulsar evolution, but will not significantly influence the γ-ray spectra at the highest energies where the cooling times are short. For a constant braking index and ages below the initial spin-down timescale τ_0, pulsars will have approximately constant energy losses (e.g. Gaensler & Slane, 2006). Therefore, for young, powerful pulsars, a constant injection energy input is not a very inaccurate approximation.

For calculating the electron spectra, only synchrotron and IC losses are considered; it is assumed that adiabatic losses and particle escape can be neglected. The solution to this problem can be obtained in a simple semianalytic form (see e.g. Atoyan & Aharonian, 1999), which is an option of the GAMERA code (Hahn, 2015). The radiation fields are assumed to be the ones from the model of Popescu et al. (2017) at the location of the sources together with the CMB and the possibility of a local enhancement. At energies above $\sim$100 TeV, the CMB becomes important for the absorption of the γ rays (e.g. Gould & Rephaeli, 1978; Vernetto & Lipari, 2016). Because the LHAASO observatory provides data up to several hundreds of TeV, the absorption will therefore be taken into account. The maximum absorption due to the CMB occurs close to 1 PeV. For the most distant pulsar, PSR 1907+0632 associated to LHAASO J1908+0621, the transmissivity at 1 PeV is 67 %.

The LHAASO collaboration gives a list of possible pulsar counterparts for the three sources located within 1° of the respective source, which are listed together with the pulsar properties in Table 3.4. For LHAASO J2226+6057, there is only one associated pulsar, but for the other sources, there are two. The pulsars associated with LHAASO J1825−1326 are the same quoted by the HAWC collaboration (Abeysekara et al., 2020), although a distance of 3.1 kpc for PSR J1826−1334 from a different reference is given, which is slightly lower than the value of 3.61 kpc quoted by (Abeysekara et al., 2020). Here, we will use the value from Cao et al. (2021). Furthermore, there is the additional less powerful pulsar counterpart PSR 1907+0631 for the source LHAASO J1908+0621 / eHWC J1907+063, which will be considered too.

To determine the model parameters, $\dot{N}_0$, α and E_{cut} were fitted to the data for a fixed magnetic and radiation field. Because the error for the cutoff energy is highly asymmetric, a separate error analysis for E_{cut} was performed. It consisted of determining

Pulsar (source)	Distance [kpc]	Age [kyrs]	L_{SD} [erg s^{-1}]	u_{ph} [eV cm^{-3}]
PSR J2229+6114 (J2226+6057)	0.8	10.0	2.2×10^{37}	0.54 (0.16)
PSR J1826-1334 (J1825-1326)	3.1	21.4	2.8×10^{36}	2.15 (0.41)
PSR J1826-1256 (J1825-1326)	1.6	14.4	3.6×10^{36}	1.21 (0.28)
PSR 1907+0602 (J1908+0621)	2.4	19.5	2.8×10^{36}	1.24 (0.28)
PSR 1907+0631 (J1908+0621)	3.4	11.3	5.3×10^{35}	1.50 (0.32)

TABLE 3.4: List of possibly associated pulsars for the three LHAASO sources LHAASO J2226+6057, LHAASO J1825−1326 and LHAASO J1908+0621 and relevant pulsar properties (Cao et al., 2021, and references therein). The source names are shown in brackets below the pulsar names in the first column. L_{SD} is the spin-down luminosity, and the last column shows the radiation energy density at the pulsar locations from the model of Popescu et al. (2017) in the IR below the wavelength $\lambda = 700\,\mathrm{nm}$ and the optical and UV energy density above this value in parentheses. The CMB is not included in the calculation of u_{ph}. Table 1 in Breuhaus et al. (2022b).

the 95 % confidence interval for the probability density function of the χ^2 distribution depending on E_{cut}.

3.5.2   LHAASO J2226+6057

Two possible astrophysical particle accelerators can be related to the source LHAASO J2226+6057, the supernova remnant G106.3+2.7 and the pulsar PSR J2229+6114. At the center of the 100 TeV emission a molecular cloud is located (Tibet ASγ Collaboration et al., 2021). This seems advantageous for a hadronic origin of the emission, where the CRs are accelerated in SNR G106.3+2.7, and the escaping particles interact with the cloud material. Such hadronic scenarios for γ-ray emission from the region have been developed (e.g. Albert et al., 2020; Yang et al., 2022). A problem for such scenarios is the age of the SNR ($\lesssim 10^4$ yrs). Exceptional conditions would be required to accelerate particles to PeV energies during this phase of the SNR evolution.

The pulsar PSR J2229+6114 has a very high spin-down luminosity of $2.2 \times 10^{37}\,\mathrm{erg\,s^{-1}}$, the highest value of all pulsars in Table 3.4. It is easily able to accelerate electrons to the required energies. The pulsar is surrounded by its PWN, the Boomerang Nebula (see e.g. Kothes et al., 2006). Kothes et al. (2006) give an estimation of the magnetic field by assuming that the observed spectral radio break at $\nu \approx 5$ GHz is due to the cooling of the accelerated electrons of $B = 2.6$ mG. The counterpart of this break in the IC emission

produced by the same electron population would be well below the LHAASO energy range. However, other works questioned the existence of such high magnetic field values on large scales (Liu et al., 2020). Other processes, such as particle escape, could produce spectral breaks too. The shape of the Boomerang Nebula is very different from usual PWN, which have a centrally peaked diffuse or a bow shock shape. To explain their radio observations, Kothes et al. (2006) proposed that the radio emission is produced at a part of the PWN hitting a reverse shock from the SNR, which collided with dense HI material in the north-east. The PWN shock in the opposite south-west direction then has very different properties making it easier that particles can be accelerated to PeV energies and subsequently escape and diffuse into a low density, low B-field region. This is consistent with the position of the LHAASO source, located $\approx 0.4°$ to the south-west of the Boomerang Nebula. Evidence for such an outflow exists at different wavelengths(Liu et al., 2020). Because the radio data given by, for example, Kothes et al. (2006) comes from a different region with different properties as the UHE γ-ray data, a simultaneous modelling would require more sophisticated multi-zone models beyond the scope of this work.

The LHAASO data alone does not allow to constrain the model parameters well. For example, a variety of models with different values for the power-law index α can explain the data equally well. This was verified by means of a Markov-Chain-Monte-Carlo analysis of the parameter space. Current theories of particle acceleration at relativistic shocks do not favour the production of power-law indices $\alpha < 2$ (e.g. Sironi et al., 2015). Therefore, the index was set to $\alpha = 2.2$. This value is compatible with the spectrum above the radio break $S_\nu \propto \nu^{-0.59}$ from Kothes et al. (2006). Without an enhancement of the radiation field and $B = 3\,\mu G$, the resulting normalisation was $\dot{N}_0 = (9 \pm 2) \times 10^{33}\,\mathrm{erg}^{-1}\,\mathrm{s}^{-1}$ and the cutoff energy $E_{\mathrm{cut}} = 420^{+210}_{-130}\,\mathrm{TeV}$, where the errors of E_{cut} are the 95 % confidence limits. The fitresult and the data are shown in Figure 3.9. The dotted line is the emission without absorption, as can be seen, the absorption is low compared to the flux level. The upper limit from Equation 3.5, corresponding to the Hillas limit or the maximum potential drop of the pulsar (see e.g. Amato & Olmi, 2021) for PSR J2229+6114 is $\sim 12\,\mathrm{PeV}$, which is well above the resulting value of E_{cut}. The high spin-down power can easily supply the necessary power, only 0.13 % of L_{SD} are needed to be injected into electrons above $1\,\mathrm{TeV}$, and ≈ 1 % above energies of $1\,\mathrm{GeV}$. Leptonic models for the multiwavelength emission by Liu et al. (2020) and Yu et al.

(2022) obtained good matches to data from different observatories for a magnetic field of $4\,\mu\text{G}$ and injection indices of $\alpha = 2.4 - 2.5$. However, their IR photon fields with an energy density of $0.3\,\text{eV}\,\text{cm}^{-3}$ are different than the one used here.

The size of the γ-ray emission region is either determined by the maximum distance particles were able to diffuse since their acceleration, or the maximum distance they diffused before being cooled. A measurement of the energy-dependent morphology could disentangle which scenario applies: In the first case, when the system size is age limited, the source extension grows with increasing energy because electrons with higher energies diffuse faster. If the size is instead cooling limited, the opposite effect could happen because the high energy particles cool more quickly than low energy particles. However, this depends on the dependence of the diffusion coefficient and the cooling time with energy. In both cases, the radial profile for a fixed energy is proportional to $1/r$. If the diffusion is spherically symmetric, the radial diffusion coefficient can be calculated as $D_{\text{r}} = R^2/4\tau$, where τ is the minimum of the age and the cooling time, and R is the radius of the emission region. With a radial size of $\approx 1°$ estimated from Fig. 1 of Cao et al. (2021) and a distance of $0.8\,\text{kpc}$ (3.4), the diffusion coefficient at $100\,\text{TeV}$ is $D_{\text{r}} = 1.5 \times 10^{27}\,\text{cm}^2\,\text{s}^{-1}$. This is above the lower limit given by the Bohm diffusion coefficient for $B = 3\,\mu\text{G}$, $D_{\text{Bohm}}(100\text{ TeV}) = 1.1 \times 10^{27}\,\text{cm}^2\,\text{s}^{-1}$, but below the average Galactic diffusion coefficient $D_{\text{Gal}} \approx 10^{26} E_{\text{GeV}}^{1/3}\,\text{cm}^2\text{s}^{-1}$. A similar result, i.e. a reduced diffusion coefficient with respect to the Galactic one, was also observed around other PWN such as Geminga (Abeysekara et al., 2017).

3.5.3   LHAASO J1908+0621

This source is the counterpart of the UHE HAWC source eHWC J1907+063 modelled with the simple equilibrium model in Section 3.4 (Abeysekara et al., 2020). The source was detected first by the Multiple Institution Los Alamos Gamma Ray Observatory (MI-LAGRO, Abdo et al., 2007), and subsequently by other observatories such as H.E.S.S. (Aharonian et al., 2009). In addition to the pulsar PSR 1907+0602, Cao et al. (2021) list an additional closeby pulsar, PSR 1907+0631. However, its spin-down luminosity of $5.3 \times 10^{35}\,\text{erg}\,\text{s}^{-1}$ is below $10^{36}\,\text{erg}\,\text{s}^{-1}$. Additionally, the middle-aged supernova remnant G40.05$-$0.5 is located nearby. Its exact distance is unknown, but the pulsar PSR 1907+0631 is located close to the centre of the SNR and might likely be the remnant of
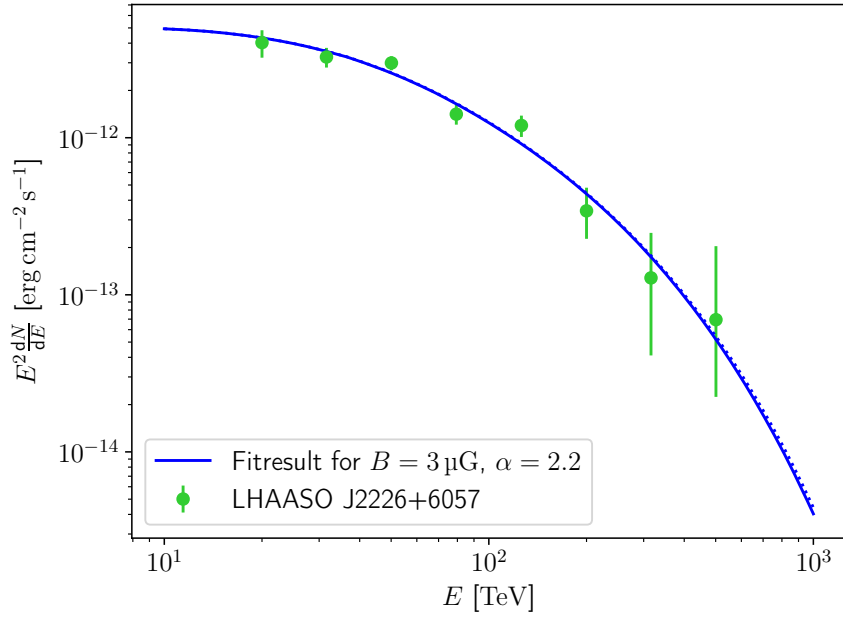
FIGURE 3.9: Data for LHAASO J2226+6057 from Cao et al. (2021) together with the fit for $B = 3\,\mu G$, no enhancement of the radiation field and a fixed injection power-law index of $\alpha = 2.2$. The resulting fitparameters were $\dot{N}_0 = (9 \pm 2) \times 10^{33}\,\mathrm{erg}^{-1}\,\mathrm{s}^{-1}$ and $E_{\mathrm{cut}} = 420^{+210}_{-130}\,\mathrm{TeV}$. The dotted line, nearly indistinguishable from the solid curve, shows the flux without absorption. Adapted version of Figure 1 in Breuhaus et al. (2022b).

the past supernova explosion (see e.g. Crestan et al., 2021). In the leptonic modelling, a fit for each pulsar was performed separately.

Figure 3.10 shows the datapoints from LHAASO (Cao et al., 2021), from HAWC and the systematical and statistical erroband from HAWC (Abeysekara et al., 2020). A fit to both datasets for $B = 3\,\mu G$, no enhancement of the photon field and an association to PSR 1907+0602 is shown in blue. The resulting parameters are $\dot{N}_0 = (10 \pm 2) \times 10^{35}\,\mathrm{erg}^{-1}\,\mathrm{s}^{-1}$ and $\alpha = 2.66 \pm 0.03$. Although the resulting cutoff energy was 10 PeV, this value is not meaningful, because E_{cut} can only be constrained to be above 1.4 PeV with a 95 % confidence level. The Hillas limit from Equation 3.5 has a value of 4.2 PeV, which was used for the curve shown in Figure 3.10. 40 % of the pulsar spin-down luminosity has to be injected into electrons above 1 TeV. Due to the soft power-law index of 2.66, more energy content is deposited at low energies. Therefore, a minumun injection energy of 240 GeV is needed to not exceed the available power input. If a break in the power-law spectrum below 1 TeV exists and the injection spectrum would be harder at lower energies, the minimum injection energy can be lower. There is observational evidence, that such a break might indeed occur (Crestan et al., 2021).

A fit for an association to PSR 1907+0631 gives $\dot{N}_0 = (4.2 \pm 0.5) \times 10^{36} \, \text{erg}^{-1} \, \text{s}^{-1}$, $\alpha = 2.79 \pm 0.03$ and $E_{\text{cut}} > 2 \, \text{PeV}$ at a 95% confidence level. The Hillas limit of this pulsar is $1.8 \, \text{PeV}$, which is below the cutoff limit from the fit. Additionally, more than seven times the energy available from the spin-down luminosity is required to be injected into electrons above $1 \, \text{TeV}$ to provide the observed emission levels. In principle, the spin-down luminosity could have been higher in the past. However, at high energies the cooling times are short, and even accounting for the evolution of L_{SD}, the pulsar is unlikely to provide the necessary power output. Hence, PSR 1907+0631 is most likely not the only contributor to the UHE γ-ray source.

The cyan curve in Figure 3.10 shows the equilibrium model developed in Section 3.4 and shown previously in Figure 3.8. It was extended to lower energies and corrected for absorption. As the blue curve, it was developed for an association with PSR 1907+0602. It matches the LHAASO and HAWC data well, although it was originally only developed for the HAWC data. The shapes at high energies of the cyan and the blue curve are slightly different due to the harder α value of the equilibrium model and its lower cutoff value. This leads to a steeper decline compared to the fit of the joint dataset. In the overlapping energy range of the HAWC and LHAASO data, the LHAASO data is below the HAWC data, which leads to a more gradual turnover of the fit.

IRAS data does not allow an enhancement of the radiation field between $60 \, \mu\text{m}$ and $100 \, \mu\text{m}$ (see Section 3.4). Therefore, the radiation field should be close to the average Galactic field. Even though the magnetic field is the only uncertain parameter, it can not be constrained well with the γ-ray data because good matches with the data also exist for magnetic fields different than the value of $3 \, \mu\text{G}$ used in the previous fit. Fits for a fixed increased magnetic field value result in reduced α and E_{cut} values. Therefore, if one requires that α should be above 2, one can put an upper limit on the magnetic field of $\sim 8 \, \mu\text{G}$, leading to a cutoff energy of $730^{+810}_{-310} \, \text{TeV}$, where the errors are the 95% confidence intervals. The limit on the magnetic field is not completely strict: The demand for $\alpha \gtrsim 2$ comes from the acceleration processes. If acceleration and emission region are decoupled, as is the case for acceleration close to the pulsar with high B-fields and diffusion into a low B-field region, an energy-dependent escape from the acceleration region could lead to a harder injection spectrum into the low B-field region. Although the cutoff energy is reduced for higher magnetic field values, the error gets larger. For the case of $B = 8 \, \mu\text{G}$ discussed above, $E_{\text{cut}} = 1 \, \text{PeV}$ is still within the error range.

Therefore, LHAASO J1908+0621 could be powered by a Galactic pevatron accelerator even for high magnetic fields.

Radio emission might help to constrain the B-field and subsequently the other parameters. However, no significant emission on the extent of the LHAASO source has been observed until now. From the non-detection of the source, Duvidovich et al. (2020) derived upper limits at $1.5\,\mathrm{GHz}$ and $6\,\mathrm{GHz}$ of $1\,\mathrm{mJy\,beam^{-1}}$ and $10\,\mu\mathrm{Jy\,beam^{-1}}$ respectively. The beamsizes for the two frequencies are $51.1'' \times 39.5''$ and $12.2'' \times 8.6''$. Assuming a source size of $1°$, estimated from Fig. 1 in Cao et al. (2021), the following upper limits are obtained: $3.0 \times 10^{-13}\,\mathrm{erg\,cm^{-2}\,s^{-1}}$ at $1.5\,\mathrm{GHz}$, and $2.3 \times 10^{-13}\,\mathrm{erg\,cm^{-2}\,s^{-1}}$ at $6\,\mathrm{GHz}$. If the same power-law index continues to lower energies, the model from the fit for $B = 3\,\mu\mathrm{G}$ is not consistent with these limits. However, requiring fulfilment of the energy constraints automatically leads to consistency with the radio limits: For a minimum injection energy of $240\,\mathrm{GeV}$ to not exceed the available power input, the model emission in the radio is below the limits and the same applies for a power-law break below $1\,\mathrm{TeV}$.

The upper limits do not exclude different leptonic models for the HAWC and LHAASO data without further assumptions, because there are also models without high minimum injection energy or a spectral break that are consistent with the radio limits. Fixing the power-law index to $\alpha = 2.2$ and instead varying the B-field, a joint fit on the HAWC and LHAASO data requiring consistency with the radio limits gives $B = (5.7 \pm 0.3)\,\mu\mathrm{G}$, $\dot{N}_0 = (2.8 \pm 0.2) \times 10^{35}\,\mathrm{erg^{-1}\,s^{-1}}$ and $E_\mathrm{cut} = 830^{+360}_{-220}\,\mathrm{TeV}$. The corresponding curve is shown with the magenta line in figure 3.10. The lower value of α allows a continuation of the injection spectrum down to lower energies without exceeding the energy budget. $30\,\%$ of the spin-down power are injected into electrons above $1\,\mathrm{TeV}$, and the minimum injection energy is $10\,\mathrm{GeV}$, more than one order of magnitude lower than for the fit with a fixed value of $B = 3\,\mu\mathrm{G}$.

As for the source LHAASO J2226+6057, an estimate of the diffusion coefficient based on the environmental model parameters can be obtained. For $B = 3\,\mu\mathrm{G}$ and a radial size of $1°$, $D_\mathrm{r}(100\,\mathrm{TeV}) = 1.3 \times 10^{28}\,\mathrm{cm^2\,s^{-1}}$. The corresponding Bohm diffusion coefficient is $1.1 \times 10^{27}\,\mathrm{cm^2\,s^{-1}}$, which is one order of magnitude lower. For a magnetic field of $B = 5.8\,\mu\mathrm{G}$, the result of the fit including the radio limits, one obtains $D_\mathrm{r}(100\,\mathrm{TeV}) =$
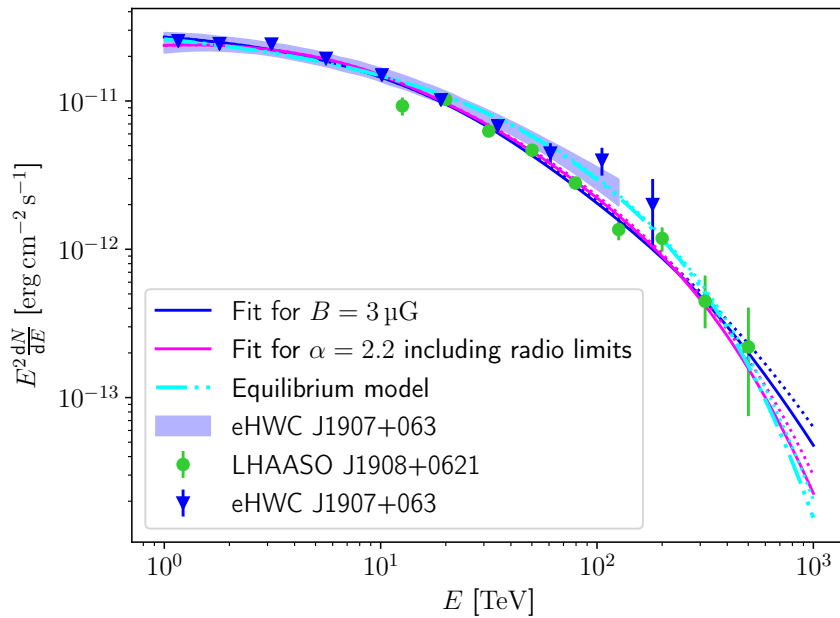
FIGURE 3.10: Data for LHAASO J1908+0621 (green) and eHWC J1907+063 (blue, together with the systematic and statistical error band) together with different models. Dotted lines in the corresponding colours show the model curves without absorption. The blue line is the result for the fit with $B = 3\,\mu G$ assuming an association to PSR 1907+0602 leading to $\dot{N}_0 = (10 \pm 2) \times 10^{35}\,\mathrm{erg}^{-1}\,\mathrm{s}^{-1}$ and $\alpha = 2.66 \pm 0.03$. The cutoff energy was set to the Hillas limit of $4.2\,\mathrm{PeV}$ since E_{cut} is only constrained to be $>1.4\,\mathrm{PeV}$. The magenta line is the fitresult including the radio upper limits, fixing $\alpha = 2.2$ and varying the B-field instead, resulting in $B = (5.7 \pm 0.3)\,\mu G$, $\dot{N}_0 = (2.8 \pm 0.2) \times 10^{35}\,\mathrm{erg}^{-1}\,\mathrm{s}^{-1}$ and $E_{\mathrm{cut}} = 830^{+360}_{-220}\,\mathrm{TeV}$. The cyan line shows the equilibrium model from Figure 3.8 corrected for absorption and extended to higher energies. Adapted version of Fig. 2 in Breuhaus et al. (2022b).

$3.9 \times 10^{28}\,\mathrm{cm}^2\,\mathrm{s}^{-1}$ and a Bohm diffusion coefficient of $5.8 \times 10^{26}\,\mathrm{cm}^2\,\mathrm{s}^{-1}$ well below the value of D_{r}.

3.5.4   LHAASO J1825−1326

The source LHAASO J1825−1326 is located in a very complex environment (see e.g. Voisin et al., 2016). Two powerful pulsars are located nearby, PSR J1826−1334 and PSR J1826−1256. PSR J1826−1334 is located closer to the centre of the emission than PSR J1826−1256, but it could be that both contribute to a potentially leptonic origin of the emission. As for LHAASO J1908+0621, we will consider both pulsars separately. The LHAASO source J1825−1326 is the counterpart of the HAWC source eHWC J1825−134, and we will perform a joint fit on both datasets.

First, an association with PSR J1826$-$1334 is considered, the B-field is fixed to $3\,\mu$G and the radiation field is the one from the radiation model from Popescu et al. (2017) without enhancement together with the CMB. The fit gives the parameters $\dot{N}_0 = (5 \pm 2) \times 10^{35}\,\mathrm{erg}^{-1}\,\mathrm{s}^{-1}$, $\alpha = 2.23 \pm 0.09$ and $E_\mathrm{cut} = 390^{+340}_{-150}\,\mathrm{TeV}$, where the errors of E_cut represent the $95\,\%$ confidence interval. $50\,\%$ of the spin-down power needs to be injected above $1\,\mathrm{TeV}$ to reach the required flux levels. If no spectral break below $1\,\mathrm{TeV}$ exists, the minimum injection energy to be consistent with the available energy budget is $90\,\mathrm{GeV}$. The Hillas limit for the pulsar is $4.2\,\mathrm{PeV}$, which is well above the cutoff energy from the fit. The fitresult is shown in Figure 3.11 with the blue curve.

Fitting the data for an association to PSR J1826$-$1256, $B = 3\,\mu$G and no enhancement of the large-scale radiation field gives $\dot{N}_0 = (4 \pm 2) \times 10^{35}\,\mathrm{erg}^{-1}\,\mathrm{s}^{-1}$, $\alpha = 2.39 \pm 0.09$ and $E_\mathrm{cut} = 410^{+380}_{-160}\,\mathrm{TeV}$. Because the resulting γ-ray emission is nearly identical to the one from the fit for PSR J1826$-$1334, it is not shown additionally in Figure 3.11. $20\,\%$ of the spin-down power are needed to be injected above $1\,\mathrm{TeV}$ and without a spectral break at low energies, the minimum injection energy to be consistent with the energy budget is $25\,\mathrm{GeV}$. The Hillas limit for PSR J1826$-$1256 of $4.7\,\mathrm{PeV}$ is well above the fitresult of E_cut. Therefore, both pulsars can potentially power the UHE γ-ray source.

The source can be matched equally well in different environments. For example, an increased B-field results in lower values for α. For $B = 5\,\mu$G, the fit for an association to PSR J1826$-$1334 gives $\dot{N}_0 = (1.8 \pm 0.8) \times 10^{35}\,\mathrm{erg}^{-1}\,\mathrm{s}^{-1}$, $\alpha = 1.9 \pm 0.1$ and $E_\mathrm{cut} = 310^{+200}_{-110}\,\mathrm{TeV}$. An enhancement of the radiation field has the opposite effect resulting in lower values of α. This highlights the importance of more information about the source region or taking into account multiwavelength data to confirm or rule out different models. Because the IRAS data in principle allows enhancements of the radiation field up to a factor of 16 (see Section 3.4), a large variety of models with higher magnetic field values exists.

The magenta line in Figure 3.11 shows the simple equilibrium model developed previously in Section 3.4. It is very similar to the fit result for $B = 3\,\mu$G and an association to PSR J1826$-$1334 and matches the LHAASO data well. The difference in terms of the environmental parameters is that in the equilibrium model, the radiation field was enhanced by a factor of 3 in the case of PSR J1826$-$1334 and a factor of 5 for PSR J1826$-$1256. The B-field strength of $3\,\mu$G was the same in all cases. The time-dependent

models with a finite source age do not require enhanced radiation fields to be able to explain the low energy HAWC data because of a cooling break in the electron spectrum, which hardens the spectrum at energies below.

The source was never detected on large scales in the radio band, however, Duvidovich et al. (2019) derived upper limits based on the non-detection. At $1.4\,\mathrm{GHz}$, they obtained a limit of of $0.24\,\mathrm{mJy\,beam^{-1}}$ with a beamsize of $9.24'' \times 6.43''$. Assuming a radial source extent of $\sim 1°$ derived from Fig. 1 in Cao et al. (2021) one obtains an upper limit of $2.3 \times 10^{-12}\,\mathrm{erg\,cm^{-2}\,s^{-1}}$. All models in this section are consistent with this constraint.

Assuming that the source extent is determined by the minimum of the system age and the cooling time, for $B = 3\,\mathrm{\mu G}$ and no enhancement of the radiation field one obtains $D_{\mathrm{r}}(100\,\mathrm{TeV}) = 2.3 \times 10^{28}\,\mathrm{cm^2\,s^{-1}}$ for an association to PSR J1826-1334 and $D_{\mathrm{r}}(100\,\mathrm{TeV}) = 6.0 \times 10^{27}\,\mathrm{cm^2\,s^{-1}}$ for PSR J1826-1256. Both values are above the corresponding Bohm diffusion coefficient of $1.1 \times 10^{27}\,\mathrm{cm^2\,s^{-1}}$.
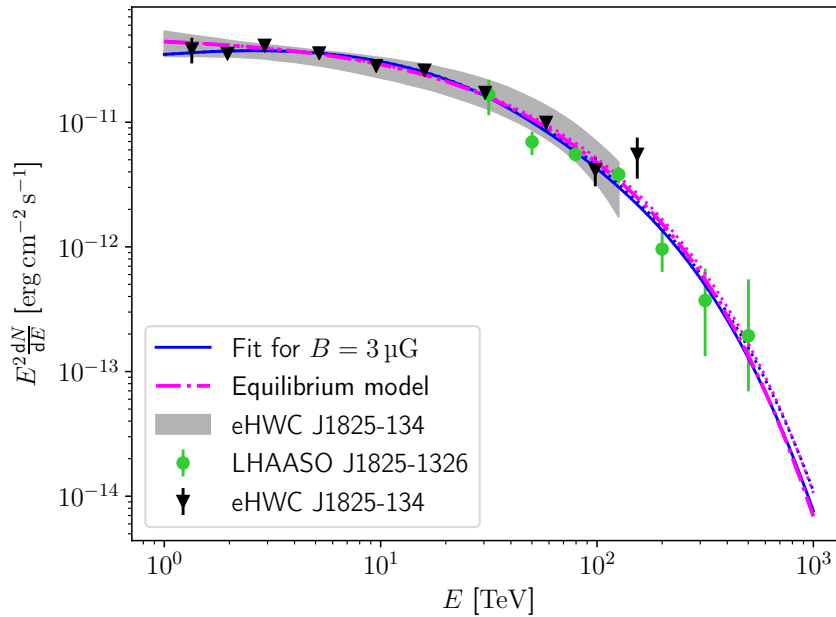
FIGURE 3.11: Data for LHAASO J1825−1326 (green) and eHWC J1825−134 (black, together with the systematic and statistical error band) together with different models. The γ-ray flux without absorption is shown with dotted lines in the corresponding colours. The blue line depicts the fit for $B = 3\,\mathrm{\mu G}$, no enhancement of the radiation field and an association to PSR J1826−1334. The resulting parameters are $\dot{N}_0 = (5 \pm 2) \times 10^{35}\,\mathrm{erg^{-1}\,s^{-1}}$, $\alpha = 2.23 \pm 0.09$ and $E_{\mathrm{cut}} = 390^{+340}_{-150}\,\mathrm{TeV}$. The magenta line shows the equilibrium model from Section 3.4 shown before in Figure 3.8 corrected for absorption and extended to higher energies. Adapted version of Fig. 3 in Breuhaus et al. (2022b).

3.6   Discussion

In regions with sufficiently strong FIR and IR radiation fields or low magnetic fields, hard IC spectra can be produced until energies of 100 TeV. The requirement is that IC energy losses dominate over synchrotron losses until sufficiently high energies. Pulsars with high energy losses are able to accelerate electrons to the required energies. If the termination shock is near the pulsar where magnetic fields are high, a decoupling of the acceleration and the emission region is required. In such scenarios, electrons can diffuse sufficiently fast outwards without substantial IC losses and fill a larger low B-field emission region.

On large scales in the Milky Way, the required conditions are only met at very large Galactic radii and high above and below the disk, where not many accelerators are expected. However, in star-forming regions or regions with increased radiation energy densities, such as spiral arms, the conditions can likely be satisfied. The same applies to regions with low magnetic fields, such as superbubbles. A requirement is that the particles can be confined long enough and that strong radiation fields do not prevent the detection of γ rays due to absorption.

With the detection of photons at PeV energies from the Crab nebula (Lhaaso Collaboration et al., 2021), strong evidence exists, that pulsars can accelerate particles to the required energies. Not many UHE sources above 100 TeV were detected so far, but this is expected to change with more observation time of the LHAASO and HAWC observatories and the future CTA and SWGO facilities. Because a larger fraction of the Galactic plane and the Galactic centre can be observed from the Southern Hemisphere, CTA-South and SWGO will be very beneficial for the detection of UHE γ-ray sources. Only two of the 12 detected sources above 100 TeV do not have a possible pulsar counterpart, which strengthens the case that pulsars might frequently accelerate particles to ultra-high energies. However, in most cases, several possible other counterparts exist, potentially contributing to the emission.

The >10 TeV emission of eHWC J2019+368, LHAASO J2226+6057, LHAASO J1908+0621 / eHWC J1907+063 and LHAASO J1825−1326 / eHWC J1825−134 can easily be explained with IC scenarios, where nearby powerful pulsars accelerate the electrons even without strong radiation fields above the average Galactic one. This is facilitated because

the spectrum of each of the sources is softer than $\propto E^{-2}$. Thus, the model parameters are not unique, and the environmental conditions have to be known well to confirm or rule out different models. Multiwavelength observations will be enormously beneficial in this regard. However, data must be carefully compared since the instruments have different angular resolutions, and data might be produced in different regions. None of the sources is clearly correlated with the occurrence of target material, which makes it more challenging to construct hadronic scenarios for the sources. However, the environment of each source is complex and deserves detailed modelling beyond the scope of this thesis.

4 γ-ray and neutrino emission from interacting Cosmic Ray nuclei

Whilst the production of hard γ-ray IC spectra until energies of $100\,\text{TeV}$ is possible in regions with low magnetic fields and high radiation energy densities, as shown in the previous chapter, such regions will be much less frequent for higher energies. Most likely, no region exists in our Galaxy, which can provide the necessary condition for hard leptonic PeV γ-ray production. Therefore, the production of hard γ-ray spectra until PeV energies is in most probably all of the cases produced by hadronic processes. As discussed in Section 2.1.5, when CRs collide with the ambient matter, different unstable particles are produced, which subsequently decay into γ rays, e^+/e^- and neutrinos. The dominant interaction channel is via the production of neutral and charged pions. Neutral pions directly decay into γ rays, and charged pions first decay into μ^+/μ^- and the corresponding muon neutrino. The muons decay further into electrons/positrons and neutrinos. These processes are illustrated in the two sketches in Figure 4.1.

Often in calculating the produced emission, the presence of nuclei in the CRs and the target material is not taken into account. Instead, it is assumed that all CRs are protons colliding with hydrogen nuclei. In other cases, the presence of nuclei is accounted for by a so-called nuclear enhancement factor.

The influence of the presence of nuclei at energies around the π^0-bump was investigated in detail in Kafexhiu (2016) and Yang et al. (2018). Several additional processes can
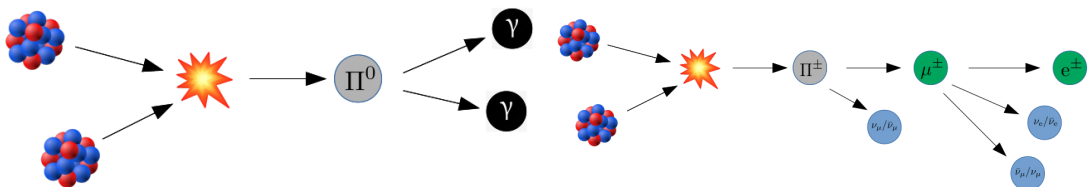

FIGURE 4.1: Sketch of the dominant γ-ray (left) and e^+/e^- and neutrino production channels (right) from the collision of nuclei.

contribute to the γ-ray emission:

- At low energies but above the Coulomb barrier, an inelastic collision or other nuclear reactions can leave a nucleus in an excited state. The de-excitation produces γ rays in the form of emission lines as well as continuum radiation. The emission lines occur primarily between 0.1 and 10 MeV, above ~10 MeV per nucleon additional continuum radiation is produced via the de-excitation of collective modes. The most important contribution stems from the giant dipole resonance producing γ rays mainly between 10 and 25 MeV.

- Above the giant dipole resonance, the spectrum becomes harder. This contribution is called the hard photons. Its origin is not yet clear, but it could likely be neutron-proton bremsstrahlung (Nifenecker & Pinston, 1989; Cassing et al., 1990; Schutz et al., 1997).

- In inelastic collisions of nuclei, pions can be produced at kinetic energies below the pion production threshold. The decay products of these so-called subthreshold pions contribute directly (π^0 decay) or indirectly ($e^\pm$ from $\pi^\pm$ decay) to the observed γ ray emission.

At higher energies, the production of particles in collisions of nuclei can be described within the framework of Glauber's multiple scattering theory (Glauber, 1955; Glauber & Matthiae, 1970; Franco & Glauber, 1966) applied in the so-called wounded nucleon model (Białłas et al., 1976; Rybczyński & Broniowski, 2011). This model will be used later to investigate the effects of heavier nuclei on γ-ray spectra. Each collision is treated as a sequence of individual nucleon-nucleon collisions. This leads to the usage of a nuclear enhancement factor to account for heavier compositions (see e.g. Gaisser & Schaefer, 1992; Mori, 2009; Kachelriess et al., 2014). Such an enhancement factor is a good approximation for the effects of heavier nuclei and depends on the composition and the spectral index of the CRs. However, the concept of the enhancement factor can not be applied in cases of sharp spectral features such as breaks or cutoffs in the CR spectra (Kachelriess et al., 2014). Therefore, because the majority of γ-ray and neutrino emitting sources are expected to have rigidity dependent maximum particle energies, a more accurate treatment of the composition in the cutoff region is necessary.

Spectral breaks also occur in the CR spectrum measured on Earth, for example at energies around the knee feature at a few PeV. As discussed in Section 2.5, the knee feature could mark the beginning of the transition from Galactic to extragalactic CRs and therefore understanding its origin is of paramount importance for the question about the origin of Galactic CRs. It is still unclear if the paradigm that SNR produce most Galactic CRs holds true or if other accelerators, such as star-forming regions or the Galactic centre, play a major role. With current and forthcoming γ-ray observatories, we will be able to probe for the first time the diffuse γ-ray emission up to PeV energies additionally to the detection of single sources (Amenomori et al., 2019; Amenomori et al., 2021b; Abeysekara et al., 2020; di Sciascio & Lhaaso Collaboration, 2016; Bai et al., 2019; CTA Consortium et al., 2019; Albert et al., 2019; Huentemeyer et al., 2019). Recently, the Tibet ASγ Collaboration obtained the first measurements of diffuse γ-ray emission above 100 TeV (Amenomori et al., 2021b), marking the start of this new era. The sensitivity in neutrino observations will increase as well, allowing additional multi-messenger observations (Blaufuss & Karle, 2017; The IceCube-Gen2 Collaboration et al., 2020). Thus, a thorough understanding of the effects of the composition of CRs on the produced emission is essential to interpret forthcoming measurements and the measurements from the Tibet ASγ Collaboration.

While few publications consider the CR composition in calculations of diffuse γ-ray or neutrino production, such as for example Lipari & Vernetto (2018), its impact is generally not discussed. Another example considering different compositions, but not discussing the effects directly, is Ahlers et al. (2016). They use two different CR models with different compositions to estimate the Galactic neutrino flux, leading to different spectra. An exception is the paper from Joshi et al. (2014), where possible implications on the spectral shape of mainly neutrinos are discussed. Later, Mascaretti et al. (2020) discussed the differences of two different compositional models for the knee region on Galactic neutrino fluxes. The common finding in these works is that a heavier composition leads to a reduction of the produced neutrinos or γ rays. Changes in the composition could also produce other spectral features such as dips, if the composition gets heavier and then lighter, or bumps, if the composition gets lighter and then heavier (Joshi et al., 2014). However, with new CR data and γ-ray data above 100 TeV, a deeper investigation focusing on all possible compositional effects, especially for γ rays, is required. An understanding of the physical effects producing different features for

changes in the composition is very important to interpret future γ-ray observations. Therefore, the effects of the composition will be explored and discussed in detail for the two important cases of sources with rigidity dependent cutoff and the diffuse emission.

The chapter is organised as follows: In Section 4.1, the method to account for heavier nuclei in colliding CRs and the target material is described in detail. After this, the implications for sources with rigidity dependent cutoff are investigated. This gives an understanding of the general compositional effects on the γ-ray emission, which apply as well to other use cases such as the diffuse emission. To assist in future studies, a parametrisation for the calculation of the γ-ray and neutrino emission from exponential cutoff distributed CRs from hydrogen until iron is developed in Section 4.3. Then, in Section 4.4, it is investigated how different compositions influence the diffuse γ-ray and neutrino emission between energies of several hundred GeV until tens of PeV. The results are compared with data from the Astrophysical Radiation with Ground-based Observatory at YangBaJing (ARGO-YBJ) (Bartoli et al., 2015) and the Tibet ASγ Collaboration (Amenomori et al., 2021b). A comparison to limits for the neutrino flux is made as well. At the end, all implications are summarised and discussed in Section 4.5. The results were published in Breuhaus et al. (2022a).

4.1 Methodology

To calculate the γ-ray and neutrino emission in nucleus-nucleus collisions, the method outlined in Kafexhiu et al. (2014) was applied in our analysis. It uses the wounded nucleon model, which models the collision of nuclei as a sequence of interactions between individual nucleons and ignores collective effects such as motions or excitations inside the whole nucleus. The individual nucleon-nucleon collisions are treated as simple pp collisions, and the total particle or photon production is the sum over all individual nucleon-nucleon interactions. For nuclei with mass numbers A and B respectively, the total average pion-production multiplicity is

$$\overline{n}_{AB,\pi} = \frac{1}{2}\overline{w}_{AB} \cdot \overline{n}_{\pi}, \qquad \overline{w}_{AB} = \frac{A\sigma_{pB} + B\sigma_{pA}}{\sigma_{AB}}. \tag{4.1}$$

Here, $\overline{n}_{AB,\pi}$ is the average pion-production multiplicity for the interaction of the nuclei, $\overline{n}_{\pi}$ the multiplicity for pp collisions, and $\overline{w}_{AB}$ the number of wounded nucleons, i.e.

the number of nucleons undergoing an interaction. The cross-sections σ_{pB} and σ_{pA} correspond to a single nucleon interacting with the nucleus A or B, while σ_{AB} is the nucleus-nucleus inelastic cross-section.

For the cross-sections, we use the same expression as Kafexhiu et al. (2014), who modified the typical expression for the cross-section at high energies from Sihver et al. (1993) to account for an expected increase above $1\,\mathrm{TeV/nucleon}$:

$$\sigma_{\mathrm{inel}}(A, B, E_{\mathrm{p,t}}) = \sigma_{\mathrm{R}}(A, B) \cdot G(E_{\mathrm{p,t}}), \tag{4.2}$$

where σ_{R} is the cross-section from Sihver et al. (1993),

$$\sigma_{\mathrm{R}} = \sigma_{\mathrm{R0}} \left[A_{\mathrm{p}}^{\frac{1}{3}} + A_{\mathrm{t}}^{\frac{1}{3}} - \beta_0 \left(A_{\mathrm{p}}^{-\frac{1}{3}} + A_{\mathrm{t}}^{-\frac{1}{3}} \right) \right]^2 \tag{4.3}$$

and

$$G(T_{\mathrm{p}}) = 1 + \log \left(\max \left[1, \frac{\sigma_{\mathrm{inel}}(E_{\mathrm{p,t}})}{\sigma_{\mathrm{inel}}(E_{\mathrm{p}}^0)} \right] \right), \qquad E_{\mathrm{p}}^0 = 1\,\mathrm{TeV}. \tag{4.4}$$

It is $\sigma_{\mathrm{R0}} = \pi r_0^2 \approx 58.1\,\mathrm{mb}$ with $r_0 = 1.36\,\mathrm{fm}$, A_{p} the mass number of the projectile CRs, A_{t} the mass number of the target material, and $\beta_0 = 2.247 - 0.915 \left(1 + A_{\mathrm{t}}^{-\frac{1}{3}} \right)$ for proton CRs, otherwise $\beta_0 = 1.581 - 0.876 \left(A_{\mathrm{p}}^{-\frac{1}{3}} + A_{\mathrm{t}}^{-\frac{1}{3}} \right)$. $E_{\mathrm{p,t}}$ is the kinetic energy per nucleon of the projectile CRs, since it are the individual nucleons participating in the interactions, and σ_{inel} the pp inelastic cross-section from Kafexhiu et al. (2014).

The resulting γ-ray emission is the emission from pp collisions scaled by the factor $\kappa(A, B, E_{\mathrm{p}}) = \frac{1}{2}\overline{w}_{AB}\sigma_{\mathrm{inel}}(A, B, E_{\mathrm{p}})/\sigma_{\mathrm{inel}}(E_{\mathrm{p}})$ summed over all combinations of particle species and integrated over the particle spectral energy densities for energies above the resulting γ-ray or neutrino energy.

To calculate the γ-ray or secondary particle spectra from pp collisions there exist different parametrisations, (e.g. Kafexhiu et al., 2014; Kamae et al., 2006; Kelner et al., 2006). The parametrisation from Kafexhiu et al. (2014) only includes the production of γ rays. However, it is the most accurate parametrisation, especially for energies close to the π^0-bump, and parametrises interactions at higher energies deduced from the Monte-Carlo codes GEANT 4.10.0, PYTHIA 8.18, SIBYLL 2.1 and QGSJET-I. In this context, differences between the underlying codes can be explored. The parametrisation

by Kamae et al. (2006) is less accurate than the one from Kafexhiu et al. (2014), but it does not only include the calculation of γ rays, but also of e^+, e^-, $\nu_{\rm e}$, $\bar{\nu}_{\rm e}$, ν_μ and $\bar{\nu}_\mu$. Kelner et al. (2006) provide parametrisations of the lepton production as well, although they do not distinguish between particles and the corresponding antiparticles because these differences are below both the measurements and the accuracy of their anaytical approximations. Despite being valid only for energies above $0.1\,$TeV, it gives accurate descriptions until $10^5\,$TeV, which is much higher than in the case of the parametrisations of Kamae et al. (2006) ($\approx 500\,$TeV) and Kafexhiu et al. (2014) ($\sim 10^3\,$TeV).

Because it is the only accurate parametrisation for γ-ray energies above $1\,$PeV and also provides parametrisations for the production of neutrinos and secondary electrons and positrons, the parametrisation of Kelner et al. (2006) was used in this work. The total inelastic pp cross-section being used is, however, not the one provided by Kelner et al. (2006), but the one from Kafexhiu et al. (2014), because the latter is an improved version taking into account data from the Large Hadron Collider. The total γ-ray or lepton production rate is calculated with

$$\frac{\mathrm{d}N(E)}{\mathrm{d}E} = \sum_{i,j} c n_j \int_E^\infty \kappa(E_{{\rm p},i}) \sigma_{\rm inel}(E_{{\rm p},i}) J_{{\rm p},i}(E_{{\rm p},i}) F\left(\frac{E}{E_{{\rm p},i}}, E_{{\rm p},i}\right) \frac{\mathrm{d}E_{{\rm p},i}}{E_{{\rm p},i}}. \qquad (4.5)$$

The indices i and j refer to the different CR and target species. Therefore, A_i is the mass number of CR species i and $E_{{\rm p},i} = E_{\rm p}/A_i$ the corresponding energy per nucleon. The energy number density of CR species i is denoted with $J_{{\rm p},i}$, κ is the scaling factor described above and $\sigma_{\rm inel}$ the inelastic cross-section from Kafexhiu et al. (2014). The function F represents the differential production rate of γ rays or $e^\pm/\nu$ from Kelner et al. (2006).

The procedure described above was implemented into the open-source GAMERA code (Hahn, 2015). Originally, GAMERA uses the parametrisation from Kafexhiu et al. (2014) to calculate γ-ray emission from π^0 decay. The implementation of Kelner et al. (2006) for γ-ray and secondary particle production was added as an additional option and is used for the calculations here. Different CR particle species and target material compositions can be used in GAMERA not only for the parametrisations from Kelner et al. (2006), but also for the original Kafexhiu et al. (2014) case.

4.2   Sources with rigidity dependent cut-off

The accelerated CR spectra from Galactic sources are expected to have rigidity dependent maximum particle energies. While hydrogen is the most abundant species in our Galaxy, environments exist with very different conditions. Winds from Wolf-Rayet stars, for example, can enrich the immediate environment of the star with heavier species (e.g. Kwitter, 1981). Such winds could also collide with winds from other stars, which potentially leads to the formation of shocks and the acceleration of particles. Furthermore, if a young SNR shock travels through the surrounding of its progenitor star, which is enriched with heavier materials, effects of the composition are important for the hadronic interpretation of the detected γ rays. This can have important implications for the Galactic CR sea and the detected diffuse emission if PeV CRs are mainly accelerated during the early SNR phases (Bell et al., 2013).

Hence, in this section I investigate the influence of different compositions on the resulting γ-ray spectrum for CRs following an exponential cutoff power-law distribution with a rigidity dependent cutoff in the particle spectra:

$$\frac{\mathrm{d}N}{\mathrm{d}E} = N \cdot \left(\frac{E}{E_0} \right)^{-\alpha} \exp\left(-\frac{E}{E_\mathrm{cut} \cdot Z} \right). \tag{4.6}$$

Here, Z is the number of protons of the respective CR species and E_cut the cutoff energy of CR protons. Studying the compositional effects in the case of rigidity dependent cutoffs will allow understanding the general influences of the composition, which is crucial to comprehend more complex cases such as the diffuse Galactic emission in the next section. I concentrate here on the implication for the γ-ray emission only. The effects for the production of neutrinos or electrons and positrons are the same because, in the wounded nucleon model, the production of any particle is multiplied by the number of wounded nucleons in each case. The neutrino emission for different compositions will be calculated in the case of the diffuse emission in Section 4.4.

Figure 4.2 shows γ-ray spectra from a hypothetical source for different ambient medium and CR compositions. In the left panel it was assumed, that the CRs follow a power-law index of $\alpha = 2$. To highlight effects of different power-law indices, the right panel shows the same as the left panel but for $\alpha = 2.5$. The cutoff energy for protons was fixed to $E_\mathrm{cut} = 1\,\mathrm{PeV}$. The source always releases the same total amount of energy into CRs

above energies of 1 GeV. Hydrogen (H) CRs interacting with a hydrogen target (dotted black line) serve as a reference case, all spectra are normalised to the value of this curve at 100 GeV. To better illustrate the differences between the curves, Figure 4.3 shows the curves from the left panel of Figure 4.2 for $\alpha = 2$ normalised to their respective values at 100 GeV (left) and every curve divided by the pure hydrogen case (right). To investigate effects of the ambient medium composition, the cases of hydrogen CRs interacting with an ISM with equal number density as in the pure H-H curve (solid cyan line) and with equal nucleon or mass number density (dashed cyan line) were considered. The effects of different CR compositions are shown with the case of iron CRs interacting with a hydrogen target (magenta line). Finally, to demonstrate combined effects, the case of a mixed CR composition with 50 % hydrogen and 50 % oxygen interacting with an ISM having the same number density as the H-H case is shown (green curve). For the ISM target material, we chose a composition with relative abundances typical for the most common elements in the local Galactic interstellar medium (ISM) for H(A=1), He(A=4), C(A=12), N(A=14), O(A=16), Ne(A=20), Mg(A=24), Si(A=28), S(A=32) and Fe(A=56) of $1 : 9.59 \times 10^{-2} : 4.65 \times 10^{-4} : 8.3 \times 10^{-5} : 8.3 \times 10^{-4} : 1.2 \times 10^{-4} : 3.87 \times 10^{-5} : 3.69 \times 10^{-5} : 1.59 \times 10^{-5} : 3.25 \times 10^{-5}$ (see e.g. Meyer, 1985). I first consider the power-law index $\alpha = 2$, because this is the value expected from standart diffusive shock acceleration.
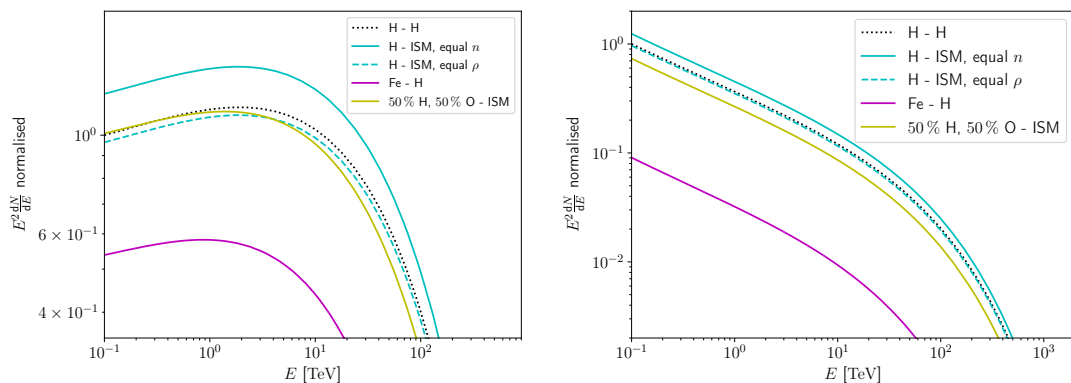

FIGURE 4.2: Comparison of γ-ray spectra of a source with rigidity dependent cutoff for different CR and ambient medium compositions. In each case, the total energy in CRs is the same. The cutoff for proton CRs is 1 PeV, and all curves are normalised with the value of the H-H case at 100 GeV. The left panel shows γ-ray curves for power-law indices of $\alpha = 2.0$, the right panel for $\alpha = 2.5$. The black dashed line shows the pure proton-proton case. The cyan lines show proton CRs colliding with the ISM, the solid line assuming the same number density as in the pure proton case and the dashed line the same mass density. The magenta line shows pure iron CRs colliding with hydrogen atoms and the green line a mix of 50 % hydrogen and 50 % oxygen colliding with the ISM. The figures are adapted versions of Fig. 1 and Fig. 2 from Breuhaus et al. (2022a).
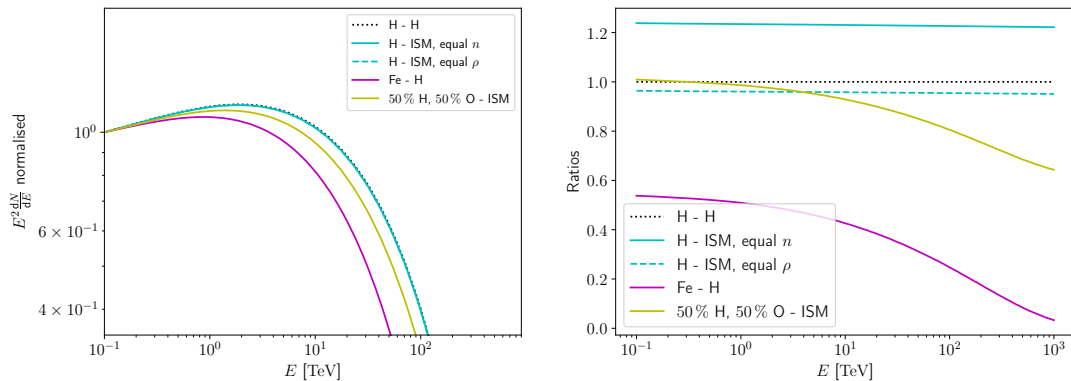
FIGURE 4.3: Comparison of the shapes and the normalisations of the spectra in the left panel of Figure 4.2. The left panel shows the γ-ray spectra normalised to their respective value at 1 GeV, and the right panel each spectrum divided by the H-H case.

Influence of the ISM composition: Comparing the emission from CR protons colliding with a pure hydrogen medium (dotted black line) and the mixed ISM in the above figures, one can see that the ISM as a target, with the same total particle number density as in the pure proton-proton case, increases the emission by $\sim 23\%$ for energies between 0.1 and 10^4 TeV. The enhancement decreases slightly with increasing energy, but the differences are below 2% and can therefore be assumed energy independent. The increase is explained by geometrical effects: If the number density is conserved but the particles get heavier, the cross-section of each particle increases because more area is covered. The outcome is different if the total number of nucleons or the total mass density is conserved (dashed cyan curve): Instead of an enhancement, there is a slight decrease in the emission of $\sim 5\%$. Changes over the energy range are again negligible. The reduction in flux is caused by the reduced area the particles are covering if they are clumped together in nuclei. If compositional effects are ignored, performing the calculations with an equal mass density is a better approximation than neglecting the size of the target nuclei and using the same total number density. The effects of the ISM composition do not depend noticeably on the spectral index of the CRs. For different CR species, the impact of the ISM changes only slightly: For Fe CRs, for example, the ISM with equal number density n gives between 22% to 19% more flux. An equal mass density leads to a decrease of 4%.

Influence of the CR composition: Two different effects can be observed if the CRs are replaced with a heavier species, illustrated in Figures 4.2 and 4.3 with the magenta

line showing iron CRs colliding with a hydrogen ISM. The first effect concerns the overall normalisation of the spectrum at energies below the cutoff. For iron CRs the flux is reduced down to $54\,\%$ of the H-H case at $100\,\mathrm{GeV}$ (see also the right panel of Figure 4.3). The reduction is caused to a small extent by the rigidity dependence of the cutoff energy: Because the cutoff for iron is at $Z \cdot 1\,\mathrm{PeV}$ with $Z = 26$, but the same amount of energy is in CRs above $1\,\mathrm{GeV}$, the overall normalisation is slightly lower. Nevertheless, the dominating effect is caused by the 3-dimensional structure of the nuclei: The nucleons in one nucleus are partially eclipsing each other, and fewer nucleons participate in the reaction as if they would be distributed in lighter nuclei. The same shielding effect played a role also in the influence of the ISM composition. The shielding effect for CRs is demonstrated additionally in Figure 4.4, which shows the same number of nucleons clumped together into H, He, O and Fe CRs. Therefore, no other effects play a role.

The second effect concerns spectral features. Even though the cutoff energy of Fe CR nuclei is higher than for protons, the observed cutoff in the γ-ray spectra is at a lower energy. This is the case because the individual nucleons produce the γ rays. The cutoff energy of the whole nucleus increases proportional to the charge Z for the rigidity dependent cutoff, but the energy per nucleon decreases with the mass number A. Therefore, the cutoff in the γ-ray spectrum will occur at an energy a factor of $Z/A \approx 0.5$ lower than for protons. This can also be seen well in the left panel of Figure 4.3, where the same SEDs are normalized to their respective value at $0.1\,\mathrm{TeV}$. The shapes of the spectra are nearly the same, but the cutoff energy for Fe occurs at 0.5 times the cutoff for proton CRs. Therefore, protons will always dominate the γ-ray emission of a source with different CR species at the highest energies in the cutoff region. Other rigidity dependent features such as spectral breaks will appear like the rigidity dependent cutoff at approximately 0.5 times the energy for hydrogen CRs.

Whereas the energy where the spectral features occur is not affected by the spectral index α of the CRs, the normalisation can be altered significantly. This is evident comparing the left panel of Figure 4.2 ($\alpha = 2$) with the right panel, where $\alpha = 2.5$. If the CRs follow a power-law with $\alpha = 2$, the same amount of energy is distributed equally at all energies. This is not true for $\alpha = 2.5$, where more energy is deposited at lower than high energies. For iron or other heavier species, the nucleons producing the same γ rays are located in nuclei with an energy a factor of A higher compared to hydrogen. Therefore, less nucleons are available to produce γ rays for $\alpha = 2.5$ compared to $\alpha = 2$.

At 100 GeV, the iron curve for $\alpha = 2.5$ is one order of magnitude below the H-H case, which is already a factor of ~ 5 lower than for $\alpha = 2$.

To investigate combined effects in more realistic scenarios, I considered additionally a source putting 50 % of its energy into H and 50 % into O CRs colliding with the ISM with an equal number density as in the H-H case. This is shown with the green curves in Figures 4.2 and 4.3. The overall normalisation for $\alpha = 2$ is nearly the same as in the H-H scenario because the increase in emission caused by the ISM is compensated by the reduction due to oxygen CRs. The cutoff occurs at an energy between the pure iron and the pure hydrogen case, as one would expect for a mixed CR composition. However, for different power-law indices the effects on the normalisation can be very different, as shown in the right panel of Figure 4.2 for $\alpha = 2.5$. Therefore, while in some cases away from spectral features, the compositional effects can be ignored, in other cases, they can not. As it will be shown in Section 4.4, compositional effects can have a significant impact on the detected γ-ray spectra of the diffuse Galactic emission.

4.3   Parametrisation of γ-ray and neutrino spectra

To assist in future analytic studies of hadronic emission, simple approximate parameterizations for the emitted γ-ray and neutrino spectra were developed. As it is standard, the case of an exponential cutoff power-law for arbitrary particle species was considered,

$$\frac{\mathrm{d}N}{\mathrm{d}E} = N_{\mathrm{p}} \cdot \left(\frac{E}{E_0} \right)^{-\alpha_{\mathrm{p}}} \exp\left(-\frac{E}{E_{\mathrm{cut,p}} \cdot A} \right), \tag{4.7}$$

with A being the mass number of the target beam. The target material was assumed to consist of the same relative abundances as in the previous Section 4.2 and normalised to a total number density of $n = 1$. After the γ-ray and neutrino spectra were calculated numerically with the implementation in GAMERA described previously, a fit with the function

$$f(E) = N \cdot \left(\frac{E}{E_0} \right)^{-\alpha} \exp\left(-\left(\frac{E}{E_{\mathrm{cut}}} \right)^{\beta} \right) \tag{4.8}$$

was performed. E_0 was set to TeV. The parameters N, α, E_{cut} and β now depend on α_{p}, $E_{\mathrm{cut,p}}$ and A. The scaling with changing N_{p} is linear. To obtain the final
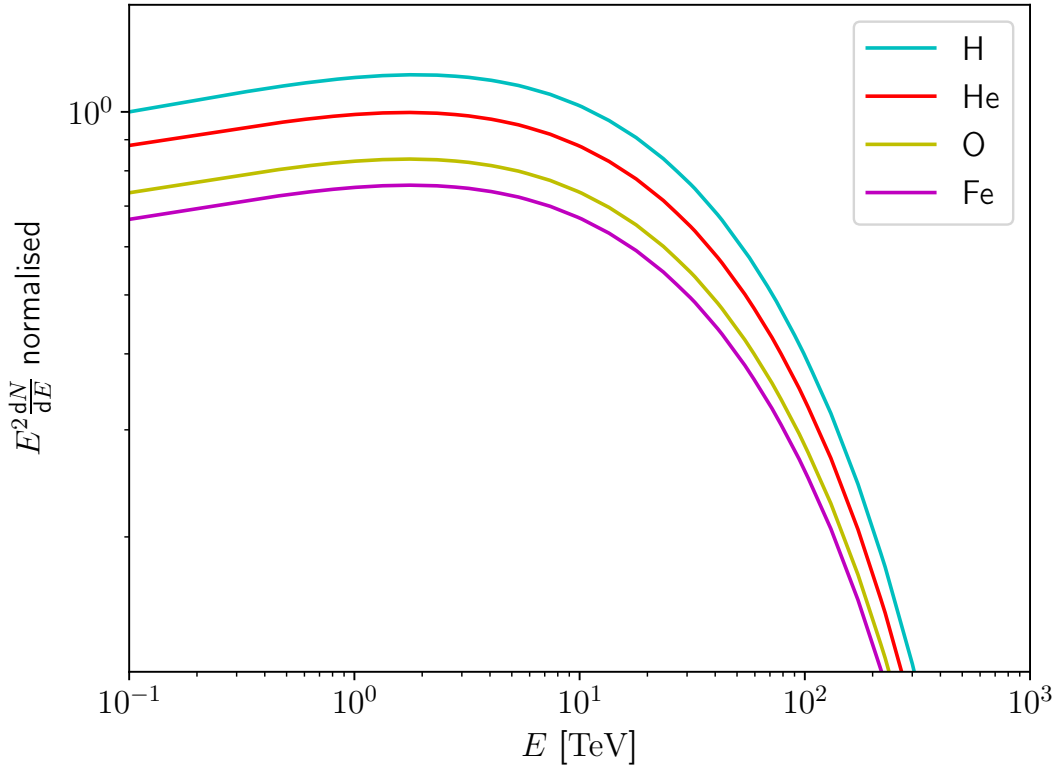
FIGURE 4.4: γ-ray spectra from the same number of nucleons clumped together into the different CR species hydrogen (H), helium (He), oxygen (O) and iron (Fe) colliding with the ISM. The cutoff energy for the H case is $1\,\mathrm{PeV}$, the spectral index is $\alpha = 2.0$. All curves are normalised to the value of the hydrogen CRs at $100\,\mathrm{GeV}$. Adapted version of Fig. A.1 in Breuhaus et al. (2022a).

parametrisation, first the dependence of $\log_{10} N$, $E_{\mathrm{cut}}/E_{\mathrm{cut,p}}$, β and $\delta = \alpha_{\mathrm{p}} - \alpha - 2$ with respect to α_{p} for fixed N_{p}, $E_{\mathrm{cut,p}}$ and A was fitted with polynomials of second degree. This is illustrated in Figure 4.5 for the case of $N_{\mathrm{p}} = 10^{17}\,\mathrm{erg}^{-1}$, $E_{\mathrm{cut,p}} = 100\,\mathrm{TeV}$ and $A = 1$. Then, the dependence of the parameters of these fitting functions w.r.t. A was investigated. Only in a few cases functions for the dependence on A were needed. At the end, the dependence of all parameters from the fitting functions with respect to $E_{\mathrm{cut,p}}$ was modelled. The following representations for N, α, E_{cut} and β as functions of N_{p}, α_{p}, $E_{\mathrm{cut,p}}$ and A were found:
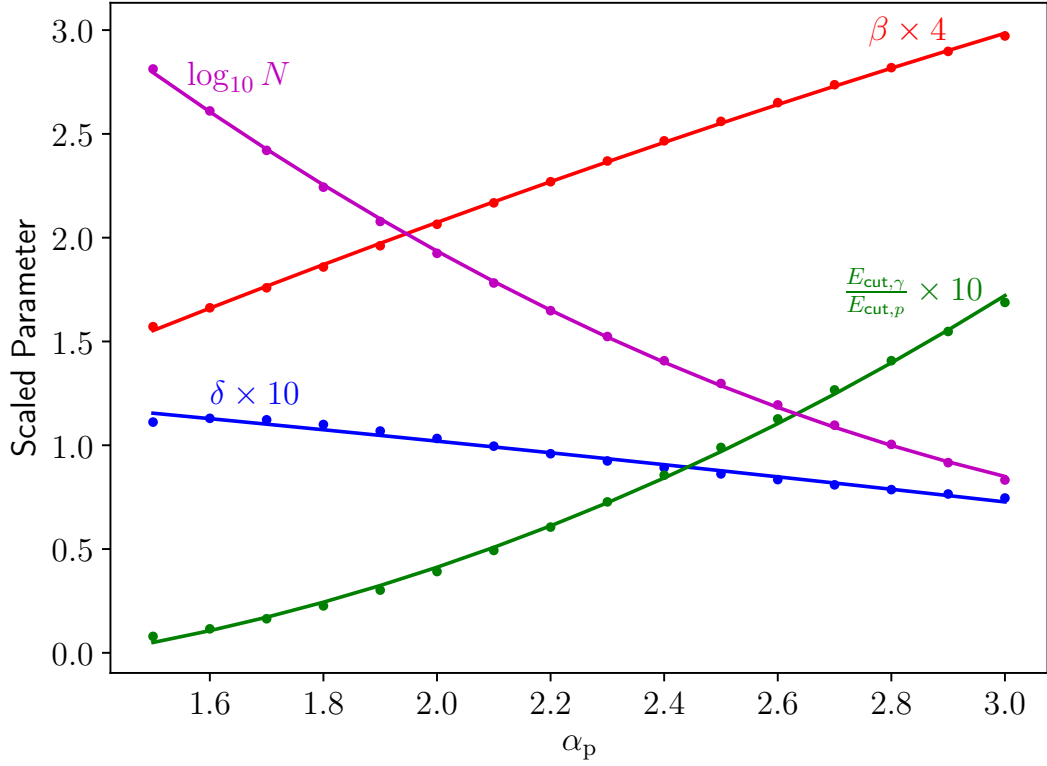
FIGURE 4.5: Scaled parameters of the fitted function 4.8 in dependence of α_{p} for $A = 1$, $E_{\mathrm{cut,p}} = 100\,\mathrm{TeV}$ and $N_{\mathrm{p}} = 10^{17}\,\mathrm{erg}^{-1}$. The fitted polynomials to model the α_{p} dependence are also shown.

$$\beta = \sum_{i=0}^{1} a_i \alpha_{\mathrm{p}}^i \ln(b_i E_{\mathrm{cut,p}}) + \alpha_{\mathrm{p}}^2 (c_3 E_{\mathrm{cut,p}}^{d_3} + e_3), \tag{4.9}$$

$$\alpha = \alpha_{\mathrm{p}} - \delta - 2 \qquad \text{with} \tag{4.10}$$

$$\delta = \sum_{i=0}^{2} \alpha_{\mathrm{p}}^i (c_i E_{\mathrm{cut,p}}^{d_i} + e_i), \tag{4.11}$$

$$E_{\mathrm{cut}} = 1000 \cdot E_{\mathrm{cut,p}} \cdot \sum_{i=0}^{2} \alpha_{\mathrm{p}}^i \left(\sum_{j=0}^{3} k_{ij} \ln^j (E_{\mathrm{cut,p}}) \right), \tag{4.12}$$

$$N = \frac{N_{\mathrm{p}} \cdot 1\,\mathrm{erg}^2}{10^{17}} \cdot 10^{\kappa}, \qquad \text{with} \tag{4.13}$$

$$\kappa = p_0 + p_1 \cdot A^{p_2} + p_3 \cdot A^{p_4} \cdot \alpha_{\mathrm{p}} \qquad \text{and} \tag{4.14}$$

$$p_i = q_{i0} \cdot E_{\mathrm{cut,p}}^{q_{i1}} + q_{i2}. \tag{4.15}$$

The in that way determined values for a_i and b_i for γ rays and neutrinos can be found in Table 4.1, the ones for c_i, d_i and e_i for γ rays in Table 4.2 (Table 4.3 for neutrinos),

for k_{ij} in Table 4.4 (Table 4.5 for neutrinos) and for q_{ij} in Table 4.6 (Table 4.7 for neutrinos), which are the same tables published in Breuhaus et al. (2022a). The unit of $E_{\mathrm{cut,p}}$ in Equations 4.9 to 4.15 is PeV. Because the parameters are obtained for a number density of one, Equation 4.8 has to be multiplied with the total number density of the ambient medium to obtain the correct flux levels of the γ-ray or neutrino spectra.

The parametrisations work well under the following conditions: γ-ray or neutrino energies between $0.1\,\mathrm{TeV}$ and $E_{\mathrm{cut,p}}$, $1.8 \leq \alpha_{\mathrm{p}} \leq 3.0$, $1 \leq A \leq 56$ and $10\,\mathrm{TeV} \leq E_{\mathrm{cut,p}} \leq 1\,\mathrm{PeV}$. The best results are achieved for $\alpha \in [2.0, 3.0]$, γ-ray energies below $0.5 \times E_{\mathrm{cut,p}}$ and neutrino energies below $0.2 \times E_{\mathrm{cut,p}}$, resulting in accuracies far better than $30\,\%$ in the majority of the cases.

The validity range for neutrinos ends at lower energies than the range for γ rays produced by the same CRs because the cutoff in the produced neutrinos manifests itself at lower energies. If the cutoff energy in the respective γ-ray and neutrino spectra is exceeded much, the accuracy of the parametrisation drops rapidly. However, this is not a big concern for most applications because the emitted fluxes above these energies are much lower than before the cutoff. Inferring the emission from sources with different compositions or fitting spectra to data is not affected significantly by the poor precision at energies well above the cutoff.

Figure 4.6 shows the parametrisation for γ rays together with the full numerical calculations using the GAMERA code for H, O, and Fe CRs and different values of $E_{\mathrm{cut,p}}$ and α_{p}. The spectra are approximated well, but in the case of H and Fe, one can already see increasing differences for energies above the cutoff. Therefore, complete numerical calculations should be executed if high accuracy is needed at such energies. The same holds for energies close to the π^0-bump. The GAMERA code, including the treatment of different compositions in CRs and target material as described in this thesis, is publicly available on GitHub, https://github.com/libgamera/GAMERA.

	γ rays		Neutrinos	
	a_i	b_i	a_i	b_i
$i = 0$	-9.23×10^{-2}	1.93×10^1	-9.83×10^{-2}	4.48
$i = 1$	7.10×10^{-2}	1.16×10^3	6.82×10^{-2}	2.65×10^2

TABLE 4.1: Parameters a_i and b_i used for the calculation of β for γ rays and neutrinos in Equation 4.9. Table B.1 in Breuhaus et al. (2022a).

γ rays

	c_i	d_i	e_i
$i = 0$	-4.91×10^{-2}	-4.81×10^{-1}	3.00×10^{-1}
$i = 1$	4.78×10^{-2}	-4.19×10^{-1}	-1.51×10^{-1}
$i = 2$	-1.25×10^{-2}	-3.63×10^{-1}	2.78×10^{-2}
$i = 3$	-1.21×10^{-1}	1.52×10^{-1}	6.47×10^{-2}

TABLE 4.2: Parameters c_i, d_i and e_i for the calculation of the parameter δ (and β) for γ rays in Equation 4.11 (and 4.9). Table B.2 in Breuhaus et al. (2022a).

Neutrinos

	c_i	d_i	e_i
$i = 0$	-2.60×10^{-1}	-2.86×10^{-1}	6.01×10^{-1}
$i = 1$	3.61×10^{-1}	-1.96×10^{-1}	-4.87×10^{-1}
$i = 2$	-1.03×10^{-1}	-1.45×10^{-1}	1.18×10^{-1}
$i = 3$	-1.25×10^{-1}	1.22×10^{-1}	8.59×10^{-2}

TABLE 4.3: Parameters c_i, d_i and e_i for the calculation of the parameter δ (and β) for neutrinos in Equation 4.11 (and 4.9). Table B.3 in Breuhaus et al. (2022a).

γ rays

k_{ij}	$j = 0$	$j = 1$	$j = 2$	$j = 3$
$i = 0$	-1.77×10^{-2}	-5.32×10^{-3}	5.46×10^{-3}	8.50×10^{-4}
$i = 1$	-3.06×10^{-2}	7.91×10^{-3}	-5.54×10^{-3}	-1.07×10^{-3}
$i = 2$	2.89×10^{-2}	-3.53×10^{-3}	1.17×10^{-3}	2.81×10^{-4}

TABLE 4.4: Table for the parameters k_{ij} for the calculation of E_{cut} in Equation 4.12 for γ rays. Table B.4 in Breuhaus et al. (2022a).

Neutrinos

k_{ij}	$j = 0$	$j = 1$	$j = 2$	$j = 3$
$i = 0$	3.10×10^{-2}	-3.98×10^{-3}	5.02×10^{-4}	1.50×10^{-4}
$i = 1$	-5.44×10^{-2}	3.48×10^{-3}	-5.34×10^{-4}	-2.45×10^{-4}
$i = 2$	2.30×10^{-2}	-9.52×10^{-4}	7.02×10^{-5}	5.68×10^{-5}

TABLE 4.5: Table for the parameters k_{ij} for the calculation of E_{cut} in Equation 4.12 for neutrinos. Table B.5 in Breuhaus et al. (2022a).

γ rays

q_{ij}	$j = 0$	$j = 1$	$j = 2$
$i = 0$	-2.69×10^{-2}	-4.54×10^{-1}	4.99×10^{-1}
$i = 1$	-1.02×10^{-1}	-5.51×10^{-1}	7.16
$i = 2$	8.74×10^{-4}	-6.24×10^{-1}	9.20×10^{-2}
$i = 3$	1.09×10^{-1}	-4.91×10^{-1}	-3.62
$i = 4$	1.67×10^{-3}	-6.13×10^{-1}	9.61×10^{-2}

TABLE 4.6: Parameters q_{ij} for the calculation of the parameters p_i for γ rays in Equation 4.15. Table B.6 in Breuhaus et al. (2022a).

4.4 Diffuse emission

Now, the compositional effects for the diffuse Galactic emission are investigated in detail and compared to recent measurements. The Galactic diffuse γ-ray emission was detected

Neutrinos

q_{ij}	$j = 0$	$j = 1$	$j = 2$
$i = 0$	-1.14×10^{-1}	-2.97×10^{-1}	6.11×10^{-1}
$i = 1$	-3.68×10^{-1}	-4.12×10^{-1}	8.21
$i = 2$	2.13×10^{-3}	-5.46×10^{-1}	8.31×10^{-2}
$i = 3$	4.38×10^{-1}	-3.42×10^{-1}	-4.34
$i = 4$	3.99×10^{-3}	-5.61×10^{-1}	8.59×10^{-2}

TABLE 4.7: Parameters q_{ij} for the calculation of the parameters p_i for neutrinos in Equation 4.15. Table B.7 in Breuhaus et al. (2022a).
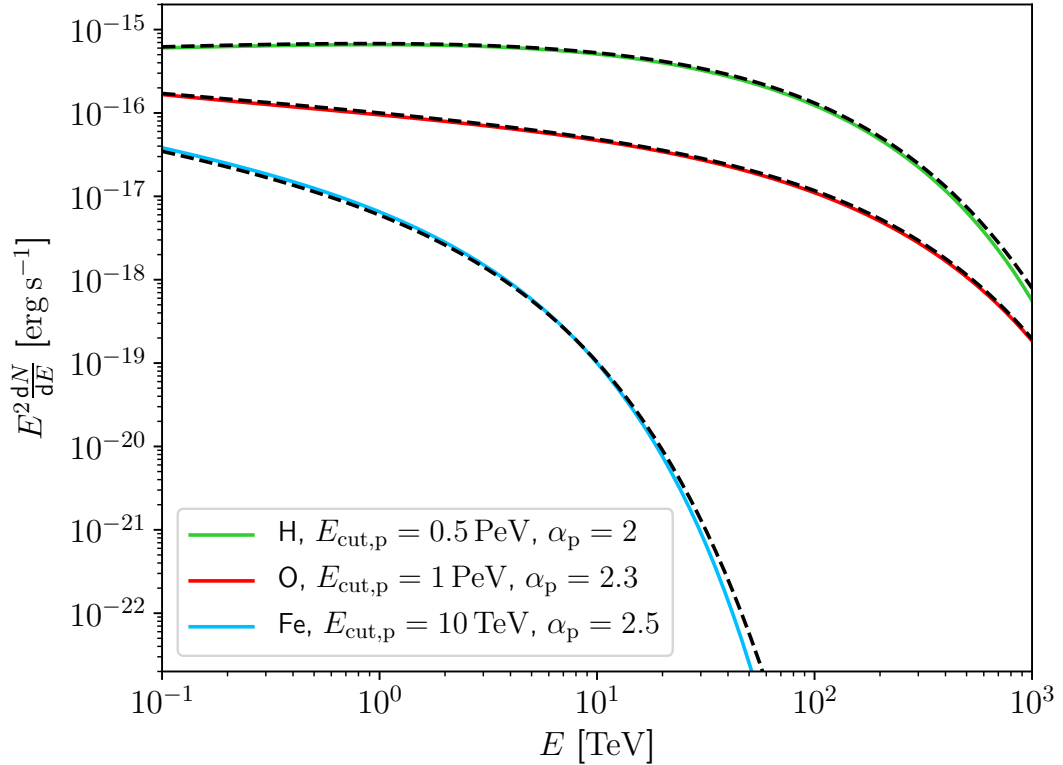
FIGURE 4.6: Comparison of the parametrisation for γ rays (black dashed lines) with the numerical calculations using the full GAMERA code for hydrogen, oxygen, iron and different values of $E_{\mathrm{cut,p}}$ and α_{p} in Equation 4.7. It is $N_{\mathrm{p}} = 1$ and the ambient density was set to $n = 1$ in all cases. Adapted version of Fig. B.1 in Breuhaus et al. (2022a).

for the first time by the Third Orbiting Solar Observatory (OSO-3) satellite around energies of 100 MeV (Kraushaar et al., 1972). Greatly improved measurements were later obtained by the Small Astronomy Satellite 2 (SAS-2), the Cosmic-Ray Satellite COS-B and the Energetic Gamma-Ray Experiment Telescope (EGRET). The best current data of diffuse γ-ray emission between $\sim$100 MeV and $\sim$1 TeV is obtained by Fermi-LAT (e.g. Ackermann et al., 2012; Acero et al., 2016; Neronov & Semikoz, 2020). Different authors investigated the impact of the composition on the diffuse γ-ray and neutrino spectra at

these energies (Mori, 2009; Kachelriess et al., 2014, among others). Because the CRs follow relatively accurate power laws, different compositions can be accounted for by nuclear enhancement factors.

At higher energies, the diffuse emission becomes relatively weaker compared to single sources due to the soft spectrum of the Galactic CRs. This makes measurements more challenging than at low energies. Nevertheless, Milagro (Abdo et al., 2008), the H.E.S.S. collaboration (Abramowski et al., 2014) and ARGO-YBJ (Bartoli et al., 2015) reported the detection of diffuse emission in the multi-TeV regime. The HAWC collaboration was able to derive upper limits between 1 and 100 TeV by the observation of passive giant molecular clouds (Albert et al., 2021b). Above 100 TeV, the Chicago air shower array - Michigan muon array (CASA-MIA; Borione et al., 1998) was able to impose constraints on the emission. However, the first direct measurements of the diffuse γ-ray emission between 100 TeV and 1 PeV were only reported last year by the Tibet ASγ Collaboration (Amenomori et al., 2021b). With the LHAASO observatory, new measurements of the diffuse emission at VHE and UHE energies are expected soon (Zhao et al., 2021).

The results from the Tibet ASγ Collaboration sparked the investigation of the implications for UHE γ-ray sources and the diffuse emission (Dzhatdoev, 2021; Qiao et al., 2021; Koldobskiy et al., 2021; Vecchiotti et al., 2021; Liu & Wang, 2021; Neronov et al., 2021; Fang & Murase, 2021; Zhang et al., 2022) and for other topics such as dark matter (Esmaili & Serpico, 2021; Maity et al., 2022) or Lorentz invariance violation (Satunin, 2021). Nonetheless, compositional effects were not investigated.

4.4.1 Local CR-model

To model the diffuse emission and to investigate the effects of the composition on the resulting γ-ray spectra, a model of the CR spectrum and its composition throughout the Galaxy is needed. First, we develop a model for the local CRs. Direct measurements of individual CR species on Earth exist from a variety of different experiments for energies below $\sim$1 PeV. At higher energies, CRs are measured solely from recordings of air showers. This makes it impossible to directly determine the species of the CR particle which created the shower, but from shower properties and the aid of Monte-Carlo (MC) codes, divisions of the all-particle spectrum into different CR mass ranges have been made (e.g. Prosin et al., 2014; The KASCADE-Grande Collaboration et al., 2013; Aartsen et al.,

2019). However, the results depend strongly on the modelling of the interactions and the specific MC code being used.

To develop a model for the local CRs, the simplified assumption was made, that the CRs are entirely made up by the most abundant species hydrogen (H), helium (He), carbon (C), oxygen (O), magnesium (Mg), silicon (Si) and iron (Fe). Most of the CR data was retrieved from the Cosmic-Ray DataBase (Maurin et al., 2014, 2020). Single-particle data from AMS-02 (Aguilar et al., 2015, 2017, 2020), CREAM-III (Yoon et al., 2017), CREAM-II (Ahn et al., 2009b), ATIC-2 (Panov et al., 2009), NUCLEON (Grebenyuk et al., 2019), Tunka-133 (Prosin et al., 2014), KASCADE-Grande (The KASCADE-Grande Collaboration et al., 2013) and IceCube/IceTop (Aartsen et al., 2019) was used together with all-paticle data from IceCube/IceTop (Rawlins & IceCube Collaboration, 2015), KASCADE-Grande (Schoo et al., 2015), NUCLEON (Grebenyuk et al., 2019), the Pierre Auger Observatory (The Pierre Auger Collaboration et al., 2015), the Telescope Array (Ivanov, 2015) and the Tunka-133 Array (Prosin et al., 2014). The all-particle data can be seen in Figure 4.7 and the data for individual species in Figure 4.8 and 4.9.

The CR model is composed of three different components. The first component is of Galactic origin, and the second one to large parts probably as well. These two components determine the shape until the ankle. To maintain the shape of the all-particle spectrum at the ankle, a third component of extragalactic origin is introduced as well.

The spectra of H and He of the first Galactic component follow an exponential cutoff power-law with two breaks:

$$\frac{\mathrm{d}N}{\mathrm{d}E} = N_0 \left(\frac{E}{E_0}\right)^{-\alpha_1} \exp\left(-\frac{E}{E_{\mathrm{cut}}}\right) \tag{4.16}$$
$$\times \left[1 + \left(\frac{E}{E_1}\right)^2\right]^{\frac{-(\alpha_2 - \alpha_1)}{2}} \left[1 + \left(\frac{E}{E_2}\right)^2\right]^{\frac{-(\alpha_3 - \alpha_2)}{2}}$$

As can be seen e.g. in Figure 4.8, the data from direct measurements from different experiments show large differences, especially at higher energies above $\sim 10\,\mathrm{TeV}$, where the statistic is low and fewer particles are detected. Taking data from different experiments would therefore result in different spectral shapes, which influence the resulting γ-ray emission. To investigate these effects, two different models are considered. In Model A, the H and He spectra follow the data from AMS-02 and NUCLEON, and in Model

	Model A		Model B	
Parameter	H	He	H	He
N_0/k	28.2	16.0	28.2	16.0
E_1 [GeV]	2.0×10^3	4.0×10^3	2.0×10^3	3.0×10^3
E_2 [GeV]	2.5×10^4	4.0×10^4	1.5×10^4	9.0×10^3
α_1	2.815	2.71	2.815	2.71
α_2	2.45	2.32	2.4	2.2
α_3	2.72	2.66	3.0	2.87
E_{cut} [PeV]	9	5	9	5

TABLE 4.8: Parameters for H and He of the first Galactic component for Model A and B (Equation 4.16). It is $k = 4\pi/(10^4 c) \cdot \mathrm{cm}^{-2}\,\mathrm{s}^{-1}\,\mathrm{GeV}^{-1}$, where c is the speed of light, such that N_0/k is unit-less. E_0 is fixed to $10\,\mathrm{GeV}$ in all cases. Table 1 in Breuhaus et al. (2022a).

	N_0/k	E_1 [GeV]	α_1	α_2	E_{cut} [PeV]
C	3.5	7.0×10^3	2.7	2.45	9
O	6.0	7.0×10^3	2.7	2.5	6
Mg	3.0	1.0×10^4	2.75	2.55	42
Si	2.5	1.0×10^4	2.7	2.5	39
Fe	10.0	1.0×10^4	2.8	2.55	36

TABLE 4.9: Parameters for C, O, Mg, Si and Fe of the first Galactic component (Equation 4.17). It is $k = 4\pi/(10^4 c) \cdot \mathrm{cm}^{-2}\,\mathrm{s}^{-1}\,\mathrm{GeV}^{-1}$, where c is the speed of light, such that N_0/k is unit-less. E_0 is fixed to $10\,\mathrm{GeV}$ in all cases. In both models, Model A and B, the parameters are the same. Table 2 in Breuhaus et al. (2022a).

B the data from AMS-02 and CREAM III. The free parameters from Equation 4.16 of both models are summarized in Table 4.8. E_0 was fixed to $10\,\mathrm{GeV}$ in all cases.

For the heavier species C, O, Mg, Si and Fe, an exponential cutoff power-law with only one spectral break was used for the first Galactic component:

$$\frac{\mathrm{d}N}{\mathrm{d}E} = N_0 \left(\frac{E}{E_0}\right)^{-\alpha_1} \left[1 + \left(\frac{E}{E_1}\right)^2\right]^{\frac{-(\alpha_2 - \alpha_1)}{2}} \cdot \exp\left(-\frac{E}{E_{\mathrm{cut}}}\right) \qquad (4.17)$$

E_0 was fixed to $10\,\mathrm{GeV}$ as for H and He. No difference is made between Model A and Model B. The corresponding parameters for each species are shown in Table 4.9.

The second Galactic component is the same in Model A and B and follows an exponential cutoff power-law for each species:

$$\frac{\mathrm{d}N}{\mathrm{d}E} = N_0 \left(\frac{E}{E_0}\right) \cdot \exp\left(-\frac{E}{E_{\mathrm{cut}}}\right). \qquad (4.18)$$

The adopted parameters can be found in Table 4.10. The second component starts

	N_0/k	α	E_{cut} [PeV]
H	6.0×10^{-6}	2.5	70
He	4.0×10^{-6}	2.5	140
C	6.0×10^{-7}	2.45	420
O	6.0×10^{-7}	2.45	560
Mg	5.0×10^{-7}	2.45	840
Si	3.0×10^{-7}	2.45	980
Fe	8.0×10^{-7}	2.4	840
H, extragalactic	1.4×10^{-7}	2.4	45×10^3

TABLE 4.10: Parameters for all species of the second component and the extragalactic component. The extragalactic component is assumed to consist solely of hydrogen for simplicity. It is $k = 4\pi/(10^4 c) \cdot \mathrm{cm}^{-2}\,\mathrm{s}^{-1}\,\mathrm{GeV}^{-1}$, where c is the speed of light, such that N_0/k is unit-less. In both models, Model A and B, the parameters are the same. Table 3 in Breuhaus et al. (2022a).

to dominate over the first Galactic component above $\approx 10^{17}$ eV and is responsible for the hardening of the spectrum above the second knee. At these energies, no direct measurements of the CR species exist. The composition is instead inferred from the air shower properties and all-particle data is divided into different elemental groups. For C, O, Mg and Si, which are separate species in the model, it was therefore assumed that the C-O group and the Mg-Si group are composed of equal parts by C, O and Mg, Si. The errors of the elemental group data are large and there are discrepancies between different observatories. Therefore, the parameters were adjusted not only to match the single-particle data, but also the all-particle data.

Above several 10^{18} eV, the all-particle CR data shows a hardening, the so-called ankle feature. To account for this hardening, a third component, most likely extragalactic, is introduced. The composition of this component is even more speculative than the second Galactic component, but evidence exists, that it becomes lighter. For simplicity, it was therefore assumed that it consists only of hydrogen. Because its contribution to the γ-ray production at PeV energies is negligible, this simplification does not have an impact on any of the results. The extragalactic component follows an exponential cutoff power-law as in Equation 4.18 and the values of the parameters are shown in Table 4.10.

Figure 4.7 shows the all-particle data together with the all-particle CR model spectrum for Model A (red line) and Model B (magenta line). The individual components of hydrogen (green) and helium (brown) are shown as well. The solid lines correspond to Model A, and the dashed lines to Model B. The components from all heavier species are the same in both models and their combined spectrum is shown with the black

line. At low energies, the contributions from H, He and all heavier nuclei combined are similar, but heavier nuclei dominate above several hundreds of TeV in Model A and above ~ 10 TeV in Model B. At the ankle, H is the only relevant contribution due to the simplified assumption, that the extragalactic component is composed out of H. Model B clearly undershoots the all-particle data from NUCLEON above ~ 10 TeV. This is the case, because the CREAM III data from H and He are below the NUCLEON data, and therefore the all-particle spectrum is below the NUCLEON data as well. At 1 PeV, Model B is lower than the all-particle data from Tunka and IceCube/IceTop, but it is still slightly above the data from KASCADE-Grande.
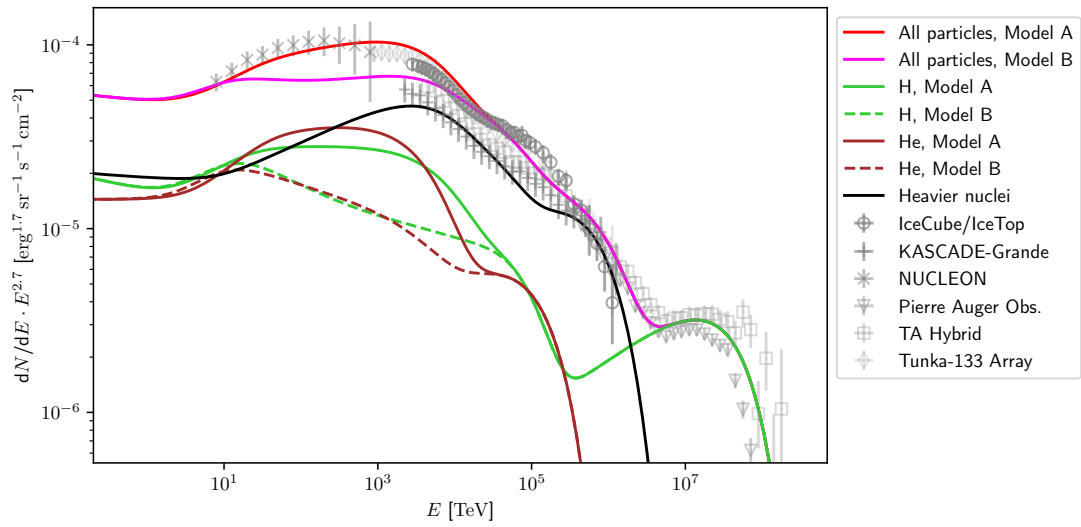
FIGURE 4.7: Illustration of the CR models together with all-particle data from Ice-Cube/IceTop (Rawlins & IceCube Collaboration, 2015), KASCADE-Grande (Schoo et al., 2015), NUCLEON (Grebenyuk et al., 2019), the Pierre Auger Observatory (The Pierre Auger Collaboration et al., 2015), the Telescope Array (Ivanov, 2015) and the Tunka-133 Array (Prosin et al., 2014). To better distinguish data from different experiments, the data from each experiment have a different transparency. The all-particle spectrum for Model A is shown with the red line, and for Model B with the magenta line. The green lines show the contributions from hydrogen and the brown lines for helium, where Model A and Model B are distinguished with solid and dashed lines, respectively. All heavier nuclei combined are shown with the black line, which is the same in both models. Single-particle data together with the respective contributions are shown in Figure 4.8 and 4.9. The figure is an adapted version of Figure 3 in Breuhaus et al. (2022a).

The single-particle data together with the individual CR model components for H and He are depicted in Figure 4.8. Solid lines show the total contribution for Model A (black) and Model B (blue), and the dashed black and blue lines show the corresponding contributions from the first Galactic components. The second Galactic component is the same for Model A and B and shown with the black dashed-dotted lines, and the
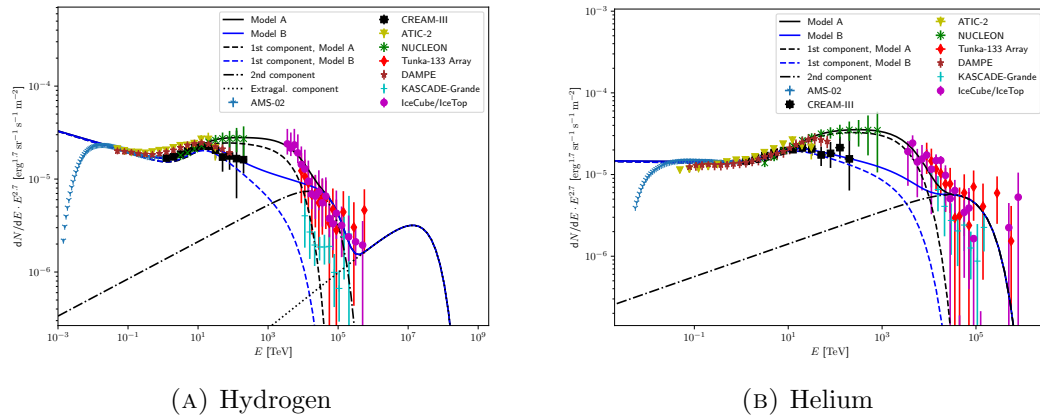
(A) Hydrogen

(B) Helium

FIGURE 4.8: Hydrogen (left) and helium (right) data together with the corresponding CR model components. The datapoints are from AMS-02 (Aguilar et al., 2015), CREAM-III (Yoon et al., 2017), ATIC-2 (Panov et al., 2009), NUCLEON (Grebenyuk et al., 2019), Tunka-133 (Prosin et al., 2014), KASCADE-Grande (The KASCADE-Grande Collaboration et al., 2013) and IceCUBE/IceTop (Aartsen et al., 2019). Black solid lines show the total contributions for Model A, and blue solid lines for Model B. Dashed lines with the corresponding colours show the contributions from the first Galactic component for each model. The black dashed-dotted lines show the second Galactic components, which are the same in both models. The dotted line in the left panel for hydrogen depicts the extragalactic component, which is as the second component the same in Model A and B. The figure is an adapted version of Figure 4 in Breuhaus et al. (2022a).

extragalactic component of H is shown with the dotted line. It can be clearly seen that Model A follows the data from NUCLEON, and Model B the data from CREAM. Model B is below the low energy data from IceCube/IceTop, but it is slightly above (H) or consistent (He) with the low energy KASCADE-Grande data. As can be seen in the figure, no compositional data exists to constrain the composition of the extragalactic component.

For the heavier nuclei C, O, Mg, Si and Fe, the data and model curves are shown in Figure 4.9. The curves are the same for Model A and Model B. As in Figure 4.8, the solid lines show the total contributions, dashed lines the first Galactic components and dashed-dotted lines the second Galactic components. It can be seen, that large uncertainties exist in the data. For C and O, data from IceCube/IceTop and KASCADE-Grande is even inconsistent with each other. In these cases, the adaptation of the parameters of the second Galactic component was mainly driven by matching the all-particle data rather than single-particle data. This is also the reason why the CR model for Fe lies slightly below the KASCADE-Grande and IceCube/IceTop data.

Figure 4.10 shows the γ-ray production rate of Model A (red) and Model B (magenta)

(A) Carbon

(B) Oxygen

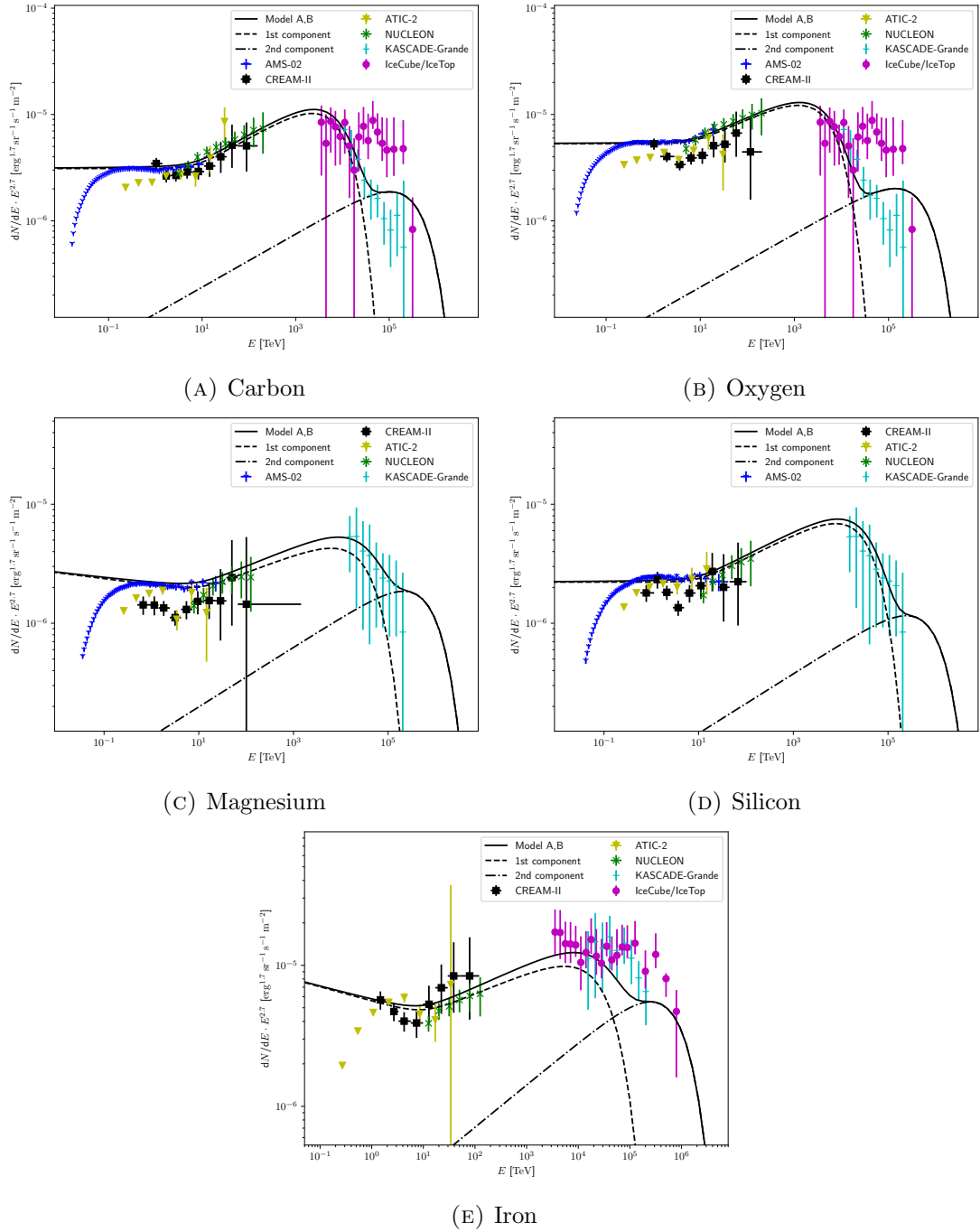(C) Magnesium

(D) Silicon

(E) Iron

FIGURE 4.9: Data for the heavier nuclei Carbon, Oxygen, Magnesium, Silicon and Iron together with the corresponding model components. The datapoints are from AMS-02 (Aguilar et al. (2017) for C and O, Aguilar et al. (2020) for Mg and Si), CREAM-II (Ahn et al., 2009b), ATIC-2 (Panov et al., 2009), NUCLEON (Grebenyuk et al., 2019), KASCADE-Grande (The KASCADE-Grande Collaboration et al., 2013) and IceCube/IceTop (Aartsen et al., 2019, for C-O and Fe). The solid lines show the total contributions, dashed lines the first Galactic components and dashed-dotted lines the second Galactic components. For Model A and Model B, the contributions are the same.
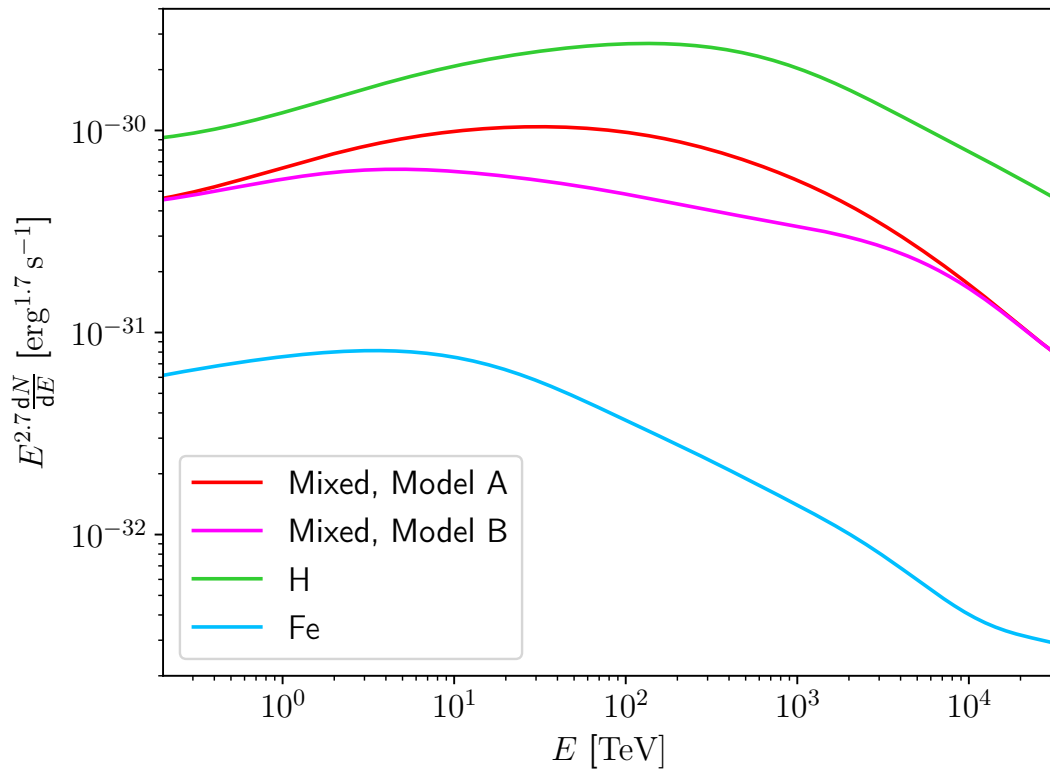
FIGURE 4.10: Emissivity of the CR models per cm^3 per second per unity ISM number density. Model A is shown with the red curve and Model B with magenta. The green and blue curves show the emission assuming all CRs from Model A are hydrogen or iron.

per cm^3 for an ISM number density of one. The ISM composition was the same as in Section 4.2. Additionally, the emission rates assuming all CR species from Model A are hydrogen (green) or iron (blue) are shown. Below TeV energies and above $\sim 10^4$ TeV, the emissivities of Model A and Model B are the same. In between, Model A gives higher fluxes. The flux level of the pure H scenario is above, and of the pure Fe case below Model A. This is caused by shielding effects and the soft power-law index < -2 of the CRs, which was discussed in Section 4.2. At 1 TeV, the pure H CRs produce 190 % and the pure Fe CRs 10 % of the γ rays from the mixed Model A. The break in the γ rays coming from the knee in the CR spectrum appears at lower energies for Fe CRs and at higher energies for H CRs compared to Model A.

4.4.2 Spatial model for the Milky Way

Direct measurements of CRs are only possible at the location of the Sun. At other places, their spectra can only be inferred indirectly from γ-ray observations or deduced from different models of the diffusion of CRs, which strongly depend on assumptions about, for example, the magnetic field turbulence and the scattering of CRs within these fields or the CR source distribution. The simplest CR model is a uniform distribution, where the CR density, composition and spectral shape are the same throughout the whole Galaxy. However, due to stronger magnetic fields in the inner parts of the Galaxy, one naturally would expect an increased CR density in the centre. Measurements from Fermi-LAT reveal an increased diffuse γ-ray emission and spectral hardening in the inner part of the Galaxy between hundreds of MeV and ∼100 GeV (Acero et al., 2016; Yang et al., 2016; Pothast et al., 2018). On the other hand, Aharonian et al. (2020); Peron et al. (2021) investigated the γ-ray emission from dense molecular clouds with Ferm-LAT data and found no confirmation of a change in CR density or spectral shape. This discrepancy could be explained by the presence of unresolved sources contributing to the measured diffuse fluxes from Acero et al. (2016); Yang et al. (2016); Pothast et al. (2018). All of these measurements are below the energy range relevant for our study.

Many CR models maintain the same spectral shape throughout the whole Galaxy. Nevertheless, different conditions can lead to spectral variations, such as e.g. if the CRs are not in a steady state, if diffusion is not everywhere the dominant CR transport mechanism or if the rigidity dependence of the diffusion coefficient is not homogeneous. Because this work intents to highlight the most important effects of CR composition and consequences of changes in the spectral shape were already investigated previously (e.g. Lipari & Vernetto, 2018), it will be assumed that the spectral shape and the composition are the same in the entire Galaxy. However, the overall CR density normalisation is allowed to vary according to the model from Lipari & Vernetto (2018), Equation 16:

$$N_{\mathrm{CR}} = N_\odot \cdot \frac{\mathrm{sech}(r/R_{\mathrm{CR}})\,\mathrm{sech}(z/Z_{\mathrm{CR}})}{\mathrm{sech}(r_\odot/R_{\mathrm{CR}})}. \tag{4.19}$$

We assume $R_{\mathrm{CR}} = 5.1\,\mathrm{kpc}$, $Z_{\mathrm{CR}} = 1\,\mathrm{kpc}$ as in Lipari & Vernetto (2018) and $r_\odot$ and $N_\odot$ are the radial distance of the Sun and the local CR density. These assumptions have the advantage that the numerical calculations can be simplified because the spatial distribution of CRs plays a role only for the γγ absorption and the normalisation of the

fluxes. Despite of spectral changes caused by absorption, the shape of the γ-ray emission will therefore be the same as in figure 4.10. For the distribution of insterstellar matter, the density model from Ferrière (1998); Ferrière et al. (2007) and for the γ-ray absorbing radiation fields the model from Popescu et al. (2017) together with the CMB will be used. Magnetic fields are not relevant for the direct production of γ rays in nucleon-nucleon collisions, but they play a role for γ-ray emission from secondary electrons and positrons. In this case, the B-field model from Jansson & Farrar (2012a,b) is utilized.

4.4.3 Emission from secondary particles

The collisions of CRs with the ambient medium do not only create γ rays and neutrinos, but also electrons and positrons. These will subsequently emit additional γ rays via IC scattering and bremsstrahlung contributing to the total observed emission. Their spectra can be calculated with the parametrisations from Kelner et al. (2006) as well, but these spectra are changing over time due to the different cooling processes, mainly the emission of synchrotron, IC and bremsstrahlung radiation. If the cooling time scales are shorter than changes in the density of the CRs and the ISM density, and the radiation fields and magnetic fields do not vary significantly on shorter time scales, an equilibrium between e^+/e^- production and losses is established. In general, the cooling times decrease with energy if IC losses are in the Thomson regime or synchrotron cooling is dominating. At the location of the Earth, for example, the cooling times at $100\,\text{GeV}$ are $\sim 8 \times 10^5$ yrs, using the B-field model from Jansson & Farrar (2012a,b), the radiation model from Popescu et al. (2017) together with the CMB, and the density model from Ferrière (1998); Ferrière et al. (2007). However, at $1\,\text{TeV}$ the cooling time is already one order of magnitude lower, decreasing rapidly with energy and reducing further for locations closer to the Galactic centre. The dynamical time for the Sun, i.e. the time it takes to complete one orbit around the Galactic centre, is $\sim 240\,\text{Myrs}$ (with $R \sim 8\,\text{kpc}$ and $v \sim 200\,\text{km s}^{-1}$); the lifetime of O stars is few million years. These time scales are both above the cooling time of electrons at $100\,\text{GeV}$, and therefore the equilibrium assumption is a reasonable choice for the calculation of the secondary emission.

The emission from the equilibrium e^+/e^- was calculated at scans throughout the Milky Way with the above-mentioned models for the magnetic field, the radiation fields and the density considering synchrotron radiation, bremsstrahlung and IC scattering. Figure
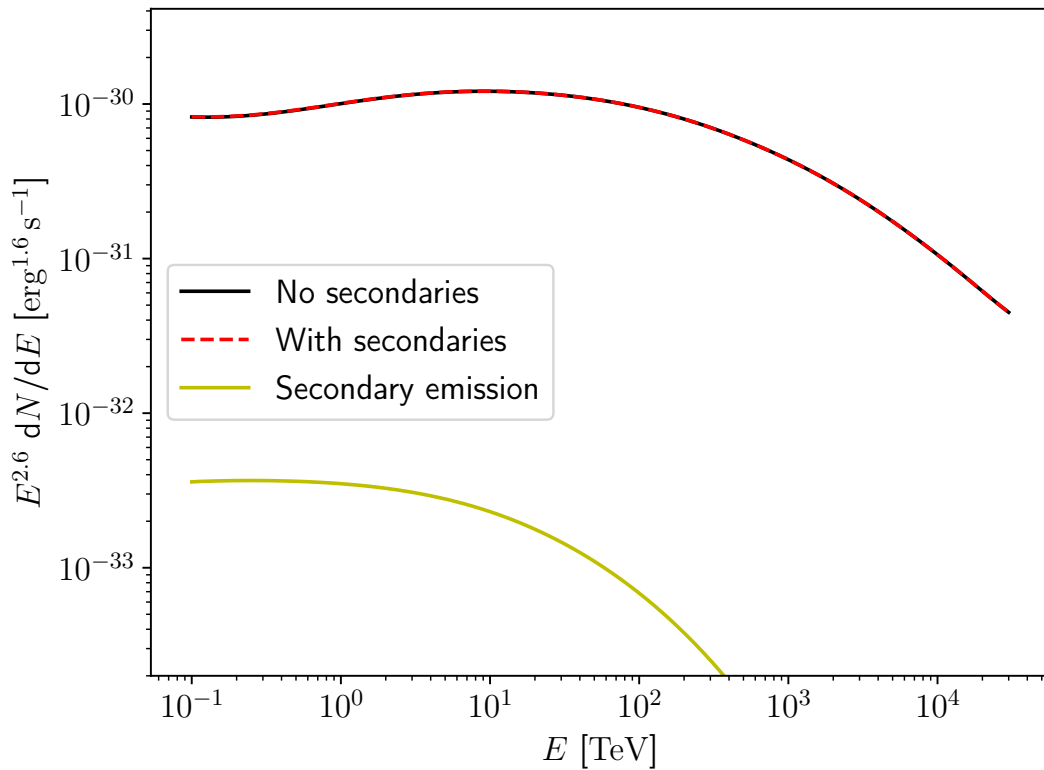
FIGURE 4.11: Emission per cm^3 at the position of the Sun for the mixed CR Model A from π^0 decay (black), from the secondary particles in equilibrium (green) and the sum of both contributions (red dashed line).

4.11 shows the contributions of direct emission for the mixed CR Model A via π^0 decay, the emission from the secondary particles and the sum at the location of the Sun. As can be seen, the emission from the secondary particles is well below the direct emission. Considering the whole Galaxy, the contribution from secondaries is still only several per cent in all cases. Even in the worst-case scenario, for zero B-fields and therefore no synchrotron losses, the emission is below $\sim$10 % for all energies above 100 GeV and CR models A and B. These results are consistent with the findings of Lipari & Vernetto (2018) and therefore, in the following calculations of the diffuse γ-ray fluxes, the emission from secondary particles was neglected.

4.4.4   Absorption

On their way to Earth, the γ rays will be absorbed due to pair production in reactions with the interstellar radiation fields and the CMB. The absorption becomes significant for energies above $\sim$100 TeV. If the composition and the spectral shape are unchanged

throughout the Galaxy, the total transmissivity along one specific line of sight can be calculated by

$$e^{-\tau} = \frac{\int_0^{d_{\max}} \exp\left(-\tau(E, x) \cdot x\right) N_{\mathrm{CR}}(x) n(x) \mathrm{d}x}{\int_0^{d_{\max}} N_{\mathrm{CR}}(x) n(x) \mathrm{d}x}. \tag{4.20}$$

Here, $d_{\max}$ is the maximum distance the γ-ray production is considered, $\tau(E, x)$ the local absorption coefficient at distance x and photon energy E, $N_{\mathrm{CR}}(x)$ the local CR density and $n(x)$ the local ISM density. Equation 4.20 has to be integrated over the specific respective sky region.

Figure 4.12 shows $e^{-\tau}$ integrated over Galactic latitudes $|b| \leq 5°$ and Galactic longitudes $25° \leq l \leq 100°$ for two different CR models: A uniform CR density (blue), and the CR density model in Equation 4.19 from Lipari & Vernetto (2018) (red). In both cases, the radiation field model from Popescu et al. (2017) together with the CMB, and the density model from Ferrière (1998); Ferrière et al. (2007) were used. The shapes of the curves for both CR density models are the same: At several tens of TeV, a drop in the transmissivity occurs, reducing the emission down to $\sim 93\%$. Both CR models suffer a very similar amount of absorption at this energy, and the non-uniform CR density model lies only slightly above the uniform model. The first drop in emission is followed by a much larger second one. Its maximum absorption occurs between 2 and 3 PeV caused by the CMB. In case of the uniform CR density, the flux is reduced to at most 56 % and for the non-uniform distribution to 61 %. Therefore, the CR density model has only a moderate effect on the total absorption in the considered case.

The CR model suffering less absorption is the non-uniform one. This can be understood considering, that γ rays produced behind the Galactic centre will suffer more absorption than CRs emitted in front of the Galactic centre. The emission of the non-uniform model is concentrated more towards the Galactic centre. Therefore, if a larger fraction of the γ rays from the uniform model comes from behind the centre than from in front, the uniform model can be expected to exhibit more absorption. This can be illustrated with a simplified calculation: At 1 PeV, the absorption is dominated by the CMB, which has the same opacity everywhere. If additionally the ISM density is assumed to be
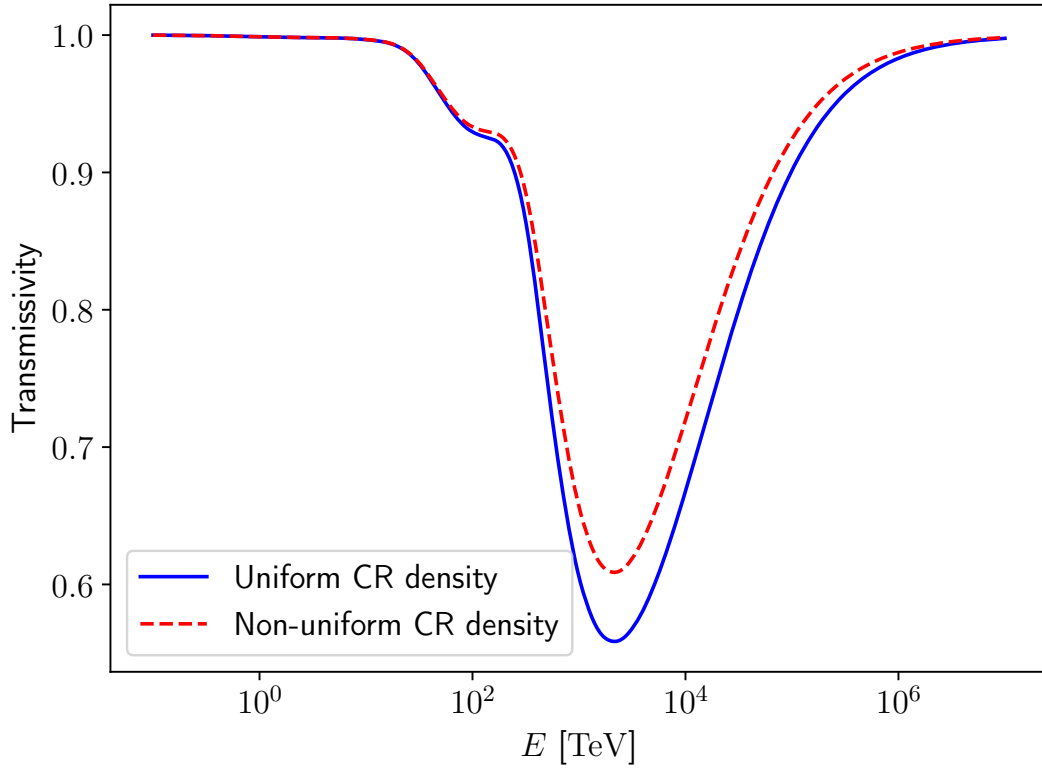
FIGURE 4.12: Integrated transmissivity of the diffuse γ-ray emission for Galactic latitudes $|b| \leq 5°$ and Galactic longitudes $25° \leq l \leq 100°$. The blue line shows the absorption for a uniform CR density, and the dashed red line for the density model from Lipari & Vernetto (2018). The figure is an adapted version of Fig. E.1 from Breuhaus et al. (2022a).

homogeneous, Equation 4.20 reduces to (see Appendix E in Breuhaus et al., 2022a)

$$e^{-\tau} = \frac{\int_0^{d_{\max}} \exp\left(-\tau_{\mathrm{CMB}} \cdot x\right) N_{\mathrm{CR}}(x) \mathrm{d}x}{\int_0^{d_{\max}} N_{\mathrm{CR}}(x) \mathrm{d}x}, \tag{4.21}$$

with the optical depth of the CMB at $1\,\mathrm{PeV}$ of $\tau_{\mathrm{CMB}} = 3.575 \times 10^{-23}\,\mathrm{cm}^{-1}$. For the simple case of a uniform CR density, one obtains

$$e^{-\tau} = \frac{1}{d_{\max}} \int_0^{d_{\max}} \exp\left(-\tau_{\mathrm{CMB}} \cdot x\right) \mathrm{d}x = \frac{1}{\tau_{\mathrm{CMB}} \cdot d_{\max}} \left[1 - \exp\left(-\tau_{\mathrm{CMB}} \cdot d_{\max}\right)\right]. \tag{4.22}$$

The case of the non-uniform CR density 4.19 for $z = 0$ and the line of sight directly through the Galactic centre gives

$$
\begin{aligned}
e^{-\tau} &= \frac{\int_0^{d_{\max}} \exp\left(-\tau_{\mathrm{CMB}} \cdot x\right) \operatorname{sech} \frac{x - r_\odot}{R_{\mathrm{CR}}} \mathrm{d}x}{\int_0^{d_{\max}} \operatorname{sech} \frac{x - r_\odot}{R_{\mathrm{CR}}} \mathrm{d}x} \\
&= \frac{\left. \frac{-2 R_{\mathrm{CR}}}{R_{\mathrm{CR}} \tau_{\mathrm{CMB}} + 1} \cdot \exp\left((r_\odot - x(R_{\mathrm{CR}} \tau_{\mathrm{CMB}} + 1))/R_{\mathrm{CR}}\right) \cdot {}_2F_1(1, a; b; c) \right|_{x=0}^{d_{\max}}}{\left. R_{\mathrm{CR}} \arctan\left(\sinh\left(\frac{x - r_\odot}{R_{\mathrm{CR}}}\right)\right) \right|_{x=0}^{d_{\max}}}
\end{aligned} \tag{4.23}
$$

with $\qquad a = \frac{1}{2}(R_{\mathrm{CR}} \tau_{\mathrm{CMB}} + 1), \qquad b = \frac{1}{2}(R_{\mathrm{CR}} \tau_{\mathrm{CMB}} + 3), \qquad c = -\exp\left(\frac{2(r_\odot - x)}{R_{\mathrm{CR}}}\right),$

and the Gaussian hypergeometric function ${}_2F_1$. The Galactic radius of the Sun is set to $r_\odot = 8\,\mathrm{kpc}$ as in the radiation model from Popescu et al. (2017) and $R_{\mathrm{CR}} = 5.1\,\mathrm{kpc}$. Considering γ-ray radiation out to Galactic radii of $24\,\mathrm{kpc}$ as in the calculations in Figure 4.12, which corresponds to $d_{\max} = 32\,\mathrm{kpc}$, results in $e^{-\tau} = 0.275$ in case of the uniform CR distribution, and 0.407 for the non-uniform CRs. The much larger differences between both CR distributions compared to Figure 4.12 are caused to a large extent by the neglection of the ISM density profile. However, the qualitative result remains the same, namely that the uniform CR distribution suffers more absorption, because a larger relative fraction of the γ-ray emission comes from behind the Galactic centre. Assuming, that γ rays are only emitted for Galactic radial distances $<8\,\mathrm{kpc}$ ($d_{\max} = 16\,\mathrm{kpc}$) results in $e^{-\tau} = 0.470$ in case of the uniform, and 0.457 for the non-uniform CR distribution. In this scenario, the same fractions of γ rays in the uniform CR model are produced in front and behind the Galactic centre, and the resulting absorption is slightly less than in the non-uniform scenario. This shows the effect which happens, if a non-uniform ISM density model is used, because then more emission is produced at short distances from the Galactic centre. The integration over Galactic latitudes and longitudes, as it is the case for the results in Figure 4.12, reduces the differences from both CR models in the calculations with $d_{\max} = 32\,\mathrm{kpc}$ as well.

The electrons and positrons produced during the $\gamma\gamma$ absorption process will radiate γ rays as well and lead to an additional contribution to the observed flux on Earth. This radiation takes place at energies much lower than the energy, where the absorption process takes place. But because the CRs follow a power-law distribution much softer than E^{-2}, the energy content in the absorption regime is much lower than at the energies where the γ rays from the leptons are produced, the flux level of the emission is well

below the direct emission (see e.g. Murase & Beacom, 2012). Therefore, the emission from $\gamma\gamma$ pair production and the subsequent cascading are ignored in the calculations of the diffuse emission in the next section.

4.4.5   Results

As stated previously, for the final calculations of the emission, it was assumed that the composition and the spectral distribution of the CRs are unchanged throughout the Galaxy, and the overall CR density normalisation followed the profile given in Equation 4.19. The Tibet ASγ collaboration published measurements of the diffuse emission above 100 TeV for two different regions of the sky (Amenomori et al., 2021b). For the region with Galactic longitudes of $25° \leq l \leq 100°$ and Galactic latitudes $|b| \leq 5°$, there exists additional data at lower energies from the Astrophysical Radiation with Ground-based Observatory at YangBaJing (ARGO-YBJ, Bartoli et al., 2015). The ARGO-YBG data at lower energies is crucial in constraining the shape of the emission for different CR compositions. Therefore, the investigations are focused on this sky region. Differences in fluxes between the sky regions are mainly caused by the underlying spatial CR distribution, the ISM density model and possible contributions from unresolved sources. These issues are not the focus of this study and were also investigated by other authors (e.g. Amenomori et al., 2021b; Vecchiotti et al., 2021; Zhang et al., 2022). Here, the γ-ray emission from Model A and Model B will not only be compared with each other but also to the extreme cases assuming all CRs from Model A are H or Fe. Because the produced γ-ray fluxes for these extreme cases are very different (see figure 4.10) and the CR density model is not very well constrained, an additional overall normalisation of the CR density profile from Equation 4.19 will be allowed in all cases. Its value will be determined by a fit to the data.

The results are displayed in Figure 4.13. The mixed CR Model A is shown with the solid red line and Model B in magenta. Additionally to these two models, two other extreme cases are shown in the upper panel, assuming that all CRs from Model A are hydrogen (green) or iron (blue). The emission without absorption is shown in the upper panel with dotted lines in the corresponding colours. The lower panel shows the total emission from the mixed Models A and B, but additionally with the contributions from

H, He, and all heavier nuclei combined. The fit of the overall normalisation in each case leads to similar flux levels of the different curves in the upper panel below $\sim$10 TeV.

The fitted normalisation parameter for the mixed Model A curve results in a flux only 23 % above a calculation without a fit using the density model from Ferrière (1998); Ferrière et al. (2007), the radiation model from Popescu et al. (2017) for the absorption and the CR density model in Equation 4.19 from Lipari & Vernetto (2018). This slightly higher flux obtained in the fit can easily be explained by uncertainties in the CR distribution and the ISM density distribution. Furthermore, in the radiation model from Popescu et al. (2017) it is assumed that the Sun is located at a distance of 8 kpc from the Galactic centre, whereas Ferrière (1998); Ferrière et al. (2007); Lipari & Vernetto (2018) use a distance of 8.5 kpc. Since in all calculations here, 8 kpc was used, the emission could be underestimated, although the uncertainty in the CO conversion factor used to construct the ISM density model might have a bigger influence. The observed γ-ray flux is therefore consistent with the expectations from ISM and CR density models.

Comparing the shapes of the mixed Model A case with the pure hydrogen case, the mixed composition leads to a softening of the emission already at energies above $\sim$30 TeV. This softening is caused by the transition to heavier nuclei at the knee, because any spectral feature for heavier CRs will occur at an energy $1/A$ lower than for hydrogen CRs. At an energy of 1 PeV, the mixed case is a factor of 2/3 lower than the hydrogen case. If all CR particles are assumed to be iron, the softening happens at $\sim$10 TeV, which is lower than in the mixed case. If the composition would be different than assumed in the mixed Model A, or if it varies throughout the Galaxy, the resulting γ-ray emission would have shapes lying in between the pure hydrogen and the pure iron case.

The magenta curve shows the emission from the mixed CR Model B. Due to the softer H and He spectra of the first Galactic component, the spectrum starts to soften at lower energies than the mixed Model A and lies in between the pure iron case and Model A. Changes in the CR spectrum therefore have similar effects as changes in the composition. Future high-resolution measurements of the diffuse γ-ray emission have to be interpreted considering both effects, and γ-ray measurements alone are not sufficient to discriminate between them.

The highest data point from Tibet ASγ is not reached by any of the models. A heavier composition as well as the omnipresent absorption make it impossible to match the
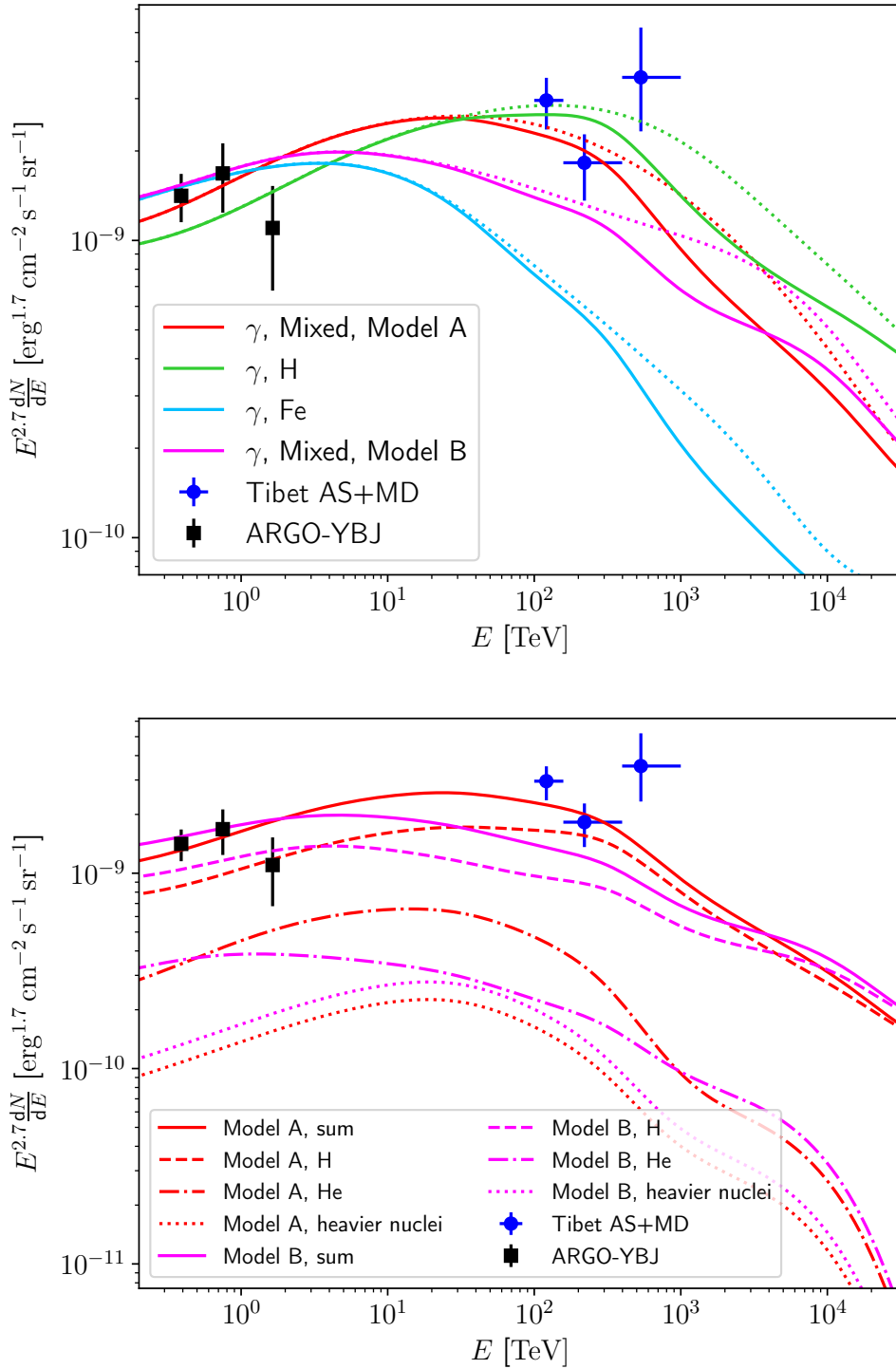
FIGURE 4.13: Diffuse γ-ray emission integrated over Galactic longitudes $25° \leq l \leq 100°$ and Galactic latitudes $|b| \leq 5°$. Data from ARGO-YBJ (Bartoli et al., 2015) is displayed with black squares and data from the Tibet air shower array and muon detector array (Tibet AS+MD, Amenomori et al., 2021b) with blue circles. The upper panel shows the emission from the mixed Model A in red and Model B in magenta. For the green and the blue line it as assumed, that all CRs from Model A are hydrogen (green) and iron (blue). Dotted lines in the same colour show the emission without absorption. The lower panel shows the same lines for the mixed CR models A and B with the saem colours as in the upper panle, but additionally with the relative contributions from H (dashed lines), He (dotted lines) and all heavier nuclei combined (dotted lines). The figure is an adapted version of the corresponding figures in Breuhaus et al. (2022a).

Figure 4.14 shows the corresponding all-sky neutrino emission.

second and the last data point simultaneously, and an additional hard component would be needed. It is therefore very likely, that unresolved sources are responsible for a large fraction of the detected emission in this energy bin. Indeed, the Tibet ASγ collaboration stated, that four of the ten detected photons come from a region not further away than 4° from the Cygnus cocoon. The Cygnus cocoon is a superbubble surrounding a massive star-forming region, which emits γ rays at energies above 100 TeV (Abeysekara et al., 2021; Amenomori et al., 2021a; Dzhappuev et al., 2021).

The first and second Tibet ASγ data points are matched best by the mixed CR Model A and the pure hydrogen case. Model B does nearly touch the errorbar of the second Tibet ASγ point, but the emission is too soft to reach the higher flux levels of the first point. Therefore, Model A leads to a more consistent prediction of the γ ray emission, and the CR data from NUCLEON gives a better overall description of the CR spectrum than the data from CREAM, if no spectral changes throughout the Galaxy occur. The pure Fe case can not account for the Tibet ASγ data points due to its much softer spectrum. In fact, a mixed CR Model with a lighter composition than Model A producing a γ-ray spectrum with a shape between Model A and the pure H case would match the data better than any of the models shown in Figure 4.13. However, the uncertainty in the data does not allow any solid conclusions. A significant amount of the emission in the Tibet ASγ energy range might as well be produced by unresolved sources or freshly accelerated CRs in the medium surrounding the sources (Vecchiotti et al., 2021; Yang & Aharonian, 2019; Zhang et al., 2022).

The species contributing most to the γ-ray emission in both mixed models is hydrogen. This is shown in the lower panel of Figure 4.13. More than $\sim 64\%$ of the γ rays from Model A are produced by CR protons, and more than $\sim 67\%$ for Model B. Helium accounts for less than $\sim 28\%$ in Model A ($\lesssim 24\%$ in Model B) and the heavier nuclei are responsible for less than $\sim 9\%$ of the γ rays in Model A ($\sim 16\%$ in Model B). Thus, not surprisingly, H and He are the most important species for the diffuse emission, and changes in their abundances or spectral shapes throughout the Milky Way have the strongest impact on the resulting emission.

The corresponding all-sky neutrino emission for the γ rays shown in Figure 4.13 is depicted in Figure 4.14. The upper panel shows the curves for Model A, Model B, and the pure hydrogen case, and the lower panel the emission from Model A and B together with
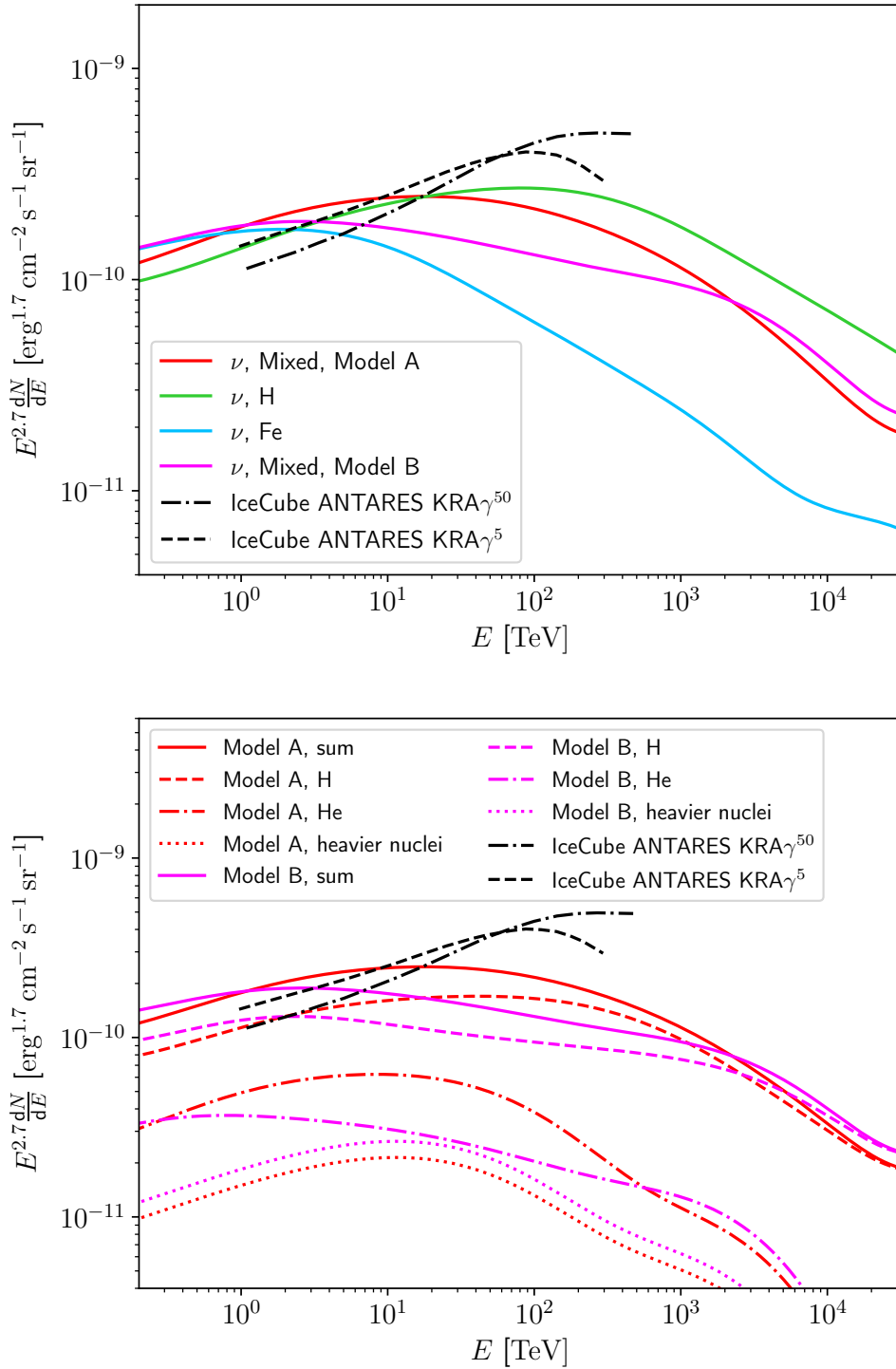
FIGURE 4.14: All-sky Galactic neutrino emission compared to the combined upper limits from IceCube and ANTARES (Albert et al., 2018) shown in black. The dashed line shows the limit for the KRAγ^5 model and the dashed-dotted line for the KRA$\gamma^5$0 model. The coloured lines are analogous to the one in Figure 4.13. In the upper panel, the red line shows the emission from Model A, the green one the emission, assuming all CRs from Model A are hydrogen nuclei and the blue line assuming all CRs from Model A are iron. The curve for Model B is shown in magenta. The lower panel shows emission for Model A and B in the same colours as in the upper panel, but additionally with the relative contributions of hydrogen (dashed lines), helium (dashed-dotted lines) and all other heavier nuclei (dotted lines). The figure is an adapted version of the corresponding figures in Breuhaus et al. (2022a).

the corresponding contributions from H, He, and all heavier nuclei combined. Because the γ rays are only from a restricted region of the sky, the all-sky neutrino emission was re-scaled according to the ISM density model and the CR distribution. The predictions are compared with combined upper limits from IceCube and the Astronomy with a Neutrino Telescope and Abyss Environmental Research project (ANTARES) (Albert et al., 2018). An important uncertainty of the neutrino limits is the underlying model, which can influence the resulting limits strongly. Figure 4.14 shows two different limits corresponding to the KRAγ^5 and the KRAγ^{50} model, which are KRAγ models with a 5 PeV and a 50 PeV cutoff (see Gaggero et al., 2015). Due to the higher cutoff energy, the KRAγ^{50} limit is lower than the KRAγ^5 limit below energies of $\sim$100 TeV. None of the neutrino emission curves is below the KRAγ^{50} limit for all energies. This is different for the KRAγ^5 limit, which is not exceeded by the pure hydrogen case. The mixed Model A only slightly overtakes the limit for energies below $\sim$10 TeV. For the pure iron and the mixed Model B curves, this happens for even lower energies. Because differences in the underlying ISM and CR density models will affect the re-scaling of the all-sky neutrino emission compared to the γ-ray curves in Figure 4.13 and the effects of different assumptions for the neutrino limit models, one can conclude, that the predicted neutrino emissions are broadly consistent with the limits. The same conclusions regarding the consistency with neutrino limits were also obtained by Fang & Murase (2021). The influences of the composition on the shapes of the neutrino emission are nearly the same as for the γ-ray emission discussed above. As for the γ rays, hydrogen CRs are responsible for the largest fraction of the emission, followed by helium and all heavier species combined (see lower panel of Figure 4.14).

4.5 Conclusion

Although the effects of different CR and ambient medium compositions are often neglected, in many cases an accurate treatment is necessary. Heavier species can have the following impacts on γ-ray and neutrino production:

- For the same number density, a heavier composition of the ambient medium increases the γ-ray and neutrino fluxes. If instead the mass density is the same, but

the nucleons are clumped together into heavier nuclei, the emission will decrease slightly. Both effects can be considered energy independent.

- The CR composition has the largest impact on the γ-ray and neutrino emission. The emission is generally reduced for heavier species due to shielding effects. The power-law index of the CR distribution has an important influence as well: Because the nucleons producing the γ rays are located in nuclei with a total energy a factor of A higher, for spectra softer than E^{-2} the emission is reduced even further.

- Spectral features will occur at an energy $1/A$ lower than for hydrogen CRs. If such a feature is rigidity dependent, it will manifest at an energy $Z/A \approx 0.5$ times lower.

In some cases, an increase in emission due to a heavier ambient medium composition can balance the reduction due to shielding. However, spectral features will still occur at lower energies. The highest energies close to a rigidity dependent cutoff are always dominated by hydrogen CRs.

In the case of the diffuse γ-ray emission above tens of TeV, compositional effects can not be accounted for by nuclear enhancement factors and an accurate treatment is required. However, if the CR composition changes throughout the Galaxy, the emission at lower energies would be reduced relative to a pure hydrogen case, and the nuclear enhancement factors have a spatial dependence. Such a reduction in flux at low energies can in principle be compensated by different ISM or CR density profiles, and it would be impossible to disentangle both effects from γ-ray data alone. At higher energies, the composition has an important impact on the shape of the knee in the γ-ray spectra, as a heavier composition will enhance the spectral break and shift it to lower energies. Changes in composition can therefore mimic changes in the spectral index or a change of the position of the knee. Therefore, future measurements have to be interpreted considering both, potential spectral changes of the CRs and compositional variations. If the CR spectrum is unchanged throughout the Milky Way, γ-ray measurements can constrain the CR composition.

The current measurements from the Tibet ASγ collaboration do not allow yet to derive firm conclusions, although the mixed Model A or a lighter composition are favoured. Disentangling contributions from unresolved sources is crucial for this effort. But this

is expected to change soon. Data from LHAASO and the future SWGO and CTA observatories will constrain individual UHE sources as well as the diffuse emission. Measurements will be possible for much smaller angular regions as with Tibet ASγ. The CR spectrum, the position of the knee and the composition will be tightly constrained and the spatial dependence disentangled. The parametrisations developed in this work will be very helpful for the community to properly account for compositional effects in UHE sources and the diffuse emission. Current neutrino limits are very close to the detection threshold, and future instruments will have the ability to surpass these limitations and complement the γ-ray measurements.

5 Non-thermal processes in η Carinae

η Carinae is a colliding wind binary (CWB) system firmly detected in γ rays. A γ-ray counterpart was also found for the CWB γ^2 Velorum (Pshirkov, 2016). Although it is not exactly clear if this γ-ray source is indeed associated with the corresponding CWB, strong hints for an orbital modulation corresponding to the period of the binary system were found recently (Martí-Devesa et al., 2020). This strengthens the case and makes it very likely that the detected γ-ray source is indeed associated with γ^2 Velorum. However, currently, η Carinae is the best object of its kind to be studied in γ rays.

Today, the apparent magnitude of η Carinae is around 6 mag. However, this has not always been the case. Between 1600 and 1800, the star was reported to have apparent magnitudes between four and two. It is not precisely known if η Carinae was merely fluctuating or rather brightening, but at 1800, it had undoubtedly reached 2 mag. After a phase of fluctuations between second and first magnitude, the star started to brighten rapidly in 1837 until reaching -1 mag in 1843 and late 1844 till early 1845, becoming the second brightest star in the sky. In 1858 it had reached the state of an apparent first magnitude star again. This phase from 1837 to 1858 is called the great eruption. A second outbreak happened from 1887 to 1895, the so-called second eruption. Since then, η Carinae was a strongly variable star, which is believed to explode as a supernova soon (see Davidson & Humphreys, 2012, and references therein).

Figure 5.1 shows images of the η Carinae system in optical (left) and X-rays (right). The optical image shows a bipolar emission and reflection nebula in the middle, consisting of two hollow shells, the so-called Homunculus Nebula. It was created during the great eruption from 1837 until 1858. Around the Homunculus, one can observe larger but fainter structures, which could be relics of earlier outbursts. The X-ray picture is not on the same scale as the optical image, and the Homunculus Nebula is slightly larger
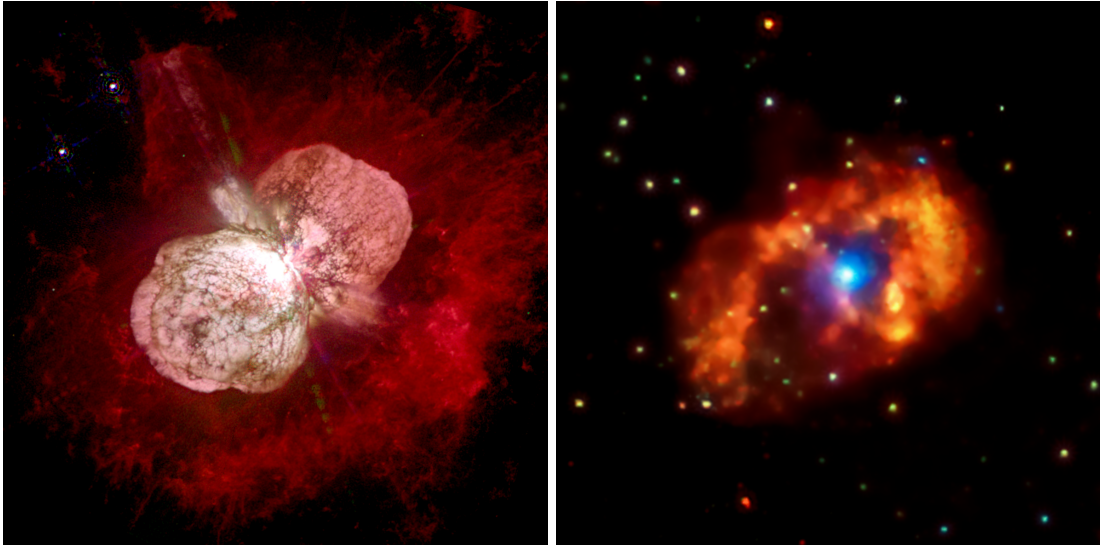
FIGURE 5.1: Left: η Carinae with the Homunculus nebula in optical. Credits: NASA/HST/ J. Morse/K. Davidson. Right: Composite image of η Carinae in X-rays created by the author from publicly available data from the Chandra X-ray Observatory https://chandra.harvard.edu/photo/openFITS/xray_data.html. Red: $0.1-1\,$keV, green: $1-3\,$keV, blue: $3-10\,$keV. Credits: NASA/CXC/GSFC/Hamaguchi et al. (2014a). The images are not to scale, the size of the right one is $\sim 2' = 4.6$ light years. The Homunculus nebula would be slightly larger than the inner blue region in the X-ray picture.

than the blue structure seen in the middle of the right panel of Figure 5.1. The X-ray picture is a composite image created by the author[1] for the energy ranges $0.1-1\,$keV (red), $1-3\,$keV (green), and $3-10\,$keV (blue). The large-scale structures emit mainly low energy X-rays, but on scales comparable to or below the Homunculus Nebula, the high energy $3-10\,$keV X-rays are produced. Unfortunately, current γ-ray observatories can not reach the same angular resolutions, but the images above show the complexity of the η Carinae environment. Inside the Homunculus Nebula, there is an additional smaller bipolar nebula, called the little Homunculus (Ishibashi et al., 2003), which is believed to be created in the second eruption from 1887 to 1895 (Smith, 2005).

The η Carinae binary star system is located inside the Homunculus Nebula and completes one orbital period in $\sim 5.5\,$yrs (Damineli et al., 2008). Both stars are very luminous with stellar luminosities of $4 \times 10^6\,\mathrm{L_\odot}$ and $0.3 \times 10^6\,\mathrm{L_\odot}$. However, the other orbital parameters and stellar properties relevant to modelling particle acceleration processes are difficult to estimate and not precisely known. The eccentricity of the orbit is above 0.8, most likely between 0.85 and 0.90 (Mehner et al., 2015). The high eccentricity

---

[1]The picture was constructed from publicly available data from the Chandra X-ray Observatory https://chandra.harvard.edu/photo/openFITS/xray_data.html, credits: NASA/CXC/GSFC/Hamaguchi et al. (2014a)

produces strong orbital variations in the physical conditions of the stellar wind region, which is reflected in X-ray lightcurves. The conditions in the acceleration zone of the wind collision region are very different for periastron and apastron. The primary star, which we refer to as η Car A, is most likely a luminous blue variable (Davidson & Humphreys, 1997). Its mass is estimated to be above $90\,M_\odot$, with an initial mass of at least $150\,M_\odot$ or higher (Hillier et al., 2001). The companion star η Car B is a late-type nitrogen-rich O or a Wolf-Rayet star (Iping et al., 2005) with a mass no larger than $30\,M_\odot$ (Hillier et al., 2001). The properties of the stellar winds from the stars are different. η Car A has a mass-loss rate of a few $10^{-4}\,M_\odot\,\mathrm{yrs}^{-1}$ up to a few $10^{-3}\,M_\odot\,\mathrm{yrs}^{-1}$ and a terminal wind velocity of $\approx 500\,\mathrm{km\,s}^{-1}$. The wind of η Car B is loaded with less mass $\sim 10^{-5}\,M_\odot\,\mathrm{yrs}^{-1}$ and much faster $\approx 3000\,\mathrm{km\,s}^{-1}$ (see Corcoran & Hamaguchi, 2007, and references therein). The magnetic fields of the stars are another important property for modelling particle acceleration in the wind collision region. Unfortunately, they are unknown. Data from radio observations of another high-mass binary system, WR 147, is consistent with surface magnetic field strengths between 30 and $300\,\mathrm{G}$ (Williams et al., 1997; Walder et al., 2012) and the magnetic fields in the η Carinae system are expected to be similar.

It is believed that particles accelerated in the wind collision region of massive binary systems are responsible for the production of non-thermal X-rays and γ rays (e.g. Eichler & Usov, 1993; Reimer et al., 2006) and that this applies to η Carinae (e.g. Bednarek & Pabich, 2011; Ohm et al., 2015). However, Ohm et al. (2010) proposed that particles might also be accelerated in the blast wave of the great eruption from 1837 to 1858. It might be that γ rays are produced by particles accelerated in both regions, the wind collision zone and the blast wave. The detected γ-ray emission associated with η Carinae shows signatures of two different components, one dominating below $\sim 10\,\mathrm{GeV}$ and the other at higher energies (Abdo et al., 2010; Farnier et al., 2011). If hadronic interactions produce the low energy component (Ohm et al., 2015), the particle acceleration and injection will behave similarly as in SNR shocks. This does not hold if the low energy component is due to IC scattering of accelerated electrons (e.g. Farnier et al., 2011; Balbo & Walter, 2017; Hamaguchi et al., 2018), which would imply conditions very different from typical SNR shocks (see Section 5.3). This would have significant consequences for a possible contribution of SFR to the sea of Galactic CRs. Therefore, understanding the particle acceleration and emission in η Carinae will not only help to understand particle

acceleration in CWBs, but also is tremendously important for the understanding of particle acceleration in SFR.

This chapter will deal in detail with the question of particle acceleration and non-thermal X-ray and γ-ray emission from the η Carinae system. First, the spectral and temporal properties of previous observations in X- and γ rays are presented in Section 5.1. Then, general physical considerations about the particle acceleration in the wind collision region are carried out (Section 5.2). In Section 5.3, a model to explain the non-thermal emission by particle acceleration in the WCR is developed and compared to the data. Possible emission from larger scales is investigated in Section 5.4, followed by a discussion in Section 5.5. Our results until Section 5.3 were previously published in White et al. (2020).

5.1   X-ray and γ-ray observations

5.1.1   X-ray observations

η Carinae has been extensively observed in the X-ray domain (see e.g. Corcoran, 2005; Hamaguchi et al., 2007, 2014b) in terms of spectral properties as well as the temporal behaviour. Corcoran et al. (2015) give a summary of X-ray observations between 1996 and 2014. Observations of the last periastron passage in 2020 were presented by Kashi et al. (2021). As can be seen in the right panel of Figure 5.1, the X-rays above 3 keV are produced on scales smaller than the Homonculus Nebula. The large majority of these high energy X-rays have to be produced in the wind collision region or close to the stars, since the time evolution clearly shows a pattern coincident with the orbital period.

The upper panel of Figure 5.2 shows η Carinae seen by the Nuclear Spectroscopic Telescope Array (NuSTAR) X-ray satellite (Harrison et al., 2013) on 7.12.2019. The data were analysed with the HEASoft package, version 6.26.1. It was calibrated with the nupipeline command neglecting data from the South Atlantic Anomaly (SAA) using the options saacalc=2 saamode=optimized tentacle=yes. η Carinae appears as a bright, circular region. The lower panel of Figure 5.2 shows the spectrum of the source, which was extracted from a circular region with a $30'$ radius centred at the source position. The background was subtracted using a circular region of the same size located away

from the source. Until energies of $\sim$30 keV, the spectrum shows thermal emission with a prominent iron line at 6.7 keV. However, at higher energies, there is a non-thermal component, which can be approximated by a power law. The detection of such a component in hard X-rays was first claimed by Viotti et al. (2004), which was later confirmed by other authors (Leyder et al., 2008; Sekiguchi et al., 2009; Leyder et al., 2010) and more recently by Hamaguchi et al. (2018).

For large parts of the orbit, the X-ray emission is relatively constant, but rapid changes are observed around periastron because of the high eccentricity of the system. The bottom panel of Figure 5.3 shows the thermal X-ray emission between 2 and 10 keV for orbital phases from 0.8 to 1.2. The observations were performed with the Rossi X-ray Timing Explorer (RXTE) and Swift over four different periastron passages in 1998, 2003, 2009 and 2014 (Corcoran et al., 2017). The phases are defined such that a phase of 0.0, 1.0 or 2.0 corresponds to the periastron. To compare the observations from different periastron passages, the curves for different periastron passages are shifted such that periastron is at a phase of 1.0 in all cases. The emission increases before the periastron until reaching a maximum at phase $\sim$0.99, followed by a rapid drop of more than an order of magnitude. The minimum is reached at phase 1.0, followed by a recovery phase until the average flux level maintained over most of the orbit is reached. Before reaching the maximum, there are clear signs of turbulent behaviour. The exact shape around the periastron can differ from passage to passage, but the qualitative behaviour remains the same. An example is the recovery phase of the 2009 passage, which is short compared to the other passages.

The increase in X-ray emission towards periastron occurs because the total X-ray luminosity is expected to scale approximately with $1/D$, where D is the stellar separation (Stevens et al., 1992). However, this does not explain the sudden drop in emission and the subsequent X-ray minimum, and different theories have been proposed as an explanation (see e.g. Parkin et al., 2009). Firstly, in the eclipse model, either the primary star itself or its dense and optically thick wind moves in front of the wind collision region and blocks the radiation. Second, the increased mass-loss model proposes that the primary star might undergo a phase of increased mass-loss rate during periastron, possibly due to tidal interactions. And lastly, due to the proximity of the stars, the WCR might move into the wind acceleration region of η Car B. Consequently, the WCR could collapse onto the surface of η Car B, which can not launch a wind in the direction of the primary star
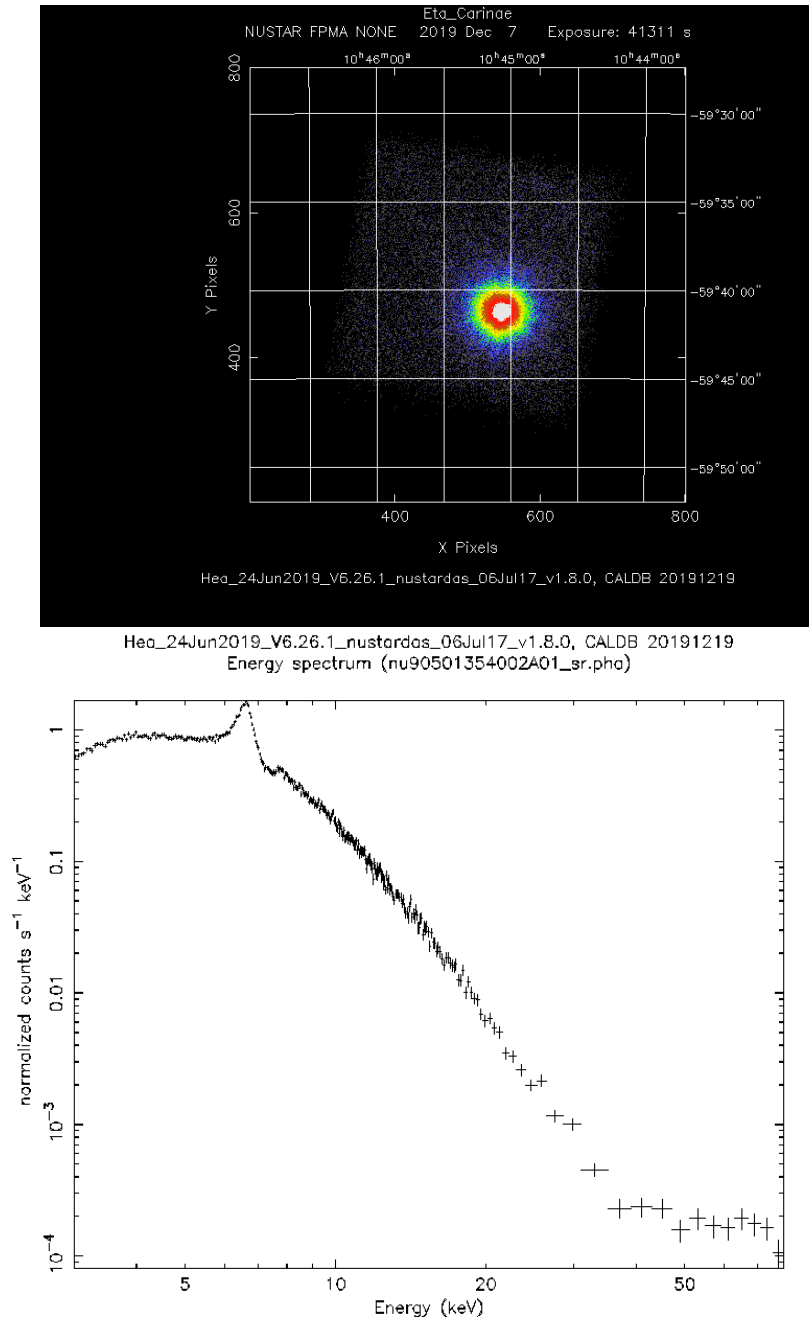
FIGURE 5.2: X-ray observations of η Carinae with the NuSTAR satellite from 7.12.2019. Top: Image of the region in logarithmic scale. Bottom: Extracted spectrum. The source signal extraction region was circular with a $30'$ radius centred at the middle of the emission from η Carinae visible in the upper panel. The background was subtracted using a circular region of the same size away from the source.

anymore. The intense radiation fields of η Car A pushing in the opposite direction of the wind from η Car B might support this process (radiative inhibition). Until now, no consensus on which processes contribute to the X-ray minimum has emerged yet. The three-dimensional simulations of Parkin et al. (2011) were able to reproduce the overall shape of the X-ray emission, but the length of the X-ray minimum was too short.

The middle panel of Figure 5.3 shows data of the hard X-ray component between 30 and 50 keV for the 2014 periastron passage from Hamaguchi et al. (2018). These measurements allowed to investigate for the first time the behaviour of the non-thermal X-ray component. One can observe the same qualitative temporal behaviour as in the thermal X-ray emission: An increase of the flux towards periastron and a drop of the emission at periastron followed by a recovery phase. However, the flux minimum at periastron shows some residual emission compared to the thermal X-rays in the bottom panel. This might indicate that the thermal and the non-thermal X-rays are produced in different parts of the wind collision region or that the heating and acceleration processes behave differently in the changing environmental conditions. We aim to explain this behaviour in Section 5.2 and 5.3.

5.1.2 γ-ray observations

γ-ray observations of η Carinae do not date back as far as the X-ray observations do. Emission from the direction of the source was first detected in 2009 by the Astro-Rivelatore Gamma a Immagini Leggero (AGILE) satellite (Tavani et al., 2009) and the Fermi Large Area Telescope (Fermi-LAT, Abdo et al., 2009b, 2010). Further analysis of more data from Fermi-LAT in the γ-ray regime was performed by Farnier et al. (2011); Reitberger et al. (2012, 2015); Balbo & Walter (2017). The shape of the γ-ray spectrum shows the presence of two components, one dominating below ~ 10 GeV and the other one at higher energies. Figure 5.4 shows the result of an analysis of Fermi-LAT data between the 4.8.2008 and the 1.7.2019 (black) compared to the earlier analysis of Reitberger et al. (2015) for Fermi-LAT data collected between the 4.8.2008 and the 18.2.2014 (red) and a hadronic model fit towards the data below 200 GeV. The grey shaded region shows the systematic error band (see White et al., 2020, for details). The black data points and the error band are consistent with the results from Reitberger et al. (2015). With more data, it was possible to constrain the emission at lower energies than
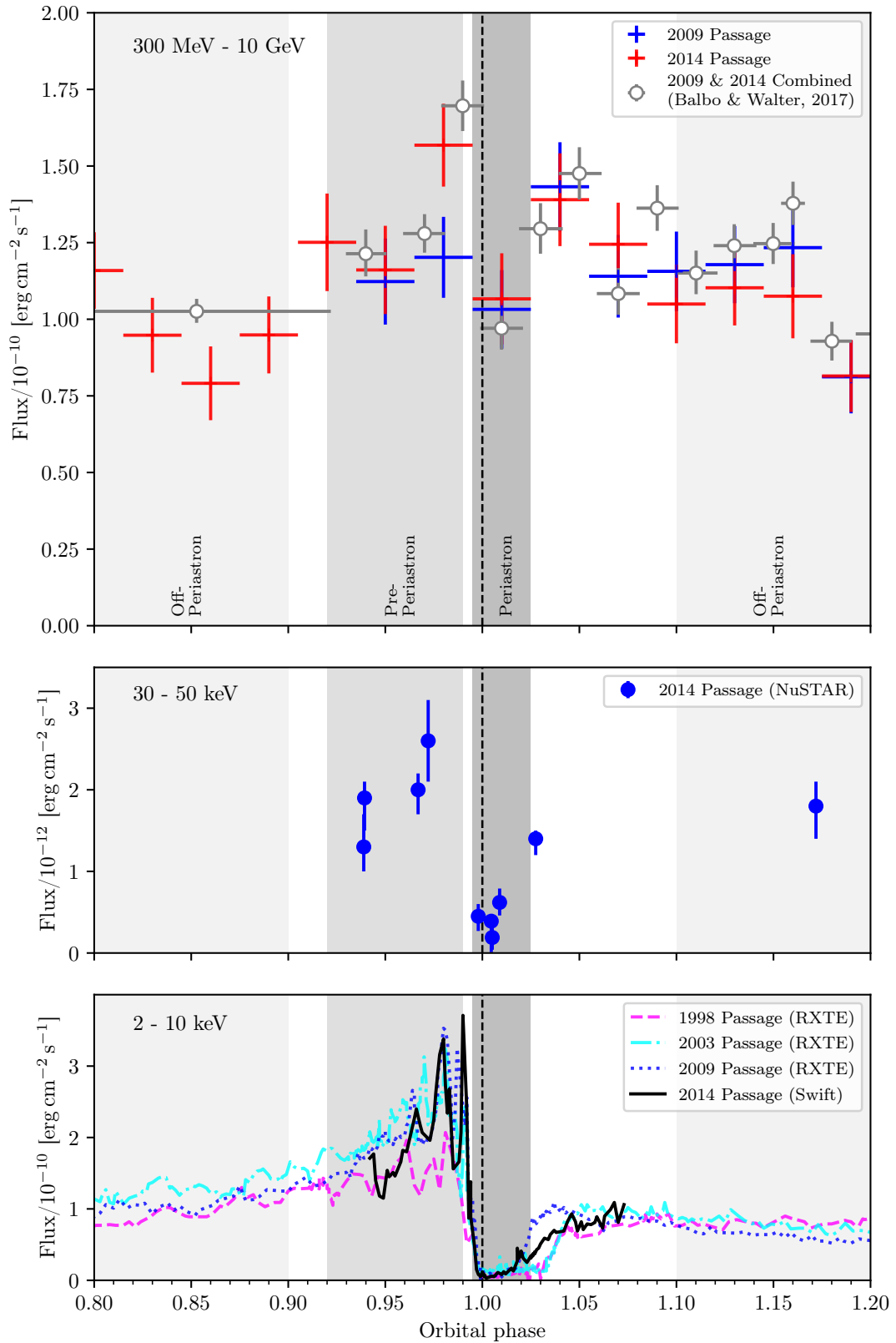
FIGURE 5.3: Lightcurves in X- and γ rays from phase 0.8 to 1.2. Top panel: Fermi-LAT data analysis for the 2009 and 2014 passages compared with the data from Balbo & Walter (2017). The grey shaded areas mark the pre-periastron, periastron and off-periastron phases used for the spectral analysis shown in Figure 5.6. Middle panel: Data from NuSTAR of the non-thermal X-ray component between $30 - 50\,\mathrm{keV}$ for the 2014 periastron passage from Hamaguchi et al. (2018). Bottom panel: RXTE and Swift data between 2 and 10 keV for the 1998, 2003, 2009 and 2014 passages. Adapted version of Fig. 2 in White et al. (2020).
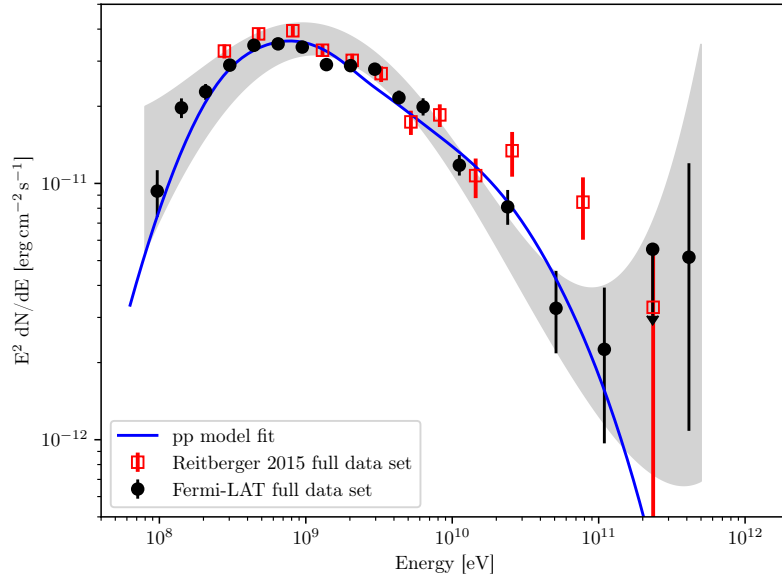
FIGURE 5.4: γ-ray observations of η Carinae together with a proton-proton collisional model fit. Black data points show the result for an analysis of the complete data set from Fermi-LAT, and the grey shaded region is the systematic error band. The red data points are the results from Reitberger et al. (2015). The model fit is shown in blue and was performed with the NAIMA software package Zabalza (2015).

what was achieved in previous works, and we detected the signature of a turnover. This spectral feature might likely be the signature of a pion bump, indicating that hadronic emission could be responsible for the low energy component. The model fit clearly shows that hadronic scenarios can naturally explain the shape of the low energy component.

A temporal analysis of the γ-ray emission from Fermi-LAT is displayed in the top panel of Figure 5.3 above the X-ray light curves. The data were binned for phase intervals of 0.03, corresponding to $\sim$60 days. The blue data points show data from the 2009 periastron passage, and the red points data from the passage in 2014. For comparison, the results of a joint analysis of both passages from Balbo & Walter (2017) are shown too. Around periastron, there is an increase in emission, which was also found previously by Reitberger et al. (2015). However, the variabilities in time are much less pronounced than in the X-ray regime, and during periastron, there is no sign of a disappearance of the emission. During both passages, the general behaviour and the flux level of the 300 MeV to 10 GeV emission are similar. Balbo & Walter (2017) found that the high energy emission above 10 GeV behaves differently in both passages, because it does not show an increase during the periastron in 2014, according to their analysis.

Figure 5.5 shows the spectral energy distributions for three different phase ranges from an analysis of Fermi-LAT data (White et al., 2020). The top panel shows data from phases 0.1 to 0.9, which are called off-periastron. This is the phase range of approximately constant X-ray flux where the stars are relatively far from each other. The middle panel shows the phases 0.92 to 0.99, the pre-periastron phase corresponding to the increase in X-ray emission, and the bottom panel phases 0.995 to 1.025, the periastron phase corresponding to the X-ray minimum. These phase ranges are also shown with grey regions in Figure 5.3. Blue data points mark an analysis for the 2009 periastron passage, and the red markers the 2014 passage. An analysis for both passages combined is displayed in grey. The high energy component is stronger during the pre-periastron and the periastron phase. However, data from both passages is consistent within errors, and we can not confirm a change of the high energy component from passage to passage as in Balbo & Walter (2017). The different results are most likely caused by the few detected photons resulting in poor statistics at these energies. Given the statistical uncertainties, one can conclude that currently no clear signature of significant variations for different phases is found.

As mentioned previously, the exact origin of the γ-ray emission is still under debate. The high energy γ-ray component of η Carinae was always attributed to be due to the collision of accelerated protons and other hadronic species with the ambient stellar wind material. Farnier et al. (2011) proposed, that the γ rays below $10\,\mathrm{GeV}$ are produced by IC emission. Subsequently, it was noted by Bednarek & Pabich (2011) that the disparate properties of the winds from η Car A and η Car B will lead to different conditions at the shock created at the side towards each star. These differences lead to the acceleration of non-thermal electrons and protons with different maximum energies at each shock. Based on these considerations, Bednarek & Pabich (2011) developed two models to explain the γ-ray emission. The first one attributes the entire γ-ray emission to be produced by two populations of electrons from each shock, and the second one proposes that the low energy γ rays are produced by electrons and the high energy ones by hadrons.

Ohm et al. (2015) expanded the approach of Bednarek & Pabich (2011) and considered a more detailed dynamical model. They found that it is very likely that both γ-ray components are produced by hadronic processes at each side of the shock. However, another model in which the low energy γ-ray component was due to IC scattering was

later developed by Balbo & Walter (2017) using data from the hydro-dynamical simu-
lations of Parkin et al. (2011). Hamaguchi et al. (2018) argued that the non-thermal
X-ray component connects smoothly with the low energy γ-ray component. However,
with the newly detected turnover below $\sim$300 MeV (see Figures 5.4 and 5.5), a direct
connection without spectral breaks is excluded. The different temporal behaviour of the
X-rays and the γ rays make this scenario very unlikely too.

5.2   Physical considerations

Before the model for the non-thermal X-ray and γ-ray emission is described in detail
in Section 5.3, some general considerations about the shock properties and the particle
acceleration are presented in this section. The values of the wind velocities, mass loss
rates, stellar luminosities, surface magnetic fields and the orbital parameters allow rough
estimates about the conditions at the shock, such as acceleration and cooling time scales.
This has implications for the maximum achievable energies or possible particle escape.
Furthermore, the strong non-isotropic radiation fields from the stars require a non-
isotropic treatment of IC scattering and lead to significant absorption of the γ rays. All
these points are essential to correctly model the resulting γ-ray emission.

As in Bednarek & Pabich (2011), we assume that on each side of the contact disconti-
nuity, there is a shock corresponding to the stellar wind of η Car A and η Car B. To
ensure particle acceleration by diffusive shock acceleration in general, the shocks must be
collisionless. This is ensured by the assumed high surface magnetic fields, which lead to
Hall parameters of $\sim 10^5$ or higher (see also Eichler & Usov, 1993). Other requirements
necessary to allow diffusive shock acceleration are discussed below.

5.2.1   Acceleration and Hillas limits

$\boldsymbol{\eta}$ **Car A** Due to the high density and the lower velocity of the wind from η Car A, the
Alfvén Mach number of the shock is $M_{\mathrm{A}} < 10$ with a minimum close to periastron. The
relatively low Mach numbers make it difficult for the accelerated CRs to produce MHD
fluctuations, which can amplify the magnetic field in the upstream region of the shock.
Because only a fraction $\chi \ll 1$ of the CR pressure P_{CR} can be converted into magnetic
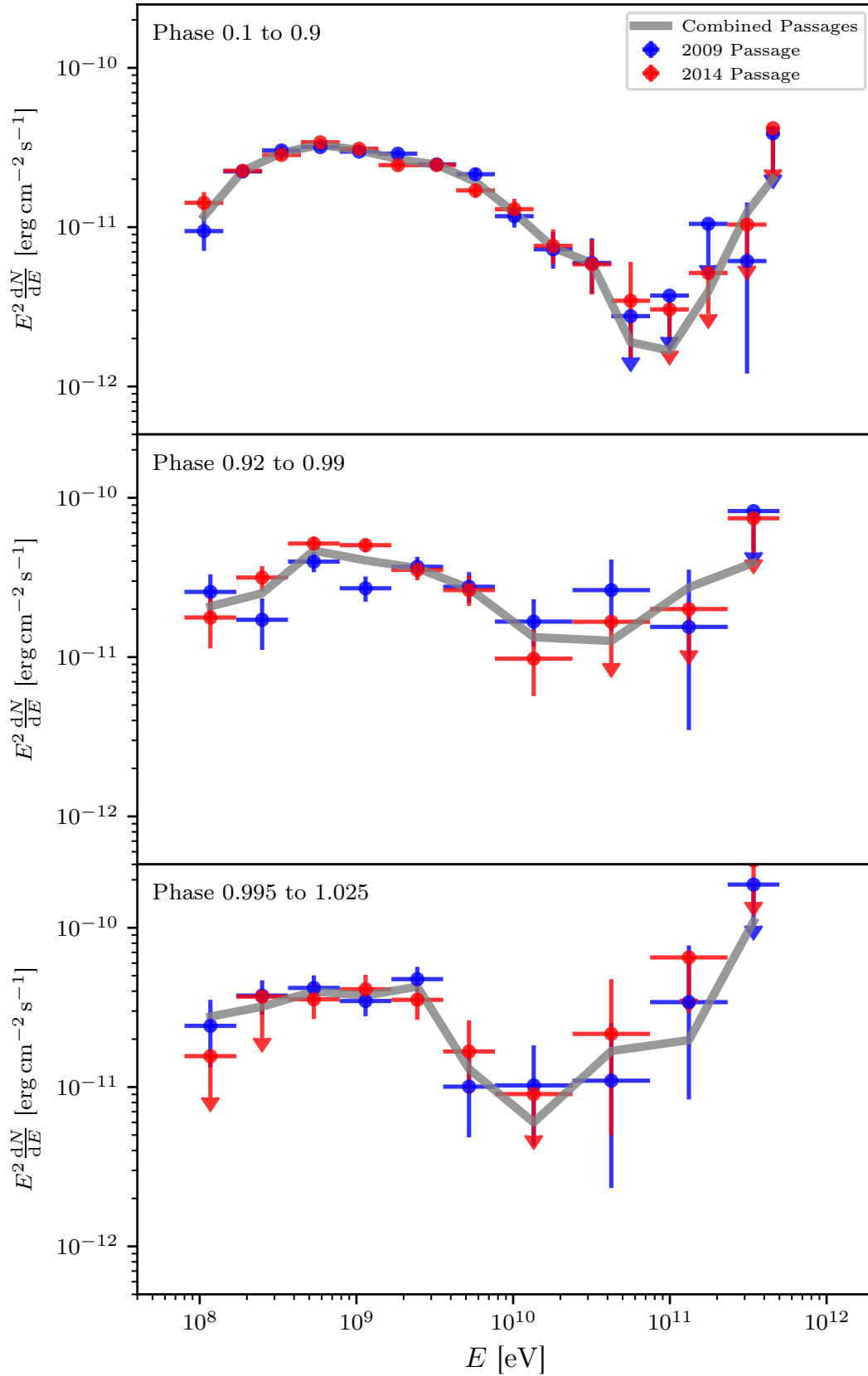fluctuations, one obtains the condition $\delta B^2/4\pi = \chi P_{\mathrm{CR}}$. Using the Alfvén Mach number

FIGURE 5.5: Spectral energy distributions from Fermi-LAT data for the 2009 passage (blue), the 2014 passage (red), and a combined analysis (grey). The top panel shows data from phases 0.1 to 0.9 (off-periastron), the middle panel for phases 0.92 to 0.99 (pre-periastron), and the bottom panel for phases 0.995 to 1.025 (periastron). Adapted version of Fig. A.2 from White et al. (2020).

$M_A = v_{sh}\sqrt{4\pi\rho}/B_0$, where B_0 is the original magnetic field and v_{sh} the shock velocity, one can rewrite the equation as

$$\frac{\delta B^2}{B_0^2} = \chi \left(\frac{P_{CR}}{\rho v_{sh}^2}\right) M_A^2 .$$ (5.1)

Bell (2004) obtained $\chi \approx v_{sh}/c$, which implies $\delta B \leq B_0$. Therefore, the self-induced magnetic fluctuations are not very significant. Assuming for simplicity a purely toroidal magnetic field, which implies $B \propto 1/r$ (see Equation 2.66) and results in stronger B fields at the shock compared to a radial or dipolar field, one obtains in the most optimistic case the Hillas limit

$$E_{Hillas} = 50 \left(\frac{B_\star}{100G}\right) \left(\frac{R_\star}{100R_\odot}\right) \left(\frac{\theta_A}{60°}\right) \left(\frac{v_{rot}}{0.1v_\infty}\right) \text{ TeV} .$$ (5.2)

The shock was assumed to have an extension of $L \approx r_{sh}\theta_A$. Although there will be no significant magnetic field amplification, efficient acceleration close to the Bohm limit might still be possible because the classical ion-cyclotron instability can grow sufficiently fast (Tademaru, 1969). Additionally to the Hillas limit given in Equation 5.2, energy losses can also limit the acceleration. As shown later, this is always the case for the acceleration at the shock on the side of η Car A for both electrons and protons.

η Car B Due to the fast wind and the lower mass-loss rate, the Alfvén Mach numbers for η Car B should be larger than the ones for η Car A. For rotation velocities of the star below 10% of the critical velocity, the magnetic field will be quasi-parallel at the shock ($<45°$) at all orbital phases and M_A increases with the distance to the star. Reasonable surface magnetic field values result in $M_A > 100$. With a terminal wind velocity of $v_\infty = 3 \times 10^3 \text{ km s}^{-1}$, one obtains $\chi \approx v_\infty/c \approx 0.01$. Therefore, according to Equation 5.1, magnetic field amplification should be taken into account. For a saturated magnetic field $P_{cr}/\rho v_{sh}^2 \approx 0.1$ (Bell, 2004), which gives a Hillas limit of $E_{Hillas} \approx 30 \text{ TeV}$. Since the statistics of the magnetic field play a crucial role too, this limit should be quite robust. Therefore, observations of the maximum γ-ray energies in η Carinae could provide insights into particle acceleration theories with self-generated MHD fluctuations. On the other hand, observations might also help to constrain the stellar parameters.

5.2.2 Electron heating and injection

Keeping in mind that the magnetic field direction and the Alfvén Mach number may vary along the orbit, the injection of electrons might be affected. For η Car A, M_A achieves a minimum near periastron. Additionally, the magnetic field is predominantly radial during periastron compared to larger distances at other orbital phases. These conditions could prevent electron injection into the acceleration process if the shock is not highly oblique. M_A could even become lower than the critical Mach number (Edmiston & Kennel, 1986), which can suppress the electron heating. This might be an alternative explanation for the observed minimum of the thermal X-ray emission at periastron.

In principle, electron acceleration could also be prevented around periastron at the side of η Car B, but the general conditions are different than for η Car A. The shock might also collapse onto the star during periastron (e.g. Parkin et al., 2011). Very weak surface magnetic fields are needed for this scenario. The detection of a significant high energy γ-ray component during periastron could rule out the collapse of the wind collision region onto the companion star, if protons indeed produce these high energy photons accelerated at the shock of η Car B as assumed in the modelling in Section 5.3. According to Eichler & Usov (1993), whistler waves propagating normal to the shock have to be well below the shock velocity for quasi-parallel shocks. This means, that $M_A \gg \sqrt{m_i/m_e}$, where m_i is the mass of the ions. A radial magnetic field $B \propto 1/r^2$ implies $M_A \propto r$. If the surface magnetic field is not very weak, this requirement might not be satisfied. To summarise the results, electron acceleration and heating might be suppressed at the shock on the side of η Car A at periastron, and even if the shock of η Car B does not collapse onto the stellar surface, the electron acceleration might still be inhibited.

5.2.3 Interactions of protons

The accelerated protons collide with the other particles and produce γ rays, neutrinos and electrons and positrons, mainly via the decay of neutral and charged pions. The newly created e^+ and e^- will produce IC emission and provide an additional contribution to the total emission. Because of the high-density wind, the cooling times for accelerated protons at the side of η Car A are only around ten days at the stagnation

point. The advection and diffusion time scales are significantly larger, and protons will lose their energy at essentially the same place they were accelerated. Therefore, the maximum achievable energy can be determined by equating the acceleration timescale $t_{\mathrm{acc}} \approx \eta_{\mathrm{acc}} r_{\mathrm{g}} c / v_{\mathrm{sh}}^2$ with the cooling time scale $t_{\mathrm{pp}} \approx (n_{\mathrm{gas}} \sigma_{\mathrm{pp}} c)^{-1}$. Here, η_{acc} is the acceleration efficiency parameter, r_{g} the gyroradius and n_{gas} the ambient density. This gives

$$E_{\mathrm{max}} \approx \frac{70}{\eta_{\mathrm{acc}}} \left(\frac{v_{\mathrm{sh}}}{10^3 \, \mathrm{km \, s}^{-1}} \right)^2 \left(\frac{B}{1 \, \mathrm{G}} \right) \left(\frac{r}{1 \, \mathrm{AU}} \right)^2 \, \mathrm{GeV} \; . \tag{5.3}$$

With a value of $\eta_{\mathrm{acc}} = 5$ and the orbital parameters being used in the modelling in Section 5.3, one obtains $E_{\mathrm{max}} < 230 \, \mathrm{GeV}$ at all phases, with a mean value of $\sim 150 \, \mathrm{GeV}$.

The situation is different at the shock on the side of η Car B because the cooling time scales are larger than the flow timescales. Hence, protons can be accelerated until they leave the shock cap, and the maximum possible energy could be, in the most optimal case, equal to the Hillas limit (see e.g. Achterberg, 2004). A fraction of the particles might escape the system and interact in regions far away from the shocks. This depends on the details of the transport mechanisms and how the wind material mixes at distances beyond the shock cap.

Additionally to hadronic collisions, the accelerated particles can also interact with the photon fields. However, the threshold energy of these processes for the radiation fields of the stars is above the expected maximum energies and can be neglected (see e.g. Schlickeiser, 2002). For interactions with the γ rays produced by the accelerated particles, the threshold is below the expected maximum particle energies. However, due to the low amount of available γ rays, the effects are negligible.

5.2.4 Electron cooling

On both sides of the shock, the cooling times for electrons are well below the time it would need to leave the acceleration region (see also Figure 2 in Ohm et al., 2015). This means that they will rapidly establish an equilibrium between injection and losses. Different cooling processes dominate at different energies. The lowest energies are dominated by ionisation and electronic excitation (Gould, 1975). Because the energy dependence of

these losses is weak, IC losses eventually dominate. Due to the Klein-Nishina suppression above $\sim$10 GeV, the highest energies are dominated by synchrotron losses. The transition from Coulomb-Ionisation losses to IC cooling will produce a break in the resulting electron spectrum. The position of the break depends on the thermal electron and the radiation energy density. Since both densities change $\propto r^{-2}$, the break energy is expected to not vary significantly along the orbit. Equating both energy loss time scales, one obtains

$$E_{\text{Break}} \approx 130 \left(\frac{\dot{M}}{\dot{M}_{\text{A}}} \right)^{\frac{1}{2}} \left(\frac{v_{\infty}}{v_{\infty,\text{A}}} \right)^{-\frac{1}{2}} \left(\frac{L}{L_{\text{A}}} \right)^{-\frac{1}{2}} \text{MeV}. \tag{5.4}$$

The index 'A' refers to the mass-loss rate, terminal wind velocity and luminosity of η Car A. The break energy for η Car A is 130 MeV, and for η Car B 30 MeV. Considering the parameters used for the modelling in Section 5.3, taking into account the radiation fields from both stars and averaging over different phases leads to the more accurate, lower values of 110 MeV (η Car A) and 15 MeV (η Car B). These energies are below the Fermi-LAT energies and above the non-thermal X-rays detected by NuSTAR, even for a different reasonable choice of parameters.

5.2.5 Anisotropic IC scattering

The photon fields from the stars are not distributed isotropically but are highly anisotropic. In such a case, the resulting IC spectrum can not be calculated anymore with Equation 2.11. Because the accelerated particles move much faster than the bulk plasma flow and are scattered around, they can still be assumed to be isotropic. In this case, the γ-ray production rate can be calculated according to Aharonian & Atoyan (1981) with

$$\frac{\mathrm{d}n_{\gamma}(\theta, E)}{\mathrm{d}E\mathrm{d}\Omega} = n_{\text{rad}}(E_{\text{rad}}, \theta)n_{\text{e}}(E_{\text{e}})\frac{r_0^2 m_{\text{e}}^2 c^5}{2E_{\text{rad}}E_{\text{e}}^2} \left[1 + \frac{z^2}{2(1-z)} - \frac{2z}{b_{\theta}(1-z)} + \frac{2z^2}{b_{\theta}^2(1-z)^2} \right],$$

$$\tag{5.5}$$

$$\text{with} \qquad b_{\theta} = 2(1 - \cos(\theta))E_{\text{rad}}E_{\text{e}} \qquad \text{and} \qquad z = E/E_{\text{e}}.$$

$$\tag{5.6}$$

The energy E of the resulting photon changes between

$$E_\mathrm{rad} \ll E \leq \frac{b_\theta}{1 + b_\theta} E_\mathrm{e}. \tag{5.7}$$

This approximation has an accuracy of at least $10\,\%$ in the worst case, and in most cases at least $3\,\%$. E_e is the energy of the electron, E_rad the energy of the photon before scattering, r_0 the classical electron radius, and θ the angle between incoming and outgoing photon. For an angular profile of the photon field, Equation 5.5 has to be integrated over the respective scattering angles between the direction of the observer and the photon field. For a distribution of photons and electrons, an integration over E_e and E_rad is required as well. The anisotropic IC scattering according to Equation 5.5 was implemented into the GAMERA code.

The impact on the resulting emission can be severe considering only one specific place at the shock cap and the radiation field from only one of the stars. Nevertheless, for the total IC emission, an integration over the whole shock cap and considering the radiation fields from both starts reduces the anisotropy effects. Furthermore, the only energy range where electrons dominate the emission and data is available additionally is the range from 30 to 50 keV, where NuSTAR data of the non-thermal component is available. In this energy range, the maximum anisotropy impact is less than $30\,\%$. Averaging over different phases (as we do later for comparison with data) reduces the differences with respect to the case of isotropic IC scattering further.

5.2.6 $\gamma\gamma$ absorption and pair production

The γ rays interact with the strong stellar radiation fields and produce electron-positron pairs. Due to the high temperatures of $2.58 \times 10^4\,\mathrm{K}$ (η Car A) and $3 \times 10^4\,\mathrm{K}$ (η Car B), this process is possible above a threshold energy of $\sim$30 GeV. Therefore, only parts of the high energy γ-ray component are affected. The pair-produced e^- and e^+ will subsequently radiate and might generate a measurable additional contribution to the total γ-ray spectrum at lower energies (see e.g. Dubus, 2006; Bosch-Ramon & Khangulyan, 2009). The amount of additional radiation depends on the fluxes emitted above 30 GeV and the orbital phase. The maximum flux is produced between 5 and 10 GeV and for most phases, the additional contribution is less than $1\,\%$. Around periastron, the stars are closer and the emission region gets smaller, which leads to a maximal enhancement

of $\sim 10\,\%$. Thus, the pair production is only treated as an absorption process, and the IC emission from the secondary particles is neglected in the modelling described in Section 5.3.

5.3 Phase-dependent model

The model to explain the non-thermal emission in the X-ray and γ-ray regime is based on Ohm et al. (2015). Some additions and refinements were made to the code used in Ohm et al. (2015), and the model parameters were adjusted to match the newly analysed Fermi-LAT data and the X-ray data from Hamaguchi et al. (2018). The parameters used in the final model are listed in Table 5.1. The eccentricity of the system was fixed to 0.9. Together with the stellar masses and the orbital period, the location of each star at all phases is determined. The acceleration efficiency η_{acc} and the wind power going into accelerated protons (P_{p}) and electrons (P_{e}) were changed to match the data. When all other parameters are fixed, η_{acc}, P_{p} and P_{e} are constrained by the resulting spectral shape and the flux normalisation. Hence, all results are valid within the accuracy of the fixed stellar parameters. Except for the surface magnetic field, the true stellar properties are not expected to be significantly different from the ones listed in Table 5.1. Since the acceleration time depends on both, η_{acc} and $B_\star$, a different $B_\star$ can be compensated to some degree by adapting η_{acc}. The shape of the electron spectrum at the highest energies might be affected, but this has no important effect on the resulting total γ-ray spectrum because the hadronic component dominates at these energies.

5.3.1 Model description

In our model, the particle acceleration region is the shock cap. The contact discontinuity is the place where the ram pressures of the oppositely directed winds are equal, which determines its shape (Canto et al., 1996; Pittard & Dawson, 2018). On both sides of the contact discontinuity between the stellar winds, shocks form and particles are accelerated via diffusive shock acceleration. As in Ohm et al. (2015), the shock cap is approximated two-dimensionally with radial and azimuthal bins. The stellar winds are assumed to be spherically symmetric and at their terminal velocity when reaching the shock cap. However, around periastron, when the stars are closest to each other, the

Parameter	η Car A	η Car B
$R_\star$ [R$_\odot$]	100	20
$T_\star$ [K]	2.58×10^4	3×10^4
$L_\star$ [10^6 L$_\odot$]	4	0.3
$\dot{M}$ [M$_\odot$/yr]	4.8×10^{-4}	1.4×10^{-5}
v_∞ [km s^{-1}]	5×10^2	3×10^3
$B_\star$ [G]	100	100
v_{rot} [v_∞]	0.15	0.15
η_{acc}	15	5
P_{p} [P_{wind}]	10 %	9 %
$P_{\mathrm{e}}/P_{\mathrm{p}}$	3 %	3 %

TABLE 5.1: Parameters used for the modelling. The value of $R_\star$ was taken from Table 1 and $T_\star$, $L_\star$, $\dot{M}$, and v_∞ from Table 4 in Parkin et al. (2009) (see references therein). The other parameters were adopted for the model. $B_\star$ is the surface magnetic field, v_{rot} the surface rotation velocity, P_{p} the fraction of wind power going into the acceleration of protons and P_{e} the fraction of wind power going into electrons above 1 GeV. Table 1 in White et al. (2020).

latter simplification can become inaccurate. Assuming a velocity profile from Castor et al. (1975),

$$v(r) = v_\infty \left(1 - \frac{R}{r}\right)^\beta,$$

for $\beta = 1$, the shock velocity on the side of η Car A is 40 % lower than v_∞, and 18 % lower for η Car B. The acceleration is modelled to take place at a speed corresponding to acceleration with Bohm diffusion scaled with the factor η_{acc}. A change in η_{acc} could compensate for a reduction of the shock velocity at periastron, but both were assumed to be constant for simplicity.

Whereas on the side of η Car A, no significant magnetic field amplification is expected, these effects have to be taken into account on the side of η Car B. If the acceleration efficiency is constant, δB^2 is proportional to ρ (Equation 5.1). Therefore, the amplification behaves in the same way as a wind with a toroidal magnetic field and the amplification is accounted for by using a large stellar rotation velocity.

As discussed previously, the cooling times for electrons on both sides of the shock are well below the flow times. Thus, the electron spectrum is calculated as an equilibrium spectrum between injection and losses in each bin for η Car A and η Car B. The subsequent

non-thermal emission is calculated using the equilibrium electron spectrum.

At the side of η Car A, the cooling times for protons are below the flow time too. Therefore, the resulting proton spectrum is again a steady-state spectrum. Additionally to the γ rays directly produced by π^0 decay, the production of secondary electrons and positrons is taken as an additional injection of leptonic particles. The γ-ray spectra of these particles are calculated by assuming equilibrium between injection and local energy losses, as for the primary electrons.

The situation for protons is different at the shock associated with η Car B because the flow times are lower than the cooling times. Thus, acceleration will take place until the particles leave the acceleration region. The particles are tracked while advecting outwards to take the non-uniform acceleration conditions into account. The details of the acceleration process are dealt with as in Ohm et al. (2015). When the particles leave the shock cap, the plasma flows outwards ballistically, and the material of the shocks from both winds mixes with each other. The mixing length of the plasma outflow is motivated by hydrodynamic simulations of Parkin et al. (2011) and is taken to be one shock cap radius. The shock cap radius is defined as the distance between the apex of the shock cap and the point where the ballistic region starts. The protons produce γ rays by interactions with the material in the shock cap and the ballistic region. The production of secondary electrons and positrons is calculated in both of these regions. They are assumed to cool in their production environment, and the equilibrium γ-ray spectra are calculated. The production of secondary particles in the ballistic region is an improvement with respect to the model in Ohm et al. (2015).

The $\gamma\gamma$ absorption is calculated with the simplifying assumption that the emission from each star is pointlike, which simplifies the numerical calculations. Unfortunately, this approximation is not valid close to periastron. However, the differences are not significant because both stars are located in opposite directions of the shock cap, and the emission region itself is extended. Additionally, the absorption becomes significant only above energies of several tens of GeV, where the statistics of the Fermi-LAT data is poor. Finally, the emission from the produced e^+-e^- pairs is assumed to be negligible too.

In each shock cap bin (i, j), where i is the azimuthal and j the radial index, a fraction ϵ of the available kinetic wind power is transferred to the derived CR power $P_{\mathrm{CR},(i,j)} =$

$\epsilon P_{\mathrm{wind},(i,j)}$. The available wind power varies along the shock cap,

$$P_{\mathrm{wind},(i,j)} = \frac{\dot{M}v_\infty^2}{2}\left(\frac{v_{n_{(i,j)}}}{v_\infty}\right)^2 \frac{\Delta\Omega_{(i,j)}}{4\pi} \ , \tag{5.8}$$

where $v_{n_{(i,j)}}$ is the wind velocity component normal to the shock and $\Delta\Omega_{(i,j)}$ the solid angle area of the respective bin. η is a free parameter of the model. If particles are accelerated and cool in situ, the power going into these specific CRs is directly set by Equation 5.8. In the case of the protons on the side of η Car B, the CRs travel through different bins and can catch up each time part of the wind power until they enter the ballistic region.

In Ohm et al. (2015), the particle acceleration was turned off in the inner $80\,\%$ of the shock cap during periastron. This was motivated by assuming that the wind collision region collapses onto the surface of η Car B. Here, a different behaviour is simulated, namely that the heating and injection of electrons is suppressed for phases between 0.995 and 1.025. This phase range corresponds to the X-ray minimum. Because the primary electrons are assumed to cool in-situ, only γ rays from hadronic collisions and secondary particles account for the emission during this phase range. The motivation for this behaviour comes from the consideration in Section 5.2. The high energy γ-ray component is not significantly reduced during the periastron phase range. Since the proton cooling times are lower than this timeframe, complete disappearance of the shock is not possible if the high energy component stems from hadrons associated with the shock of η Car B.

5.3.2 Results

Figure 5.6 shows the model results compared to the data integrated over the off-periastron phase (phases 0.1 to 0.9, top panel), the pre-periastron phase (phases 0.92 to 0.99, middle panel), and the periastron phase (phases 0.995 to 1.025, bottom panel). The black circles show the Fermi-LAT data analysed for the total data set, including the 2009 and the 2014 passages. Non-thermal X-ray data from Hamaguchi et al. (2018) is represented with the blue triangles. Given that there are several X-ray data points in each phase range, all the data within the respective phase range are shown. The solid black line represents the model's total γ-ray emission, and the dashed black line is the emission

without absorption. The individual contributions from protons (magenta), primary electrons (cyan) and secondary electrons (yellow) from the side of each star are depicted as well. The upper panel for the off-periastron phase also shows the upper limits derived from H.E.S.S. observations (Abramowski et al., 2012), which are consistent with the model predictions.

The Fermi-LAT data is matched well for all three phases. The following parameters were adapted to reproduce the observed spectral shape and the flux levels: $\eta_{\mathrm{acc}} = 15$ for η Car A and $\eta_{\mathrm{acc}} = 5$ for η Car B, while $10\,\%$ (η Car A) and $9\,\%$ (η Car B) of the available wind power is transferred into accelerated protons above $1\,\mathrm{GeV}$. The emission from primary electrons is insignificant in the Fermi-LAT energy range. However, it is determined by the non-thermal NuSTAR data in the off-periastron and pre-periastron phases. The ratio between the wind power going into primary electrons and the wind power going into protons is $3\,\%$ for both sides of the shock cap.

The low energy γ rays are dominated by emission from protons of η Car A and the higher energies by protons from η Car B. In the X-ray regime, the main part of the non-thermal emission is produced by electrons accelerated at the side of η Car B. This is the case even if P_{e} at the primary side would be increased by one order of magnitude. Consequently, $P_{\mathrm{e}}/P_{\mathrm{p}}$ for η Car A is only poorly constrained by the data and was taken to be the same as on the companion side. During the periastron phase, it was assumed that the electron acceleration is halted. Therefore, the only contributors to the X-ray emission in the lower panel of Figure 5.6 are the secondary electrons produced in hadronic collisions. As can be seen, their flux level can account for the residual emission measured by NuSTAR and thus provides a natural explanation for the different behaviour of the non-thermal X-ray component during the X-ray minimum compared to the thermal X-rays at lower energies. The contribution from secondary electrons from the side of the primary star is more significant than the one from the companion side, although the differences are smaller than for the directly accelerated electrons.

The transition from ionisation or excitation losses to IC losses as the dominant cooling mechanism produces the spectral breaks observed in all IC emission curves at low energies. Since the densities are higher at the side of η Car A, the break is at higher energies compared to η Car B in the case of the directly accelerated electrons. Differences in the break position are less pronounced for the secondary electrons because a large part of

the secondary IC emission from η Car B is produced in the ballistic region, where the material from both winds mixes.

Comparing the top panel of Figure 5.6 with the bottom panel, one can observe that the flux level of the hadronic emission from η Car A does not vary much, but for η Car B, it increases notably towards periastron. This occurs because a large fraction of the accelerated protons escapes on the side of η Car B. During periastron, the densities increase, and a larger amount of particles interact. At the side of η Car A, the protons are assumed to cool in-situ. Therefore, the total emission depends only on the variation of the total power transferred to accelerated protons. The solid angle of the shock cap does not vary significantly, and a similar amount of wind power is available for particle acceleration at all phases.

As mentioned before, the emission from directly accelerated electrons from η Car A is small compared to η Car B. Additionally, the ratio between hadronic γ-ray emission and the emission from directly accelerated electrons is larger for η Car A than for η Car B. One reason for the lower emission from the η Car A electrons is that approximately 1/4 of the wind power compared to η Car B is available (see Ohm et al., 2015). Additionally, some of the protons from η Car B can escape, whereas the electrons do not and lose all their energy in the shock cap. Both factors combined explain the observed behaviour.

Above energies of $\sim 100\,\mathrm{GeV}$, absorption of the γ-ray by the powerful radiation fields of the stars becomes significant. At periastron, the stars are close to each other, and consequently, the radiation fields get stronger and the emission region smaller. Therefore, the maximum absorption occurs during this phase range. The absorbed radiation stems nearly exclusively from protons accelerated by η Car B. Since a large fraction of them interacts in the ballistic region, a different mixing length would affect the amount of absorption, especially during periastron passages.

Finally, we note that even though the shock velocities and the acceleration parameters were not adjusted during periastron, the flux levels are described well. This can either be explained if both parameters do not vary significantly or if the variation in one of the parameters counterbalances the effects of the other one.
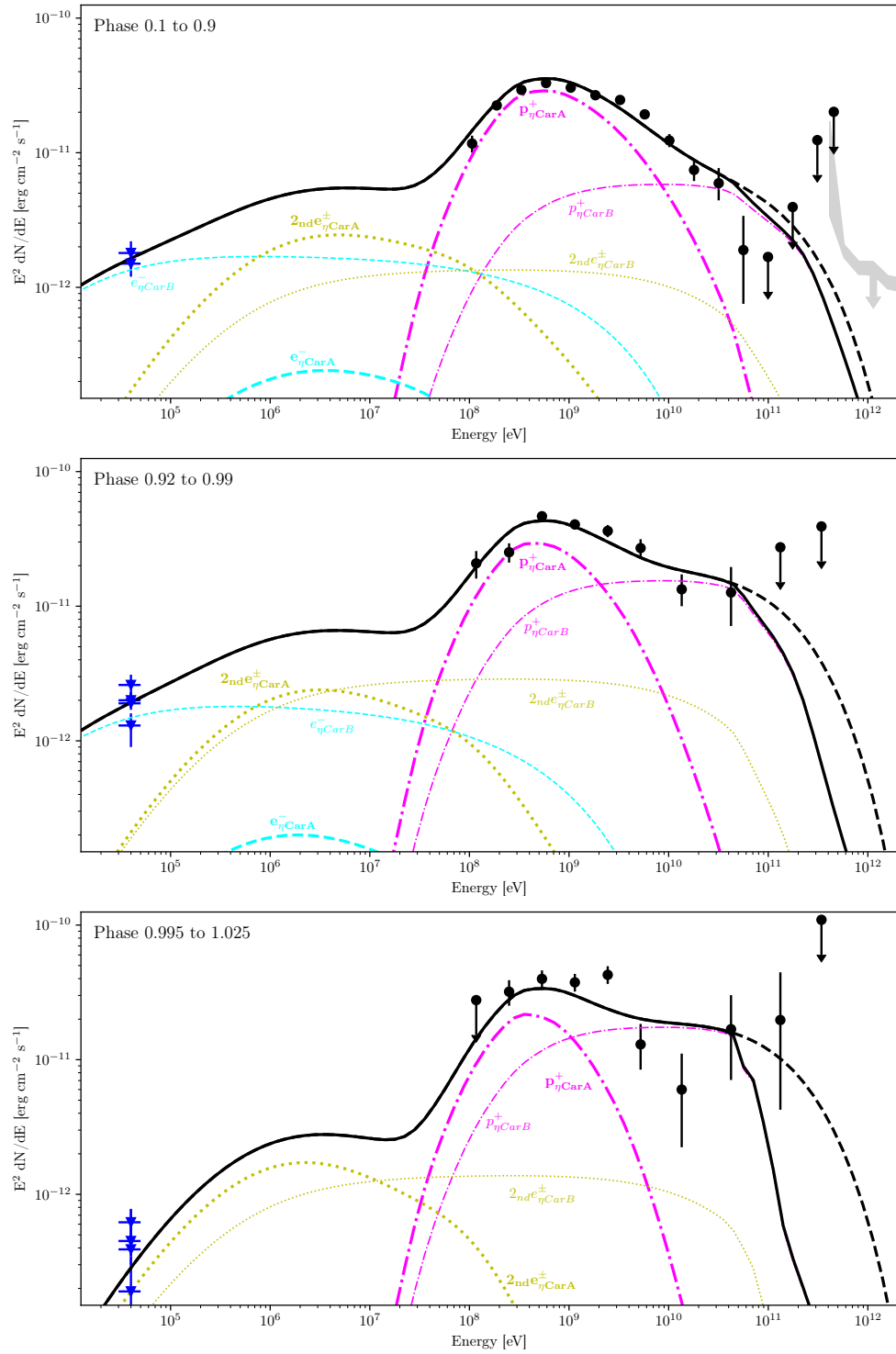
FIGURE 5.6: Data from different phase ranges compared to the model. The top panel shows the off-periastron, the middle panel the pre-periastron, and the bottom panel the periastron phase. γ-ray data from Fermi-LAT is shown with black circles and X-ray data from NuSTAR (Hamaguchi et al., 2018) with blue triangles. The grey shaded region in the top panel represents the upper limit from H.E.S.S. (Abramowski et al., 2012). The total model prediction is shown with the black curve, and the dashed black curve is the emission without absorption. The coloured lines show the individual contributions to the total model curve from η Car A (bold) and η Car B (thin) of protons (magenta), primary electrons (cyan), and secondary electrons (yellow).

5.4 Emission on larger scales

While the model presented in Section 5.3 can describe the data well, the situation might be more complex. In the model, part of the protons accelerated at the shock of η Car B escape from the system. There are several regions around η Carinae where they potentially could interact. These regions and their respective distances and spatial extent are displayed in Figure 5.7.

In the shock cap region, the spatial extent varies with phase, but on average, it operates on distances between 1 and 20 AU from the stars. The shock cap is embedded into a region we call the wind region. The latter is dominated by the winds of the stars, and the densities are well below the densities in the shock cap. However, numerical simulations revealed that there might be some higher density patches created by the interaction between the winds and the stars orbiting around each other (Parkin et al., 2011; Clementel et al., 2014). Depending on the details of the CR transport, the particles might, for most of their time, be trapped in low-density regions, in which case no significant emission is expected. On the other hand, if the particles enter high-density regions and stay within them for a significant time, a non-negligible amount of radiation might be released.

The wind region is bounded by the so-called Little Homunculus Nebula (see the third picture from the left in Figure 5.7). It is located inside the Homunculus Nebula and has a bipolar structure like the Homunculus. Its mass is estimated to be $0.1\,M_\odot$ (Smith, 2005). Likely, the Little Homunculus was ejected during the second eruption in 1890 and since then was accelerated by the stellar winds to its current speed of $\sim$250 km s^{-1}. The Little Homunculus mainly consists of a thin shell with a thickness of probably $\sim$1 AU. Due to the bipolar structure, the distance towards the stars range between 2×10^3 AU and 6.5×10^3 AU, deduced from figures in Smith (2005).

At larger distances than the little Homunculus, there is the Homunculus Nebula. It consists of two shells, a thin outer shell, where most of the mass is located, and a thicker, warmer inner shell. The total mass is larger than $10\,M_\odot$ (Smith, 2006), and most likely between $15\,M_\odot$ and $35\,M_\odot$ (Smith & Ferland, 2007). Thus, the thin shell contains far more mass than the Little Homunculus or the wind region. If the escaping protons reside long enough in the high-density shell, a significant amount of γ rays might be produced. However, the thickness is only $\sim$600 AU (Smith, 2006) and the particles
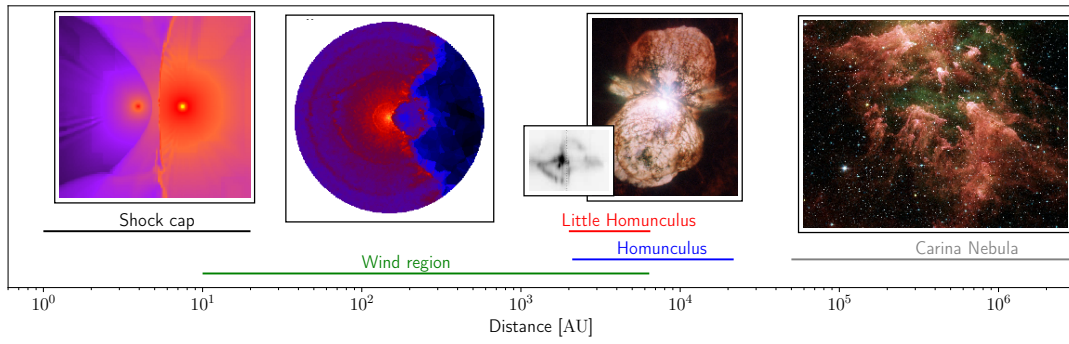
FIGURE 5.7: Possible emission regions and their sizes compared with each other and plotted logarightmically. The size ranges are: 1 to 20 AU (shock cap), 10 to 6.4×10^3 AU (wind region), 2×10^3 to 6.5×10^3 AU (little Homunculus), 2.1×10^3 to 21.69×10^3 AU (Homunculus) and $>50 \times 10^3$ AU (Carina Nebula). Credits for the individual pictures: Parkin et al. (2011), Clementel et al. (2014), Smith (2005), HST, SST.

might pass the shell too quickly. The distance to the stars ranges from 2.1×10^3 to 21.69×10^3 AU.

Lastly, η Carinae and the Homunculus are located in the Carina Nebula, which contains many molecular clouds. These clouds are potential interaction places of the escaped particles from η Carinae. At such large distances, the Fermi-LAT telescope might even be able to resolve emission from individual clouds. However, other hidden particle accelerators could also contribute to the potential γ-ray production in these clouds.

Any emission on larger scales is not expected to show significant signs of orbital variations. This is caused by the extent and shape of the different regions, but would also be affected by the details of particle transport, especially in the wind region. Different effects can happen if particles need a significant amount of time to enter a high-density patch, where a significant amount of radiation is released. In that case, orbital variations could even be shifted in phase. However, a steady background flux in the γ-ray regime from any unresolved region is easily feasible. It is also consistent with the data if a lower amount of γ rays is emitted on scales of the model from Section 5.3.

5.4.1 Emission from the wind region and the detection of η Carinae by H.E.S.S.

In 2020, after the publication of White et al. (2020), the H.E.S.S. collaboration reported a detection of η Carinae at energies above the Fermi-LAT range (H. E. S. S. Collaboration

et al., 2020). The source was observed from phase 0.78 to phase 1.10 at different days. Two different datasets were analysed, the first one containing the data from phase 0.78 to 0.96, and the second one from phase 0.96 to phase 1.10. These phase ranges correspond approximately to the pre-periastron and periastron phases used to analyse the Fermi-LAT data shown in Figure 5.6.

Figure 5.8 compares the H.E.S.S. data for the phase ranges mentioned above with the model for the same phases. The upper panel shows the phases from 0.78 to 0.96 and the lower panel from to 0.96 to 1.10. The blue points are the data from H.E.S.S., and the blue shaded region is the combined statistical and systematic error band. The model is shown in the same colours as in Figure 5.6, but the individual contributions from electrons are not shown for simplicity. As a comparison, we also show the Fermi-LAT data from the previous analysis for the phase ranges 0.92 to 0.99 (pre-periastron) and 0.995 to 1.025 (periastron). Although the Fermi-LAT phase range is slightly different, the model matches the data well.

While the unabsorbed model is consistent with the H.E.S.S. error bands, the absorbed model is not. The consistency of the dashed black line in the upper panel is improved, if instead of the phase range 0.78 to 0.96, the range 0.92 to 0.99 from Figure 5.6 is compared to the data. Given that four of the five observations for the H.E.S.S. data in the upper panel are from phase 0.89 to 0.96, this can be considered to be not a bad comparison. However, the absorption would be even stronger in that case.

The strong absorption by the radiation fields during periastron prevents fluxes from being observed at these energies. Therefore, the γ rays have to be produced further out in the system. It could also be that the shock cap is larger than assumed in the model. A detailed analysis of the absorption was performed to investigate the required distances. The anisotropy and the angular size of the stars were taken into account. It was found that at distances of $\sim$50 AU, the absorption during periastron is sufficiently low. The observations from H.E.S.S. indicate that the wind region around η Carinae could be a potential source of γ rays. If the H.E.S.S. γ-ray fluxes are steady, they could in principle be produced in, for example, the Homunculus Nebula.

The errors of the emission detected by H.E.S.S. are large. This is linked to the strong night sky background in this sky region, which makes extracting data exclusively from η Carinae very challenging. Therefore, the H.E.S.S. results might be less restrictive than
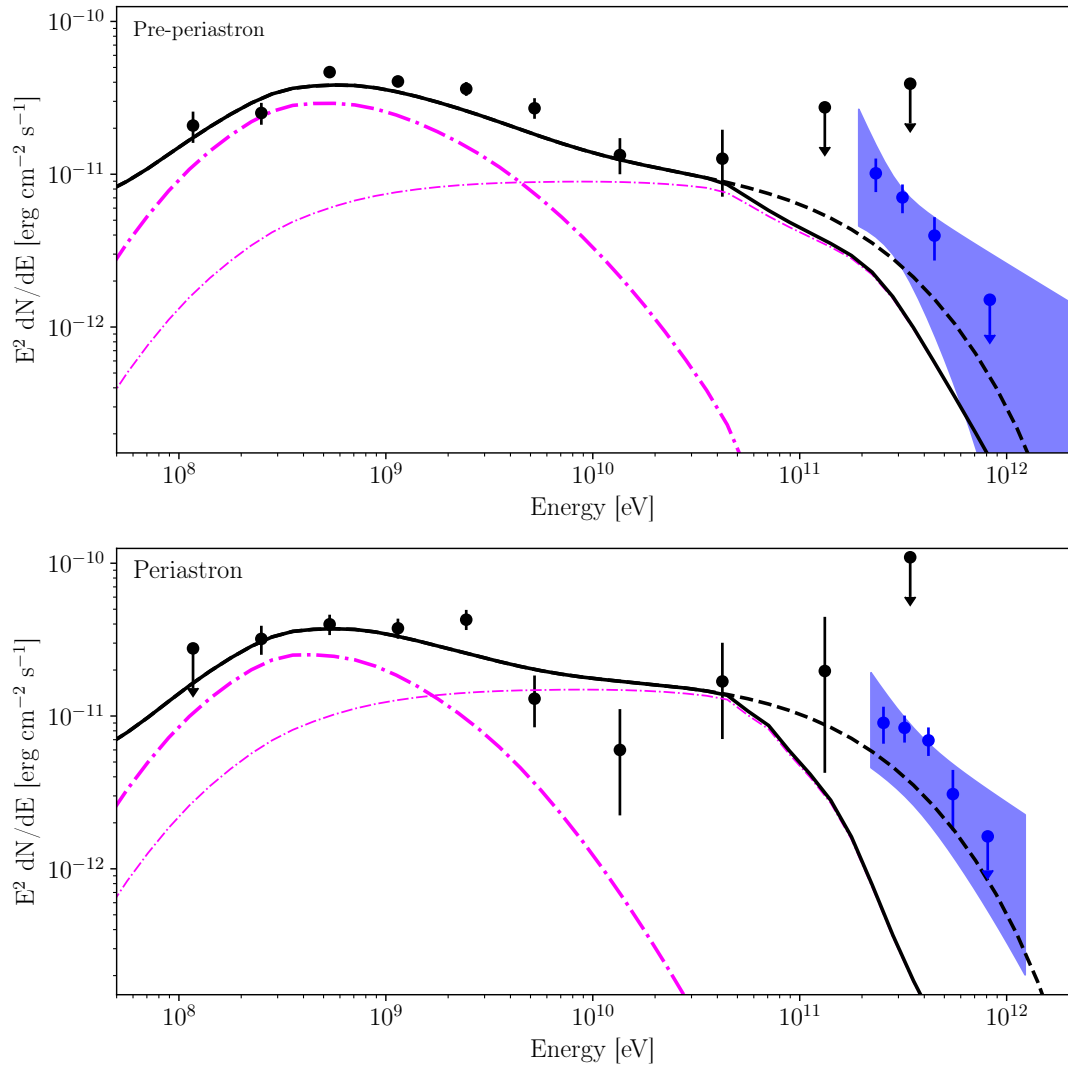
FIGURE 5.8: Model for the phase ranges 0.78 to 0.96 (pre-periastron) and 0.96 to 1.10 (periastron) together with the corresponding H.E.S.S. data in blue. The blue shaded region shows the combined systematic and statistical H.E.S.S. error band. The black points represent the Fermi-LAT data as shown in Figure 5.6 for the phases 0.92 to 0.99 (pre-periastron) and 0.995 to 1.025 (periastron). The total emission predicted by the model is shown with the solid black line, and the corresponding dashed line is the emission without absorption. The magenta lines are the hadronic emission from η Car A (thick line) and η Car B (thin line). For simplicity, the components from electrons are not shown. Although the Fermi-LAT phase range is slightly different, the model matches the data well.

they appear to be. More and better data are crucial to constrain models about the particle acceleration in η Carinae, and the future CTA observatory will be tremendously beneficial in this regard.

5.4.2 Escaped protons in the Homunculus

Knowing that the Homunculus Nebula is the most massive nearby region where the escaped protons from η Carinae can interact, we will constrain the possible contribution to the γ-ray emission by interactions of these protons in the nebula. To do so, it is assumed that the escaping protons do not suffer significant losses until they reach the Homunculus, and that the spectral shape is unchanged. The Homunculus is modelled as a shell with a diameter of 600 AU and a density of $10^7\,\mathrm{cm}^{-3}$ (Smith, 2006). Using the flux of escaping protons from the model in Section 5.3, a lower limit on the emission can be obtained, assuming that the CRs do not get trapped in the Homunculus but simply pass through.

However, magnetic fields in the Homunculus could lead to diffusion through the nebula. Aitken et al. (1995) estimated the magnetic field in the Homunculus to be at least of the order of µG. If dust grains are directly aligned by the field, Aitken et al. (1995) concluded that the field has to be >100 µG. While such high magnetic fields might be unlikely, it is possible that the B-field is significantly enhanced compared to the ISM. Field strengths of several tens of µG might be easily feasible. The diffusion in the Homunculus is assumed to follow the following energy dependence:

$$D(E) = D_0 \left(\frac{E}{1\,\mathrm{GeV}} \right)^{\delta}. \tag{5.9}$$

For $D_0 = 1.25 \times 10^{23}\,\mathrm{cm}^2\,\mathrm{s}^{-1}$, approximately all protons at 1 GeV will interact leading to the maximum possible emission in the hundreds of MeV to several GeV range. The value of D_0 is below the ISM diffusion coefficient, but above the Bohm diffusion coefficient at 1 GeV in a 10 µG field of $3.3 \times 10^{21}\,\mathrm{cm}^2\,\mathrm{s}^{-1}$. The amount of particles interacting at higher energies depends on the slope δ determining the energy dependence of $D(E)$. Given that higher energy particles diffuse faster, the resulting γ-ray spectrum from the Homunculus is expected to soften with respect to emission created by the original particle spectrum. However, if D_0 is smaller, there will be a certain energy until which

all particles from the original spectrum interact. Only above this energy, the influence of the energy-dependent diffusion will influence the shape of the γ rays.

Figure 5.9 shows the case of the particles passing through the nebula without diffusion (blue) compared to the case of $D_0 = 1.25 \times 10^{23}\,\mathrm{cm^2\,s^{-1}}$ (red). In the latter case, δ was chosen to be 0.4, a value between Kreichnan and Kolmogorov diffusion. Since the spatial extension of the Homunculus will mask any effect of orbital variations, an estimation of the average escaping particle spectrum was used. The Fermi-LAT data for phases 0.1 to 0.9 is also shown in Figure 5.9. If the particles pass quickly through the Homunculus, only a negligible amount of radiation is produced (see blue curve). However, if the particles are trapped longer, significant γ-ray fluxes are possible. At $100\,\mathrm{GeV}$, the Fermi-LAT data could be explained exclusively by particles interacting in the Homunculus. At GeV energies, where the flux level corresponds to the maximum possible emission from the Homunculus, the emission is below the data. Nevertheless, a large fraction of the detected emission could originate from the nebula. In this case, the model from Section 5.3 would have to be adopted to not overshoot the data. Because variations in the detected γ-ray spectra during periastron are not as strong as in the X-ray regime, a large amount of steady emission from the Homunculus is possible.

Knowing that the non-thermal X-ray emission is dominated by electrons accelerated at the side of η Car B, one could explain the total emission solely by particle acceleration at the shock of η Car B. In this scenario, the escaped protons interacting in the Homunculus Nebula account for most of the low energy γ-ray emission below $\sim 10\,\mathrm{GeV}$. To investigate such a scenario, all emission from the primary side was neglected. To account for emission in the Homunculus, D_0 was again set to $1.25 \times 10^{23}\,\mathrm{cm^2\,s^{-1}}$. To be able to reach the required flux levels, the number of escaping protons from the side of η Car B was increased by a factor of 2.84, δ was set to 0.8. This was necessary to avoid the overproduction of the γ-ray fluxes at high energies.

The results for the off-periastron, the pre-periastron and the periastron phase are displayed in Figure 5.10. The blue line shows the emission from hadronic interactions in the Homunculus. Similarly to Figure 5.6, the black curve represent the total emission, including the Homunculus. It was again assumed, that electron acceleration during periastron is switched off. The Fermi-LAT data is reasonably well matched for the pre-periastron and the periastron phase. However, in the upper panel, the emission from
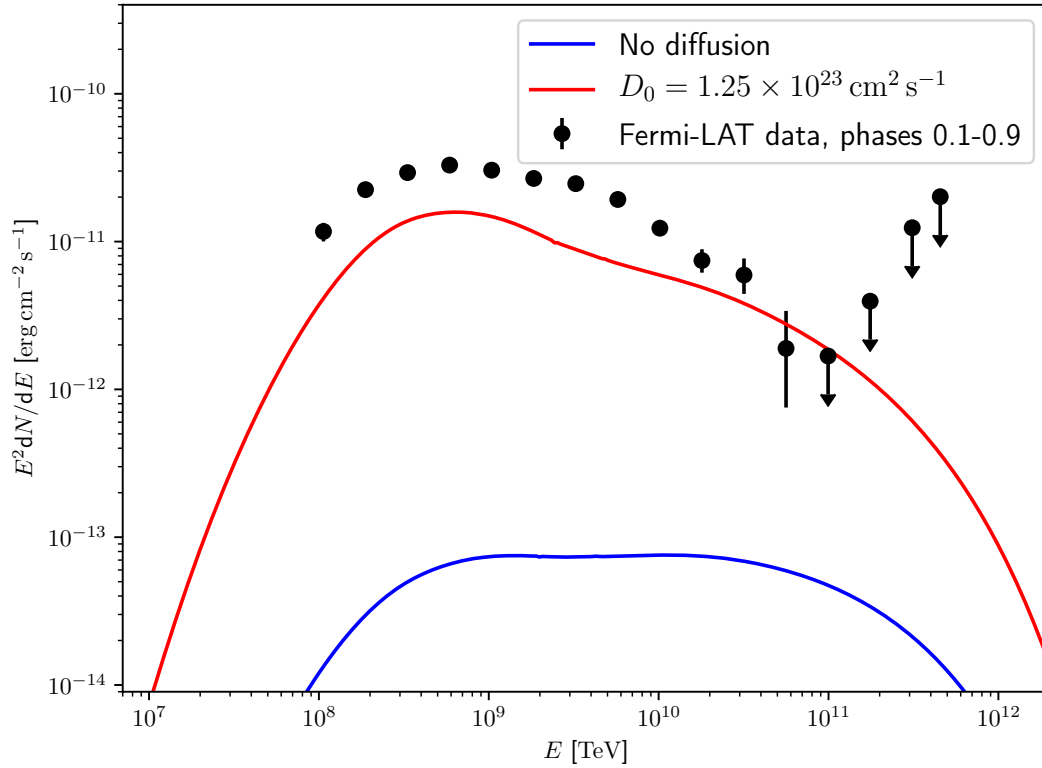
FIGURE 5.9: Emission from the Homunculus Nebula from escaped protons. Black points show the Fermi-LAT data fo the off-periastron phase range from 0.1 to 0.9.

the model underestimates the data between $\sim 1\,\text{GeV}$ and $10\,\text{GeV}$ slightly. A different behaviour of diffusion in the Homunculus could improve this issue. If the diffusion coefficient increases, the protons until higher energies will lose all their energy in the Homunculus, which will harden the spectrum. The emission above $\sim 10\,\text{TeV}$ might be overproduced, but this could be compensated, if the protons above a certain energy are rather passing through the thin Homunculus shell than diffusing.

At periastron, the secondary electrons from η Car B can not alone produce the required flux level of the non-thermal X-ray emission. However, sufficient non-thermal X-rays can be produced, if the acceleration of electrons is not entirely stopped, but merely hindered. Therefore, a smaller amount of electrons is available to ensure consistency with the X-ray data. It has to be noted, that a possible contribution from secondary electrons produced in the Homunculus was neglected. Their emission could potentially account for the fluxes needed at periastron, but a detailed investigation is left for future research. One can conclude, that models for the non-thermal emission of η Carinae only considering particle acceleration at the shock of η Car B are viable and can provide an

alternative scenario.

5.5   Discussion

η Carinae is a very complex system. Non-thermal emission is observed in X-rays and γ rays. The non-thermal X-ray emission increases towards periastron, followed by a sudden drop with some residual emission left. Afterwards, the emission increases to the average level maintained for most of the orbital phases (Hamaguchi et al., 2018). The γ-ray emission increases towards periastron, but no clear sign of a drop in the emission was detected (Balbo & Walter, 2017; White et al., 2020). White et al. (2020) detected a turnover at energies below several hundreds of MeV as discussed in Section 5.1. After the publication of the paper by White et al. (2020), Martí-Devesa & Reimer (2021) analysed Fermi-LAT data from η Carinae including the periastron passage in 2020. They confirmed the variability behaviour. A turnover below 1 GeV was also detected. However, the authors concluded, that it is not entirely clear if this feature is caused by difficulties in the analysis at these low energies.

The observed variability patterns allow to derive conclusions about the origin of the emission. The observed 5.5 yrs patterns corresponding to the orbital period of the system mean, that the largest amount of the non-thermal X-ray emission and at least some fraction of the γ rays are produced in the wind collision region or within distances of few tens of AU to the stars.

5.5.1   Origin of the GeV emission

The turnover in the low energy γ-ray emission makes a hadronic origin very likely. This is in line with the conclusions from Ohm et al. (2015). In our model described in Section 5.3, the maximum proton energy on the side of η Car A is restricted by the energy losses due to collisions with the high-density material. These protons account for the low energy γ-ray component. At the side of η Car B, protons are accelerated until they leave the shock cap. Therefore, higher energies can be reached, and these protons account for the high energy γ-ray component. Most of their energy is released in the ballistic region, where the low-density material from η Car B mixes with the higher density material from η Car A. The details of the mixing influence not only the
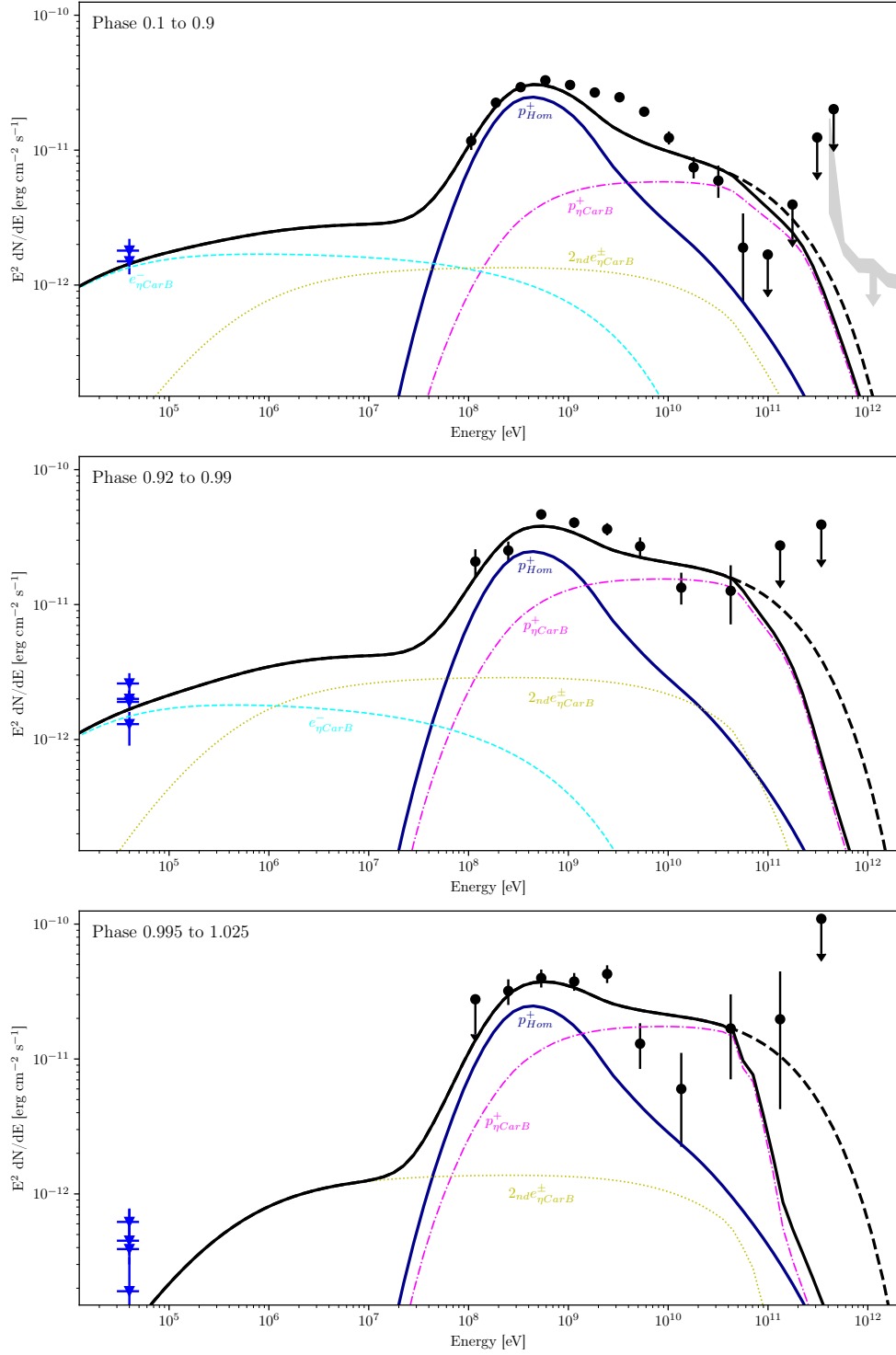
FIGURE 5.10: Emission from η Car B and the Homunculus compared to data for the same phase ranges as in Figure 5.6. Fermi-LAT data is shown with black circles and NuSTAR data with blue triangles. The total model curve is shown in black, and the dashed black line shows the emission without absorption. The colours for the individual contributions from η Car B are the same as in Figure 5.6, and the contribution from the Homunculus is shown with the blue curve.

hadronic emission, but also affects the emission from secondary electrons, especially the position of the low energy break caused by the transition from Coulomb cooling to IC cooling. The model can successfully reproduce the γ-ray spectra. As shown in Section 5.4, the low energy γ-ray emission could also be explained by a steady emission from escaped protons interacting in the Homunculus Nebula. In this scenario, only the shock on the side of η Car B serves as a particle accelerator. The variability in the low energy γ rays is accounted for by changes in the γ-ray fluxes from accelerated electrons and secondary electrons in the wind region. Although the scenario shown in Figure 5.10 does not match well the shape of the off-periastron spectrum, different diffusion properties in the Homunculus shell could improve this aspect.

5.5.2   Leptonic origin of the γ-ray emission

Although the emission above $\sim 10\,\mathrm{GeV}$ was always attributed to hadronic interactions, leptonic and hadronic scenarios for the low energy component were proposed previously (e.g. Farnier et al., 2011; Ohm et al., 2015; Reitberger et al., 2015; Balbo & Walter, 2017; Hamaguchi et al., 2018). Hamaguchi et al. (2018) proposed, that the same population of accelerated electrons produces the non-thermal X-ray emission. The detection of a turnover at a few hundreds of MeV makes such a scenario very unlikely. Furthermore, due to the different variability of the non-thermal X-ray emission compared to the low energy γ rays, scenarios in which the same population of particles produces both components are strongly disfavoured. In the model from Section 5.3, the non-thermal NuSTAR emission is nearly exclusively produced by electrons from the side of η Car B. Therefore, it is in principle possible that electrons accelerated at the side of η Car A account for the low energy γ rays. However, to account for the turnover, an equilibrium spectrum harder than $E^2 \mathrm{d}N/\mathrm{d}E \propto E^{1/2}$ is required. Such a hard spectrum can not be achieved with standard diffusive shock acceleration. On the other hand, the turnover is a natural outcome of hadronic scenarios. Let us suppose that the low energy γ-ray emission would indeed be due to electrons from η Car A and the non-thermal X-rays from η Car B electrons. In that case, it is puzzling why the total hadronic emission at both shocks is low compared to the emission from electrons. Similarly, previous leptonic models required a comparable amount of energy in leptons and hadrons (e.g. Farnier et al., 2011; Balbo & Walter, 2017). This would imply, that the particle acceleration in η Carinae is very different from acceleration in SNRs. Models for SNRs commonly need

$\sim 10\%$ of the available shock power in accelerated hadrons and a ratio between electrons and protons of $\sim 10^{-4} - 10^{-2}$ (e.g. Helder et al., 2010; Zirakashvili & Aharonian, 2010). Contrary to lepto-hadronic models for the γ-ray emission in η Carinae, in the models developed in this chapter, the particle acceleration at the shocks in η Carinae is similar to hadronic models of SNR shocks.

5.5.3   Leptonic emission and NuSTAR observations

The non-thermal component in the NuSTAR data detected by Hamaguchi et al. (2018) is well below the energies of any π^0 bump feature. This is a clear sign of the presence of accelerated electrons. Secondary particles in our model from Section 5.3 can not account for the fluxes away from periastron. The electrons will have a break in their spectra caused by the transition from ionisation and excitation losses to IC losses. Due to the large densities, the break occurs at higher energies for η Car A. For η Car B, the break in the γ-ray spectrum is close to the NuSTAR regime, but the total γ-ray emission softens between the NuSTAR and the Fermi-LAT energy range caused by emission from secondary particles. Given that a large fraction of the protons from η Car B interacts in the ballistic region, the break in the resulting secondary electrons is shifted to higher energies compared to the primary electrons. Therefore, data between the NuSTAR and Fermi-LAT energy range could help to constrain densities in the ballistic region where the material from both winds mixes. Unfortunately, the amount of directly accelerated electrons from η Car A is not well constrained.

At periastron, the emission from secondary particles can account for the residual NuSTAR emission. Since no sign of a disappearance of the γ-ray flux is observed, a complete collapse of the shock onto the companion star is unlikely. If η Car B is responsible for the high energy γ-ray component, at least in the outer part of the wind collision region, shock acceleration has to be ongoing. Here, we proposed an alternative scenario, in which the heating and electron injection at the side of η Car A is stopped by the low Alfvén Mach numbers. The electron acceleration at the side of η Car B is assumed to be prevented, because the whistler phase speed exceeds the shock velocity. If this is indeed the case, η Carinae would be a powerful tool to test particle acceleration theories.

5.5.4   Highest energies and H.E.S.S. observations

Away from periastron, the maximum particle energies are constrained to be around 400 GeV by the Fermi-LAT observations and the H.E.S.S. upper limit. At pre-periastron and periastron, the Fermi-LAT data alone only constrains the emission to be larger than $\sim$500 TeV. However, the detection from H.E.S.S. during these phases points towards cutoff energies around few TeV. As Gupta & Razzaque (2017) noted, η Car would have been a potential neutrino source, but the constraints on the maximum energies make it very unlikely. Even for maximum particle energies above 12 TeV, which need acceleration efficiencies of $\eta_{\mathrm{acc}} = 1$, the neutrino fluxes above 1 TeV would be less than $2 \times 10^{-11}\,\mathrm{erg\,cm^{-2}\,s^{-1}}$, and above 10 TeV less than $3.3 \times 10^{-13}\,\mathrm{erg\,cm^{-2}\,s^{-1}}$. However, to be consistent with H.E.S.S. measurements, protons above few TeV would have to be able to escape the ballistic region without significant interactions.

The model from Section 5.3 can not explain the H.E.S.S. observations. While the maximum required energies can be approximately achieved, the absorption by the stellar photon fields prevents any detection. Consequently, the high energy emission has to be produced further out in the wind region at distances of the order of $\sim$50 AU or larger. A revision of the model is required, and potential emission regions in the wind region have to be identified. The details of the resulting emission will depend on the transport mechanisms.

A potential emission from the Homunculus Nebula is unlikely to be able to explain the H.E.S.S. data, because the high energy particles will pass the nebula quickly. However, models in which the Homunculus nebula is responsible for a large part of the low energy γ rays are viable. In this case, the shock at the side of η Car B is responsible for the acceleration of all particles, and the shock on the side of η Car A might be not able to accelerate particles because of low values of the Alfvén Mach number M_{A}. A possible contribution from particles directly accelerated at the expanding Homunculus as proposed by Ohm et al. (2010) is also possible. More observations in different energy bands are required to disentangle different scenarios.

6 Summary and conclusion

In Chapter 3 of this thesis, it was shown that UHE IC emitters can exist in environments of increased far-infrared radiation fields or regions with low magnetic fields. Pulsars are able to accelerate particles to these energies, and the HAWC and LHAASO sources modelled in Chapter 3 can be explained with such scenarios. A decoupling between the acceleration region and the emission zone is likely required for UHE γ-ray sources. In the case of LHAASO J2226+6057, there is strong evidence for such a decoupling. Radio images show a clear outflow from the Boomerang Nebula towards the direction of the centre of the LHAASO source (Liu et al., 2020). These images also show the importance of additional multiwavelength data to discover more about the true nature of the sources.

A clear limitation of this work is that only data for energies >1 TeV was used for the analysis. Each of the sources modelled in Chapter 3 deserves an extended study, which should be done in the future. Using additional data from Fermi-LAT will be very important to determine cooling breaks or to detect any potential signatures of a pion bump. A detection of large-scale synchrotron emission would be beneficial to constrain the magnetic field, but unfortunately, no detection has been achieved yet. Such radio data would be especially beneficial for LHAASO J1908+0621 / eHWC J1907+063 since an enhancement of the radiation field is excluded by the IRAS data, leaving the magnetic field as the only unknown environmental parameter. Additional X-ray data would also be useful to constrain potential synchrotron emission and the magnetic fields. A first step towards a better understanding of the sources should include an analysis of Fermi-LAT data and a combined modelling to further constrain the environmental and other model parameters.

However, data from different wavelengths must be combined carefully, because they could originate from different regions. The environment of each source is complex, and more than one source might contribute to lower energy emission. Important conclusions about the leptonic or hadronic origin of the sources can also be achieved by studies of the energy-dependent morphology at ultra-high energies. If the extension of the source is not increasing with energy, its size is cooling limited, which is a clear sign of a leptonic origin. High-resolution data from CTA will provide significant insights in this regard.

Apart from the sources analysed in this thesis, more LHAASO sources should be investigated. Since LHAASO is constantly collecting data, a detailed analysis of the spectral energy distribution of these sources is expected in the near future. Most of the sources have a possible pulsar association, and likely, at least several of them are indeed associated with these pulsars. However, if most of the LHAASO UHE sources are leptonic sources, the question is raised why only a few hadronic sources producing the diffuse CRs until the knee energies are observed. One possible explanation might be that the particle acceleration of hadronic CRs occurs in low-density environments and produce fewer hadronic emissions. Furthermore, CRs with high energies escape faster and, therefore, might release a large fraction of their energy further away from their sources. If most of the PeV CRs are produced during short transient events, such as the first years of supernova explosions, the detection of such sources is less likely.

In Chapter 4, it was shown that a heavier CR composition reduces the resulting hadronic emission, and spectral features occur at lower energies. If a spectral feature is rigidity dependent, it manifests at a γ-ray energy of $\approx 1/2$ of the pure hydrogen case. These effects are especially important for the shape of the γ-ray and neutrino emission produced by CRs in the knee region. Compositional effects should be considered in the interpretation of future measurements. Current observations do not lead to firm conclusions yet, but this will change with more data from LHAASO, SWGO, and CTA. γ-ray measurements of the diffuse emission are a tool to constrain the CR composition in the knee region in different places of the Galaxy. However, the data has to be analysed carefully to subtract contributions from unresolved sources (see also e.g. Vecchiotti et al., 2021). If the composition varies across the Galaxy, it would be impossible to disentangle these effects from changes in the spectral index with γ-ray data alone. A detection of possible spatial variations of the knee signature in γ-ray measurements can have different reasons. For example, the CRs might not be in a steady state. It is also possible that local sources

have a significant impact, and not all sources produce CR spectra with the same spectral shape and composition in all regions of the Milky Way. Furthermore, the spectral shape will also be affected, if the CR propagation is not everywhere well described by diffusion with the same diffusion coefficient. The rigidity dependence of the diffusion coefficient could also change throughout the Galaxy.

Chapter 5 was aimed at disentangling the origin of the γ-ray emission in η Carinae. We successfully reproduced the spectral and temporal behaviour of the non-thermal X-ray and the γ-ray emission detected by Fermi-LAT. In the future, a more detailed investigation of possible emission from the Homunculus Nebula and the wind region is necessary, especially to explain the H.E.S.S. observations. A hadronic origin of the γ-ray emission seems more likely than a leptonic one, especially because of the detection of the pion bump. In such models, $\sim 10\%$ of the wind power are transferred into the acceleration of protons, and approximately two orders of magnitude less into the acceleration of electrons. It is likely, that combined shocks from stellar winds in SFRs behave similarly.

The orbital variabilities of η Carinae offer a unique laboratory to study the effects of, for instance, low Alfvén Mach number on the injection of particles into the acceleration process. In the model in Section 5.3, the flux of secondary particles accounted fully for the non-thermal X-ray emission at periastron, and the secondary IC emission has a different spectral index in the NuSTAR regime compared to the primary electrons. Hence, the scenario of an inhibited primary electron acceleration can be tested by analysing the spectral index of the non-thermal X-ray emission for different phases.

7 Personal bibliography

M. Breuhaus, J. A. Hinton, V. Joshi, B. Reville, and H. Schoorlemmer. Galactic gamma-ray and neutrino emission from interacting cosmic-ray nuclei. *Astronomy & Astrophysics*, Volume 661, A72, May 2022.

M. Breuhaus, B. Reville, and J. A. Hinton. Pulsar wind nebula origin of the LHAASO-detected ultra-high energy γ-ray sources. *Astronomy & Astrophysics*, Volume 660, A8, April 2022.

M. Breuhaus, J. Hahn, C. Romoli, B. Reville, G. Giacinti, R. Tuffs, and J. A. Hinton. Ultra-high Energy Inverse Compton Emission from Galactic Electron Accelerators. In *37th International Cosmic Ray Conference (ICRC2021), Proceedings of Science*, Volume 37 of *International Cosmic Ray Conference*, 2021.

M. Breuhaus, J. Hahn, C. Romoli, B. Reville, G. Giacinti, R. Tuffs, and J. A. Hinton. Ultra-high Energy Inverse Compton Emission from Galactic Electron Accelerators. *The Astrophysical Journal Letters*, Volume 908, Issue 2, L49, February 2021.

R. White, **M. Breuhaus**, R. Konno, S. Ohm, B. Reville, and J. A. Hinton. Gamma-ray and X-ray constraints on non-thermal processes in η Carinae. *Astronomy & Astrophysics*, Volume 635, A144, March 2020.

Bibliography

Aartsen, M. G., Ackermann, M., Adams, J., et al. 2019, Phys. Rev. D, 100, 100

Abdo, A. A., Ackermann, M., Ajello, M., et al. 2010, ApJ, 723, 649

Abdo, A. A., Ackermann, M., Ajello, M., et al. 2009a, Science, 325, 840

Abdo, A. A., Ackermann, M., Ajello, M., et al. 2009b, ApJS, 183, 46

Abdo, A. A., Allen, B., Aune, T., et al. 2008, ApJ, 688, 1078

Abdo, A. A., Allen, B., Berley, D., et al. 2007, ApJ, 664, L91

Abeysekara, A. U., Albert, A., Alfaro, R., et al. 2017, Science, 358, 911

Abeysekara, A. U., Albert, A., Alfaro, R., et al. 2021, Nature Astronomy, 5, 465

Abeysekara, A. U., Albert, A., Alfaro, R., Alvarez, C., et al. 2019, ApJ, 881, 134

Abeysekara, A. U., Albert, A., Alfaro, R., et al. 2020, Phys. Rev. Lett., 124, 021102

Abramowski, A., Acero, F., Aharonian, F., et al. 2012, MNRAS, 424, 128

Abramowski, A., Aharonian, F., Ait Benkhali, F., et al. 2014, Phys. Rev. D, 90, 122007

Acero, F., Ackermann, M., Ajello, M., et al. 2016, ApJS, 223, 26

Achterberg, A. 2004, in Accretion Discs, Jets and High Energy Phenomena in Astrophysics, ed. Beskin, V. et al., Vol. 78, 313–401

Achterberg, A., Gallant, Y. A., Kirk, J. G., & Guthmann, A. W. 2001, MNRAS, 328, 393

Ackermann, M., Ajello, M., Allafort, A., et al. 2013, Science, 339, 807

Ackermann, M., Ajello, M., Atwood, W. B., et al. 2012, ApJ, 750, 3

Adriani, O., Barbarino, G. C., Bazilevskaya, G. A., et al. 2013, Phys. Rev. Lett., 111, 081102

Agaronyan, F. A. & Ambartsumyan, A. S. 1985, Astrophysics, 23, 650

Agaronyan, F. A., Atoyan, A. M., & Nagapetyan, A. M. 1983, Astrophysics, 19, 187

Agostinelli, S., Allison, J., Amako, K., et al. 2003, Nuclear Instruments and Methods in Physics Research Section A: Accelerators, Spectrometers, Detectors and Associated Equipment, 506, 506

Aguilar, M., Aisa, D., Alpat, B., et al. 2015, Phys. Rev. Lett., 114, 171103

Aguilar, M., Alberti, G., Alpat, B., Alvino, A., et al. 2013, Phys. Rev. Lett., 110, 141102

Aguilar, M., Ali Cavasonza, L., Alpat, B., et al. 2017, Phys. Rev. Lett., 119, 251101

Aguilar, M., Ali Cavasonza, L., Alpat, B., et al. 2019a, Phys. Rev. Lett., 122, 101101

Aguilar, M., Ali Cavasonza, L., Ambrosi, G., et al. 2019b, Phys. Rev. Lett., 122, 041102

Aguilar, M., Ali Cavasonza, L., Ambrosi, G., et al. 2020, Phys. Rev. Lett., 124, 211102

Aguilar, M., Ali Cavasonza, L., Ambrosi, G., et al. 2021, Physics Reports, 894, 894

Aharonian, F., Akhperjanian, A. G., Anton, G., et al. 2009, A&A, 499, 723

Aharonian, F., Akhperjanian, A. G., Bazer-Bachi, A. R., Beilicke, M., et al. 2006, ApJ, 636, 777

Aharonian, F., Peron, G., Yang, R., Casanova, S., & Zanin, R. 2020, Phys. Rev. D, 101, 101

Aharonian, F., Yang, R., & de Oña Wilhelmi, E. 2019, Nature Astronomy, 3, 561

Aharonian, F. A. 2004, Very high energy cosmic gamma radiation : a crucial window on the extreme Universe (World Scientific)

Aharonian, F. A. & Atoyan, A. M. 1981, Ap&SS, 79, 321

Ahlers, M., Bai, Y., Barger, V., & Lu, R. 2016, Phys. Rev. D, 93, 013009

Ahn, E.-J., Engel, R., Gaisser, T. K., Lipari, P., & Stanev, T. 2009a, Phys. Rev. D, 80, 094003

Ahn, H. S., Allison, P., Bagliesi, M. G., et al. 2009b, ApJ, 707, 593

Aitken, D. K., Smith, C. H., Moore, T. J. T., & Roche, P. F. 1995, MNRAS, 273, 359

Albert, A., Alfaro, R., Alvarez, C., et al. 2021a, ApJ, 911, L27

Albert, A., Alfaro, R., Alvarez, C., et al. 2021b, ApJ, 914, 106

Albert, A., Alfaro, R., Alvarez, C., et al. 2021c, ApJ, 911, 143

Albert, A., Alfaro, R., Alvarez, C., et al. 2020, ApJ, 896, L29

Albert, A., Alfaro, R., Ashkar, H., et al. 2019, arXiv e-prints, arXiv:1902.08429

Albert, A., André, M., Anghinolfi, M., et al. 2018, ApJ, 868, L20

Aloisio, R. 2012, arXiv e-prints, arXiv:1211.2004

Amato, E. & Blasi, P. 2018, Advances in Space Research, 62, 2731

Amato, E. & Olmi, B. 2021, Universe, 7, 448

Amenomori, M., Bao, Y. W., Bi, X. J., et al. 2019, Phys. Rev. Lett., 123, 123

Amenomori, M., Bao, Y. W., Bi, X. J., et al. 2021a, Phys. Rev. Lett., 127, 031102

Amenomori, M., Bao, Y. W., Bi, X. J., et al. 2021b, Phys. Rev. Lett., 126, 141101

Atoyan, A. M. & Aharonian, F. A. 1999, MNRAS, 302, 253

Atwood, W. B., Abdo, A. A., Ackermann, M., et al. 2009, The Astrophysical Journal, 697, 697

Axford, W. I., Leer, E., & Skadron, G. 1977, in International Cosmic Ray Conference, Vol. 11, International Cosmic Ray Conference, 132

Bai, X., Bi, B. Y., Bi, X. J., et al. 2019, arXiv e-prints, arXiv:1905.02773

Balbo, M. & Walter, R. 2017, A&A, 603, A111

Balogh, A. & Treumann, R. A. 2013, Physics of Collisionless Shocks – Space Plasma Shock Waves, first edition edn., ISSI Scientific Report No. SR-12 (Heidelberg-Berlin-New York: Springer-Verlag), xII, 500 pp, 170 illustr., 38 in colour

Bartoli, B., Bernardini, P., Bi, X. J., et al. 2015, ApJ, 806, 20

Bednarek, W. & Pabich, J. 2011, A&A, 530, A49

Bell, A. R. 1978, MNRAS, 182, 147

Bell, A. R. 2004, MNRAS, 353, 550

Bell, A. R. & Lucek, S. G. 2001, MNRAS, 321, 433

Bell, A. R., Schure, K. M., Reville, B., & Giacinti, G. 2013, MNRAS, 431, 415

Bergström, L., Bringmann, T., & Edsjö, J. 2008, Phys. Rev. D, 78, 103520

Bernard, J. P., Paradis, D., Marshall, D. J., Montier, L., et al. 2010, A&A, 518, L88

Beskin, V. S. 2018, Physics Uspekhi, 61, 353

Bethe, H. & Heitler, W. 1934, Proceedings of the Royal Society of London Series A, 146, 83

Białas, A., Bleszyński, M., & Czyż, W. 1976, Nuclear Physics B, 111, 461

Bianchi, S. 2007, A&A, 471, 765

Bignami, G. F., Boella, G., Burger, J. J., et al. 1975, Space Science Instrumentation, 1, 245

Bigongiari, C. 2005, in International Europhysics Conference on High Energy Physics, HEP2005, 20

Blandford, R. & Eichler, D. 1987, Phys. Rep., 154, 1

Blandford, R. D. & Ostriker, J. P. 1978, ApJ, 221, L29

Blaufuss, E. & Karle, A. 2017, A Next-Generation IceCube: The IceCube-Gen2 Facility for High-Energy Neutrino Astronomy, ed. T. Gaisser & A. Karle, 183–197

Blumenthal, G. R. & Gould, R. J. 1970, Reviews of Modern Physics, 42, 237

Borione, A., Catanese, M. A., Chantell, M. C., et al. 1998, The Astrophysical Journal, 493, 493

Bosch-Ramon, V. & Khangulyan, D. 2009, International Journal of Modern Physics D, 18, 347

Breuhaus, M., Hahn, J., Romoli, C., et al. 2021, in Proceedings of 37th International Cosmic Ray Conference — PoS(ICRC2021), Vol. 395, 932

Breuhaus, M., Hahn, J., Romoli, C., et al. 2021, ApJ, 908, L49

Breuhaus, M., Hinton, J. A., Joshi, V., Reville, B., & Schoorlemmer, H. 2022a, A&A, 661, A72

Breuhaus, M., Reville, B., & Hinton, J. A. 2022b, A&A, 660, A8

Bühler, R. & Blandford, R. 2014, Reports on Progress in Physics, 77, 066901

Bykov, A. M., Marcowith, A., Amato, E., et al. 2020, Space Sci. Rev., 216, 42

Canto, J., Raga, A. C., & Wilkin, F. P. 1996, ApJ, 469, 729

Cao, Z., Aharonian, F. A., An, Q., et al. 2021, Nature, 594, 33

Cassing, W., Metag, V., Mosel, U., & Niita, K. 1990, Physics Reports, 188, 188

Castor, J. I., Abbott, D. C., & Klein, R. I. 1975, ApJ, 195, 157

Cerutti, B. & Beloborodov, A. M. 2017, Space Sci. Rev., 207, 111

Cesarsky, C. J. 1980, ARA&A, 18, 289

Cholis, I. & Hooper, D. 2013, Phys. Rev. D, 88, 023013

Clementel, N., Madura, T. I., Kruip, C. J. H., Icke, V., & Gull, T. R. 2014, MNRAS, 443, 2475

Conti, P. S. & Ebbets, D. 1977, ApJ, 213, 438

Coppi, P. S. & Blandford, R. D. 1990, MNRAS, 245, 453

Corcoran, M. F. 2005, AJ, 129, 2018

Corcoran, M. F. & Hamaguchi, K. 2007, in Revista Mexicana de Astronomia y Astrofisica Conference Series, Vol. 30, 29–34

Corcoran, M. F., Hamaguchi, K., Liburd, J. K., et al. 2015, arXiv e-prints, arXiv:1507.07961

Corcoran, M. F., Liburd, J., Morris, D., et al. 2017, ApJ, 838, 45

Crestan, S., Giuliani, A., Mereghetti, S., et al. 2021, MNRAS, 505, 2309

CTA Consortium, Acharya, B. S., Agudo, I., et al. 2019, Science with the Cherenkov Telescope Array

Damineli, A., Hillier, D. J., Corcoran, M. F., et al. 2008, MNRAS, 384, 1649

Davidson, K. & Humphreys, R. M. 1997, ARA&A, 35, 1

Davidson, K. & Humphreys, R. M. 2012, Astrophysics and Space Science Library, Vol. 384, Eta Carinae and the Supernova Impostors (Springer-Verlag)

Davies, L. J. M., Driver, S. P., Robotham, A. S. G., et al. 2016, MNRAS, 461, 458

De Looze, I., Fritz, J., Baes, M., et al. 2014, A&A, 571, A69

de Oña Wilhelmi, E., López-Coto, R., Amato, E., & Aharonian, F. 2022, ApJ, 930, L2

Dermer, C. D. & Schlickeiser, R. 1991, A&A, 252, 414

DeYoung, T. & HAWC Collaboration. 2012, Nuclear Instruments and Methods in Physics Research A, 692, 72

Di Sciascio, G. 2022, Applied Sciences, 12, 12

di Sciascio, G. & Lhaaso Collaboration. 2016, Nuclear and Particle Physics Proceedings, 279-281, 166

Dopita, M. A., Groves, B. A., Fischera, J., et al. 2005, ApJ, 619, 755

Dubus, G. 2006, A&A, 451, 9

Duvidovich, L., Giacani, E., Castelletti, G., Petriella, A., & Supán, L. 2019, A&A, 623, A115

Duvidovich, L., Petriella, A., & Giacani, E. 2020, MNRAS, 491, 5732

Dzhappuev, D. D., Afashokov, Y. Z., Dzaparova, I. M., et al. 2021, ApJ, 916, L22

Dzhatdoev, T. 2021, arXiv e-prints, arXiv:2104.02838

Edmiston, J. P. & Kennel, C. F. 1986, J. Geophys. Res., 91, 1361

Eichler, D. & Usov, V. 1993, ApJ, 402, 271

Erber, T. 1966, Reviews of Modern Physics, 38, 626

Esmaili, A. & Serpico, P. D. 2021, Phys. Rev. D, 104, L021301

Evoli, C., Amato, E., Blasi, P., & Aloisio, R. 2021, Phys. Rev. D, 103, 083010

Fang, K. & Murase, K. 2021, ApJ, 919, 93

Farnier, C., Walter, R., & Leyder, J. 2011, A&A, 526, A57+

Fermi, E. 1949, Physical Review, 75, 1169

Ferrière, K. 1998, ApJ, 497, 759

Ferrière, K., Gillard, W., & Jean, P. 2007, A&A, 467, 611

Fichtel, C. E., Hartman, R. C., Kniffen, D. A., et al. 1975, ApJ, 198, 163

Fletcher, R. S., Gaisser, T. K., Lipari, P., & Stanev, T. 1994, Phys. Rev. D, 50, 5710

Franco, V. & Glauber, R. J. 1966, Phys. Rev., 142, 142

Funk, S. 2015, Annual Review of Nuclear and Particle Science, 65, 245

Gaensler, B. M. & Johnston, S. 1995, MNRAS, 277, 1243

Gaensler, B. M. & Slane, P. O. 2006, ARA&A, 44, 17

Gaggero, D., Grasso, D., Marinelli, A., Urbano, A., & Valli, M. 2015, ApJ, 815, L25

Gaisser, T. K. 1990, Cosmic rays and particle physics. (Cambridge University Press)

Gaisser, T. K. & Schaefer, R. K. 1992, ApJ, 394, 174

Giacinti, G. & Kirk, J. G. 2018, ApJ, 863, 18

Giacinti, G., Mitchell, A. M. W., López-Coto, R., et al. 2020, A&A, 636, A113

Ginzburg, V. L. & Syrovatskii, S. I. 1964, The Origin of Cosmic Rays

Ginzburg, V. L. & Syrovatskii, S. I. 1965, ARA&A, 3, 297

Glauber, R. J. 1955, Phys. Rev., 100, 100

Glauber, R. J. & Matthiae, G. 1970, Nucl. Phys. B, 21, 21

Goldreich, P. & Julian, W. H. 1969, ApJ, 157, 869

Gould, R. J. 1975, ApJ, 196, 196

Gould, R. J. & Rephaeli, Y. 1978, ApJ, 225, 318

Gould, R. J. & Schréder, G. P. 1967, Physical Review, 155, 1408

Grebenyuk, V., Karmanov, D., Kovalev, I., et al. 2019, Advances in Space Research, 64, 2546

Greisen, K. 1966, Phys. Rev. Lett., 16, 16

Groves, B., Dopita, M. A., Sutherland, R. S., et al. 2008, ApJS, 176, 438

Gupta, N. & Razzaque, S. 2017, Phys. Rev. D, 96, 123017

Gusev, A. S. 2002, Astronomical and Astrophysical Transactions, 21, 75

H. E. S. S. Collaboration. 2018, A&A, 612, A1

H. E. S. S. Collaboration, Abdalla, H., Adam, R., et al. 2020, A&A, 635, A167

Hahn, J. 2015, in International Cosmic Ray Conference, Vol. 34, 34th International Cosmic Ray Conference (ICRC2015), 917

Hamaguchi, K., Corcoran, M. F., Gull, T., et al. 2007, ApJ, 663, 522

Hamaguchi, K., Corcoran, M. F., Pittard, J. M., et al. 2018, Nature Astronomy, 2, 731

Hamaguchi, K., Corcoran, M. F., Russell, C. M. P., et al. 2014a, ApJ, 784, 125

Hamaguchi, K., Corcoran, M. F., Russell, C. M. P., et al. 2014b, ApJ, 784, 125

Hansen, B. M. S. & Phinney, E. S. 1997, MNRAS, 291, 569

Harrison, F. A., Craig, W. W., Christensen, F. E., et al. 2013, ApJ, 770, 103

Hartman, R. C., Bertsch, D. L., Bloom, S. D., et al. 1999, ApJS, 123, 79

Haug, E. 1975, Zeitschrift Naturforschung Teil A, 30, 1099

Haug, E. 1981, Zeitschrift für Naturforschung A, 36, 36

Haverkorn, M., Brown, J. C., Gaensler, B. M., & McClure-Griffiths, N. M. 2008, ApJ, 680, 362

Helder, E. A., Kosenko, D., & Vink, J. 2010, ApJ, 719, L140

Hess, V. F. 1912, Phys. Z., 13, 13

Hewish, A., Bell, S. J., Pilkington, J. D. H., Scott, P. F., & Collins, R. A. 1968, Nature, 217, 709

Hillas, A. M. 1984, ARA&A, 22, 425

Hillier, D. J., Davidson, K., Ishibashi, K., & Gull, T. 2001, ApJ, 553, 837

Hinton, J. A. & Aharonian, F. A. 2007, ApJ, 657, 302

Hinton, J. A. & HESS Collaboration. 2004, New A Rev., 48, 331

Huentemeyer, P., BenZvi, S., Dingus, B., et al. 2019, in Bulletin of the American Astronomical Society, Vol. 51, 109

Huo, X. A., Ding, K. L., Ren, R. J., et al. 1990, in International Cosmic Ray Conference, Vol. 2, International Cosmic Ray Conference, 427

Hutchings, J. B. 1981, PASP, 93, 50

Iping, R. C., Sonneborn, G., Gull, T. R., Massa, D. L., & Hillier, D. J. 2005, ApJ, 633, L37

Ishibashi, K., Gull, T. R., Davidson, K., et al. 2003, AJ, 125, 3222

Ivanov, D. 2015, in International Cosmic Ray Conference, Vol. 34, 34th International Cosmic Ray Conference (ICRC2015), 349

Jansson, R. & Farrar, G. R. 2012a, ApJ, 757, 14

Jansson, R. & Farrar, G. R. 2012b, ApJ, 761, L11

Jokipii, J. R. 1973, ARA&A, 11, 1

Jones, F. C. 1968, Physical Review, 167, 1159

Joshi, J. C., Winter, W., & Gupta, N. 2014, MNRAS, 439, 3414

Joshi, V. 2019, Reconstruction and analysis of highest energy gamma-rays and its application to pulsar wind nebulae, PhD thesis, Heidelberg

Kachelriess, M., Moskalenko, I. V., & Ostapchenko, S. S. 2014, ApJ, 789, 136

Kafexhiu, E. 2016, Phys. Rev. C, 94, 94

Kafexhiu, E., Aharonian, F., Taylor, A. M., & Vila, G. S. 2014, Phys. Rev. D, 90, 123014

Kamae, T., Karlsson, N., Mizuno, T., Abe, T., & Koi, T. 2006, ApJ, 647, 692

Kashi, A., Principe, D. A., Soker, N., & Kastner, J. H. 2021, ApJ, 914, 47

Kelner, S. R., Aharonian, F. A., & Bugayov, V. V. 2006, Phys. Rev. D, 74, 034018

Kennel, C. F. & Coroniti, F. V. 1984, ApJ, 283, 694

Kippenhahn, R. & Moellenhoff, C. 1975, Elementare Plasmaphysik (Bibliographisches Institut Mannheim/Wien/Zürich, B.I.-Wissenschaftsverlag)

Kirk, J. G., Guthmann, A. W., Gallant, Y. A., & Achterberg, A. 2000, ApJ, 542, 235

Kirk, J. G., Melrose, D. B., Priest, E. R., Benz, A. O., & Courvoisier, T. J. L. 1994, Plasma Astrophysics (Springer-Verlag)

Klebesadel, R. W., Strong, I. B., & Olson, R. A. 1973, ApJ, 182, L85

Koldobskiy, S., Neronov, A., & Semikoz, D. 2021, arXiv e-prints, arXiv:2105.00959

Korpi, M. J., Brandenburg, A., Shukurov, A., & Tuominen, I. 1999, A&A, 350, 230

Kothes, R., Reich, W., & Uyanıker, B. 2006, ApJ, 638, 225

Kraushaar, W. L. & Clark, G. W. 1962, Phys. Rev. Lett., 8, 106

Kraushaar, W. L., Clark, G. W., Garmire, G. P., et al. 1972, ApJ, 177, 341

Krennrich, F., Bond, I. H., Boyle, P. J., et al. 2004, New A Rev., 48, 345

Krymskii, G. F. 1977, Akademiia Nauk SSSR Doklady, 234, 1306

Kwitter, K. B. 1981, ApJ, 245, 154

Lagage, P. O. & Cesarsky, C. J. 1983, A&A, 125, 249

Levinson, A. 1992, ApJ, 401, 73

Leyder, J., Walter, R., & Rauw, G. 2010, A&A, 524, A59+

Leyder, J.-C., Walter, R., & Rauw, G. 2008, A&A, 477, L29

Lhaaso Collaboration, Cao, Z., Aharonian, F., et al. 2021, Science, 373, 425

Li, C. & Ma, B.-Q. 2022, Physics Letters B, 829, 829

Lipari, P. & Vernetto, S. 2018, Phys. Rev. D, 98, 043003

Liu, R.-Y. & Wang, X.-Y. 2021, ApJ, 914, L7

Liu, S., Zeng, H., Xin, Y., & Zhu, H. 2020, ApJ, 897, L34

Longair, M. S. 2011, High Energy Astrophysics (Cambridge University Press)

López-Coto, R., Hahn, J., BenZvi, S., et al. 2018, Astroparticle Physics, 102, 1

Lucek, S. G. & Bell, A. R. 2000, MNRAS, 314, 65

Lund, N. 1984, Advances in Space Research, 4, 5

MacLachlan, J. M., Matthews, L. D., Wood, K., & Gallagher, J. S. 2011, ApJ, 741, 6

Maity, T. N., Saha, A. K., Dubey, A., & Laha, R. 2022, Phys. Rev. D, 105, L041301

Malkov, M. A. & Drury, L. O. 2001, Reports on Progress in Physics, 64, 429

Manchester, R. N., Hobbs, G. B., Teoh, A., & Hobbs, M. 2005, AJ, 129, 1993

Manchester, R. N. & Taylor, J. H. 1977, Pulsars

Martí-Devesa, G. & Reimer, O. 2021, A&A, 654, A44

Martí-Devesa, G., Reimer, O., Li, J., & Torres, D. F. 2020, A&A, 635, A141

Martínez-Huerta, H. & Pérez-Lorenzana, A. 2017, Phys. Rev. D, 95, 063001

Mascaretti, C., Blasi, P., & Evoli, C. 2020, Astroparticle Physics, 114, 22

Mastichiadis, A. 1991, MNRAS, 253, 235

Mastichiadis, A., Marscher, A. P., & Brecher, K. 1986, ApJ, 300, 178

Maurin, D., Dembinski, H. P., Gonzalez, J., Mariș, I. C., & Melot, F. 2020, Universe, 6, 102

Maurin, D., Melot, F., & Taillet, R. 2014, A&A, 569, A32

Mehner, A., Davidson, K., Humphreys, R. M., et al. 2015, A&A, 578, A122

Meyer, J. P. 1985, ApJS, 57, 173

Misiriotis, A., Popescu, C. C., Tuffs, R., & Kylafis, N. D. 2001, A&A, 372, 775

Mizuno, T., Tanaka, N., Takahashi, H., et al. 2017, ApJ, 841, 104

Moderski, R., Sikora, M., Coppi, P. S., & Aharonian, F. 2005, MNRAS, 363, 363

Mori, M. 2009, Astroparticle Physics, 31, 341

Mork, K. J. 1967, Phys. Rev., 160, 160

Murase, K. & Beacom, J. F. 2012, J. Cosmology Astropart. Phys., 2012, 043

Murray, N. & Rahman, M. 2010, ApJ, 709, 424

Neronov, A. & Semikoz, D. 2020, A&A, 633, A94

Neronov, A., Semikoz, D., & Vovk, I. 2021, A&A, 653, L4

Neugebauer, G., Habing, H. J., van Duinen, R., Aumann, H. H., et al. 1984, ApJ, 278, L1

Nifenecker, H. & Pinston, J. 1989, Progress in particle and nuclear physics, 23, 23

Ohm, S., Hinton, J. A., & Domainko, W. 2010, ApJ, 718, L161

Ohm, S., Zabalza, V., Hinton, J. A., & Parkin, E. R. 2015, MNRAS, 449, L132

Ostapchenko, S. 2006, Nuclear Physics B - Proceedings Supplements, 151, 151

Ostriker, J. P. & Gunn, J. E. 1969, ApJ, 157, 1395

Pacini, F. 1967, Nature, 216, 567

Pacini, F. 1968, Nature, 219, 145

Pacini, F. & Salvati, M. 1973, ApJ, 186, 249

Panov, A. D., Adams, J. H., Ahn, H. S., et al. 2009, Bulletin of the Russian Academy of Science, Phys., 73, 564

Parkin, E. R. & Pittard, J. M. 2008, MNRAS, 388, 1047

Parkin, E. R., Pittard, J. M., Corcoran, M. F., & Hamaguchi, K. 2011, ApJ, 726, 105

Parkin, E. R., Pittard, J. M., Corcoran, M. F., Hamaguchi, K., & Stevens, I. R. 2009, MNRAS, 394, 1758

Peron, G., Aharonian, F., Casanova, S., Yang, R., & Zanin, R. 2021, ApJ, 907, L11

Pittard, J. M. & Dawson, B. 2018, MNRAS, 477, 5640

Pittard, J. M. & Stevens, I. R. 1997, MNRAS, 292, 298

Popescu, C. C., Misiriotis, A., Kylafis, N. D., Tuffs, R. J., & Fischera, J. 2000, A&A, 362, 138

Popescu, C. C., Tuffs, R. J., Dopita, M. A., et al. 2011, A&A, 527, A109

Popescu, C. C., Yang, R., Tuffs, R. J., et al. 2017, MNRAS, 470, 2539

Pothast, M., Gaggero, D., Storm, E., & Weniger, C. 2018, J. Cosmology Astropart. Phys., 2018, 045

Prilutskij, O. F. & Usov, V. V. 1975, Astronomicheskij Tsirkulyar, 854, 1

Prosin, V. V., Berezhnev, S. F., Budnev, N. M., et al. 2014, Nuclear Instruments and Methods in Physics Research A, 756, 94

Pshirkov, M. S. 2016, MNRAS, 457, L99

Qiao, B.-Q., Liu, W., Zhao, M.-J., Bi, X.-J., & Guo, Y.-Q. 2021, arXiv e-prints, arXiv:2104.03729

Rawlins, K. & IceCube Collaboration. 2015, in International Cosmic Ray Conference, Vol. 34, 34th International Cosmic Ray Conference (ICRC2015), 334

Reimer, A., Pohl, M., & Reimer, O. 2006, ApJ, 644, 1118

Reitberger, K., Reimer, A., Reimer, O., & Takahashi, H. 2015, A&A, 577, A100

Reitberger, K., Reimer, O., Reimer, A., et al. 2012, A&A, 544, A98

Rybczyński, M. & Broniowski, W. 2011, Phys. Rev. C, 84, 84

Satunin, P. 2021, European Physical Journal C, 81, 750

Schlickeiser, R. 2002, Cosmic Ray Astrophysics (Springer-Verlag)

Schoo, S., Apel, W. D., Arteaga-Velázquez, J. C., et al. 2015, in International Cosmic Ray Conference, Vol. 34, 34th International Cosmic Ray Conference (ICRC2015), 263

Schutz, Y., Martinez, G., Marques, F., et al. 1997, Nuclear Physics A, 622, 622

Schwinger, J. 1949, Phys. Rev., 75, 75

Sekiguchi, A., Tsujimoto, M., Kitamoto, S., et al. 2009, PASJ, 61, 629

Sihver, L., Tsao, C. H., Silberberg, R., Kanai, T., & Barghouty, A. F. 1993, Phys. Rev. C, 47, 47

Sironi, L., Keshet, U., & Lemoine, M. 2015, Space Sci. Rev., 191, 519

Sjöstrand, T., Mrenna, S., & Skands, P. 2006, Journal of High Energy Physics, 2006, 2006

Smith, N. 2005, MNRAS, 357, 1330

Smith, N. 2006, ApJ, 644, 1151

Smith, N. & Ferland, G. J. 2007, ApJ, 655, 911

Spitkovsky, A. 2006, ApJ, 648, L51

Stevens, I. R., Blondin, J. M., & Pollock, A. M. T. 1992, ApJ, 386, 265

Tademaru, E. 1969, ApJ, 158, 959

Tammann, G. A., Loeffler, W., & Schroeder, A. 1994, ApJS, 92, 487

Tavani, M., Sabatini, S., Pian, E., et al. 2009, ApJ, 698, L142

The IceCube-Gen2 Collaboration, :, Aartsen, M. G., et al. 2020, arXiv e-prints, arXiv:2008.04323

The KASCADE-Grande Collaboration, :, Apel, W. D., et al. 2013, arXiv e-prints, arXiv:1306.6283

The Pierre Auger Collaboration, Aab, A., Abreu, P., et al. 2015, arXiv e-prints, arXiv:1509.03732

Tibet ASγ Collaboration, Amenomori, M., Bao, Y. W., et al. 2021, Nature Astronomy, 5, 460

Uesugi, A. & Fukuda, I. 1982, Catalogue of stellar rotational velocities (revised)

Usov, V. V. 1992, ApJ, 389, 635

Usov, V. V. & Melrose, D. B. 1992, ApJ, 395, 575

Vecchiotti, V., Zuccarini, F., Villante, F. L., & Pagliaroli, G. 2021, arXiv e-prints, arXiv:2107.14584

Vernetto, S. & Lipari, P. 2016, Phys. Rev. D, 94, 063009

Vink, J. 2020, Physics and Evolution of Supernova Remnants (Springer-Verlag)

Viotti, R. F., Antonelli, L. A., Rossi, C., & Rebecchi, S. 2004, A&A, 420, 527

Voisin, F., Rowell, G., Burton, M. G., et al. 2016, MNRAS, 458, 2813

Völk, H. J., Berezhko, E. G., & Ksenofontov, L. T. 2005, A&A, 433, 229

Votruba, V. 1948, Phys. Rev., 73, 73

Walder, R., Folini, D., & Meynet, G. 2012, Space Sci. Rev., 166, 145

Weber, E. J. & Davis, Leverett, J. 1967, ApJ, 148, 217

Webster, A. S. & Longair, M. S. 1971, MNRAS, 151, 261

Wentzel, D. G. 1974, ARA&A, 12, 71

Westfold, K. C. 1959, ApJ, 130, 241

White, R., Breuhaus, M., Konno, R., et al. 2020, A&A, 635, A144

White, R. L. 1985, ApJ, 289, 698

Williams, P. M., Dougherty, S. M., Davis, R. J., et al. 1997, MNRAS, 289, 10

Winkler, C. 1995, Experimental Astronomy, 6, 71

Woltjer, L. 1972, ARA&A, 10, 129

Yang, C., Zeng, H., Bao, B., & Zhang, L. 2022, A&A, 658, A60

Yang, M., Dai, S., Li, D., et al. 2021, Research in Astronomy and Astrophysics, 21, 141

Yang, R. & Aharonian, F. 2019, Phys. Rev. D, 100, 063020

Yang, R., Aharonian, F., & Evoli, C. 2016, Phys. Rev. D, 93, 93

Yang, R.-z., Kafexhiu, E., & Aharonian, F. 2018, A&A, 615, A108

Yoon, Y. S., Anderson, T., Barrau, A., et al. 2017, ApJ, 839, 5

Yu, H., Wu, K., Wen, L., & Fang, J. 2022, New A, 90, 101669

Zabalza, V. 2015, Proc. of International Cosmic Ray Conference, 34, 922

Zatsepin, G. T. & Kuz'min, V. A. 1966, Soviet Journal of Experimental and Theoretical Physics Letters, 4, 78

Zdziarski, A. A. & Krolik, J. H. 1993, ApJ, 409, L33

Zhang, P.-p., Qiao, B.-q., Yuan, Q., Cui, S.-w., & Guo, Y.-q. 2022, Phys. Rev. D, 105, 023002

Zhao, S., Zhang, R., Zhang, Y., & Yuan, Q. 2021, in Proceedings of 37th International Cosmic Ray Conference — PoS(ICRC2021), Vol. 395, 859

Zhu, J. & Huang, M. 2014, A&A, 564, A111

Zirakashvili, V. N. & Aharonian, F. A. 2010, ApJ, 708, 965